AuCuAl Shape Memory Alloys for Use in Opto-Mechanical Nanoactuators

This thesis is submitted in fulfilment of the requirements for the degree of Doctor of Philosophy (Science) at the University of Technology, Sydney

by

Vijay Kumar Bhatia B.Sc. (Nanotechnology) Hons

Certificate of Authorship / Originality

I certify that the work in this thesis has not previously been submitted for a degree nor has it been submitted as part of the requirements for a degree except as fully acknowledged within the text.

I also certify that the thesis has been written by me. Any help that I have received in my research work and the preparation of the thesis itself has been acknowledged. In addition, I certify that all information sources and literature used are indicated in the thesis

Signed:

Acknowledgements

First and foremost, my sincerest thanks go to my supervisors, who each made invaluable contributions towards this research and taught me so much along the way. Professor Michael Cortie was the one who started me on this path, and has been a constant source of information, inspiration and support along the way. I would also like to thank Dr Annette Dowd for her generosity in sharing her knowledge of optics and thin films (and her understanding regarding my lack of skill with the written word!) The general idea of activating shape memory alloy devices with a light source (at the macroscale) came out of a discussion in 2007 between then Honours student Sylvan Rudduck and Michael Cortie, and I thank Sylvan for starting a train of thought which has ended up in the present project on plasmonic shape memory nano-actuators. My project also built on the prior work of Dr Fiona Levey, in which the basic physical metallurgy of the Spangold alloy was established. And, last but not least, I would like to thank Dr Gordon Thorogood for the countless hours that he spent in the XRD lab modifying equipment, discussing unexplainable results, and for always being there when I needed someone to talk to. I am also extremely grateful for the many other people who have assisted me with this research over the years. These include Dr Richard Wuhrer (who taught me how to operate an SEM, and inspired what I expect will be a lifelong love of the analytical technique), Dr Catherine Kealley (who not only shared her knowledge and enthusiasm for science with me but also organised for us to participate in collaborative research with some amazing people and facilities around the world), Jean-Pierre Guerbois and Geoff McCredie (who spent hours adjusting equipment and were instrumental in the production of my samples), Dr Angus Gentle who assisted me with the determination of the dielectric function of my thin films, and the metallography staff at the Institute of Materials and Engineering Science, ANSTO (who helped me to prepare my samples for imaging). I also thank AINSE for the funding and the access to ANSTO's equipment and amazing staff that I have received throughout my PhD. Finally I would like to thank my family and friends for supporting me, always being there when times got tough, and reminding me every now and then that there is more to life than science.

Table of Contents

Certificate of Authorship / Originality i
Acknowledgements ii
Table of Contents iii
List of Figures viii
List of Tables xiv
Abstract xv
1 Introduction 1
2 Literature Review 4
2.1 Shape Memory Alloys 4
2.1.1 Introduction 4
2.1.2 Bulk TiNi SMAs 8
2.1.3 Bulk Cu-Al SMAs 10
2.1.4 Aging 17
2.2 Thin Films of Shape Memory Alloys 19
2.2.1 Introduction 19
2.2.2 Manufacturing 20
2.2.3 Properties of SMA Thin Films 21
2.2.4 Typical Compositions of Thin-film SMAs 23
2.2.5 Applications 26
2.3 Plasmonic Phenomena in Nanoscale Films and Structures 28
2.3.1 Introduction 28
2.3.2 Materials, Nano-structures and Sensors 29
2.3.3 Numerical Simulations of Plasmon Resonances 32
3 Materials and Method 35
3.1 Bulk Sample Preparation 35

3.1.1 Casting and Annealing 35
3.1.2 Sectioning 37
3.1.3 Mounting 38
3.1.4 Grinding and Polishing 40
3.2 Differential Scanning Calorimetry (DSC) 42
3.2.1 Shape Memory 44
3.2.2 Aging of Spangold 44
3.3 Optical Microscopy 45
3.3.1 Bright Field 45
3.3.2 Nomarski Interference Contrast (NIC) 47
3.4 Scanning Electron Microscopy (SEM) 47
3.5 Energy Dispersive Spectroscopy (EDS) 50
3.6 X-ray Diffraction (XRD) 51
3.7 Synchrotron Powder Diffraction 54
3.8 Neutron Powder Diffraction (NPD) 55
3.9 Thin-film Sample Preparation 56
3.9.1 Magnetron Sputtering 56
3.9.2 TEM Sample Preparation 58
3.9.3 Polishing 58
3.9.4 Ion Beam Milling / Thinning / PIPS 59
3.10 Grazing Incidence XRD (GIXRD) 59
3.11 X-ray Reflectometry 61
3.12 Transmission Electron Microscopy (TEM) 61
3.13 Profilometer 64
3.14 Electrical Resistance 64
3.15 Secondary Ion Mass Spectroscopy (SIMS) 65

3.16 Spectrophotometer 66
3.17 Computer Modelling of Optical Properties 66
4 Beta-phase AuCuAl SMAs 68
4.1 Introduction 68
4.2 Experimental 71
4.3 Results 72
4.4 Discussion 78
4.4.1 Phases present in alloys of varying Al wt.% 78
4.4.2 Differences in transformation with various Al wt.% 80
4.4.3 High temperature crystal structures 82
4.4.4 Low temperature crystal structures 84
4.5 Conclusion 87
5 Transformation Temperature and Aging of AuCuAl SMAs 88
5.1 Introduction 88
5.2 Experimental 89
5.3 Results 90
5.4 Discussion 97
5.5 Conclusion 102
6 Deposition of AuCuAl Thin Films 103
6.1 Introduction 103
6.2 Experimental 103
6.3 Results 106
6.4 Discussion 130
6.4.1 Setting up deposition conditions 130
6.4.2 Films deposited at less than 300ºC 133
6.4.3 Films deposited at greater than 300ºC 135

6.4.4 Films deposited with varying Al content 139
6.5 Conclusion 144
7 Properties of AuCuAl SMA Thin Films 145
7.1 Introduction 145
7.2 Experimental 145
7.3 Results 146
7.4 Discussion 153
7.4.1 Size limitation of SMAs 153
7.4.2 Cause of low transformation temperature 154
7.4.3 Lack of high temperature transformations 156
7.4.4 Increased transformation range 158
7.4.5 Effect of Al content on transformation temperature 160
7.5 Conclusion 161
8 Optical Properties of AuCuAl SMA Thin Films and Nanoactuators 162
8.1 Introduction 162
8.2 Experimental 163
8.3 Results 165
8.4 Discussion 176
8.4.1 Au actuators 176
8.4.2 SMA actuators 177
8.4.3 Limitations 178
8.4.4 Alternate designs and practical applications 183
8.5 Conclusion 188
9 Overall Conclusion 189
9.1 Bulk AuCuAl SMAs 189
9.2 AuCuAl Thin-film SMAs 191

9.3 Future Work 193

10 References 194

List of Figures

Figure 2.1 Austenite and martensite transformation mechanisms in shape memory alloys [43]. **5**

Figure 2.2 Differential scanning calorimetry (DSC) graph of shape memory transformation. **6**

Figure 2.3 SMA actuators used in Boeing variable geometry chevrons [39]. **8**

Figure 2.4 Spangold® jewellery. Photo by M. Cortie. **15**

Figure 2.5 Chemical ordering of the A2, B2, $L2_1$ and DO_3 structures [68]. **16**

Figure 2.6 Stability of phases in terms of chemical free energy, showing how lowering the free energy of the martensite phase will shift the M→A transformation temperature upwards, from T_1 to T_2. ..... **18**

Figure 2.7 Precipitation of γ_2 phase (black) in a CuAlMn SMA aged at 300°C [58]. **19**

Figure 2.8 Stress/temperature loops of TiNi thin films [5]. **22**

Figure 2.9 Electron micrograph of a linear actuator, made from TiNi thin-film [90]. **27**

Figure 2.10 Electron micrograph of a SMA MEM gripper [90] **28**

Figure 3.1 Example of OHS safety equipment worn by operators. **36**

Figure 3.2 Depth of deformation in different metals due to cutting method [144]. **38**

Figure 3.3 Example of cast alloy sample mounted in resin. **40**

Figure 3.4 Struers Knuth-Rotor 2 rotary sander. **41**

Figure 3.5 Struers RotoPol 22. ..... **42**

Figure 3.6 Thermal Analysis DSC 2920. ..... **43**

Figure 3.7 Ziess Axiotech, with a Media Cybernetics Evolution MP digital camera. **46**

Figure 3.8 Zeiss Supra 55 VP scanning electron microscope. **50**

Figure 3.9 Panalytical X'pert Pro X-ray diffractometer was also used with an Anton PAAR TTK 450 temperature stage. **53**

Figure 3.10 Synchrotron powder diffraction experiment. **55**

Figure 3.11 Comparison of X-ray and neutron cross section for some elements. X-ray scale has been reduced by a factor of approximately 1.5 [155]. 56
Figure 3.12 Magnetron sputtering chamber diagram. 57
Figure 4.1 Isothermal sections through the Al-Au-Cu ternary phase diagram showing the presence of various intermetallic compounds with a β-phase. (top) 500ºC section [34], (bottom) 750ºC section [30]. 69
Figure 4.2 Isopleth through the Al-Au-Cu ternary system with 76 wt.% Au [32]. . 70
Figure 4.3 SEM backscatter images of polished samples showing single phase and dual phase alloys. Top left – R3, top right – R4, bottom left – R5 and bottom right – R6. 72
Figure 4.4 SEM backscatter images of R4 (left) and R5 (right) after transformation showing martensite laths. 73
Figure 4.5 Nomarski interference images of cast samples before and after transformation showing martensitic laths. 76
Figure 4.6 Synchrotron X-ray powder diffraction of austenite phase samples. Data vertically offset for clarity. Wavelength - 1.15970 Å. 77
Figure 4.7 Transformation temperature vs. Al content (wt.%) or electron-to-atom ratio (E/A) of cast samples with Al content varying from 5.79 to 2.64 wt.%. 81
Figure 4.8 $L2_1$ structure model. A site - grey, B site - black, C site - white. 82
Figure 4.9 Synchrotron X-ray diffraction patterns of SMAs with various Al wt.% cooled below respective martensite transition temperatures. Left shows $L2_1$ (200) 2θ region and right shows (220). Wavelength - 1.15970 Å. 84
Figure 4.10 Synchrotron X-ray diffraction patterns of 5.79 Al wt.% SMA cooled to differnt temperatures. Left shows $L2_1$ (200) 2θ region and right shows (220). Wavelength - 0.42646 Å. 85
Figure 4.11 Phase diagram for CuAl composition showing transformation temperature trend and martensite structures formed [142]. 86
Figure 5.1Transformation temperatures of SMAs aged at given soak temperatures. 91
Figure 5.2 Transformation temperatures of SMAs aged at 90°C for given lengths of time. 93

Figure 5.3 X-ray diffraction patterns of SMA during *in-situ* aging at 90°C for given lengths of time. Offset for clarity. 94
Figure 5.4 NIC images before and after martensite transformation. Extracted from video (Appendix A) from 1:00 – 4:00 minutes at 20 sec intervals. 96
Figure 5.5 Aging of SMA under NIC imaging. Top left image before transformation, top right image 2 minutes after transformation, bottom left image 23.5hrs aging at 90°C, bottom right difference image. 97
Figure 6.1 Ternary diagram showing approximate composition ranges along blue line [35]. 105
Figure 6.2 Profilometer thickness of films (nm) vs. deposition temperature (°C). Error bars given as +/-1 std deviation of 5 measurements. Line of best fit added. 108
Figure 6.3 Phases produced through varying base pressure and target power. Grey - gamma phase, blue - beta phase (austenite), red - beta phase (martensite), yellow - alpha phase. 110
Figure 6.4 SEM images of segregated cubic domains of Au after annealing AuCuAl films at 450°C. 111
Figure 6.5 XRR curves for films deposited at given temperatures. Offset for clarity. 112
Figure 6.6 XRR data and fit models for 23, 100 and 150°C depositions. 113
Figure 6.7 SEM images of depositions with increasing temperature. 114
Figure 6.8 TEM images of films deposited at increasing temperature. 115
Figure 6.9 GIXRD of AuCuAl thin films deposited at temperature. 116
Figure 6.10 SIMS profiles of films deposited at temperature showing compositional variations throughout the thickness of the films. 118
Figure 6.11 Element map of film made at 400°C. O (top left), Al (top right), Cu (bottom left) and Au (bottom right). The Si substrate is on the right hand side of these images and the top surface of the film on the left hand side. 119
Figure 6.12 Images of regions for EDS analyses (film deposited at 300°C). 122
Figure 6.13 Images of regions for EDS analyses (film deposited at 400°C). 124
Figure 6.14 Images of regions for EDS analyses (film deposited at 23°C). 127

Figure 6.15 Digital photograph of films deposited at temperature as indicated show colour differences amongst films deposited at different temperatures indicating oxidation. **127**
Figure 6.16 GIXRD of films deposited with various Al contents showing the gradual change in crystal structure **129**
Figure 6.17 TEM images of samples deposited with various Al contents. Top left Beta 4, top right Beta 11, bottom Beta 17. ..... **130**
Figure 6.18 GIXRD patterns of films deposited at different base pressures. Offset for clarity. **132**
Figure 6.19 XRR of AuCuAl films deposited at 300, 350 and 400°C. Offset on vertical scale for clarity. **136**
Figure 6.20 SEM images of 250, 300, 350 and 400°C depositions showing spherical particles in films. **137**
Figure 6.21 Vishnoi *et al*'s FESEM images of Ni–Mn–Sn films deposited at (a) 450, (b) 500, (c) 550, (d) 600 and (e) 650 °C, showing the effect of substrate temperature on the morphology of the films [201]. **139**
Figure 6.22 GIXRD of first depositions after venting. Nominal compositions, Beta 1 – 5.7 Al wt.%, Beta 3 – 5.4 Al wt.%, Beta 8 – 4.8 Al wt.%. Offset for clarity. **140**
Figure 6.23 SIMS profiles of Al series films showing compositional variation. Ordered from highest to lowest Al content. **141**
Figure 7.1 Electrical resistance measurements of select films showing phase change. Offset for clarity. **147**
Figure 7.2 Electrical resistance measurement with first derivative. **147**
Figure 7.3 Electrical resistance measurement of martensite structured film. **148**
Figure 7.4 In-situ GIXRD of cooled austenite structured films at approximately -75°C. **150**
Figure 7.5 In-situ GIXRD of heated (~ 150°C) and cooled (~ -75°C) martensite structured film **150**
Figure 7.6 In-situ XRD of Beta 4 (top) and Beta 22 (bottom) showing change in diffraction pattern with temperature. Offset for clarity. **152**

Figure 8.1 Proposed actuator movement positions. Curvature value given below each model. Orientation of incident electromagnetic wave for all simulations shown in *b* = 1000. 164

Figure 8.2 Films arranged with increasing Al concentration from a nominal 1.5 wt.% (left) to 7 wt.% (right) and show the change of colour associated with the compositional variation. 165

Figure 8.3 Change in reflection spectra with varying Al content films. Reflection spectra offset for clarity, varying from nominal Al concentration of 7 wt.% (top) to 1.5 wt.% (bottom). 166

Figure 8.4 a*b* Colour chart of deposited films. Colour variation across depositions with varying nominal Al composition. a—1.5 wt.% Al, b—3 wt.% Al, c—5.8 wt.% Al, d—7 wt.% Al. 167

Figure 8.5 a*b* Colour chart from bulk alloys [33]. Colour variation across the76 wt.% Au vertical section; a— 0 wt.% Al, b—3 wt.% Al, c—5.8 wt.% Al, d—7.2 wt.% Al. 168

Figure 8.6 Optical ε_1 and ε_2 values for bulk materials and films. 169

Figure 8.7 Simulated Au extinction (top left), absorption (top right), scattering (bottom left) and modulation factor (bottom right) for different states of proposed actuator conformation. The values of actuator state shown correspond to their respective values of parameter *b*. 170

Figure 8.8 Simulated $Au_7Cu_5Al_4$ extinction (top left), absorption (top right), scattering (bottom left) and modulation factor (bottom right) for different states of proposed actuator conformation. The values of actuator state shown correspond to their respective values of parameter *b*. 171

Figure 8.9 Simulated Beta 22 extinction (top left), absorption (top right), scattering (bottom left) and modulation factor (bottom right) for different states of proposed actuator conformation. The values of actuator state shown correspond to their respective values of parameter *b*. 172

Figure 8.10 Simulated change in peak extinction (top), absorption (middle) and scattering (bottom) through a range of proposed actuations for Au, $Au_7Cu_5Al_4$ and Beta 22 actuators. The values of actuator state shown correspond to their respective values of parameter *b*. 173

Figure 8.11 Imaging of electric field as electromagnetic wave passes through Au actuator from left to right and imaged with wave at angle of 100° (left) and 280° (right). Blue indicates magnitude of field from left to right and red indicates magnitude of field from right to left. 175

Figure 8.12 Simulated thick Au actuator extinction (top left), absorption (top right), scattering (bottom left) and modulation factor (bottom right) for different states of proposed actuator conformation. The values of actuator state shown correspond to their respective values of parameter *b*. 180

Figure 8.13 Simulated thick $Au_7Cu_5Al_4$ actuator extinction (top left), absorption (top right), scattering (bottom left) and modulation factor (bottom right) for different states of proposed actuator conformation. The values of actuator state shown correspond to their respective values of parameter *b*. 181

Figure 8.14 Simulated thick Beta 22 actuator extinction (top left), absorption (top right), scattering (bottom left) and modulation factor (bottom right) for different states of proposed actuator conformation. The values of actuator state shown correspond to their respective values of parameter *b*. 182

Figure 8.15 Proposed actuator orientations in a hypothetical array. 184

Figure 8.16 Simulated transmission spectra for array of nano-actuators. 185

Figure 8.17 Simulated colour change for an array of nano-actuators. Left column shows simulated colour for actuators with *b*=30, right column shows simulated colour for actuators with *b*=1000. 186

List of Tables

Table 3.1 Polishing methodology guidelines **59**
Table 4.1 Composition of cast AuCuAl samples in at.% **74**
Table 4.2 Composition of cast AuCuAl samples in wt.% **74**
Table 4.3 Transformation temperature for cast samples **75**
Table 4.4 Best-fitting solutions to lattice occupancies for AuCuAl A_2BC β-phases at different Al contents. Accuracy of entries estimated to be not better than 0.05 due to residual texture effects in samples **83**
Table 6.1 Target power vs. deposition rate **107**
Table 6.2 Identified phases, and their deposition conditions **109**
Table 6.3 EDS composition analysis of select regions in film deposited at 300°C **120**
Table 6.4 EDS composition of select regions in film deposited at 400°C **123**
Table 6.5 EDS composition of select regions in film deposited at 23°C **125**
Table 6.6 Deposition conditions for films deposited with various Al concentrations **128**
Table 6.7 Deposited film properties and nominal Al content **143**
Table 6.8 Summarised film phases relative to the power of each target **144**
Table 7.1 Summary of transformation values. All values in °C **148**

Abstract

Shape memory alloys (SMAs) are a remarkable family of metallic materials that have the ability to return to their initial state and shape after being deformed. The key attribute that candidate alloys must possess is the existence of a reversible martensitic phase transformation. The most commonly used SMA, NiTi or 'Nitinol', has been proposed for a number of practical and theoretical applications [1-4], however a 100 nm lower limit has been found when producing thin films of this material for nanoscale applications. It has been shown that TiNi films thinner than this lose their shape memory effect due to oxide formation [5]. In the present work I explore whether variations of the $Au_7Cu_5Al_4$ SMA could be used as an alternate material for nanoscale SMA applications due to the resistance of $Au_7Cu_5Al_4$ to both aging [6] and oxidation [7]. A bonus is that the high Au content of this alloy may allow it to support a surface plasmon resonance in the visible part of the electromagnetic spectrum.

My project involved the investigation of both bulk and thin-film samples. A range of techniques were used to examine the properties of both the bulk and thin-film alloys including SEM, TEM, EDS, SIMS, powder diffraction (X-ray and neutron), thermal analysis, electrical resistance and spectrophotometry. Various types of mathematical modelling were then used to interpret the results as well as to simulate the operation of hypothetical devices made with this alloy.

Bulk AuCuAl SMAs with Al content varying along the Au 85 wt.% Au line of the AuCuAl ternary diagram were produced and their microstructures, physical properties and phase transformations studied. The extent to which the prototypical $Au_7Cu_5Al_4$ alloy resisted aging was investigated and the mechanisms that lead to some small changes in the transformation temperature under particular circumstances were considered. Whilst these alloys are very resistant to aging at high temperatures, aging below approximately 140°C in the austenite phase field results in a surprising and significant drop in the subsequent martensite-to-austenite transformation temperature.

Nanoscale films of AuCuAl with similar compositions to those of the bulk alloys were then synthesised. The phase transformation characteristics in these samples were also determined and found to be sensitive to the Al content and deposition conditions. The sub-100 nm-thick films were produced following the same compositional trend as the bulk ternary samples, producing a sequence of α-, β- and γ-structured films as the Al content was systematically increased. It is shown that, when deposited under the right conditions and with the correct compositions, AuCuAl films could be produced with the ability to undergo a reversible austenite/martensite phase transformation. Reflection and transmission spectra of these films were measured and used to calculate their dielectric function (complex refractive index). These data were in turn used to model the localised surface plasmon resonances in hypothetical, opto-mechanical nano-actuators made from $Au_7Cu_5Al_4$. The calculations predict that the extinction of light of a wavelength of 740 nm could be modulated by a factor of 26 times by a suitably designed, SMA actuator.

This project has paved the way for the possible future fabrication and testing of new opto-mechanical devices based on these principles.

1 Introduction

Shape memory alloys (SMAs) are a remarkable set of materials with the ability to revert back to an original shape or state after they have been deformed. The first metal recorded to have shape memory properties was AuCd, discovered in 1932 [8]. Since then many other shape memory alloys were found within a variety of different metallic binary and ternary systems, but it was not until the discovery of NiTi (trademarked Nitinol®) in 1961 by the Naval Ordinance Laboratories that shape memory alloys really started to become of wide interest [9]. This was due to the fact that the NiTi alloy was able to recover from quite large strains and did not suffer from the brittleness of its Cu-based counterparts.

From these beginnings SMAs have been extensively studied. Their structure and physical properties have been resolved, and a wide range of uses demonstrated. These metals have been used in everything from the under-wires of bras to arterial stents and intricate jewellery [3, 7, 10-13]. One new application that has been proposed for this material is for use in MEMS (Micro Electro Mechanical System) [14-22], microactuators and other small sensing devices. This has driven research in the area of thin-film SMAs in order to understand the changes that occur in these materials when produced in such small dimensions. A wide range of thin-film compositions and thicknesses have been produced for use in meso- and micro-scale devices. Films where the thickness is of the order of microns tend to behave with bulk properties, however new properties and limitations are observed in films of nanoscale thickness. This creates specific issues which need to be considered when designing nanoscale devices from these materials.

As with the bulk, the most common thin-film SMA is TiNi due to its familiarity and desirable large recoverable strain. A variety of thin-film SMA devices have been designed. Use of a thin-film SMA offers large advantages over other materials, including high power density, large displacement and low operating voltage, which are important when designing devices such as MEMS. The use of these materials in sensors

is also being explored as they are sensitive to environmental changes such as heat, physical stress, or (in certain SMAs) electric and magnetic fields. I will show here however that a SMA may also be developed to be sensitive to the optical environment. A suitable material for this is the gold-based shape memory alloy $Au_7Cu_5Al_4$. Due to this alloy's high gold content it is possible for it to support a plasmon resonance in the visible spectrum. The ability of nanoparticles of gold or silver to interact resonantly with light has been demonstrated for centuries [23] and there has been much research on the effect of size and shape of the nanoparticle on the localised surface plasmon resonance produced [24-26]. However, there has been virtually no research yet on the plasmonic properties of shape-changing, metallic nanostructures due, probably, to the absence of a suitable candidate material.

Enter $Au_7Cu_5Al_4$. This alloy is commonly known as Spangold® and it was developed by Wolff and Cortie for use in jewellery as it is 18 karat gold [7, 10]. Most of the bulk properties for this material are well known [7, 27-37] however no literature exists on the properties of this material when synthesised as a film. This alloy exhibits many interesting properties, including a unique colour and surface texture. Most importantly for the present work, it is a SMA, with M_s (onset of martensite transformation) and A_s (onset of austenite transformation) at about 25 and 75 ºC respectively. However due to the alloy's high manufacturing cost it has received little attention. This limitation falls away when thin films are made due to the small amounts of material required but a new question arises: what is the minimum practicable thickness of such a film? TiNi thin-film alloys have been shown to have a limiting thickness of around 100 nm which has been attributed to oxidation [5, 38]. In contrast, as $Au_7Cu_5Al_4$ is quite oxidation resistant, it is expected that this limit can be decreased further, allowing sub-100 nm actuators to be created.

This project aims to further the understanding of AuCuAl shape memory alloys, including the changes that occur as the Al content is varied, as the composition is known to have significant effects on the shape memory properties. It also looks at the extent to which these alloys are resistant to aging and the mechanisms which cause it. I will address the synthesis of AuCuAl thin films under 100 nm, varying the Al content to

produce films across the ternary diagram, whilst examining changes that occur to the physical properties in order to obtain the ideal deposition conditions. Thin films which exhibit a β-phase crystal structure are of particular interest and will be tested for the characteristic phase transformation from austenite to martensite that occurs in SMAs. The properties and structure of these films will then be compared to those of bulk materials in order to identify any differences due to nanoscale confinement.

Whilst this project did not reach the stage of actually producing discrete nanoscale actuators, the optical properties of these SMA thin films were measured and used in simulations to predict the performance of various theoretical actuator designs. The models were used to simulate the LSPR (Localised Surface Plasmon Resonance) of these nanoactuators as they change shape, with the intended purpose of such a device being to modulate the intensity of light.

2 Literature Review

2.1 Shape Memory Alloys

2.1.1 Introduction

A shape memory alloy (SMA) is a metal which demonstrates the ability to return to an initial shape after it has been deformed. This ability is due to a solid-to-solid phase transformation that occurs at critical temperatures specific to the type of alloy. The phases involved in the transformation are generically known as austenite and martensite; which are the high temperature and low temperature states respectively [39]. This is analogous to the austenite and martensite phases in steel. There are similarities in the lath-like structure formed in the martensites of both SMA and steel, and in the cooling process required to form them [39]. However, the austenite and martensite phases of shape memory alloys typically possess quite different crystal structures to the ferrous phases of the same names.

The first work explaining these phase transformations in SMAs was documented in 1949 by Kurdjumov and Khandros, based on one of the first SMAs - AuCd [40]. In most SMAs, the alloy has a body centred cubic (BCC) packing of atoms in the high-temperature, 'austenite' state, but as the temperature decreases the stability of the austenite decreases, until a temperature is reached at which the lattice spontaneously shears itself into the more closely packed martensite structure [41]. This phase transformation occurs because the martensite structure is more stable at lower temperatures, resulting in a diffusionless rearrangement of the atoms. The temperature at which this starts to occur is known as the M_s (martensite start) temperature. The rate of transformation is greatest at M_p (martensite peak) temperature and it finishes at the M_f (martensite finished) temperature. The process is reversible : as the temperature of martensite is increased the stability of the martensite structure relative to the austenite structure decreases until a temperature is reached at which the distorted lattice reverts back to the BCC packing of the austenite and recovers its original shape (Figure 2.1). There are A_s, A_p and A_f temperatures which are analogous to those defined for the

martensite. It is this ability of the atomic structure to change back to its original BCC form that allows the alloy to have shape “memory”. Even when the alloy is further deformed due to mechanical forces applied to the low temperature martensite, the atoms are still able to recover their original cubic shape upon heating past the transformation temperature. This process is known as the shape memory effect.

Another property of shape memory alloys is their superelasticity. This is also commonly referred to as the pseudo-elastic effect. This process is very similar to the shape memory effect however the transformation to martensite is prompted by an external force applied to the alloy rather than a change in temperature [42]. This external force is often applied by bending of the alloy. When the force is released the martensite slowly transforms back to austenite and the alloy recovers its original shape. This cycling effect can be repeated, making the material appear to have a very high recoverable strain (strain recovered when stress is removed), and therefore appear to be extremely elastic. The forward and reverse reactions are accompanied by a significant change in enthalpy, Figure 2.2.

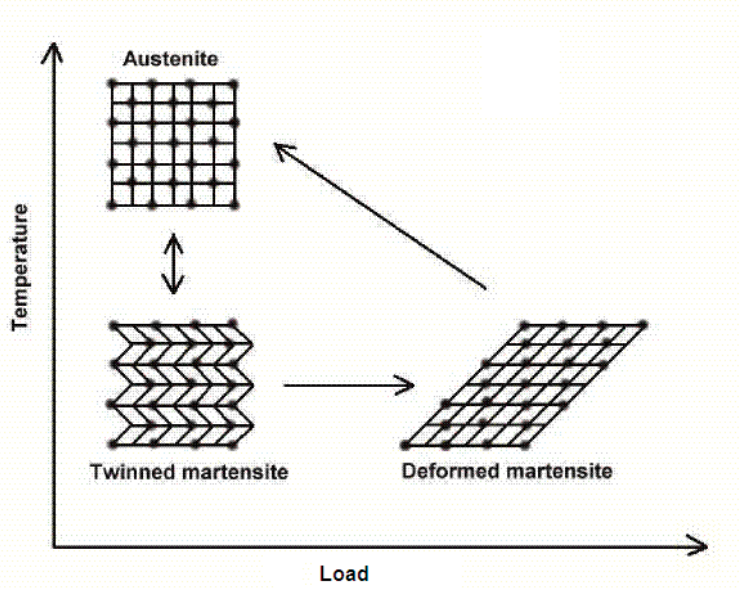

Figure 2.1 Austenite and martensite transformation mechanisms in shape memory alloys [43].

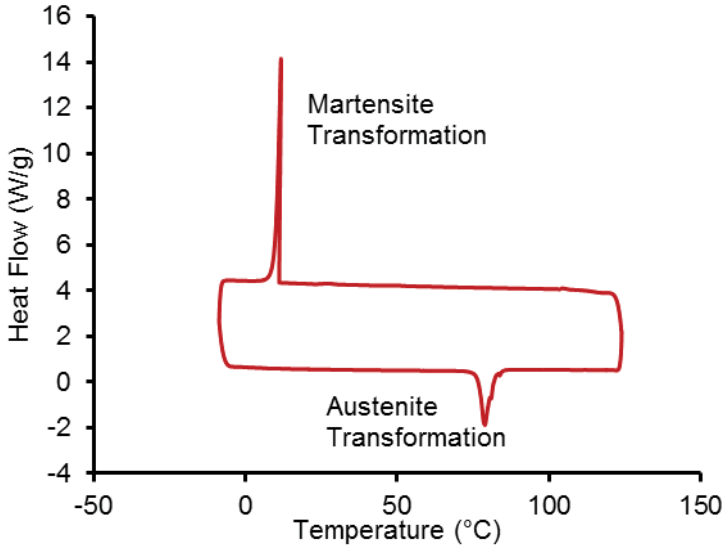

Figure 2.2 Differential scanning calorimetry (DSC) graph of shape memory transformation.

There are a wide variety of known SMAs with different elemental compositions. Discovered by Buehler and co-workers in the 1960s, NiTi is commonly referred to as NITINOL due to its discovery at the Naval Ordnance Laboratory (NOL) [39]. NITINOL is one of the most common shape memory alloys in industrial use, and has been the focus of much research, leading to thorough documentation of its properties [1-4]. Such studies have found that NiTi has good mechanical properties, reasonable workability and an excellent shape memory effect [9]. Once the shape memory effect (SME) became well known, many other alloys were created. A number of these were based on NiTi where percentages of Ni or Ti were substituted with Fe, Pt, Au, Al, Cu, Zr or Hf [9].

Completely new compositions of alloys were also created in the search for alloys that showed a reversible martensite phase transformation. The extent to which these alloys showed a SME was very varied, with some showing a recovery of up to 8% (such as TiNiNbCo [1]). All of these alloys are made through a similar process in which precise quantities of very pure elements are melted together. This is usually done in a vacuum furnace to prevent oxidation. After solidification, they are then annealed at a high temperature to create a homogeneous alloy and bring the alloy into the correct phase, typically the BCC-packed β-phase. The alloy is then quenched in order to prevent the β-

phase from decomposing (as, in many cases, the β-phase of binary non-ferrous alloys will decompose into α-phase plus some other intermetallic phase if held for a long time at an intermediate temperature). The properties and possible applications of some of these alloys are discussed below.

The transformation temperatures of SMAs are subject to change due to an effect known as aging. When a SMA is held in one phase (austenite or martensite) for a long period of time or at elevated temperatures, the crystal structure is 'stabilised'. This in turn leads to a change in the temperature of its next transformation [44, 45], which creates a significant problem when trying to design any product that requires an extremely precise transformation temperature in order to function as it was intended. This has hindered the replacement of complex multi-component systems with a simple SMA component in some instances [46]. Nevertheless, SMAs have been used in many common applications such as mobile phone aerials, bra underwires, frames for spectacles and sunglasses, medical stents and wires for orthodontic braces [1] or in aircraft design, Figure 2.3. Most of these applications do not require a very precise transformation temperature, but rather work on a hot/cold or on/off system or exhibit superelasticity (SE) over quite a large range of temperatures. Discussed below are some of the alloys that are used and their properties. The literature review is divided into two sections corresponding to bulk and thin film alloys respectively. This division mirrors the structure of the experimental part of this thesis. It makes sense to divide the discussion like this because bulk and thin-film alloys have different application areas and to some, extent, different issues.

Figure 2.3 SMA actuators used in Boeing variable geometry chevrons [39].

2.1.2 Bulk TiNi SMAs

TiNi is one of the most commonly used shape memory alloys due to its large recoverable strain of 8%. It is produced in many forms, such as sheets, wire, and rods. Since its discovery in the 1960s its properties have been well studied, including the effect of a variation in composition. At equiatomic NiTi the austenite transformation temperature resides at approximately 120°C. Decreasing the Ni content has very little effect on the transformation temperature, however (due to the small width of the phase field) it does have the effect of forming Ti-rich precipitates. Similarly, an increase in the Ni content results in a tendency to form Ni-rich precipitates, but with a small increase of Ni (approximately 1 at.%) a significant decrease in the austenite transformation temperature is also observed. This effect can produce an alloy with transformation temperatures below -40°C, allowing for a suitable shape memory operation below room temperature. Although stable at room temperature, these alloys can still form Ti_3Ni_4 precipitates when aged at high temperatures.

TiNiCu

Substitution of Cu for Ni in the TiNi SMA is quite common as it has the effect of reducing the hysteresis between the austenite and martensite transformations to within 5°C. This is important when designing devices that require a high frequency response between transitions, such as actuators. It also has the effect of making the transformation temperature less sensitive to changes in the Ni:Ti ratio and therefore making it easier to produce the alloy with transformation temperatures of around 40°C. This substitution comes at the cost of a reduced recoverable strain, which decreases to approximately 4% in 10 at.% Cu alloys. Whilst a wide range of compositions are possible for the TiNiCu alloy (with up to 20 at.% Cu having been documented), typically a range of between 5 – 10 at.% Cu is chosen as above 10 at.% the alloy tends to undergo embrittlement.

TiNiNb

The effects of adding Nb to the TiNi SMA were reported in 1986, when it was found that, upon small additions of Nb, the hysteresis between the martensite and austenite transformation temperatures increased. Shape memory alloys with a wide hysteresis are important for some practical applications where a transformation is disadvantageous within a fluctuating temperature range. An example of this is the use of fasteners or couplings, where the shape memory effect is used to tighten a joint upon cooling. The joint needs to maintain its shape throughout a wide range of operating temperatures. TiNiNb achieves this with a hysteresis in the range of 100°C, allowing for safe transport or use in ambient conditions. Nb has a much higher melting point than Ti or Ni, making it very hard to produce a solid solution. Instead, Nb rich precipitates form even in low (3 at.%) concentrations. These precipitates form regions of irrecoverable strain, and are associated with the widening of the hysteresis. They are also responsible for the lowered recoverable strain of 4%.

High temperature TiNiX SMAs (X = Pd, Pt, Hf or Zr)

As some mechanical applications for SMAs require high temperature transformations, there have been many attempts to increase the TiNi transformation temperature through ternary alloying. Early work on PdTi and PtTi showed that these alloys underwent a reverse transformation similar to the AuCd SMAs, however they present much higher transformation temperatures. This work was furthered by studies performed on the TiNiPd alloy. The results demonstrated that the transformation temperature was dependent on the Pd content, ranging from an austenite transformation temperature of 580°C in TiPd to 230°C in 30 at.% Pd additions to TiNi. TiNiPt was also found to undergo the same high temperature transformations with a maximum austenite transformation temperature of 626°C in 30 at.% Pt alloys. These materials however have limited practical application due to the high cost of Pd and Pt, so Hf and Zr have been used as alternative ternary elements. These alloys, whilst much cheaper to produce, fail to achieve the extremely high transformation temperatures, with maximum austenite transformation temperatures of 200°C for TiNiHf additions and 265°C for TiNiZr.

2.1.3 Bulk Cu-Al SMAs

Cu-Al shape memory alloys are not as common as NiTi despite being much easier and cheaper to manufacture (which is an important factor when it comes to producing greater quantities for large scale systems). The mechanical properties of these alloys are not very favourable as those of the TiNi-based SMAs as they are brittle and have low thermal stability [47]. In addition, the SME of the Cu-Al SMAs does not possess as great a recoverable strain as other alloys, and shows quite a large hysteresis after cycling through its transformation. For example, the transformation temperature can vary by up to 50 Cº from its initial point [48]. As a result, the binary SMA Cu-Al is less useful for practical applications, however when it is alloyed with even a small amount of other metals its properties dramatically improve while still maintaining low manufacturing costs. In general terms, when CuAl is alloyed with small amounts of Ni, Co, Fe, or Mn it is possible to reduce the hysteresis by up 25%. It is also possible to change the martensite transformation temperature from 100°C to – 200°C, creating the

ability to customise the alloy so that it exhibits the SME at a given temperature [48]. It is crucial, however, to choose appropriate alloys which provide the desired effect with minimal side effects (such as increased aging, unwanted precipitation, multiple unwanted phases and decreased stability of transition temperatures).

CuAlNi

One of the most common CuAl-based SMAs is CuAlNi. This provides numerous improvements to the binary CuAl alloy, with the key improvement being a higher thermal stability and resistance to decompositional aging [49]. Another advantage of this alloy over the others is that it has an operating temperature close to 200°C (whereas most of the other CuAl-based alloys have a maximum operating temperature closer to 100°C [50]). With these two properties, the alloy can be operated at temperatures around 200°C without any significant aging effects.

However, there is a problem when the material is required to be plastically deformed, as these deformations can only occur at temperatures above 700°C [51]. When the CuAlNi alloy is treated at such high temperatures the precipitation of the intermetallic compound NiAl occurs, leading to the decomposition of the original β-phase [50] and increased brittleness. This decomposition therefore creates a loss in the SME as the precipitation is not reversible and it reduces the amount of material that exhibits the SME.

When more Al is added to this ternary system it is possible to lower the martensite temperature, however there is a limit as adding Al leads to the precipitation of a brittle γ phase and creates a change in the martensite structure, creating a 2H martensite instead of an 18R [51]. These two factors make it impossible to lower the transformation temperature much without losing the shape memory properties and creating an even more brittle alloy. This highlights why it is important to find an alloy that is stable at both high and low temperatures.

CuZnAl

Compared to the other ternary SMAs based on CuAl, CuZnAl contains a relatively high amount of Zn (as high as 30 wt.% Zn [47]) as the additional element in the CuAl system. As with most other CuAl based SMAs, it is substantially cheaper to produce than TiNi-based SMAs and exhibits a reasonably good SME [52]. As a result it has been looked at extensively as a possible replacement. However, CuZnAl suffers from the same aging problems as other CuAl-based SMAs [52]. This material has a strain recovery of approximately 2% at 200 MPa however there is almost no hysteresis observed when operated between 60 – 100°C, which is a very important factor when being considered for some applications [47].

CuZnAl seems to have only a limited range of compositions which will produce these properties. If the composition differs even slightly from the optimum it will lead to major side-effects such as precipitation of unwanted phases, more undesirable stabilising effects in different states, and the loss of SME [53]. Asanovic [52] and Larochette [53] showed that the optimum composition is dependent on the electron concentration. When the alloy has an electron concentration of approximately 1.44 ± 0.05 conducting electrons to atoms, the equilibrium phases will be stable and therefore resist phase precipitation and unwanted stabilisation of other phases [53]. Whilst having the correct percentage of elements will minimize many of the problems faced by this SMA, it still suffers from both poor ductility and intergranular cracking [54]. These problems are usually a product of large grain size within the alloy and are the major downfall of most Cu-based shape memory alloys. The issue can be alleviated by alloying it with rare earth metals to cause grain refinement [54] but this leads to an increase in manufacturing costs and can also lead to precipitation of complex phases. Despite this significant problem, springs or other devices made with CuZnAl alloy have been proven to have a *shape* recovery of approximately 85% [54] which is very good for applications for mechanical action.

CuAlMn

Manganese additions to the basic Cu_xAl SMA provide the material with improved oxidation resistance and a transformation temperature that can be customized over a

wide range (from -100°C to 200°C) [55]. This customisation is achieved with very small changes in the Mn and Al percentages, resulting in this system being rather sensitive to changes in composition [55]. As with many other SMAs, if precipitation creates a change in the composition of the matrix phase then it will also cause large variations in the transformation temperature [56]. One advantage of using Mn as the alloying element for the SMA is that the product can have better ductility compared to other CuAl SMAs [55, 57]: when the alloy contains a low amount of Al, the $L2_1$ parent phase has a low degree of ordering which reduces its brittleness [58]. This property, when combined with a good elastic strain recovery over a wide range of compositions, leads to alloys with low percentages of Al and higher amounts of Mn exhibiting excellent SME [57]. The other major benefit of having good ductility is that it is much easier to machine and process, thus increasing its range of potential applications.

CuAlBe

When beryllium is added to the basic Cu_xAl shape memory alloy composition it improves many of the mechanical properties. With only small amounts of beryllium it is possible to stabilise the β-phase against aging. As noted above, many of the other Cu-based SMAs are susceptible to aging and precipitation of other phases, particularly if the composition is changed due to attempts at lowering the transformation temperature [59]. This is not a problem with CuAlBe as the transformation temperature of the martensite can be decreased dramatically with very small amounts of Be. Less than 0.6 wt.% of Be is required to lower the M_p from 150°C to -100°C [59]. The resulting β-phase is stable at both room temperature and at elevated temperatures [59].

All these features make this alloy very desirable for many applications, however a major drawback for this alloy is the fact that Be is a very toxic substance. Be is used in other alloys such as CuBe in order to provide similar mechanical advantages however it has been noted that people exposed to this alloy can suffer from the disease known as Chronic Beryllium Disease (CBD) [51]. The alloy in the referenced study was made with beryllium contents in the order of 1 – 2 % [51], which is considerably larger than the percentages used in most CuAlBe SMAs. The effect and danger of Be-toxicity is

apparent. This danger significantly limits its applications as it cannot be used in any that involve human contact. Disposal of the alloy must also be considered as release of Be may occur if incorrectly disposed. The second very significant problem of using Be as an alloying material is its high cost - 175 US $/Kg when compared to the price of aluminium which is approximately 0.3 US $/Kg [60].

AuCuAl

There are two AuCuAl shape memory alloys documented. A phase diagram of the Al-Au-Cu system is provided on page 71. The first of the two alloys has the composition of $Au_7Cu_5Al_4$ and is commonly referred to as Spangold® [7, 32-37, 61] . This alloy has a composition on the 18 karat gold line and the only documented use of it at the present time is for jewellery (Figure 2.4) [33]. One property that makes it desirable for jewellery is the unique spangled finish that appears on the polished surface of the alloy after cycling through at least one austenite/martensite transformation cycle [10]. This is easily achieved by placing the alloy in hot water after the item has been manufactured and polished. The finish results from martensite needles that re-orient themselves once the material transforms to the martensite phase. The transformation places a strain on the surface that is sufficient to cause macroscopic needles to slightly lift out of the bulk of the material [7, 35, 62]. This results in laths that are oriented at various angles across the surface resulting in a “spangled” finish.

Spangold® has other properties that make it suitable for use in jewellery such as good castability, high strength and wear resistance, rich colour and excellent corrosion resistance [7, 10, 33, 62]. The one limitation of Spangold® is its poor workability due to its large average grain size and its brittle structure [62]. While these properties are important when using this material for jewellery applications, they are not important when it is being considered for SMA applications such as micro electronics or small mechanical devices. Here it is the material’s excellent resistance to corrosion [7] that is very attractive as well as the fact that it is relatively resistant to the effects of aging [6]. Heat treatments performed on Spangold® samples show that the reverse transformation temperature will only increase by 5 C° [6]. It is also more stable at higher temperatures

due to the β-phase being more stable at lower temperatures than that of other SMAs [32], meaning that when the alloy is left at elevated temperatures it will not decompose into other phases.

The other benefit of Spangold® is that its nominal composition provides a low temperature transformation for the martensite and austentite phases, at approximately 70ºC and 20ºC respectively [36]. This allows the different states to remain stable at room temperature and for transformations to take place at readily accessible temperatures. I will show later that another unique property of this SMA is its ability to support a plasmon resonance due to its high Au content.

One other AuCuAl SMA has been reported in a Japanese patent [63]. This has a composition of $Au_{50\text{-}0.5x\ wt.\%}Cu_{50\text{-}0.5x\ wt.\%}Al_{x\ wt.\%}$ where *x* ranges between 2 to 4 wt.%.

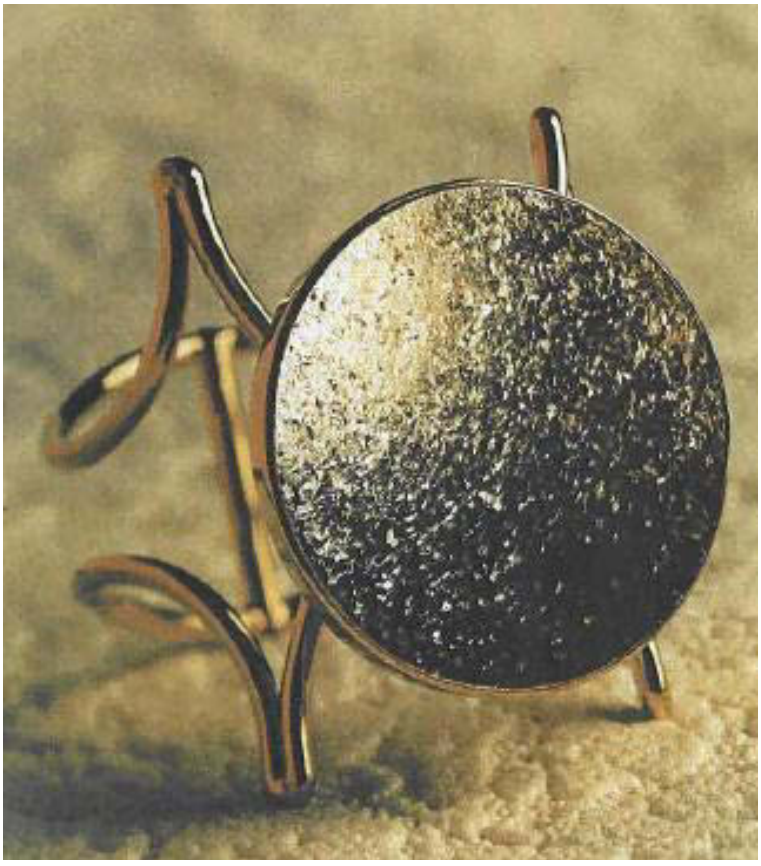

Figure 2.4 Spangold® jewellery. Photo by M. Cortie.

The high temperature phase of $Au_7Cu_5Al_4$ was initially misidentified as being similar to the $L1_0$ phase formed from (Au,Cu) [64, 65], it was later shown that it is a Hume–Rothery β-electron compound [37]. However, it is clear that this parent phase can exist in more than one condition. For example when these alloys are quenched from above 450°C the parent phase has been reported to have the B2 structure [66] or mixtures of ordered phases of a nature intermediate between the A2, B2, $L2_1$ or DO_3 types [36, 37, 66, 67]. Alternatively when the sample is aged between 100 and ~150 °C samples possessed a parent phase with $L2_1$ ordering and well-developed shape-memory effect [36, 37]. A schematic illustration of the A2, B2, DO_3 and $L2_1$ structures is provided in Figure 2.5, in which it can be seen that all are variations of a body-centered cubic ABC_2 type packing. For the A2 structure the site occupancies of C are the same as those of A and B (i.e. A = B = C), for the B2 (A = B)≠C while for the DO_3 (A = C) ≠ B. In the $L2_1$ structure A ≠ B ≠ C.

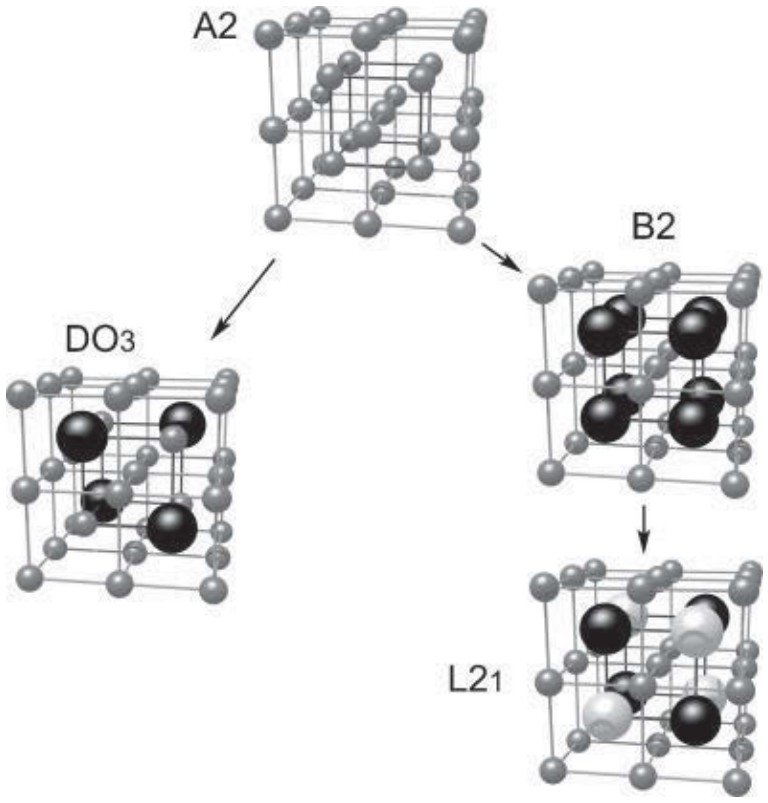

Figure 2.5 Chemical ordering of the A2, B2, $L2_1$ and DO_3 structures [68].

2.1.4 Aging

There are two processes that can occur when a shape memory alloy is aged and both can affect the transformation temperature of the alloy. The first is the 'stabilisation' of the martensite; this occurs at relatively low temperatures and creates a change in the subsequent transformation temperature [69]. The second occurs at higher temperatures and involves the decomposition of the martensite or austenite into more stable phases [69]. Whilst both of these processes are considered to be forms of aging, the way in which they change the alloys is different. Understanding these, and how they limit the applications of SMAs, is important if these issues are to be overcome.

Stabilisation

Martensite 'stabilisation' has a big effect on shape memory alloy performance and applications. The phenomenon causes the temperature of the reverse transformation (martensite to austenite) to rise after several days or weeks of aging. Ostensibly the martensite has become more stable relative to the austenite. Many mechanisms have been proposed to describe the stabilisation of the martensite in SMAs. Initially it was believed that the most likely processes were the diffusion or reordering of the atoms, and the pinning of lattice interfaces or nucleation sites [70, 71]. These two processes would work together to result in an overall lowering of the SME and a change in the transformation temperature. The pinning of the martensite interfaces was seen as a mechanical process which physically stopped the reverse martensite transformation due to a decreased mobility or freedom of the interfaces to move back to their correct positions during the transition [72]. In this model, pinning can be thought of as friction between the interfaces within the alloy that resist the planes slipping back into position. This resistance therefore requires extra force to overcome it in order to complete the transformation, and is the reason for a change in the transformation temperature. As the alloy is heated or cooled past the transformation temperature, more force is applied until it overcomes the larger energy barrier created by the friction [72]. Pinning occurs in SMAs due to a migration of vacancies and defects to the martensite/martensite or martensite/austenite interfaces [69]. Most SMAs are manufactured through a quenching process which creates a large number of quenched-in defects and, unless these defects

are removed, they have the potential to either be located at an interface or migrate to the interface [73]. This diffusion process is dependent upon temperature and time, so the longer the material is left at a high temperature the greater the number of defects that can migrate. Similarly, if the temperature is increased it provides more thermal energy for these defects to migrate at a faster rate.

More recently the Symmetry Conforming Short Range Order (SC-SRO) mechanism was proposed. This mechanism of aging occurs when the SMA is transformed into the martensite structure and is given enough energy and time to allow for atoms within the lattice to undergo short range rearrangements. The changes occur because the chemical ordering of the cubic austenite phase has inappropriate symmetry for the non-cubic martensite crystal structure. After a period of time, the initial cubic atomic ordering of the martensite structure changes to conform to its orthorhombic or monoclinic symmetry. The overall effect of this is to increase the reverse A_p transformation temperature by stabilizing the martensite structure. This process is reversible, as cycling the alloy back into the austentite structure returns the chemical ordering into the preferred cubic arrangement, destabilizing the martensite structure when 'freshly' transformed [74]. The rearrangement will create a higher energy barrier, Figure 2.6, which must be overcome in order to reverse the transformation back to austenite because once the atoms have moved they are no longer in the "correct position" to return to the austenite sites [75].

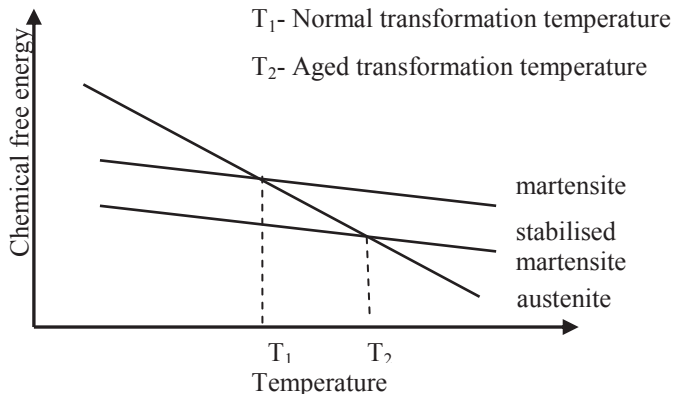

Figure 2.6 Stability of phases in terms of chemical free energy, showing how lowering the free energy of the martensite phase will shift the M→A transformation temperature upwards, from T_1 to T_2.

Decomposition

Aging due to decomposition involves the precipitation of new phases and therefore typically occurs at higher temperatures than those associated with stabilisation [48, 50]. During this form of aging migration and rearrangement of atoms occurs such that new phases form around nucleation sites (Figure2.7). As more atoms migrate to this new phase there will be a corresponding change in the composition of the surrounding shape memory alloy. This can change the transformation temperature but, more importantly, it degrades the shape memory properties of the alloy [48, 50]. Unlike stabilisation, the process is not reversible by simply cycling the alloy through its transformation. Reversing the change would require a high temperature annealing heat treatment to take the precipitates up into solution again [50]. This would not only affect the shape memory properties of the alloy but may also impair its mechanical properties such as hardness or ductility [50].

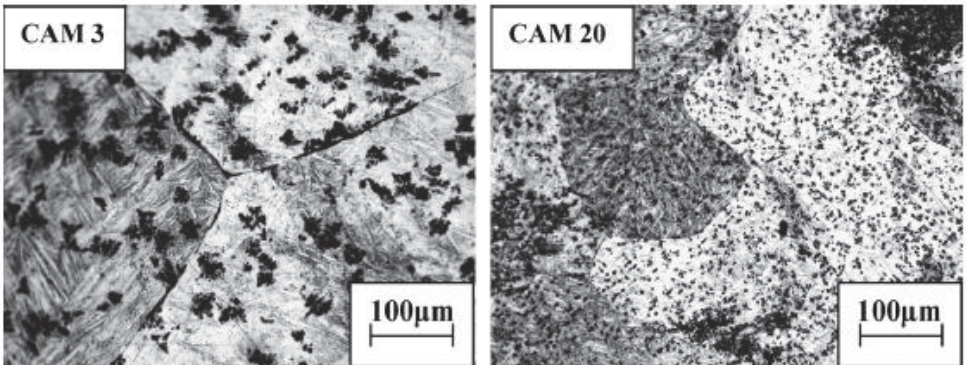

Figure 2.7 Precipitation of γ_2 phase (black) in a CuAlMn SMA aged at 300°C [58].

2.2 Thin Films of Shape Memory Alloys

2.2.1 Introduction

I discussed the properties of *bulk* SMAs above, and this topic occupies most of the SMA literature. However, there is also interest in *thin films* of SMAs and a number of papers have been published on this topic. This work has almost exclusively been centred on the more common TiNi SMA as its bulk properties have been extensively studied and are well understood. A wide range of film thicknesses have been produced ranging from 48 nm [5] to 8100 nm [76], which possess a surprisingly wide range of different

properties. In this section the processes of manufacturing and testing these different thin films are explored. The properties and uses resulting from these findings are also reported. There are no references to AuCuAl SMA thin films yet in the literature, so it is important to understand the properties of the more common TiNi thin films so that they may serve as a comparison for the films produced in the current project.

2.2.2 Manufacturing

The main process documented to produce these films is DC magnetron sputtering using either a dual sputtering target or three-target sputtering in the cases where dopants are added [20, 38, 76-84]. This is one of the most common techniques as it gives very accurate control of the composition and allows for small additions of other elements. This is important as small changes in the proportion of Ni and Ti or amounts of dopant can have a large effect on the transformation temperature. Other techniques that have been used include ion beam sputtering [85], sputtering, laser ablation, pulsed laser deposition, flash evaporation, electron beam deposition [16], vacuum plasma spraying and molecular beam epitaxy [86, 87]. While these techniques all have their advantages, DC magnetron sputtering is still the preferred method, as it is relatively cheap and fast, with good control of composition being achieved through the use of two- or three-target systems. Separate elemental Ti and Ni targets are typically used as they have different sputtering coefficients [20] but sometimes an alloyed Ti/Ni target is used in conjunction with an additional Ni or Ti target to overcome the difference in sputtering rates [88].

In the case of a single-target sputtering system a Ti/Ni target is alloyed with higher amounts of Ti than are required in the final film in order to overcome the differences in sputtering efficiencies of each element [89]. There are a large number of variables to consider when making SMA thin films as the alloy is very sensitive to small changes in its metallurgical state, even in the bulk. The transformation temperatures are affected by variables such as alloy composition, contamination, thermal and mechanical stress, aging and annealing [90-92]. In addition, when developing any thin-film consideration needs to be given to issues such as target power, gas pressure, sputtering distance, type of substrate and substrate temperature [91-93]. One critical factor in the manufacturing

process is the crystallisation of the alloy. If deposition occurs at room temperature then the alloy is largely amorphous, and requires a post annealing treatment to create the correct phase/ crystal structure [87, 94-97]. These temperatures tend to be above 450°C. However, if deposition is done on a heated substrate, approximately 300°C is adequate to form a properly crystallised material due to the combined energy of the sputtered atoms and the heated substrate [91].

2.2.3 Properties of SMA Thin Films

Crystal structure

Standard TiNi films have the same three distinct crystal structures as the bulk alloy [91]. These are a B2-ordered austenite phase, a rhombohedral phase and a monoclinic B19 martensite phase [19, 88, 98]. However, when the films become very thin some differences are noted. In Fu *et al.* [5] a series of X-ray diffraction (XRD) patterns were demonstrated for films ranging from 105 nm to 4110 nm thick in both the austenite and martensite structures. It can be seen that, as the thickness decreases, the intensity of the peaks decreases and the peak width increases. In the 105 nm films, almost no peaks are observed for the martensite structure.

Limiting size

A film thickness of about 100 nm has been identified as the minimum for a TiNi SMA to have an observed structural change [5]. As stated earlier, films of below this thickness have no visible shape memory effect, showing no change in crystal structure when heated or cooled. Fu also states that, below this thickness, oxidation and oxygen diffusion layers dominate the film, leaving a minimal amount of film with the correct composition [5]. However nano crystals (30 – 100 nm) in a bulk amorphous matrix or in a bulk alloy with nano-sized grains (15 – 60 nm) still exhibit a phase transformation [99-102], so the SME itself can still occur in structures as small as 15 nm. Nevertheless, as the crystallite size is decreased, an energy barrier is approached where thermally induced martensite cannot be achieved and, even before this limit is reached, the transformation to the rhombohedral phase stops. This suggests that a shape memory

effect is possible in thinner films; provided that the crystallites are above 15 nm in size and that any oxidation or diffusion layers are limited.

Transformation temperature

The transformation temperature in thin films is largely the same as the bulk until a certain limit in thickness (about 1000 nm), is approached [5, 103]. As the film thickness decreases below this limit there is a tendency for the transformation temperature to also decrease. This trend was found in films ranging from 105 nm to 4110 nm [5]. However, both an applied or residual stress, and the grain size [104] of the films will also affect the transformation temperatures, indicating that there may be more than one possible reason for changes in the transformation temperature.

Fu *et al*. [5] recorded a stress/temperature curve for films of TiNi of different thicknesses (Figure 2.8) using a Tencor FLX-2908 laser system that measured the curvature of the silicon and film while it was being heated. The change in curvature was then converted to stress. These results showed the films undergoing the characteristic SMA loop with thinner films showing smaller curves. The 105 nm film was the thinnest film to show this loop effect with the 45 nm film presenting a linear trend of stress against temperature i.e. no SME [5].

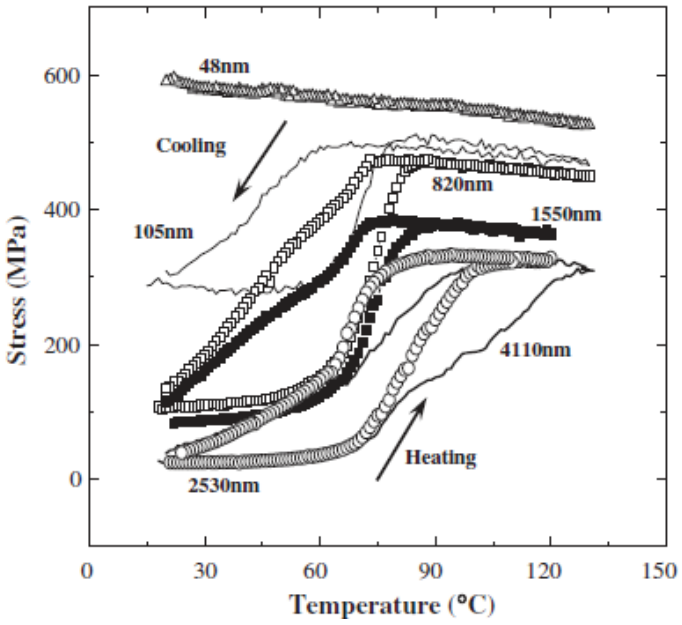

Figure 2.8 Stress/temperature loops of TiNi thin films [5].

2.2.4 Typical Compositions of Thin-film SMAs

Similar to the bulk alloys, the most common thin-film shape memory alloy is based on $Ti_{50}Ni_{50}$. This is due to the high levels of inducible strain in this alloy. However, as in the bulk, there is a wide range of variations of this alloy with many different dopants/ternary additions to improve the properties of the alloyed thin film. By adjusting the ratio of Ti to Ni it is possible to adjust the transformation properties of the thin films. However, as mentioned in section 2.1.2, there is a limit to this as too great a change can result in precipitates in the SMA.

Ti-rich

When sputtering TiNi thin films, there is only a small compositional range that produces a pure B2 parent phase. Similar to the bulk, a second phase precipitates outside of this range. However, in Ti-rich thin films the precipitate appears to be a non-equilibrium phase that is not present in bulk samples. When annealed at 470°C for one hour, this phase forms as nano-sized plate-like precipitates. The precipitates formed as the B2 phase can only support up to 49.5 at.% Ti, and any excess Ti forms as Ti-rich precipitates. If annealed at slightly higher temperatures it is possible to produce Ti_2Ni precipitates, also seen in the bulk alloy. The formation of these precipitates does not change the transformation temperatures as the B2 phase still maintains the same composition [87, 91].

Ni-rich

In thin films with higher Ni content it is possible for the alloy to produce Ti_3Ni_4 precipitates that can change the stoichiometry of the SMA matrix [91]. Ni-rich films tend to have lower transformation temperatures and are only operable below room temperature [87]. The benefit of Ni-rich films over Ti-rich ones is that the transformation temperature remains relatively unchanged with annealing temperatures up to 725°C. The martensite transformation only rises from -61°C to -26°C and the austenite transformation temperature does not change [87]. The formation of Ti_3Ni_4 precipitates in Ni-rich films has been shown to have a useful impact on mechanical

properties too. In particular, it increases the hardness of the film by forming thin platelets that are densely dispersed throughout the film [86].

TiNiX

A wide variety of TiNi*X* thin films are reported where *X* is a ternary alloying element. The ternary addition is made to change specific properties of the SMA, however this can result in negative side-effects depending on the type and concentration of the addition (as detailed below).

One of the most common additions to the Ti-Ni system is Cu. This is added to reduce the hysteresis width between the transformation temperatures, and therefore improves the response time of the SMA. The standard TiNi alloy has a hysteresis of approximately 30°C, so a large change in temperature is required in order to drive the forward and reverse transformations. A high frequency response is clearly difficult under these circumstances. With the addition of 9.5 at.% Cu the hysteresis can be reduced to 11°C [91]. This reduction in hysteresis is associated with a dramatic reduction in the heating temperature and only a small reduction in the cooling temperature [105].

The addition of Cu also reduces the system's sensitivity to changes in Ti and Ni content, and improves the mechanical properties [79, 81, 91, 106]. The negative side of this is a reduction in the recoverable strain. This becomes significant at 9.5 at.% Cu and, when the Cu addition reaches 18 at.%, the recoverable strain is reduced by approximately 75%. This dramatic reduction is attributed to a change in the crystal structure of the martensite from monoclinic to orthorhombic in alloys of high Cu content. It has also been noted that small additions of copper in films reduces the crystal size and therefore improves the flexibility of thicker films [107].

TiNi thin films have a maximum transformation temperature of approximately 75°C. There are some applications that have operating temperatures well above this. Additions of Pd above 15 at.% increase the transformation temperature up to 116°C at 22 at.%,

however below 15 at.% it also has the effect of lowering the transformation temperature [91]. This allows for a wide range of potential operating temperatures, as well as reducing the hysteresis of the transformation temperatures dramatically - down to approximately 10°C at higher Pd content. Again, however, this alloy has less recoverable strain than that of the binary TiNi alloys and under nominal composition has less than even the TiNiCu alloys [91, 94, 108]. Another drawback to using Pd is that it is relatively expensive when considering large scale applications, even if these films are produced in micron thicknesses. At 22 at.% Pd these costs can still be significant [94].

Another TiNi based ternary shape memory alloy that is used to achieve higher operation temperatures is TiNiPt. Minimal research has been conducted into this alloyed film, but it has been shown that with a composition of $Ti_{54}Ni_{26}Pt_{20}$ it is possible to produce a shape memory alloy thin-film with martensite and austenite transformation temperatures of approximately 345°C and 490°C respectively [109]. This is one of the highest temperature functional shape memory alloy thin films with a relatively small hysteresis in comparison with films of similar operating temperatures, making it a favourable option for high temperature applications. Little work has been done on the stability of these films at these temperatures, however it has been demonstrated that precipitates form during annealing at 600°C [109, 110]

Shanjabi *et al.* [111] have shown that TiNiHf thin films produce a very large range of transformation temperatures dependent on the Hf concentration. The martensite transformation temperature can be suppressed to as low as -51.6°C at approximately 5 at.% Hf, and can be increased to 272°C with an increasing concentration of up to 24% Hf. This high temperature response allows these thin films to be used in more practical areas, such as in systems which produce large amounts of heat (for example engines or high temperature electrical components). This alloy is able to operate at even higher temperatures than the TiNiPd system, but the drawback to this system is that as more Hf is added, the hysteresis in the transformation becomes larger and results in a slower response.

Ti can also be substituted with Zr. With small additions of Zr (< 5 at.%), a decrease in the transformation temperature is observed. As this is increased above 5 at.% however, the transformation temperature increases up to a Zr content of 19.5 at.% [96]. This substitution produces a range of martensite transformation temperatures from approximately 30°C to 170°C. This is not as high as that for the Hf substitutions, but the benefit is that there is little increase in hysteresis over the binary TiNi alloy. As with the TiNiHf, TiNiZr is also a much cheaper option when compared to TiNiPt or TiNiPd. One final problem with this alloy is that, as with all of the other ternary-based TiNi alloys, it has a reduction in recoverable strain when compared to TiNi. Nevertheless, even a 1.3% recoverable strain is enough to make it a viable thin-film actuator. [95, 96]

2.2.5 Applications

The large range of thicknesses possible for these films results in a corresponding diversity of applications. Thicker films are generally proposed for use in meso-scale actuators, whereas thinner films are proposed for use in micro electro mechanical systems (MEMS) and other small devices. In the present project, film thicknesses of tens of nanometres are aimed for, which would technically be for application in nano electro mechanical systems (NEMS). Regardless of scale, all of these devices exploit either the shape memory effect or the super-elastic effect of the material.

Mesoscale

When creating micron-thick films, the force generated by these films is relatively large and can therefore be exploited to move meso-sized objects [14, 38, 103, 112]. As these films have similar physical and shape memory properties to those of bulk samples, the applications are very similar. The form factor does allow for some more specific applications however. For example, the one-way shape memory effect can be used as an expansion joint for couplings or fastening rings in order to apply a force that maintains the tension on the joint [90].

Micro actuators

Thick film SMAs may be used to create a wide range of actuators (Figure 2.9) and micro valves. As with most other SMA applications, micro actuators require a temperature change in order to pass the alloy through its transformation. This can be achieved through either an increase in the ambient temperature (which allows it to also act as a sensor) or through a localised electrical heating of the component. The shape memory effect is used to create three different types of actuator: (1) devices that can be used in the classic sense to return a deformed actuator back to its original shape as long as there is no load on the material, (2) devices that can apply a large amount of force because they are constrained and thus prevented from returning to their original shape or (3) devices that do work on the constraining load when heated and then return when cooled (or vice versa) [90].

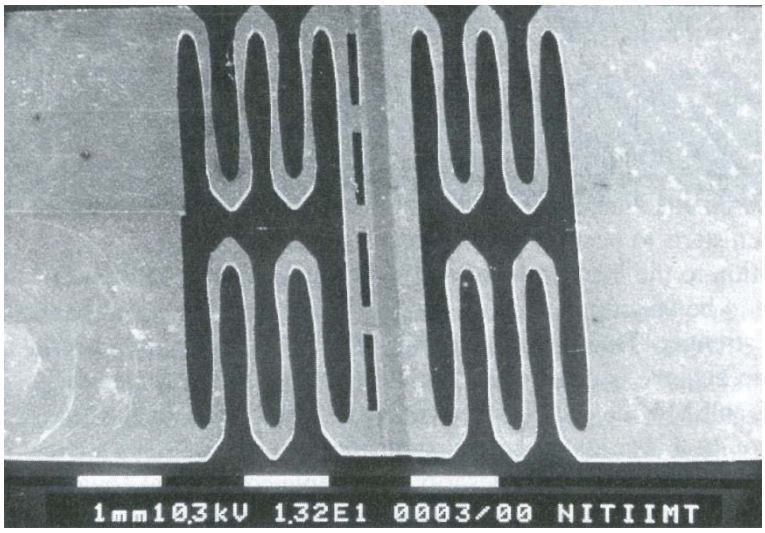

Figure 2.9 Electron micrograph of a linear actuator, made from TiNi thin-film [90].

MEMS

MEMS (Micro Electro Mechanical Systems) are used in a wide range of areas such as sensors, emitters and actuators. These all provide interactions with the real-world environment on a small scale. MEMS have been introduced into many consumer devices such as inkjet heads, gyroscopes and accelerometers, displays, optical switches, microphones, and pressure sensors [90]. Due to their small size they can be placed into

almost any device where needed, and with large scale production the cost of these has made them so affordable they are even used in disposable items. Many existing MEMS are developed using piezoelectric materials. SMAs are a viable alternative in some applications as they can exert large amounts of force and also have the ability to generate significantly larger displacements. There are many different MEMS systems where TiNi films have been used. Examples include micro pumps and diaphragms (used for direct drug delivery) chemical sensors, micro grippers (which manipulate small objects or take small biological samples, Figure 2.10), and micro sensors or switches (that react to changes in temperature and either have a primary response of activating a switch or a secondary response which can be detected through optical changes) [91].

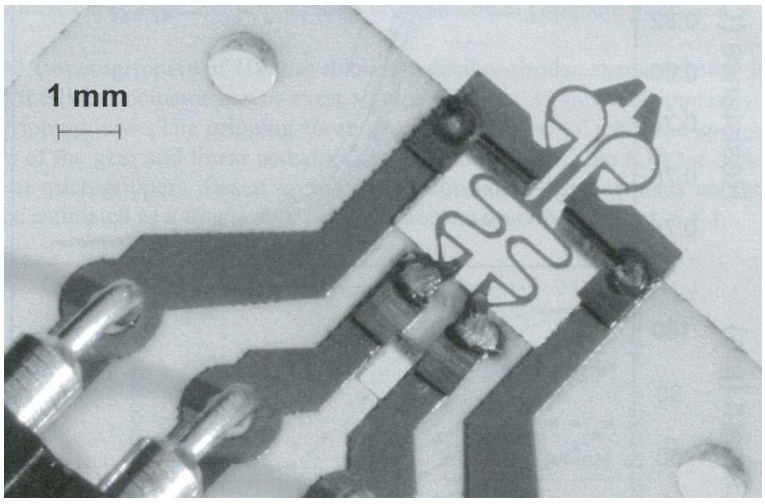

Figure 2.10 Electron micrograph of a SMA MEM gripper [90]

2.3 Plasmonic Phenomena in Nanoscale Films and Structures

2.3.1 Introduction

As mentioned, one of the unique attractions of the $Au_7Al_5Cu_4$ SMA is that it is likely to be able to undergo a plasmon resonance with light due to the nature of its constituent elements. Metals differ from most other materials as the outer shell electrons are not localised to the atom but rather form an unbound 'sea' of mobile electrons within the material. Light consists of a magnetic and an electric field which will interact with these

electrons when the photon energy corresponds to wavelengths in the vicinity of the visible part of the spectrum. Light of shorter wavelengths than the visible (i.e. UV and X-rays) will generally interact with the nuclei of the metals and not their electrons - a phenomenon that is of no further interest here. The interaction between the photon and the electrons produces a charge oscillation in the material, known as a plasmon.

Broadly speaking there are two kinds of plasmon. Provided that the incident photons have suitably matched momenta, it is possible for plasmons to form on an interface between the metal and a dielectric (or vacuum) and then travel along it for a distance of several microns. Such a travelling plasmon is known as a surface plasmon-polariton (SPP). However, the need to match the momenta means that special techniques are required to excite these on smooth metal surfaces. SPP's are of little relevance to the present project and will not be discussed further.

In contrast, when the size of the metallic structure is reduced down to the nano-scale, the need to match the momenta of photon and plasmon disappears. In these small structures the resultant plasmon oscillation is confined (i.e. is like a standing wave). At certain frequencies resonances occur and the magnitude of the oscillation is maximized. These are known as localised surface plasmon resonances (LSPR). Au nanospheres of approximately 20 nm diameter in a vacuum possess a resonant frequency close to that of green light. Consequently that green light is then strongly absorbed by the particle. In the case of gold, the blue wavelengths are always attenuated by interband transitions of the electrons, so that the remaining transmitted light has an intense red to purple colour. This phenomenon has been well documented and has attracted a lot of attention due to the ability to customise the absorption and scattering spectra depending on the size and shape of the particle [113].

2.3.2 Materials, Nano-structures and Sensors

Any nanostructure made of a conductive material has the potential to sustain a LSPR. Much of the research, however, has been based around Au and Ag. There are three reasons for this - the LSPRs that can be produced in these materials fall in the visible

light spectrum; the resonances are sharp due to minimal dampening; and stable nano-structures of these metals can be produced by simple chemistry [113]. Wet chemistry may be the most popular of the many methods available for synthesising plasmonic structures as it is possible to produce nanoparticles of different shapes and sizes, including nanorods, cuboctahedrons, nanocubes, truncated octahedrons, octahedrons, and nanobars [24]. It is also possible to produce more complex hollow shapes using nano-sized templates and a layered synthesis method.

The deposition of thin films is also used in the synthesis of nanostructures. In order to create three-dimensional shapes, these films need to either be templated onto existing nano-structures, or machined using milling techniques such as e-beam chemistry or focused ion beams [114-117].

The amplitude and frequency of the resonance peak exhibited by such a nanostructure depends on a number of factors including its size and shape, the type of metal and the dielectric that surrounds it. By changing these factors, it is possible to engineer nanostructures with a LSPR to meet the optical requirements for a range of practical applications. In simple, small nano-structures, only one dipolar surface plasmon is excited. As larger structures are produced it becomes possible to excite multiple poles. These multi-polar resonances result in absorption at additional wavelengths and can be combined to create distinct absorption profiles [113].

Plasmonics has been shown to be useful in three main types of sensors: biological, chemical, and physical measurements [118]. The main way in which LSPRs are used involves observing changes in the reflected or transmitted spectra due to changes in the nature of the LSPR. Due to the localised nature of surface plasmons and the high concentration of energy in the electromagnetic near-field, they are very sensitive to changes in the average dielectric properties at the metal-dielectric interface.

The most common premise for using LSPRs in sensors is that the frequency of the plasmon resonance is dependent on the dielectric medium in contact with the nanostructure. This means that any molecules that are brought into the near field of the

nanostructure will change the absorption spectrum of the plasmonic material. It is possible to create a change in the LSPR spectrum by functionalising the metallic surface of a nano structured/patterned thin-film so that only specific biological molecules will adhere to it. In this way a sensor can be designed to detect only those selected molecules. Some of the first experimental sensors used antigen-antibody binding as this was a well known selective coupling [119-121]. This was further developed to look at the interaction between DNA and proteins and even the conformational changes in pinned proteins [118]. Chemical sensors work on a very similar principle. In this case the metallic film is coated with a compound that will either react with or absorb an analyte. The most common type involves absorption layers which bind to specific molecules within a vapour such as hydrocarbons, aldehydes and alcohols by absorption in polyethylene glycol films, chlorinated hydrocarbons in polyfluoroalkylsiloxane, tetrachlorethene in polydimethylsiloxane and aromatic hydrocarbons in Teflon films [118, 122-125]. Sensors based on plasmons are also able to detect environmental changes such as humidity [126] and temperature [127].

The sensors that have been cited previously operate through a change in the dielectric properties of the surrounding medium. There are two other ways in which the LSPR can be actively changed. The first option is to change the dielectric properties of the conductive/metallic material itself. This can be achieved, for example, by selecting a material that undergoes a phase change between two states with different dielectric properties. VO_2 is one material that has been employed for this purpose [128-131]. VO_2 exhibits a phase change at approximately 67°C. In its low temperature state, it has a monoclinic structure and is semiconducting. However, when heated above the phase transformation temperature this shifts to a tetragonal structure. The high temperature phase has significantly increased electrical conductivity and the optical properties change to become similar to those of a metal [132, 133]. Thus, this material possesses two distinctly different dielectric properties which have been used to design nano-particles with LSPRs that change as the local temperature heats or cools through this phase change [128, 129]. One other material that exhibits a phase change that corresponds with a large change in its dielectric properties is Ga. It has been shown that

a nano particle produced from Ga will exhibit a measurable change in the reflected light as it transitions through its different phases when heated and cooled [134, 135].

The other option is to change the shape of the nanostructure. The LSPR is sensitive to the shape and orientation of the nanostructures [136-138], however very few articles that discuss producing nanoparticles of different structures have mentioned the possibility of dynamically transforming from one shape to another. There is a large gap in the literature on active nano materials that have the ability to change their shape given an external stimulus such as heat, applied electric current or magnetic field.

2.3.3 Numerical Simulations of Plasmon Resonances

Numerical simulations are used in order to understand which parts of the nanostructures are generating these resonant frequencies, and which LSPR frequencies might be produced in theoretical structures. Another reason for using these simulations is that there are cost, time and physical/equipment issues that limit the actual production of complex nanostructures, so simulations are a convenient way to explore what might be possible. However there are still some limitations in the current methods of simulating these phenomena.

Computer simulations of the LSPR effects are based on solutions to the Maxwell equations for small particles. One of the first people to work on a solution to the Maxwell equations for these particles was Gustav Mie who developed a solution for small spherical particles. Mie theory uses an infinite series to describe the scattering and extinction cross section of a particle given by the formulae $\sigma_{scat} = \frac{\lambda^2}{2\pi}\sum_{n=0}^{\infty}(2n+1)(|a_n|^2 + |b_n|^2)$ and $\sigma_{ext} = \frac{\lambda^2}{2\pi}\sum_{n=0}^{\infty}(2n+1)\,\mathrm{Re}\{a_n + b_n\}$ where a_n and b_n are sums that involve the relative size of the particle, the incident wavelength and Ricatti-Bessel functions [139].

Whilst this solution provided useful information for the purpose of simple particles, it has its limitations. One of these is that the plasmonic device or particle may not

necessarily be an easily defined specific shape such as the sphere or ellipsoid geometries for which an analytical solution is available. Another complicating issue is that, even for nanostructures, there is still a significant delay as an electromagnetic wavefront moves from one side of a nanoparticle to the other. In addition, simulation techniques that assume lossless or non-dispersive dielectric functions, or quasistatic electric fields, are inadequate for metallic materials. A variety of numerical techniques have been developed to overcome these problems, including the Green Dyadic Method (GDM) [140], Discrete Dipole Approximation (DDA) [141], the Finite Difference Frequency Domain (FDFD) method [140], and the Finite Difference Time Domain method (FDTD).

A popular method is the Discrete Dipole Approximation (DDA) [140]. This method assigns a grid of polarisable dipoles to depict a defined object. These polarisable dipoles then interact with a local electric field produced by an incident electromagnetic wave, resulting in their acquiring specific dipole moments [141]. The approximation of the object is governed by the size and number of polarisable points used, and whether they are spread uniformly or non-uniformly throughout the material. This method can only be used to model a metallic object embedded in a uniform medium as the calculation for each individual dipole assumes that the surrounding dielectric medium is homogeneous [141]. An advantage of the DDA is that it can make use of an experimentally derived dielectric function in tabular form. I will present the results of calculations made with the DDA in Chapter 8.

The finite difference methods use finite difference approximations for the derivatives in the differential equations, therefore approximating a continuous problem with a discrete one [140]. A disadvantage of this technique is that, in general, it cannot make use of a tabular dielectric function. Instead, in order to approximate the dispersion properties of these metals, a combination of Drude and Lorentz terms must be used to approximate the dielectric function. The combination of these terms expands the range of wavelengths for which the Drude model alone can approximate the dielectric constant. While this provides a good approximation for some metals, it does not adequately simulate the sharp absorption peaks seen in noble metals, unless a large number of

Lorentz terms are used [140]. Also, due to the nature of surface plasmons, the fields generated are localised around the interfacial region between the metal and the dielectric, and decay exponentially from this region. This requires very fine grid spacing to model the field accurately. As with the DDA method, a grid is used to define the magnitude of the field in discrete nodes across the model. I did not make use of finite difference techniques in this thesis.

3 Materials and Method

3.1 Bulk Sample Preparation

3.1.1 Casting and Annealing

The bulk samples for this project were manufactured using a casting method. Using high purity base metals of Al (99.99+%), Au (99.9999%) and Cu (99.9%), the required amounts were weighed out and placed into specimen jars. The melting and casting of the samples was done in alumina crucibles with a diameter of 17 mm and a height of 27 mm. A ceramic engineering furnace was used at 1100°C. According to the literature, the melting points for the base metals are 1083°C for Cu, 1064°C for Au and 660°C for Al. Whilst Cu has the highest melting point, the Au and Al metals would melt first and would start to attack the Cu, incorporating it into the molten alloy which has a much lower melting point. At these elevated temperatures oxidation was a major concern especially with the aluminium, therefore specific measures had to be put in place to minimise any oxidation that might occur. In order to eliminate oxygen in the system, a constant positive pressure of N_2 gas was applied to the furnace and a protective layer of carbon pellets were placed on top of the crucible to prevent oxidation of the alloy.

Another precaution taken was to melt the Au first, as gold does not oxidise. Once the Au was molten, the Al and Cu were added so that the Al would be incorporated into the alloy more quickly, and the Al metal would not have to be exposed to the high temperatures for as long. The alloys were left in the oven for 10 minutes, and once the metals were completely molten they were removed from the furnace and stirred so as to ensure the alloy had a uniform composition. The alumina crucible was then left to cool at room temperature and finally cooled in water. The samples were removed from the crucible and examined. Throughout this procedure ‘Occupational, Health and Safety’ (OHS) guidelines were strictly adhered to, requiring safe procedures to be followed and protective clothing worn. A leather apron was used by both operators along with leather spats and full length gloves. Face shields were also used by both participants. Having two operators is recommended in order to increase safety by decreasing the need for

multiple tasks to be carried out by one person while dealing with molten metals (Figure 3.1).

Figure 3.1 Example of OHS safety equipment worn by operators.

The same equipment was also used to anneal the samples. Annealing is a key step in the manufacturing and examination of SMAs as it is imperative that they be in the β-phase, however most of these alloys have a β-phase that only exists at high temperatures. In order to make this phase stable at room temperature it must be annealed in the β-phase then quickly quenched to room temperature to stabilise the β-phase. The quenching must be done quickly so as to prevent any precipitation of other phases [142]. Typically the annealing temperature is chosen to be just above the β-phase transition so that grain size does not increase dramatically, however in this project the aim was slightly different. It was to map out and find many different compositions of the SMA. Therefore a higher temperature was chosen. The other reason for annealing all the samples at the same temperature was so that when plotting the ternary diagram it was all done at a single isotherm.

An annealing temperature of 700ºC was selected on the basis of some exploratory Differential Thermal Analysis (DTA) along with a consideration of the current ternary and binary diagrams. This was high enough to ensure that the alloys were in the β-

phase but low enough to avoid melting. The samples were then annealed in the furnace for one hour to make sure that they reached the equilibrium point. While the samples were annealing, iced brine solution was made up to quench the samples in. Finally, the samples were quickly removed from the furnace and dropped into the solution.

Similar processing was used to manufacture the AuCu magnetron sputtering target. The base metals Au (99.9999%) and Cu (99.9%) were first alloyed together in a large alumina crucible. This was placed inside a ceramic crucible containing charcoal pellets. Once the base metals had become molten, they were stirred with an alumina rod to increase homogeneity. The alloy was then allowed to solidify and cool at room temperature. Once the alloy had solidified it was placed into a graphite mould that was 51 mm in diameter and 3.1 mm deep. A graphite lid with a weight was placed on top and this was placed inside a sealed alumina tube that contained a partial pressure of nitrogen. This was heated in the furnace at 900°C for one hour and then allowed to cool. The alloyed target was then removed from the mould and cleaned using sandblasting and an ultrasonic bath of ethanol.

3.1.2 Sectioning

After the samples were cast, they were then sectioned for metallographic examination so as to provide a flat working area that was representative of the bulk. Other parts of the samples were further processed for use in other techniques such as DSC (differential scanning calorimetry) or PD (powder diffraction). A low-speed, diamond saw was chosen to section the sample as it would produce the least amount of waste. This is important as the sample ingots were approximately 10 mm x 17 mm in diameter and had quite high percentages of gold making it imperative to make only very thin cuts. The other reason for choosing the low-speed, diamond saw over the abrasive cut-off wheel is that it creates less alteration in the sample [143] because cutting the sample can introduce heat or deformation that can change the microstructure. All efforts were made to minimise the heat and stress on the sample, however no matter how many precautions are taken some deformation is inevitably introduced (Figure 3.2). From the literature it can be seen that the low-speed, diamond saw produces the smallest depth of

deformation (Figure 3.2) [144]. Some of these sections were powdered using either a hardened-steel ring mill for 15 minutes or by grinding against silicon carbide or carborundum paper. Powdered samples were then annealed at 200°C in an inert atmosphere to remove strain.

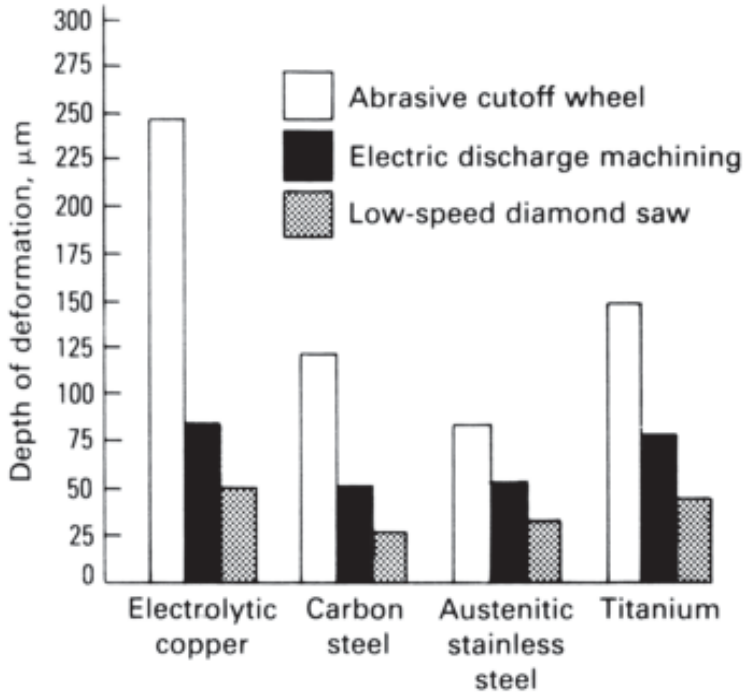

Figure 3.2 Depth of deformation in different metals due to cutting method [144].

Deformation can be removed with a small amount of grinding and polishing. In order to minimise the deformation the Leci VC-50 low-speed, precision, diamond saw was set to 38 rpm with a 125 x 0.35 mm blade and the fluid tray was filled with water so as to lubricate and cool the sample while cutting. The weight slide was moved to the half position so as to provide enough weight to cut the sample at an even rate.

3.1.3 Mounting

Mounting the samples is very important as many of the samples produced by casting were very valuable, small and some were quite brittle. Mounting made them easier to handle and stopped any pieces breaking off and being lost. It also created a standard size that could be used in the clamps for the polishing and grinding wheels and made it

easier to prevent uneven wear and edge retention while polishing. The other main reason for mounting a sample is so that it can be more easily identified with the use of markings on the mount itself rather than inscribing or writing on the sample which can be non-permanent or hard to do on an uneven sample surface [145]. For these samples a cold mounting resin was used as it provided a strong bond to the sample and adequate hardness. The liquid epoxy resin produces an adhesive bond to the sample, which makes it less likely to pull away from the sample and create fissures due to thermal expansion. It is also a clear mounting method which allows the sample to be seen from the sides and allows for permanent markings to be set in the resin. One of the major reasons for choosing a castable resin over a hot pressing technique was to avoid the thermal stress and physical pressure that is applied to the sample in the latter case. As these samples may have potential shape memory which is triggered by temperature and stress changes, it is desirable to avoid these factors. The down-side to using the resins is that they are more expensive and take longer to cure [145], but when working with only a few samples this is not an important issue as all the samples can be mounted at one time and not much resin will be needed.

A 25 mm diameter polyethylene mould was used with a removable cap. The mould was sprayed lightly with a Leco silicone grease to prevent the epoxy resin from sticking to the sides. Once the moulds were greased, the samples were then placed inside the mould with the lids on. The Leco resin was made up as per the instructions: mixing in gently with a glass rod, 5 parts resin with 1 part hardener into a glass beaker. Once the resin was sufficiently mixed together, it was poured into the moulds to a height of approximately 18 mm. It was then left to set for 12 hours. As can be seen in Figure 3.3, the final mounts were very hard and even, with a good bond to the samples.

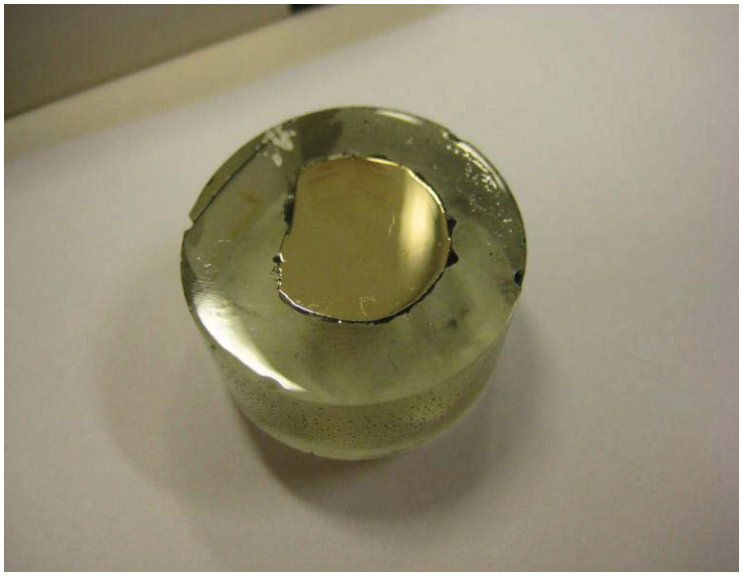

Figure 3.3 Example of cast alloy sample mounted in resin.

3.1.4 Grinding and Polishing

Grinding and polishing was a very important process for these samples as many of the analytical techniques required a very flat and smooth surface. The first step was to grind the samples using an abrasive silicon carbide paper. Using a Struers Knuth-Rotor 2 rotary sander (Figure 3.4) the samples were ground down through a range of grits 120, 320, 600 and 1200 FEPA (Federation of European Producers of Abrasives) grit silicon carbide paper. Running water was used through all the different stages so as to remove debris, decrease heating and provide lubrication. This is very important as it is possible to damage the sample if too much pressure or heat is applied to the sample surface. It has been noted in the literature [146] that deformation is introduced into the sample below the surface and can extend further than just the surface scratches. In order to remove this deformation, each successive step of grinding must be performed to remove not just the layer of scratches on the surface, but also any deformation that was introduced from the larger grit abrasive paper used in the preceding step [146].

Figure 3.4 Struers Knuth-Rotor 2 rotary sander.

Polishing, like grinding, uses abrasive particles to remove fine layers from the surface of the sample, however with polishing the particles are typically a lot finer and are not in a fixed position. The usual process is for a paste containing abrasive particles to be administered to a cloth, where the fibres of the cloth hold the particles loosely. This then provides a surface against which the samples are physically rotated. A lubricant is also used to decrease heat build up. This is repeated using increasingly smaller particle sizes. This project used a Struers polishing system starting with a 9 micron diamond paste on a Susp pad, using a Struers RotoPol 22 (Figure 3.5). The samples were rotated in an anti clockwise direction against the rotation of the polishing pad for 5 min. The process was then repeated with a 3 micron diamond paste on a Dur pad for 5 min and finally with a 1 micron diamond paste on a Dur pad that was used for Fe-based samples. This was used to polish the samples for 15 min to allow the particles to break down and produce a fine polish. Similar precautions as those from the grinding step were required as deformations can still be introduced below the scratched surface due to the fine particles [146]. This process produced samples with a very smooth, mirror-like surface which is important for obtaining valid results from the optical characterisation techniques.

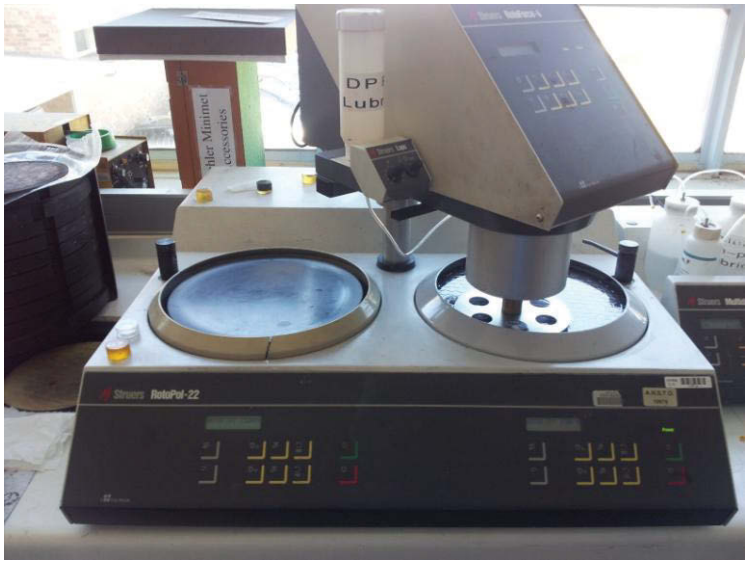

Figure 3.5 Struers RotoPol 22.

3.2 Differential Scanning Calorimetry (DSC)

Differential scanning calorimetry is a technique used to measure the energy difference created when a material undergoes an enthalpy change [147]. The sample and a reference are heated or cooled at an identical rate so that any anomalous changes in temperature in the sample can be identified. These changes in enthalpy can undergo during some phase transitions such as melting, solidification, sublimation, decomposition, or crystal structure change as occurs in the cases of an allotropic transformation or the martensite transformation [147]. There are two main types of DSC - power compensation and heat flux. The one used in this experiment was a Thermal Analysis DSC 2920 (Figure 3.6) which is built on a heat flux design where there is one heating unit inside the chamber. This heater is connected to two pads; one for the reference and one for the sample. They are connected with a low, heat-flow-resistant path. When a change in enthalpy occurs in the sample, the heat energy will transfer through this path either towards or away from the sample depending on whether the transformation is exothermic or endothermic [147]. By knowing the exact weight of the sample this energy can then be quantified and the enthalpy of the reaction can be found. This technique is perfect for analysing SMAs as these alloys work by a solid-to-solid phase transformation, and with that transformation there is a transfer of energy. A very

distinct peak in energy flow is observed for both the martensite and austenite transformations, allowing for the exact transformation temperatures to be found as well as the start and finish points for both phase transitions. When using the DSC to perform heat treatments on the SMA it is also very useful to be able to identify if the heat treatment changes the energy of the transformation as well.

Figure 3.6 Thermal Analysis DSC 2920.

It is also possible to identify the different forms of aging discussed in Chapter 2.1.4. When aging occurs due to stabilisation, this can be seen on the DSC as a change in the peak position and a change in the peak shape. The peak typically becomes narrower and produces an increased peak height, due to the increased amount of energy required to perform the transformation. The peak also shifts to a higher temperature for the M_p or A_p. However, in the case of aging due to decomposition, it can be seen in the decreasing size and enthalpy of the peaks on the DSC scan. This is due to the fact that less of the sample is composed of the phase that undergoes the transformation and therefore less heat flow is produced. The actual decomposition can also be detected if it occurs at a sufficiently fast rate. The decomposition and precipitation of new phases are also chemical reactions, which can absorb and release energy that can be monitored using DSC [148].

3.2.1 Shape Memory

The first batch of DSC analyses was focused on finding any shape memory transformation in the various cast samples. This involved a similar process to the aging of the Spangold, however no other heat treatments were involved. The DSC was programmed to scan through a wide range of temperatures and record any changes in enthalpy. The program was set to ramp up at 10°C/min and then ramp down at 10°C/min across the range of -100 and 400°C. If repeatable exothermic and endothermic peaks were found on the ramp up and ramp down respectively, the sample was further cycled to determine whether these changes were due to martensite and/or austenite transitions. Different combinations of temperature and ramping sequences were programmed into the DSC to try a range of different possibilities for finding an austenite or martensite transition. In order to get the DSC down to -100°C, N_2 gas was passed through liquid nitrogen and then into the inlet chamber of the DSC as seen in Figure 3.6.

3.2.2 Aging of Spangold

For the aging experiments, a disc of Spangold ($Au_7Cu_5Al_4$) designated FL (this sample had been prepared by Dr Fiona Levey some years ago) was cut from an ingot and then small pieces were broken off from this disc. These small fractions were weighed out and placed into aluminium pans. Each sample was broken so that it weighed between 20 mg and 40 mg so that it would fit into the pan and the differences in the measurements could be minimised. The original FL sample had been aged at room temperature for nine years allowing all of the fractured samples to be in the same state. Samples were cycled through the transformation temperature to identify M_p and A_p temperatures. Aging was performed on sample FL by cooling to -4°C then cycling the alloy through its transformation temperature and holding for different lengths of time at 90°C. The cycle was then repeated to observe changes in the transformation temperatures. A second type of aging was also performed where sections of sample FL were heated past the A_p temperature and held over a range of temperatures between 85 – 450°C. The sample was then cooled past the M_p temperature and heated to collect the aged A_p temperature.

3.3 Optical Microscopy

Optical microscopy is an important method for analysing bulk samples. Information such as microstructure, homogeneity, volume percentages of phases, colour, and contamination can all be identified using optical microscopy. While the quality of the result depends on the time and effort spent on the sample preparation, if the steps stated earlier are done correctly, a high quality image can be produced. In order to get the most out of this technique the sample must first be observed at low magnifications so that the overall topography of the sample can be observed [149]. Key features can then be observed under higher magnifications as their relative positions will be known. An optical microscope can be used in many ways to observe different structures or give more detail to certain features. By combining optical microscopy with polarised filters, interference enhancement, and chemical etching, a very detailed examination of the samples can be achieved.

3.3.1 Bright Field

Of all of the different modes of imaging, bright-field imaging is the most common and is seen as the standard form of imaging. This mode works by producing a light that is transmitted to the sample perpendicular to the surface, and then reflected into the objective lenses. Features on the surface of the sample will vary in the amount of light they reflect depending on their angle to the incident light. Features that are not perpendicular to the incident light will reflect less into the objective lens and therefore seem darker - the greater the angle, the darker the feature. This mode also allows for colour variations to be observed as they appear on the sample. The colour seen in the eyepiece or on the camera monitor will vary depending on the true colour of the sample features, the types of incident light used, and whether any filters are being used. The detail seen on the sample will vary depending on the contrast produced by the sample and the capability of the microscope [149].

Bright field imaging was used on all of the samples. The instrument used was a Ziess Axiotech, with a Media Cybernetics Evolution MP digital camera to record the images (Figure 3.7). The samples were imaged under the 2.5, 5, 20, and 50 times objectives. An image of a scale was also taken using all the objectives so that a relative size scale could be used with the images of the samples.

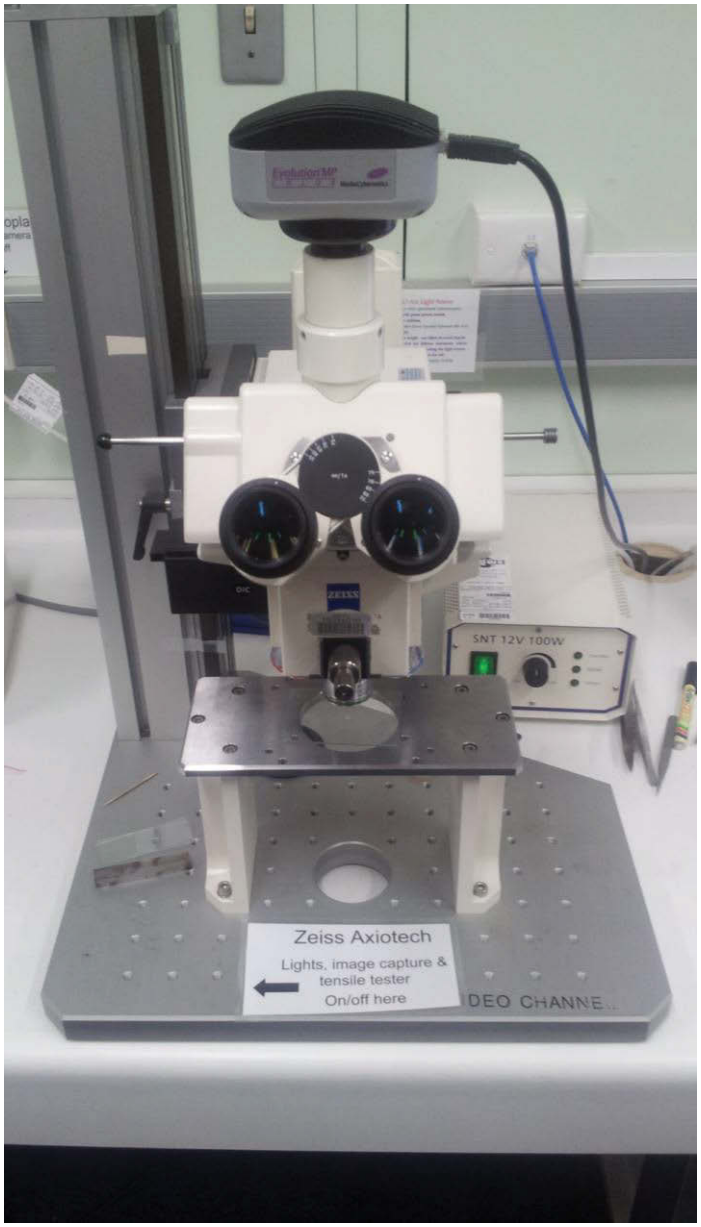

Figure 3.7 Ziess Axiotech, with a Media Cybernetics Evolution MP digital camera.

3.3.2 Nomarski Interference Contrast (NIC)

The other type of optical imaging mode used for this project was Nomarski interference contrast (NIC). As the human eye cannot detect differences in the phase of light (only differences in colour or contrast), the purpose of this technique is to convert different various phases of light into different colours or brightness. This method works by passing light first through a linear polariser and then a Wollaston prism. The Wollaston prism separates the incident light into two orthogonal linearly polarized beams, the light then passes through the objective lens and reflects off the sample. Any differences in height will cause small relative phase shifts in the reflected light which then returns through the Wollaston prism [149], [150]. As the light returns through the Wollaston prism, the two separated light sources of different phases are recombined and they interfere with each other. Depending on the extent of difference between the two phases this generates differences in contrast when viewed through the microscope. This can be interpreted as changes in altitude of the surface of the sample.

This technique was used to observe the needle-like martensite structures present in the samples exhibiting shape memory. When a polished sample is transformed, martensite needles, or more correctly laths, 'pop' out of the surface plane to relieve the stresses that are occurring due the shape memory effect. These laths produce a low surface topography that, when imaged through the NIC, are differentiated by colour or contrast. The samples were imaged before and after transformation to highlight that a displacive transformation had occurred.

3.4 Scanning Electron Microscopy (SEM)

Scanning electron microscopy has become a very common technique for the analysis of metals and alloys as it offers a wide range of information from one instrument. It provides a resolution down to several nanometres [151]. SEM produces images in many different modes without the need to remove the sample. This enables a comparison to be made of the data gathered by these modes. The various modes work by collection of the different energy signals that are produced in the sample when it is struck by the high energy electron beam of the SEM. For this project, only the back-scattered electrons,

secondary electrons and characteristic X-rays produced by the sample were used. However some SEMs are also capable of analysing UV photons and photons in the visible spectrum [151].

Backscatter mode was chosen to analyse the bulk samples as it produces a large amount of contrast between areas of different average atomic number. This is due to the way that backscattered electrons are produced. Backscattered electrons occur when an incoming electron is scattered at a large angle back out of the sample or, if a number of small angle reflections occur, to scatter electrons out of the sample. The energy and number of electrons that are scattered is closely related to the atomic number - the larger the atomic number, the more electrons are reflected. This means that the different phases of a sample will show greater contrast (i.e. they will be brighter) in the areas of higher average atomic number. Backscattered electrons have up to as much energy as the incident electrons which is much higher when compared to secondary electrons. In order to detect these, a detector must be placed above the sample to capture the reflected electrons. This detector is usually a scintillator which is situated around the electron beam aperture. Whilst backscattered electrons create great contrast between phases, the mode can also be used to measure some surface structure, however topography is not as evident as in secondary electron mode.

Secondary electrons were not used for the bulk samples as topography was not important as the samples were highly polished. However in the thin-film specimens topography and surface features were very important in order to see crystallite sizes and roughness of the film. Secondary electrons also can provide a higher resolution image and are therefore very useful when imaging thin films. They are produced when the incident electron beam interacts with the sample and excites low energy electrons within the atoms. These ionised electrons are then ejected with very low energies (typically in the range of a few eV). If these electrons are close enough to the surface, they are ejected into the vacuum. Due to the low kinetic energy, the secondary electron detector has a large bias applied to a surrounding screen which attracts the ejected electrons towards the detector, accelerating them into the scintillator. Due to the low energy of these electrons, this technique is very surface sensitive, producing a much larger signal

from peaks and edges than from flat surfaces. This is what provides the contrast required for seeing the topography of the sample.

A Zeiss Supra 55 VP scanning electron microscope (Figure 3.8) was used at 20 keV on high current mode with a 120 μm aperture in backscatter mode. The backscatter detector was used to image the bulk samples as it was able to provide the greatest contrast between any different phases present and due to the fact that the samples had been polished flat. For the thin-film samples an accelerating voltage of 10 – 20 keV was employed along with a 30 μm aperture and the in-lens detector. This was chosen as it provided the highest resolution and greatest contrast between features of the film. Before the mounted samples were loaded into the SEM, a small amount of conductive silver paint was spread from the edge of the sample to the edge of the mounting holder. This provides a conductive path for any electrons absorbed from the electron beam. If this was not provided, the absorbed electrons would build up and create a localised negative charge. This charge appears as a bright spot on the image because the large negative potential reflects more electrons into the detector. While silver paint was used for this experiment, any other method which creates a conductive path will provide the same result.

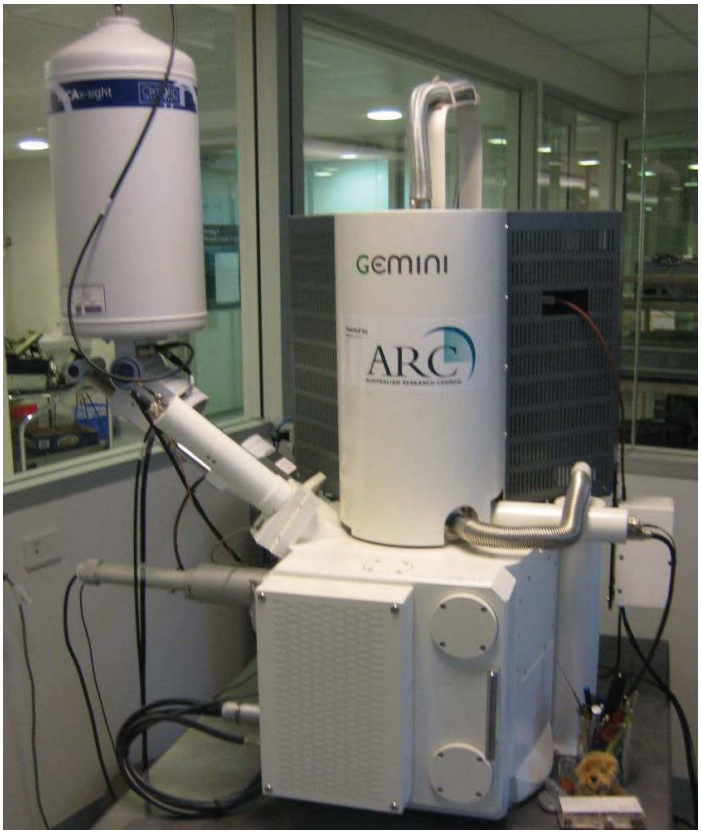

Figure 3.8 Zeiss Supra 55 VP scanning electron microscope.

3.5 Energy Dispersive Spectroscopy (EDS)

The interaction of high energy electrons with matter produces many different energy signals, one of which is characteristic X-rays. The X-rays are produced by the energy that is released when excited electrons relax back to their ground state. This means that the X-rays emitted will depend on the electron configuration of the atom, although some atoms may produce X-rays of similar wavelengths. By using the X-ray emission lines from multiple shells, it is possible to differentiate between different atoms. By comparing the intensities and spectrum of energies emitted with a database of known elemental excitations, it is then possible to get an elemental composition of the sample. This can also be used in a quantitative analysis if the EDS is calibrated using a standard, allowing for the exact composition to be recorded. EDS was performed on all bulk samples while being imaged in the Zeiss Supra 55 VP scanning electron microscope. By using an accelerating voltage of 20 keV it was possible to excite multiple orbital shells within the atoms providing very accurate characterisation of the samples. In order to determine the percentage composition, the EDS was calibrated using Cu and Si

standards. This method of standardisation is better than a standard-less calibration where no physical calibration sample is used and is best used in conjunction where the microscope is also calibrated using software for factors such as backscattering and electron retardation (ZAF). It was important to find the overall composition of the sample, as well as the composition of the different phases (if they were present) so that they could be accurately mapped out on the ternary diagram.

EDS was also performed on the TEM specimens using a JEOL JEM-2200FS in order to determine the composition of selected films, and identify contaminants. EDS mapping was also performed on these samples to identify compositional differences across various regions within the films. An accelerating voltage of 200 keV was selected used with an Oxford X-Max 80 mm^2 SD detector. In order to perform the EDS mapping the TEM was used in scanning mode, this is discussed in detail in the TEM section.

3.6 X-ray Diffraction (XRD)

X-ray diffraction (XRD) is a common technique that can be performed in many ways, but for these samples a Bragg-Brentano configuration was required. X-ray diffraction works by projecting a collimated monochromatic beam of X-rays at the sample. The X-rays are reflected when the Bragg condition $n\lambda = 2d\sin\theta$ (where λ is the wavelength of the incident radiation, d is the interplanar spacing and θ is the reflected angle) is satisfied [152]. If the sample consists of a large number of crystals oriented randomly in every possible position every one of these crystals has the potential of diffracting the X-rays. When the intensity of the combined diffraction is recorded as a function of angle, a complete diffraction pattern can be created and used to identify the crystal structure by comparing the reflection peaks and their relative intensities with a large database of patterns from known samples, produced by the International Centre for Diffraction Data (ICDD) known as the Powder Diffraction File (PDF) [152]. If the phase has not been recorded in the database, the crystal structure may need to be calculated using modelling software where lattice parameters and atom positions are input and then varied to simulate an XRD pattern similar to the experimental data. It is also possible to identify whether multiple phases are present in the sample as in that case the diffraction pattern

will contain peaks from more than one crystal structure. The relative amounts of each phase can be estimated by comparing the intensity (or integrated area) of these peaks. As the metal samples have many different grains and, for the present samples, within these grains are multiple crystal orientations due to twinning and martensitic phase transformations, the sample behaves as a powder which eliminates the need for further sample preparation [152]. However, some residual effects due to texture, or preferred crystallographic orientation in the sample, are still expected, in the bulk samples. In order to eliminate this, milling the sample into a fine powder followed by annealing can be done.

XRD was performed on all the bulk samples using a Panalytical X'pert Pro X-ray diffractometer (Figure 3.9). The samples were scanned from 2θ of 22 to 80º using CuK_{α} 1.5406 Å X-rays, providing an angular wide range which would include all the peaks required to identify the crystal structure. The samples were rotated to maximize the number of orientations and grain sampling.

In-situ XRD was performed to replicate the DSC aging experiment that held the sample at 90°C. The sample was first cooled to -4°C and then allowed to warm to room temperature, at which point a powder diffraction pattern was taken. The sample was then heated to 90°C and another powder diffraction pattern was taken. Holding the sample at this temperature for 18 hours, scans were simultaneously taken at logarithmic intervals, similar to the time scales used for DSC measurements. The sample was then cooled and powder diffraction patterns were taken at 20°C, 10°C and 0°C to observe changes to the martensite structure. The powder diffraction scans were performed on a Panalytical X'pert Pro X-ray diffractometer with an Anton PAAR TTK 450 temperature stage, Figure 3.9. Scans were taken from 25 to 70° 2θ, with a step size of 0.0334° and a scan time of 330 equivalent seconds per step.

Figure 3.9 Panalytical X'pert Pro X-ray diffractometer was also used with an Anton PAAR TTK 450 temperature stage.

3.7 Synchrotron Powder Diffraction

Synchrotron radiation is emitted when charged particles (for example electrons) moving at velocities close to the speed of light are forced to change direction under the action of a magnetic field. This change in direction is equivalent to the particle accelerating. It is this acceleration which produces the synchrotron radiation. The electromagnetic radiation is emitted in a narrow cone at a tangent to the orbit of the particles. Synchrotron radiation has high brightness, high collimation, and a wide energy spectrum. It is also tuneable to any wavelength within the emitted spectrum by the use of a monochromator, and is highly polarized. The electrons are generated by an electron gun, and travel through a linear accelerator and then a booster ring, accelerating towards the speed of light. Once they are at relativistic velocities, they are transferred to an outside storage ring. Confinement to a circular orbit is achieved by bending and alignment magnets that are separated by straight sections [153]. With suitable tailoring, the beams are used to perform a range of experiments including, in the case of this research, powder diffraction.

The majority of the synchrotron experiments were performed on the powder diffraction beamline at the Australian Synchrotron (Figure 3.10) [154]. Powder from the bulk samples was loaded into a 0.3 mm quartz capillary, which was then rotated in the beam to increase the number of grains sampled at different orientations. Data were collected from the LaB_6 Standard (NIST 660b) to accurately calibrate the wavelength and determine the instrument contributions to the observed line profiles. Samples were analysed at an incident wavelength calculated to be 1.15970 ± 0.00001 Å as it provided the best peak shape and peak-to-background ratio within the available energy range of the instrument or at an incident wavelength of 0.42646 ± 0.00001 Å to reduce air scattering and absorption of the beam by the sample. Patterns were collected at temperatures above and below the respective A_p and M_p temperatures for each sample by using a hot air blower and placing the samples in either a freezer set to -4°C or liquid nitrogen before scanning at room temperature. The Mythen microstrip detector was used in all experiments as it provides high-speed data acquisition of a large 2θ range at high resolution. All of this data was collected with the assistance of the beam line scientist Dr

Kia Wallwork. Laboratory XRD required three hours per pattern and does not provide sufficient resolution to index the structures. Hence, the speed and flux of the synchrotron is crucial to monitor the phase transitions in-situ, as a function of temperature.

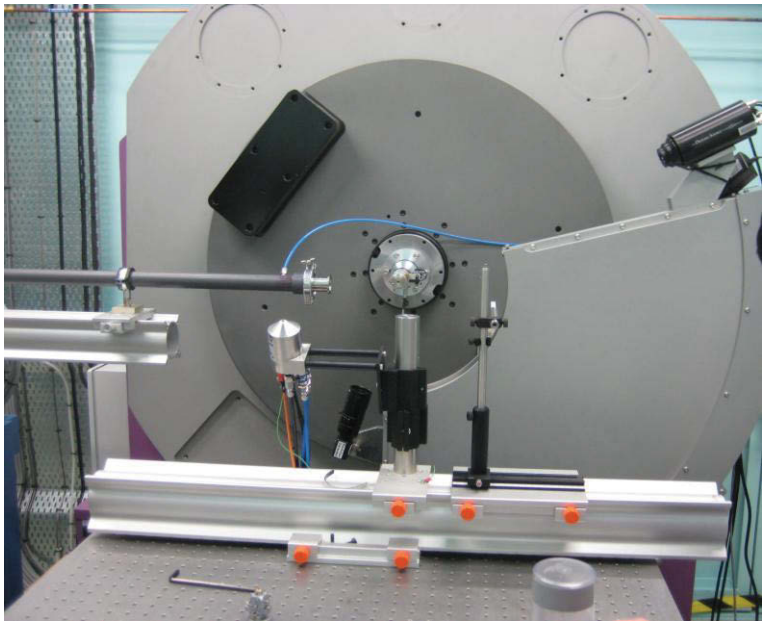

Figure 3.10 Synchrotron powder diffraction experiment.

3.8 Neutron Powder Diffraction (NPD)

Similar to XRD, NPD is able to provide information on the crystal structure of the material being examined. The major difference is that the neutrons interact with the nucleus of the atom whereas X-rays interact with the electron cloud. The main advantages of neutrons over X-rays are (1) that they can penetrate bulk samples of several millimetres in thickness and (2) that the cross-sections for neutron interaction of low-*Z* atoms are sometimes much higher than those for X-rays, as the contrast between elements is random rather than being based on atomic number (Figure 3.11). This is important when the material being studied includes elements of low Z number. The nucleus is much smaller than the electron cloud therefore more precise atom positions can also be gained from NPD. The disadvantage of NPD is that the detected diffracted intensity is much lower than that of typical XRD patterns. This is due to the neutron

source producing a lower number of neutrons compared to X-ray sources, and a large proportion of neutrons are not scattered by the sample because the nucleus is only a small fraction of the atomic volume.

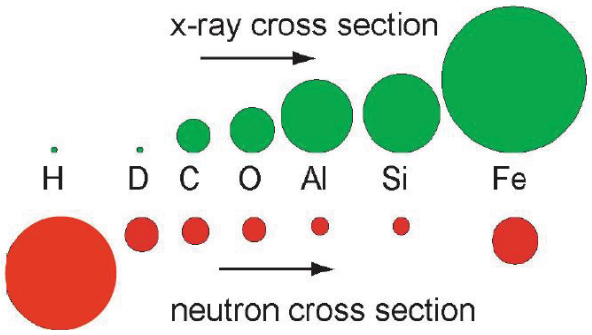

Figure 3.11 Comparison of X-ray and neutron cross section for some elements. X-ray scale has been reduced by a factor of approximately 1.5 [155].

The high resolution powder diffraction beam line (Echidna) [156] was used at the OPAL reactor in Australia as it is able to provide more information on the Al occupancy within the crystal lattice and limits the Au dominance from the diffraction pattern as the scattering length of Au and Cu are similar. By dual refinement of the XPD and NPD data it is possible to generate a much more accurate model for the crystal structure of the material. Diffraction patterns were collected for samples of varying Al wt.% using a neutron wavelength of 1.622 Å ± 0.001Å. The powdered samples were placed into a vanadium can and placed in a cryo-furnace. Three sets of four-hour scans were collected above and below the austenite and martensite transformation temperatures for each of the given samples. This data was collected with the assistance of the beam line scientist Dr Maxim Avdeev.

3.9 Thin-film Sample Preparation

3.9.1 Magnetron Sputtering

Magnetron sputtering like many other sputtering techniques works by creating a plasma which is used as a carrier of the target ions to the substrate. Magnetron sputtering has an advantage over other sputtering techniques as the plasma is localised near the surface of the target. This is achieved by the use of a strong magnetic field which confines the

electrons to the surface of the target and therefore increases the ionisation of gas molecules close to the surface of the target. This results in more ionised gas molecules interacting with the target and therefore increasing sputtering rates.

The AuCu (58 at.% Au) target was mounted into one of the magnetron guns and a pure Al 99.999% target was mounted into the other gun. The deposition chamber is equipped with a rotary roughing pump and a high-vacuum diffusion pump. The cross-over point from roughing pump to high vacuum is at approximately $2x10^{-1}$ Torr. The diffusion pump then pumps down to between $1x10^{-5}$ and $8x10^{-7}$ Torr. Once adequate pressure is reached, Ar gas is backfilled into the chamber so that the pressure is increased to approximately $2.1x10^{-3}$ Torr. This partial pressure of Ar is required to allow a plasma to be generated. The plasma is induced using a power (W) regulated source as the deposition rate has been found to be related to power (W) [157]. A load locking chamber was also implemented, reducing the need to vent the entire deposition chamber, Figure 3.12, between each sample's subsequent deposition. After each deposition the load lock is used to extract the sample, and is then isolated from the high vacuum and vented to atmosphere.

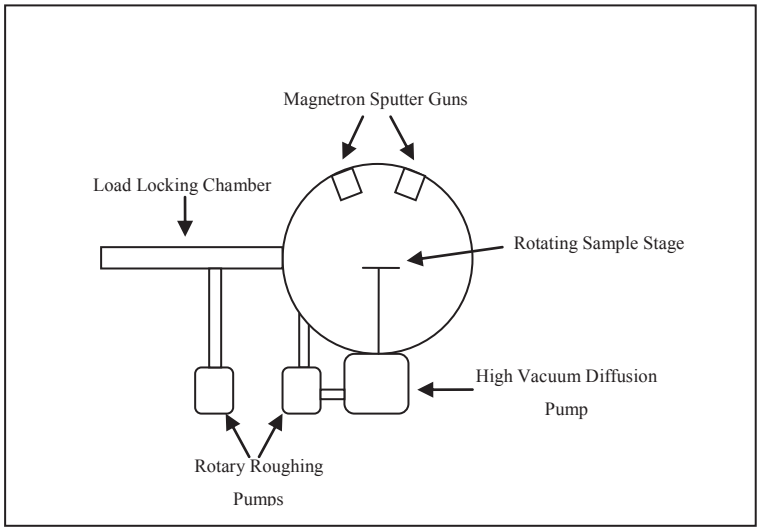

Figure 3.1 Magnetron sputtering chamber diagram.

3.9.2 TEM Sample Preparation

Cross section samples for transmission electron microscopy (TEM) were prepared by taking the thin films deposited on Si wafers and preparing 3 mm x 1 mm pieces. These were then glued together using an epoxy resin, creating a two layer “sandwich” of silicon with the films in the middle. This method affords the opportunity for four attempts to be made at imaging the film, and also allows for uniformity of features to be checked as one hole milled in the centre will expose four film edges. The sample is then left to cure overnight to ensure structural integrity. Once hardened the silicon/sample sandwich is glued on to a polishing stub using 'crystal bond'. Crystal bond is a thermal softening glue that is soluble in acetone. The stub is then attached to a Gatan disk grinder and polished using the technique described in Chapter 3.1.4. Once one side of the silicon is sufficiently polished, the silicon wafer is glued to a Mo TEM grid using epoxy resin, and left overnight to cure. The stub is then heated to loosen the crystal bond so that the sample can be removed, cleaned using acetone, and glued to the stub using crystal bond so that the other side can be polished. Once the polishing has been completed, the stub is heated and the sample is removed and placed into acetone and ethanol to remove crystal bond residue. This amount of specimen preparation is only required for TEM analysis. For many of the other techniques used, “as produced” films can be analysed with no need for further preparation.

3.9.3 Polishing

Polishing of TEM samples was achieved using a Gatan disk grinder and several different grades of silicon carbide paper. The sample is thinned down to specific thicknesses with finer grade silicon carbide paper as seen in Table 3.1. The samples were polished in a figure of eight pattern so that material was removed evenly. The sample was examined under an optical microscope before it was removed and the other side of the film polished.

Table 3.1 Polishing methodology guidelines

Grade of Silicon Carbide Paper	First side	Second side
	Polished to Thickness (um)	
500	600	*
800	500	320
1200	400	220
2400	340	120
4000	320	80

*Thickness added from Mo TEM grid

3.9.4 Ion Beam Milling / Thinning / PIPS

In order to thin the cross sectional sample so that it is electron transparent, a precision ion polishing system (PIPS) was employed. PIPS works by producing an Ar plasma which is directed over the region of the specimen that requires thinning. As the charged gas plasma is streamed across the specimen at a very shallow angle, small amounts of the specimen are removed. As the guns alternate between milling from the top and bottom, a very thin hole is formed in the middle of the sample making the specimen electron transparent. The PIPS used to prepare the TEM specimens was made by GATAN. Sample preparation times varied between 3 – 8 hours. The milling process involves the chamber initially being pumped down to $5x10^{-6}$ Torr, after which an Ar gas is backfilled into the chamber at 0.1 cc/min to achieve an operating pressure of between $2x10^{-5}$ to $2x10^{-4}$ Torr. The ion guns operate at between 1 - 6 keV but a voltage of 4 keV was selected for the cross sectioned Si substrate samples. The samples were milled at + and – 5°.

3.10 Grazing Incidence XRD (GIXRD)

GIXRD is used mainly for thin films or where diffraction data are only required from the surface of a sample. This is achieved by lowering the angle of the incident X-ray beam so that the penetration depth is limited. Depending on the material and the desired

penetration depth, the angle can be adjusted so that signal is only produced from the area of interest. However GIXRD has the disadvantage that peaks are asymmetrically broadened and shifted by the small incident angle so rigorous quantitative analysis of the diffractograms is not as straight forward as in the Bragg-Brentano configuration [158]. For materials with a larger X-ray scattering cross section, a higher incident angle can be used proving better resolution. A Bruker D8 Advance diffractometer using Cu Kα1,2 radiation, a Göbel mirror for the incident beam, a multiple sample holder and Sol-X detector fitted with a parallel plate collimator was used to determine the crystalline phases present in the thin films. An incident angle of 0.8° to 2° was used for GIXRD with the detector scanning a 2θ range of 10° to 80°, with a step size of 0.05° and a collection time of 20 seconds per step.

In-situ GIXRD was also performed on the samples above and below the transformation temperatures recorded by electrical resistance measurements. This was achieved by blowing nitrogen on the surface which was cooled by passing through a liquid nitrogen Dewar flask or heated via a copper coil resistance heater. A 2θ scan range of 38 to 44° (Cu Kα) was chosen as this region encompasses the greatest change in the diffraction pattern between the two phases, and allows for a faster acquisition.

Theta/2θ diffraction was also performed on thin-film samples using the Panalytical X'pert Pro X-ray diffractometer fitted with an Anton PAAR TTK 450 temperature stage to observe the crystal structure of the films at temperature. While this measurement was performed in regular diffraction mode and therefore produced weaker intensity from the peaks, a distinct pattern was still seen. Initially scans were taken on films that exhibited β-phase crystal structure over the 2θ range of 38° to 43° for the reason given previously. Films were heated and cooled in the range of 450°C to -150°C in order to collect patterns. After suitable transformation temperatures had been identified, whole pattern scans were taken in the martensitic and austenitic states from 20° to 70° in 2θ.

3.11 X-ray Reflectometry

X-ray reflectometry is a useful technique for assessing the quality and properties of thin films with minimal specimen preparation. When X-rays are directed at a surface at a glancing angle they are reflected at a given intensity following the Fresnel reflectivity law. However if the X-rays penetrate to the back surface of the film reflections will occur from each interface and, these reflections can interfere with each other creating periodic fringes. These fringes are recorded as the incident beam and detector scan through a small angular range and the intensity is plotted against Q which is equal to $4.\pi.sin(\theta)/\lambda$. Using modelling software and the assistance of Prof. Michael James, these recorded fringes are fitted with a number of parameters. The variables considered are roughness of the film and substrate, density, thickness, reflectivity both real and imaginary parts, etc. X-ray reflectometry was used to measure the thickness and surface roughness of the deposited films, using Motofit least squares fitting software [159] to model the results. A Panalytical X'Pert Pro was set up for reflectometry to scan across the omega-2θ axis, with a start angle of 0.05° and an end angle of 4°. A step size of 0.005° was used with a count time of 1 second.

3.12 Transmission Electron Microscopy (TEM)

Transmission electron microscopy is capable of producing images of high magnification with sub-1 nm resolution however, the specimen preparation (see earlier) can require a large amount of time and the use of the microscope itself may involve a substantial amount of time to align the beam optics. A TEM is made of several parts: the electron gun, a condenser lens, objective and intermediate apertures, a range of electromagnetic lenses and the fluorescent screen or CCD detector. These components are housed in a large column which is kept at low pressure typically in the order of 10^{-9} Torr. There are two main types of electron beam sources in a TEM, either a LaB_6 or tungsten filament that is connected to a high potential typically in the order of 100 to 300 keV. When enough current is passed through the filament, electrons will be ejected into the vacuum of the column through either a thermionic process or field electron emission. The electron beam is then controlled with the electromagnetic lenses and apertures. The first

part of the optics is composed of two or three condenser lenses used to control the spot size of the beam on the sample as well as the intensity of the beam. A condenser aperture is selected which is used to limit the beam intensity and remove some aberrations from high angle electrons generated by the lenses. The electron beam then passes through the sample and is focused using the objective lens. The objective and selected area apertures are also used to define the region of interest in the sample or select specific diffracted electrons to image. Intermediate and projector lenses then expand the beam to produce an enlarged image on to a phosphor screen or CCD camera. There are several ways in which a TEM can provide contrast in an image such as, mass-thickness contrast or diffraction contrast [160].

Selected area electron diffraction patterns can be generated by adjusting the electromagnetic lenses so that the back focal plane is coincident with the CCD camera or phosphorus screen rather than the imaging plane. For crystalline samples this produces an image of small bright spots that represent electrons that have met the diffraction condition and one large central spot from the direct beam of electrons passing through the sample. In polycrystalline or amorphous samples these diffraction conditions occur through a range of positions and produce rings on the detector. Using the position and angles of the diffraction pattern it is possible to identify the crystal structure of the material [160].

Bright field produces an image where contrast is based on the number of electrons transmitted through different regions within the sample. Therefore thicker, denser or areas of higher average atomic number will produce darker areas due to the increased number of scattered electrons. In order to increase contrast from only the unscattered electrons the objective aperture is used to select only the direct beam seen on the electron diffraction pattern [160].

Dark field allows for differences in crystal structure and orientation to be identified by selecting electrons that are dispersed within the material due to Bragg scattering. Depending on the orientation and crystal structure, electrons are collected in discreet regions of the back focal plane. If any one of these diffraction spots is selected then

areas of the sample that do not diffract electrons into this particular reflection will appear dark including areas where there is no sample, hence the name dark field. This allows for the identification of similar crystals or preferred orientation and defects in the crystal lattice [160].

A TEM may also be operated in a scanning mode known as STEM, where the incident beam is focused on the sample and rastered across the surface. This is achieved by increasing the power of the final condenser lens so that the electron beam converges, and using a pair of scanning coils which direct the beam so that it rasters the incident beam parallel to the optical axis, mimicking the parallel beam of a standard TEM. Similar to regular TEM it is possible to produce bright field and dark field images however the method of collecting this information is different. For a bright field image instead of using an aperture to collect only the central beam of electrons, an electron detector is placed under the sample, this detects the amount of signal produced as the incident beam is scanned. The signal is then processed and correlated to the beam position so that the intensity is recorded for a given pixel, producing a final image on the screen. For dark field detection, a secondary annular detector is used that is positioned around the bright field detector so as to collect only the scattered electrons [160]. STEM mode was used in the present project whenever it was necessary to collect EDS data.

Transmission electron microscopy (TEM) was performed using a JEOL JEM 2010F (JEOL, Japan) equipped with a field emission gun (FEG) electron source operated at 200kV. The TEM was equipped with an energy dispersive X-ray (EDX) spectrometer and NORAN System SIX microanalysis system (Thermo Electron Corporation, USA). Bright field and dark field images and selected area diffraction patterns (SADPs) were recorded using the 1k x 1k CCD camera in the GIF 2001.

Transmission electron microscopy (TEM) was also performed using a JEOL JEM 2200F S (JEOL, Japan) equipped with a field emission gun (FEG) electron source operated at 200kV. An omega filter electron energy spectrometer is integrated into the electron column of the TEM for electron energy loss spectroscopy and energy filtered

imaging. The TEM was equipped with a Silicon Drift Detector (SDD) type energy dispersive X-ray (EDX) spectrometer and Aztec Energy microanalysis system (Oxford Instruments, UK). The microscope was also operated in STEM mode in order to obtain an EDX map of the samples. This was done over 5 minute collection times using the beam lock system and collecting full spectra. These points were later analysed using the Oxford Instruments INCA system. The TEM images and EDS analysis were collected with the assistance of Mark Blackford.

3.13 Profilometer

A profilometer is able to measure differences in height of very small *z* ranges with sub-nanometre resolution. The profilometer consists of a stylus with a diamond tip that is dragged across the surface at a constant rate and with a desired load. As the stylus moves across the surface the changes in height are recorded with a transducer which converts the vertical motion into electrical oscillations that are amplified. This analogue signal is then processed using software that digitizes the data and reads out the changes in height producing a two-dimensional image of the sample. Using software analysis it is possible to measure the height of any features, the average roughness of the surface and the standard deviations in height. Using a glass-tipped scribe, sections of the deposited film were removed from the silicon substrate and the height difference in these areas was measured using a KLA Tencor Alpha Step IQ. The profilometer was then scanned across these pits at 20 μm/s with a sampling rate of 500 Hz. Using the automated step height measurement an average height was taken across all of the pits.

3.14 Electrical Resistance

Electrical resistance measurements are an effective way of identifying a phase transition in most materials. This is due to Matthiessen's rule which states that the total electrical resistance of an alloy is the sum of the resistance due to electron scattering by phonons and the resistance due to electron scattering because of lattice imperfections and impurities. Phase transformations affect both factors, therefore, a graph of electrical resistance versus temperature provides an effective means for detecting the formation of

various phases in shape memory alloys [161]. In addition, the martensite and austenite phases themselves possess slightly different resistances so it is possible to plot the resistance versus temperature and see distinct changes in slope that relate to the transformations that take place at specific temperatures [162]. A two-point probe was used to measure the electrical resistance of the films. Two copper contacts were attached to the film and the sample was placed in a small vacuum chamber, so as to prevent ice formation on cooling. The electrical resistance measurements were recorded using a Keithley 197A auto-ranging microvolt DMM and logged using LabVIEW 2011®. The films were then heated or cooled in order to take them past their respective transformation temperatures while measuring the electrical resistance of the film. Films in the martensite structure at room temperature were heated to approximately 190°C and then cooled below room temperature. Films that were in the high temperature austentite structure at room temperature were cooled to approximately -150°C and then heated. This allowed for the transformation temperature to be precisely recorded for both forward and reverse transformations. The measurements were conducted under a vacuum.

3.15 Secondary Ion Mass Spectroscopy (SIMS)

SIMS is a technique used to profile a film's composition and thickness. This technique works by accelerating a focused primary ion beam at a sample and bombarding the surface, sputtering the material. The primary beam ions are usually gaseous and surface ions. Gaseous ions are generated using electron ionisation and typically use noble gases or oxygen. Surface ions of caesium are generated by vaporising caesium atoms through a charged porous tungsten ionizer. In both cases these ions are then focused on to the surface of the sample and rastered over a selected area of interest, damaging the bonds within the material. Once the bonds have been broken, secondary ions are ejected from the surface of the material. The ejected secondary ions are guided down the chamber towards a charge separator and a mass energy separator. This screens the incoming ions for only the type selected, which continue to the detector. Depending on the counts of the species, the detector will either be a Faraday cup or a CCD camera which records the number of ion impacts [163]. A Cameca SIMS system was used for these thin films

with Cs^+ ions selected for sputtering the sample. A 250 x 250 μm raster was used with a beam current of 8.3 nA. The instrument was operated by Dr David Nelson.

3.16 Spectrophotometer

In order to understand the optical properties of a material, its absorption, reflection and transmission over a range of wavelengths is required. A spectrophotometer consists of three main elements - a light source, a monochromator and a detector. There are two types of spectrophotometers, a single source and a dual source. In a single source, a spectrum is run with no sample to create a baseline. In the dual source the sample is illuminated as well as a reference, so that the transmitted or reflected intensities can be simultaneously referenced against the source intensity. Spectrophotometers can scan the electromagnetic spectrum from the IR to the UV through the use of multiple light sources and monochromators. This is important when modelling the optical properties of the material for different uses. A Varian Cary 50 spectrophotometer with a Labsphere was used to measure the transmission and diffuse reflection from 300 to 1100 nm with a slit width of 1 nm. This was used in conjunction with a custom piece of software (written by Prof M.B. Cortie based on the ASTM standard G173) to calculate and plot the CIE LAB colour of these films. A Perkin Elmer Lambda 950 spectrophotometer with a universal reflectance attachment was also used on some films to measure the transmission and reflection from 300 to 2500 nm with a slit width of 5 nm from 300 to 789 nm and a slit width of 20 nm from 790 to 2500.

3.17 Computer Modelling of Optical Properties

Using the transmission and reflection spectra of specific deposited films, the optical constants *n* and *k* were extracted using WVASE32 software version 3.486 by Woollam and the assistance of Dr Angus Gentle. The optical constants were obtained by fitting Lorentz oscillator models to the transmission and reflection spectra, which ensured the Kramers Kronig consistency. The film thicknesses for the models were initially fixed using measurements obtained from the profilometer.

The optical properties and LSPRs of candidate nanostructures were simulated using the Discrete Dipole Approximation for Scattering and Absorption of Light by Irregular Particles (DDSCAT) software of Draine and Flatau version 7.1 [164]. The discrete dipole approximation (DDA) method assigns a grid of polarisable dipoles to approximate a defined object. These polarisable dipoles interact with a local electric field produced by an incident electromagnetic wave, resulting in them acquiring specific dipole moments [141]. The approximation of the object is governed by the size and number of polarisable points used, and whether they are spread uniformly or non-uniformly throughout the material. This method can only be used to model a metallic object embedded in a uniform medium as the calculations for each individual dipole assume that the dielectric medium is homogeneous [141]. Two important parameters that affect the accuracy of the scattered electromagnetic waves in these simulations are the effective radius, a_{eff}, and dipole spacing (d). a_{eff} is defined as the radius of a sphere with the same volume as that of all the dielectric materials in the target. The dipole spacing is simply the spacing between the polarisable points assigned to the target. Accurate results are obtained provided that a_{eff} and d are small enough so that $2.\pi.a_{eff}/\lambda<25$ and $2.\pi.d.|m|/\lambda<1$ where m is the complex refractive index.

A custom-written program ('E and B Processor', written by M. Cortie) was used to image the electric fields, and hence plasmon modes, around the actuator for given resonance peaks. This program repeatedly calls DDFIELD (a component of the DDSCAT suite that calculates the electric field vector at some position in x,y,z space) in order to build up a 2D or 3D image of the electric field. The resulting data can be visualized in a variety of ways, including as a contour plot, as field lines, or as a colour-coded map.

4 Beta-phase AuCuAl SMAs

4.1 Introduction

Shape memory alloys (SMAs) are a remarkable group of materials with the unique ability to revert to a predefined shape after they have been deformed. Background information on these materials was provided in Chapter 2. As mentioned, an example of a gold-based alloy that exhibits this transformation is the β-phase alloy that has the stoichiometry $Au_7Cu_5Al_4$. This alloy was initially misidentified as being similar to the $L1_0$ phase formed from (Au,Cu) [165] [65], but it was later shown that it forms part of a Hume Rothery β-phase electron compound that extends up through the AuCuAl ternary diagram to a maximum of approximately 45 - 55 at.% Au, depending on temperature [30, 34], Figure 4.1.

At 75 wt.% Au (the 18 karat level) the β-phase has the composition of approximately $Au_7Cu_5Al_4$ [28]. This alloy has good castability, oxidisation and wear resistance, and an interesting 'apricot' colour making it potentially suitable for use in jewellery [64]. It has shape memory properties but, unlike many other SMAs, it is resistant to aging at high temperatures [29]. Furthermore, it can support a surface plasmon in the visible spectrum [166]. These properties have stimulated some interest in this alloy as they differ from those of the more common titanium- or copper-based SMAs. One drawback of the material is it is very difficult to cold work.

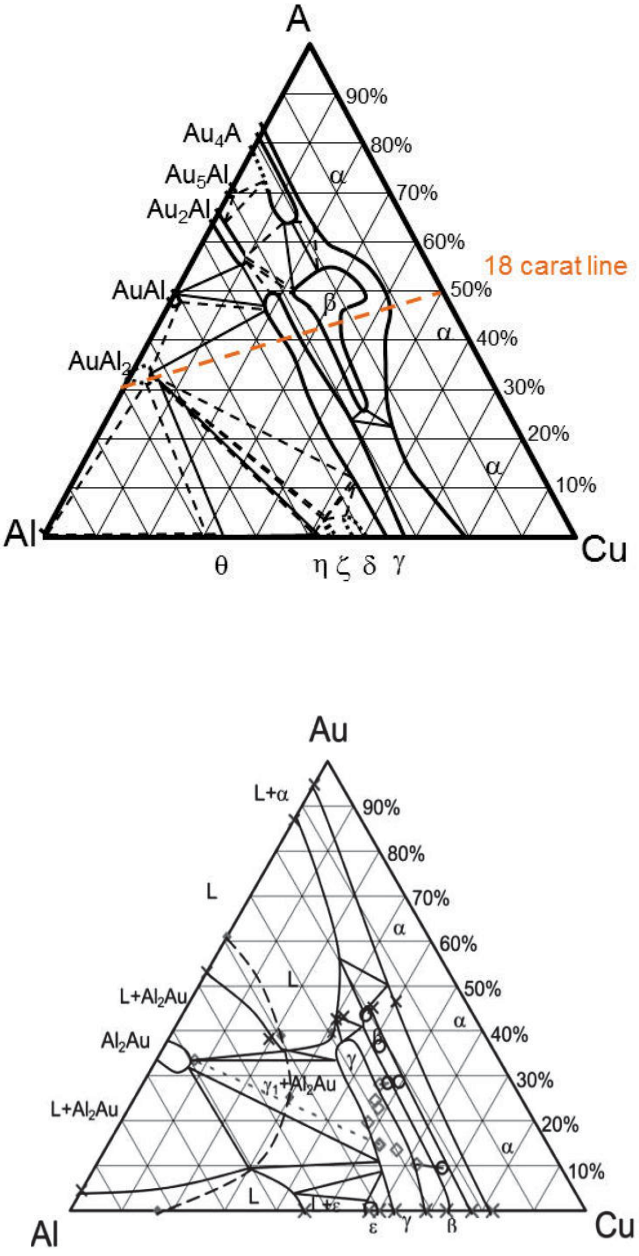

Figure 4.1 Isothermal sections through the Al-Au-Cu ternary phase diagram showing the presence of various intermetallic compounds with a β-phase. (top) 500ºC section [34], (bottom) 750ºC section [30].

The properties of the $Au_7Cu_5Al_4$ alloy in particular have been previously explored through the use of a wide range of techniques, including microscopy, X-ray diffraction, mechanical testing and thermal analysis [29, 30, 32-37, 61]. The focus of this prior work was largely on properties in relation to its possible use in 18 karat jewellery. However, the properties of the other β-phase compositions in the AlAuCu system have been studied far less. In particular, the effect of Al content across the β-phase field has only been studied with respect to the trends in colour and hardness of the alloys [33], and the phase boundaries along the 18 karat isopleth [32], Figure 4.2. There appear to have been no systematic studies yet on the effect of Al on the crystallographic structure of the β-phase or its martensite, nor on the transformation temperatures between these two phases. Given that the thin films of SMA studied elsewhere in this thesis differ mainly by Al content, this omission needed to be rectified in order to compare the differences between bulk and thin-film AuCuAl SMAs.

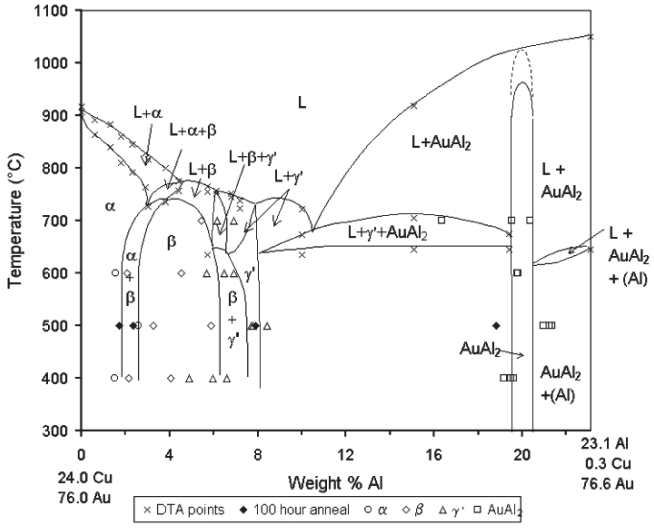

Figure 4.2 Isopleth through the Al-Au-Cu ternary system with 76 wt.% Au [32].

In this chapter I will investigate the effect of varying the Al content of a series of samples across the width of the β-phase revealed by the above isopleth. The changes in the transformation temperature and crystal structure that result are then studied.

4.2 Experimental

Four samples were manufactured as described in the Experimental chapter by casting from high-purity, base metals of Al (99.99+%), Au (99.9999%) and Cu (99.9%). The amounts were calculated from the atomic percent composition required for each sample across the β-phase according to the ternary phase diagram in [30, 34]. These were then converted and measured out to be 6, 5, 4 and 3 wt.% Al and 76 wt.% Au, with the balance being weighed out in Cu. These samples were designated R6, R5, R4 and R3 respectively. Another two samples made through similar processes were labelled FL and S10. These contained nominally 5 and 5.8 wt.% Al respectively.

DSC analyses were performed in order to measure the transformation temperatures of the alloys. A Thermal Analysis DSC 2920 was used with a ramp rate of 10°C/min.

Synchrotron based powder diffraction was undertaken at the Australian Synchrotron (10BM1: Powder Diffraction) [154]. Patterns were collected at temperatures above and below the respective A_p (austenite peak transformation) and M_p martensite peak transformation) temperatures for each sample. X-ray patterns of bulk samples were also obtained on laboratory machines using Cu Kα radiation. Due to the large grain size of the material, the patterns of the bulk samples were strongly affected by texture.

The X-ray patterns were dominated by the scattering from the Au component. Hence, in order to resolve the site occupancies, complementary neutron powder diffraction data were collected on Echidna (the high resolution powder diffractometer) [156] at the OPAL reactor at ANSTO in Australia, because neutron diffraction is more sensitive to the Al positions in this system.

Bulk samples were imaged through a Zeiss Axiotech, with a Media Cybernetics Evolution MP digital camera under bright field and Nomarski interference contrast conditions. SEM images were obtained using a Zeiss Supra 55VP with a 20 KeV electron beam, a 120 μm aperture and a backscatter detector to observe any in-

homogeneities in composition. Composition was simultaneously determined by averaging EDS analysis over 5 positions for each phase.

4.3 Results

SEM backscatter images were collected of the polished samples as this imaging method highlights distinct differences between phases with different compositions in the samples. From these images it can be seen that sample R3 and R6 both consist of a microstructure of uniform composition, whereas sample R4 and R5 both contain a second phase (Figure 4.3).

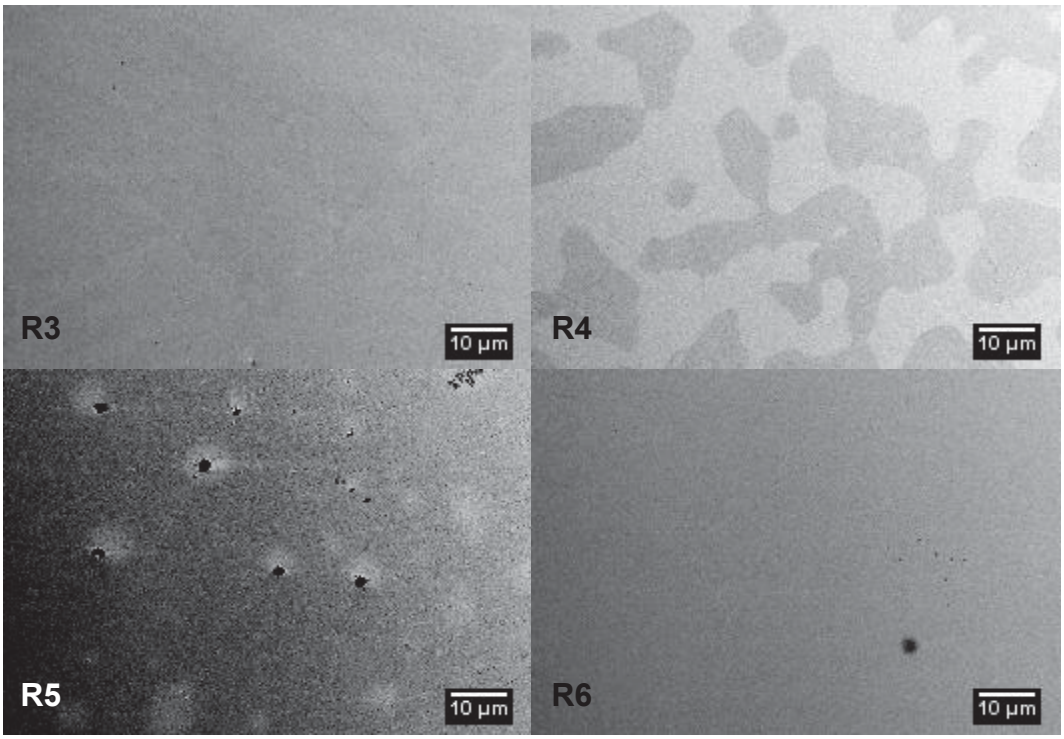

Figure 4.3 SEM backscatter images of polished samples showing single phase and dual phase alloys. Top left – R3, top right – R4, bottom left – R5 and bottom right – R6.

SEM images were also taken of the dual-phase samples after being cycled through their respective transformation temperatures (Figure 4.4).

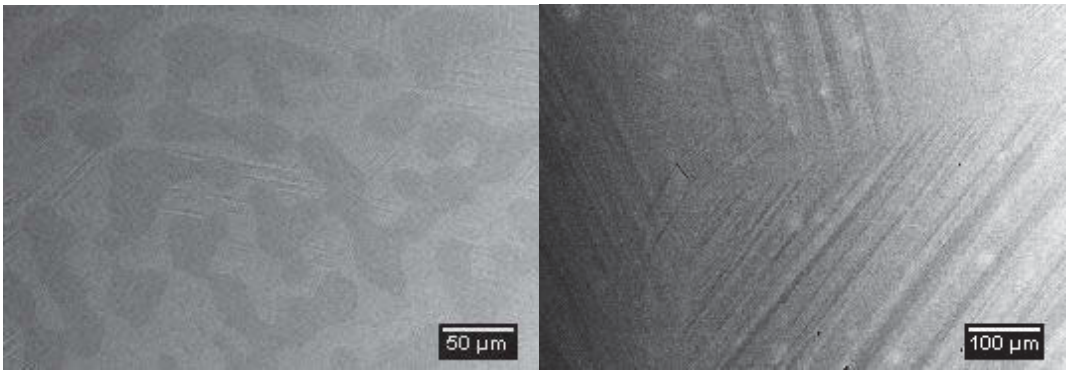

Figure 4.4 SEM backscatter images of R4 (left) and R5 (right) after transformation showing martensite laths.

Volume fraction of individual phases within dual-phase alloys was determined through the use of ImageJ software and SEM backscatter images. Using the thresholding function to distinguish between the light and dark phases, the measurement tool was able to provide an estimate for the number of pixels corresponding to each of these phases. Taking these values and, since surface area ratios and volume ratios are equal (a basic axiom of quantitative metallography), volume fractions were estimated for the individual phases.

Table 4.1 and Table 4.2 show the composition of the samples determined by EDS after heat treatments. The composition of the individual phases was also found with all measurements in atomic or weight per cent. All EDS results were calculated with an error of ± 0.5% statistically, from an average of five spectra. From Monte Carlo simulations it was found that the interaction volume of the electron microscope at 20 keV was approximately 1 µm for these samples, with smaller volumes for the higher weight per cent gold, and larger volumes for lower weight per cent gold samples. As the lighter phase in sample R5 is most likely a precipitate, the composition of this phase may not reflect its true homogeneous composition due to matrix effects.

Table 4.1 Composition of cast AuCuAl samples in at.%

	Total			Darker Phase			Lighter Phase		
Sample Number	Al at.%	Cu at.%	Au at.%	Al at.%	Cu at.%	Au at.%	Al at.%	Cu at.%	Au at.%
R3	12.3	37.5	50.1						
R4	15.4	35.3	49.3	13.9	38.0	48.1	16.6	33.0	50.4
R5	19.5	31.7	48.8	19.5	32.0	48.5	20.1	26.5	53.4
R6	22.9	30.4	46.7						
S10	20.9	35.7	43.4						
FL	24.2	32.3	43.5						

Table 4.2 Composition of cast AuCuAl samples in wt.%

	Total			Darker Phase			Lighter Phase		
Sample Number	Al wt.%	Cu wt.%	Au wt.%	Al wt.%	Cu wt.%	Au wt.%	Al wt.%	Cu wt.%	Au wt.%
R3	2.6	18.9	78.5						
R4	3.4	18.1	78.5	3.0	19.7	77.3	3.6	16.8	79.6
R5	4.3	16.6	79.1	4.4	16.8	78.8	4.3	13.2	82.5
R6	5.3	16.4	78.3						

DSC analysis showed that all of these alloys undergo a reversible transformation, however in the case of R3 it needed to be heated to 400°C first before the transformations were seen. The transformation temperatures of the alloys generally decrease with increasing Al content. This is seen initially with the large decrease in temperature from R3 to R4.

Table 4.3 Transformation temperature for cast samples

	A_{p1}	M_{p1}	A_{p2}	M_{p2}
R3		166	241	169
R4	94	61	86	61
R5	77	32	71	32
R6	85	23	83	27

Nomarski interference images taken of the samples before transformation show an evenly polished surface with some voids due to casting porosity. Some structure is visible due to 'anti-laths' (formed when heating during polishing causes a martensite or austenite lath to 'pop in' with respect to the polished surface) and/or the preferential polishing of the softer phase in the dual-phase alloys. The differences in height generated by these features are minimal and evident in the small changes in colour in the Nomarski interference images. Images taken after the samples are passed through their respective transformation temperatures show clear laths in the Nomarski images, representing large changes in height and surface deformation. The difference between the samples before and after transformation can be seen in Figure 4.5.

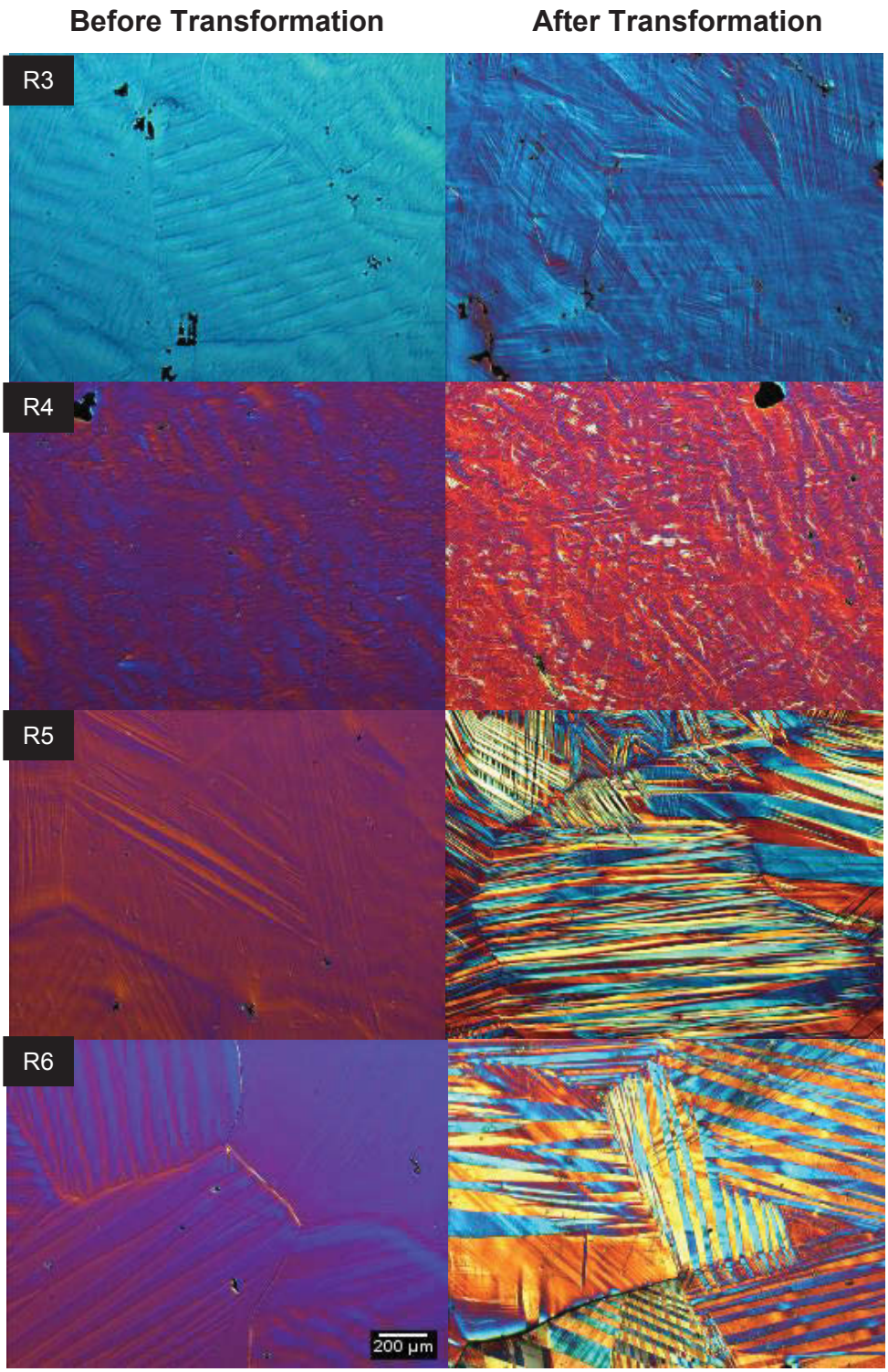

Figure 4.5 Nomarski interference images of cast samples before and after transformation showing martensitic laths.

Synchrotron and neutron powder diffraction patterns taken at above and below the respective transformation temperatures for all alloys indicate a clear distinction between the austenite and martensite phases. During heating from low temperatures, the martensite phase transforms into the high temperature parent phase, presumably by the same kind of displacive, first-order phase transformation already known for $Au_7Cu_5Al_4$. The transition occurs between 71 and 241°C, depending on composition and prior thermal history. Figure 4.6 shows the synchrotron X-ray powder diffraction patterns for all six alloys with increasing Al wt.% and the temperature at which each pattern is collected. All six alloys displayed peaks that align with the $L2_1$ β-phase crystal structure in scans collected above the austenite transformation temperature. High temperature diffraction patterns also displayed peaks not related to the $L2_1$ β-phase structure in some samples (e.g.) the 5.26 Al wt.% sample. As the martensite and austenite β-phase peaks are the only ones of interest for this study, any peaks that did not change between the high and low temperature state were easily identified and designated as either polishing media (i.e. SiC) or minor phases. The martensite phase has a relatively complex crystal structure, which is easily recognizable on the diffraction patterns. Refinement of its crystal structure is not considered within the scope of this chapter.

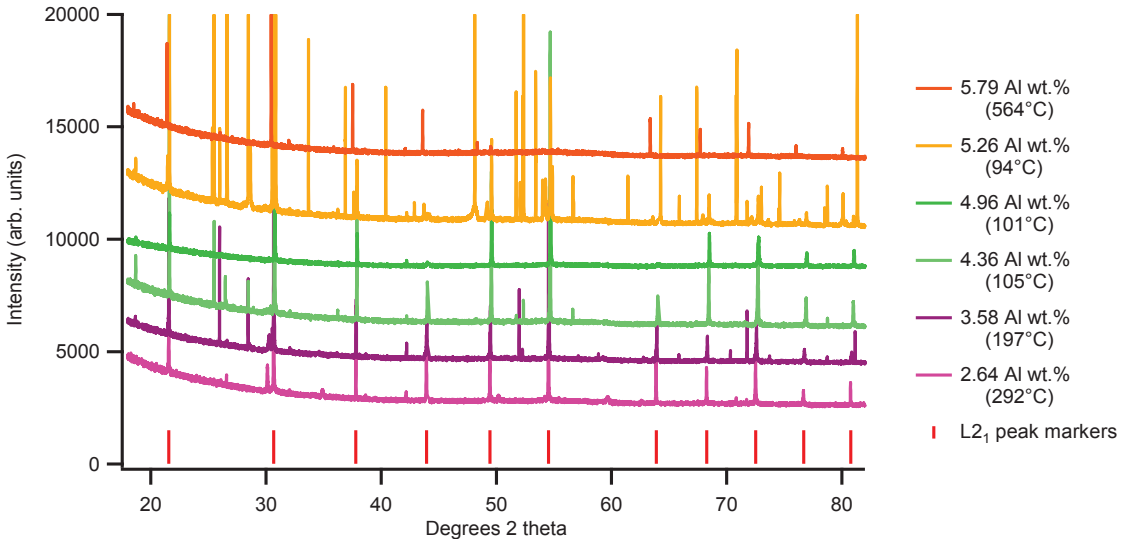

Figure 4.6 Synchrotron X-ray powder diffraction of austenite phase samples. Data vertically offset for clarity. Wavelength - 1.15970 Å.

4.4 Discussion

4.4.1 Phases present in alloys of varying Al wt.%

The AuCuAl 750°C ternary diagram as described in [30] and shown in Figure 4.1 indicates several phases that extend from the binary edges into the ternary by a few atomic per cent, however the three major phases that plunge deep into the ternary diagram are the α, β and γ phases. The alloys cast in this project were all originally designed to have compositions which would place them inside the β-phase. However, when the compositions were analysed using EDS the Al% was reduced, most likely due to oxidation. While these alloys were melted under an inert atmosphere, partial pressures of oxygen within the oven may have been high enough to oxidize part of the Al as this was not a vacuum furnace. The β-phase along the 18 karat gold line is quite narrow, therefore small deviations in the desired composition can cause drastic changes in the structure and properties of these alloys. When looking at the composition tables, it can also be seen that these alloys have a higher Au percentage than expected, positioning them away from the 18 karat gold line. These two factors have created alloys which were not originally desired, but which have nevertheless provided insight into the ternary diagram, as well as information about the transformation temperature and properties of these alloys.

R3 was originally designed to have 3 wt.% Al but was analysed to have 2.64 wt.% Al. According to the literature, this small change in weight per cent pushes it into what was originally thought of as the α-phase region of the ternary diagram [30]. The high temperature powder diffraction pattern for this alloy shows that it does not exhibit the simple α-phase cubic structure, but rather the high temperature β-phase austenite structure. This is most likely due to the slightly higher Au content. From the 500°C ternary diagram (Figure 4.1) it can be seen that the β-phase field extends out to lower Al concentrations at higher Au concentrations, therefore it is likely that the R3 sample falls within this region.

Samples R4 and R5 both exhibited dual-phase systems, which can be seen clearly in the backscattered SEM images (Figure 4.4), where dark and light areas indicate regions of

different composition. Sample R4 shows a distinct dendritic structure. The composition of the lighter phase constituent is higher in both Au and Al than that of R3. SEM images of R4 taken after the alloy had undergone a displacive transformation show that this lighter region has surface relief features in the form of laths. From these two factors it can be deduced that this phase represents the β-phase (i.e. the austenite peaks present in the high temperature diffraction patterns). The darker phase must therefore represent the α-phase constituent present in the powder diffraction pattern. From the area analysis, it was found that R4 consists of approximately 79% β-phase and is therefore able to add useful information on the β-phase shape memory alloy series. The α-phase constituent is not of importance to this study and will not be discussed further.

R5 is also a dual-phase alloy, however due to its positioning relative to the ternary β-phase it consists of only four volume per cent of the second phase. From both the SEM images (Figure 4.4) and NIC images (Figure 4.5) after it has cycled through the displacive phase transformation, it can be seen that the major phase has the surface relief patterning. This indicates that the alloy is composed of 96% β-phase. This fits in with the current knowledge of the AuCuAl ternary phase diagrams, showing that the β-phase boundary extends to approximately 48 at.% Au at 700°C, and in between the 55 and 45 at.% Au for the 500 and 750°C ternary diagrams respectively. The second tie line of this minor phase extends out towards the Au – Al binary edge of the ternary diagram, however due to the small volume and matrix effects these measurements do not indicate the true equilibrium composition of this phase. SEM images show a large number of voids produced in the minor phase. This is most likely due to the minor phase being harder and more brittle than the matrix. It is therefore likely that this minor phase is a derivative of the Au_4Al phase, as this phase is known to be very brittle and extends into the ternary diagram towards the measured EDS composition.

From the powder diffraction pattern and SEM images, sample R6, Fl and S10 were identified to be solely β-phase.

4.4.2 Differences in transformation with various Al wt.%

The prominence (vertical height) of the laths produced by the transformations can be judged by the differences in their colours when viewed using Nomarski interference. (As mentioned, Nomarski interference translates a difference in height to a colour signal. A perfectly smooth sample would be monochrome.) In Figure 4.5 it can be seen that the laths in the R6 and R5 protrude out of the surface of the alloy much more (they have brighter and more varied colours) than those of R4 and R3. Due to the dendritic structure of R4, the surface relief from the displacive phase transformation of the β-phase is diminished. This does not occur in R5 as it consists of a large un-obstructed distribution of β-phase. After aging R3 at 300°C for 30 minutes, the presence of small laths were seen in the Nomarski image. These laths were much finer than those produced in any other sample, producing only small variations of colour in the Nomarski interference image. Similar results are seen in other Cu-Al-based SMAs with low Al wt.% alloy producing finer martensite laths due to the formation of a different martensite crystal structure [167].

Comparing the DSC results of R3, R4, R5 and R6 (Table 4.3), it can be seen that the martensite transformation temperatures decrease with increases in Al or (equivalently) the electron-to-atom ratio (Figure 4.7). At low Al wt.% the transformation temperature increases significantly. In this graph, other alloys (S10 and FL) cast via similar processes are also included and are found to follow the same trend. Similarly two extra samples are added to the atomic ratio plot from previous work by Dr. Fiona Levey, and are also found to follow the same trend. The exact Al wt.% of these alloys were not recorded and could therefore not be plotted on this graph. The austenite transformation temperature plateaus at a transformation temperature of approximately 80°C, with the lowest transformation temperature measured from sample R5 (4.36 Al wt.%). This minimum in the austenite transformation temperature is most likely due to the differences in the Au:Cu ratio, as this has been shown previously to lower the transformation temperature [31].

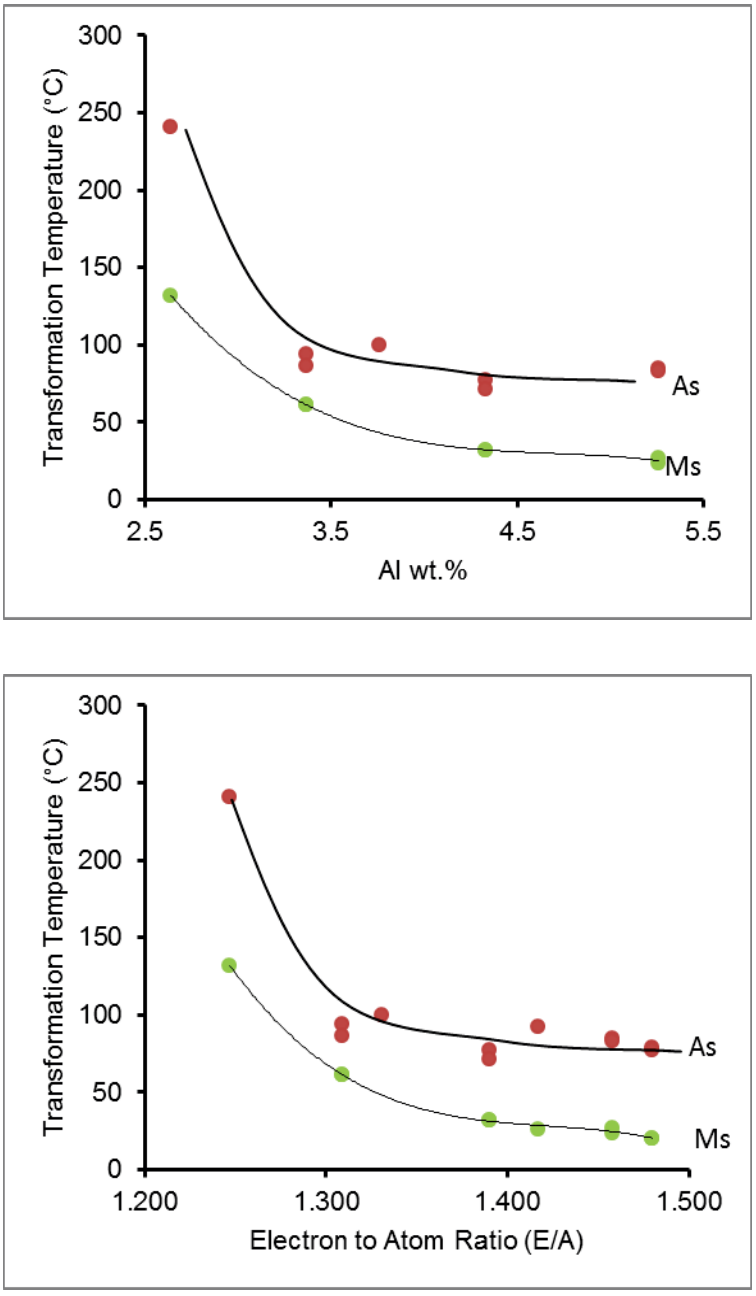

Figure 4.7 Transformation temperature vs. Al content (wt.%) or electron-to-atom ratio (E/A) of cast samples with Al content varying from 5.79 to 2.64 wt.%.

Similarly, when comparing both the martensite and austenite transformations we can see an initial decrease in the difference in transformation temperatures between M_s and A_s (i.e. hysteresis) with increasing Al%. At the lowest Al wt.%, however, there is an increase in hysteresis (Figure 4.7). This reduction in the hysteresis is significant as it is one of the most common problems encountered when creating practical applications for shape memory alloys, and typically limits the application to an on-off state obtained

through large temperature variations. Further work will aim to reduce this hysteresis further, allowing for a smaller range between temperature triggers which, in turn, may allow for more useful applications.

4.4.3 High temperature crystal structures

It was shown in [68] that the high temperature $Au_7Cu_5Al_4$ β-phase alloy has the $L2_1$ ternary ordering (shown in Figure 4.8) to a temperature of about 630ºC. Loss of $L2_1$ ordering starts at approximately 610°C and it is completely removed by 650°C leaving only the presence of the B2 phase up until the melting point. The B2 phase was identified using the prominent and characteristic (200) and (220) peaks. However, formation of the $L2_1$ phase upon cooling is fast, and even samples quenched from 700°C show some ternary ordering, as evidenced by the presence of a (111) peak (only present in ternary ordering, either $L2_1$ or DO_3) and by the ratio of this peak to the (220) peak being very small (indication of $L2_1$) [37] . There are multiple permutations of site occupancies which produce similar powder diffraction patterns but, through consideration of the X-ray and neutron data simultaneously, it was possible to estimate the occupancies of each atom on the A,B and C sites [68].

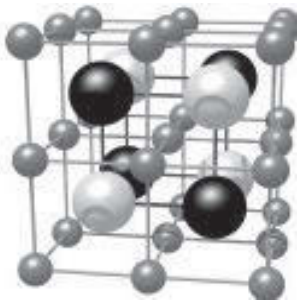

Figure 4.8 $L2_1$ structure model. A site - grey, B site - black, C site - white.

Using a similar method we can estimate the site occupancies in the alloys presented here. When observing the high temperature structure for these alloys, we can see the distinct austenite $L2_1$ structure peaks present in samples ranging from 2.64 to 5.79 Al wt.% indicated by the $L2_1$ peak markers (Figure 4.6). This structure is also seen in the neutron diffraction patterns, however no neutron pattern was collected for R6 (5.26

Al wt.%) and therefore the Al occupancies could not be refined as accurately. Estimates of the occupancy for each of these alloys are listed below in Table 4.4. These values show that, across all compositions, the A site is predominantly occupied by Au, ranging from 88 to 100%, except for S10 (4.86 Al wt.%) which was cast with a lower Au concentration. The remainder of this site is filled with Cu. Similarly the B site predominantly consists of Al at high Al concentrations, however, as the Al content within the cast alloys decreases, the Al is substituted with Cu. The C site has very little to no Al in this position and is occupied manly by Cu with the remainder consisting of Au. The Cu occupancy on this site is between 72 to 93%. While these values are taken to be estimates with an error no better than 5% due to residual texturing, it does provide a guide as to the preferential site ordering across the 18 karat line of the Au_xCu_yAl $L2_1$ phase.

Table 4.4 Best-fitting solutions to lattice occupancies for AuCuAl A_2BC β-phases at different Al contents. Accuracy of entries estimated to be not better than 0.05 due to residual texture effects in samples

2.64 Al wt.%	A	B	C	4.96 Al wt.%	A	B	C
Au	0.88	0.15	0.09	Au	0.68	0.15	0.22
Al	0.00	0.31	0.18	Al	0.02	0.79	0.01
Cu	0.12	0.54	0.73	Cu	0.30	0.06	0.77
3.58 Al wt.%	A	B	C	5.26 Al wt.%	A	B	C
Au	0.92	0.00	0.17	Au	0.88	0.00	0.12
Al	0.00	0.59	0.08	Al	0.00	0.91	0.00
Cu	0.08	0.41	0.75	Cu	0.123	0.09	0.88
4.36 Al wt.%	A	B	C	5.79 Al wt.%	A	B	C
Au	1.00	0.01	0.13	Au	0.80	0.06	0.07
Al	0.00	0.78	0.02	Al	0.02	0.94	0.00
Cu	0.00	0.21	0.85	Cu	0.18	0.00	0.93

4.4.4 Low temperature crystal structures

From the powder diffraction patterns taken at a temperature below each SMA's respective martensite transformation temperature, it can easily be seen that there are three distinct types of martensite structures formed. When these alloys form the martensite structure, the main (220) peak of the austenite $L2_1$ structure splits to form multiple peaks. Figure 4.9 shows the right hand side (high 2θ range) of this split peak. In the low Al wt.% samples, R3 (2.64 Al wt.%) and R4 (3.58 Al wt.%), only a single peak is produced in this range. R5 (4.36 Al wt.%) and S10 (4.96 Al wt.%) however produce two peaks, indicating a lower symmetry. In the case of the high Al wt.% samples, R6 (5.26 Al wt.%) and FL (5.79 Al wt.%), three peaks can be identified relating to the martensite structure. These three peaks are caused by two separate martensite structures similar to those of the low and higher symmetry phases. Similar differentiations can be drawn from the martensite peaks that split from the (200) reflection with the higher symmetry martensite producing two distinct peaks and the lower symmetry producing three.

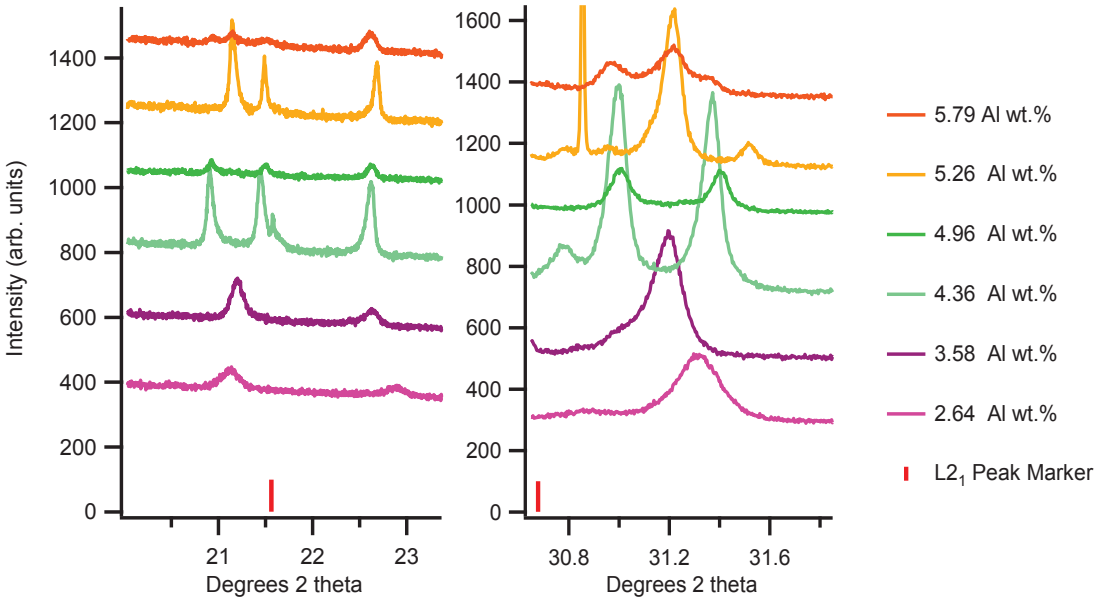

Figure 4.9 Synchrotron X-ray diffraction patterns of SMAs with various Al wt.% cooled below respective martensite transition temperatures. Left shows $L2_1$ (200) 2θ region and right shows (220). Wavelength - 1.15970 Å.

When the 5.79 Al wt.% sample was cooled to liquid N_2 temperatures, the lower symmetry phase was reduced/removed (Figure 4.9).

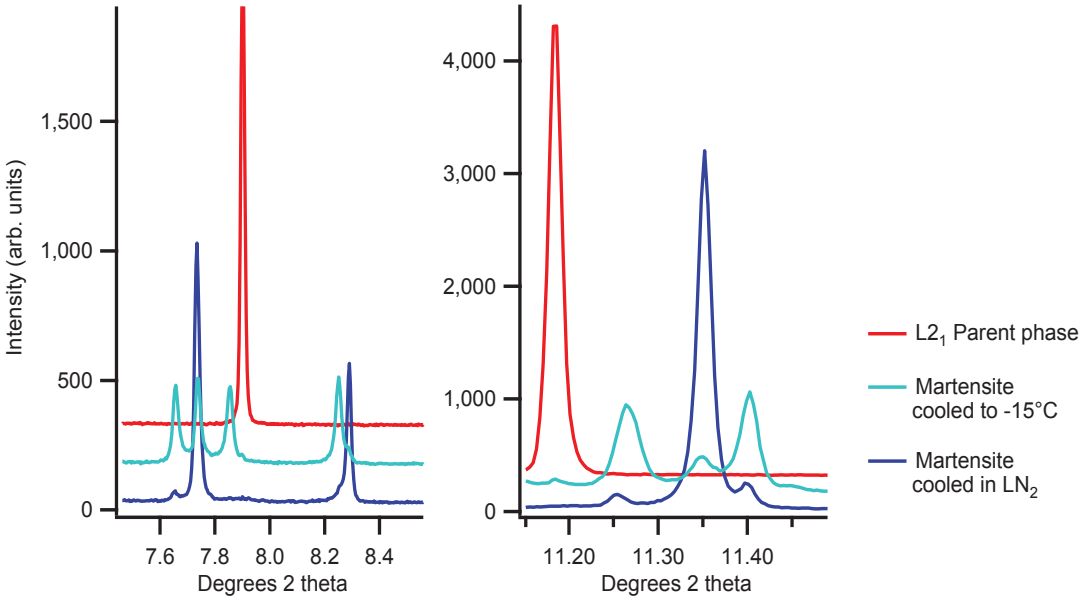

Figure 4.10 Synchrotron X-ray diffraction patterns of 5.79 Al wt.% SMA cooled to differnt temperatures. Left shows $L2_1$ (200) 2θ region and right shows (220). Wavelength - 0.42646 Å.

From these differences and initial Rietveld refinements, the indication is that at low Al wt.% an orthorhombic martensite is formed. As the Al content is increased, a monoclinic martensite forms. High Al wt.% samples form a mixed structure of orthorhombic and monoclinic, but cooling in liquid N_2 reduces the amount of monoclinic phase, leaving a dominant orthorhombic structured martensite.

This is very similar to what is seen in the CuAl SMA, where differences in Al content can produce either an β' (internally faulted FCC martensite), β_1' (internally faulted tetragonal martensite), a mixture of β_1'+ γ', or just γ' (internally twinned orthorhombic martensite) [168]. In the CuAlNi only the β_1', β_1'+ γ' and γ' are present. These structures are a monoclinic (C2/m) and an orthorhombic (Pmmn) structure respectively [169]. Figure 4.10 shows the Al content required to generate each individual martensite structure and the related transformation temperature in CuAl SMAs [142]. Recarte *et al.* [167] expands on this by showing how the phase boundaries change with the addition of Ni. Although this system is limited to only 6 wt.% Ni, it demonstrates that the different

martensite phases are still present in ternary SMAs. This is also the case in some other ternary based CuAl SMAs such as CuAlMn [58].

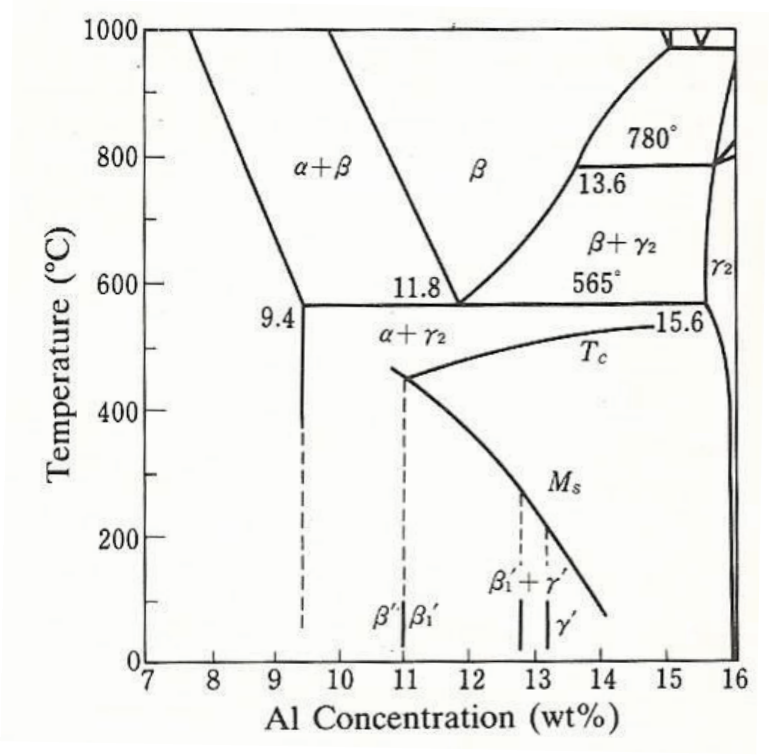

Figure 4.11 Phase diagram for CuAl composition showing transformation temperature trend and martensite structures formed [142].

From [30] it was shown that the AuCuAl shape memory alloys presented here form part of a continuous Hume Rothery ternary β-phase that extends from about 76 wt.% Au down to the CuAl binary edge, and that the SME is exhibited throughout this range. This is in contrast to the CuAlNi alloys, which only exhibit a diffusionless transformation up to a couple of wt.% Ni. It is likely then that the existence of the different martensite structures may continue throughout the β-phase, at least as far as 76 wt.% Au (which seems to be the limit of the ternary β- phase in this system). It is also interesting to note that in the high-Au-content alloys synthesised in this study there is still no equivalent γ' martensite phase formed, even in the highest Al content alloy (5.79 Al wt.%). Instead, the phase field finishes with the dual phase structured β_1'+ γ'. The single phase variant is only produced upon cooling to liquid nitrogen temperatures. From [32] it is shown that the β-phase field finishes at approximately 6 Al wt.%,

indicating that the equivalent γ' martensite field of the CuAl and CuAlNi has either been reduced significantly, or does not exist in high Au content alloys.

Structural co-refinement of the synchrotron and neutron powder diffraction patterns performed by Dr Margaret Elcombe (ANSTO) was able to provide detailed information about the phases present within each alloy. The refinements of the martensite structures shown here are not ready for publication but indicated the most likely crystal lattice system for each martensite phase.

4.5 Conclusion

The transformation temperatures of the β-phase can be controlled by varying its Al content. An increased Al content had the effect of generally depressing the A_s and M_s transformation temperatures. At 18 karat (75 wt.% Au) the addition of about 3.6 wt.% Al suppresses the formation of α-phase. Increasing the Au content a small amount (to about 78 wt.%) resulted in the α-phase being suppressed with an addition of only 2.64 wt.% Al. This indicates a sloping phase boundary. Although additions of Al generally decreased the transformation temperatures, the effect on the M_s is stronger, so that the hysteresis (A_s-M_s) increases with Al content. The $L2_1$ A_2BC sites are dominantly occupied by Au, Al and Cu respectively. If the concentration of Au or Al is reduced, then the Cu content on the A or B site respectively is increased. Finally, the appearance of different martensite structures in alloys of varying Al content was observed. This is similar to the situation in Cu-based shape memory alloys, and indeed the present alloys may in a sense be considered to be an extension of the CuAl shape memory alloy. In these alloys, the martensite phase was found to change from an orthorhombic to a monoclinic structure. In the highest Al content alloys, a mixed phase of both structures is seen. The monoclinic phase however is suppressed by further cooling.

5 Transformation Temperature and Aging of AuCuAl SMAs

5.1 Introduction

Shape memory alloys (SMAs) have many practical applications and have been used in a wide range of areas from arterial stents to seals in liquid nitrogen containers and frames for glasses [13, 46, 170]. One factor limiting the use of these alloys in an increased number of applications is an effect known as aging. This time-dependent effect (which was discussed in detail earlier) can change the temperatures at which a SMA's characteristic displacive phase transformations occur. This is undesirable, as reproducible values of the martensite peak (M_p) and austenite peak (A_p) temperatures (i.e. "cyclic stability") are needed for most technological applications of SMAs. Changes in the transformation temperature of these alloys can move the memory effect outside of the operating conditions for the desired purpose [44, 53, 75, 171, 172]. Therefore, it is important to understand what conditions can cause aging in these alloys and what the mechanisms responsible for this are.

For the more common Cu-, AuCd- and TiNi-based SMAs, the changes in the transformation temperature have been attributed to five principal mechanisms: (1) the symmetry-conforming short range order phenomenon (SC-SRO), which removes martensite anti-site defects [74, 172]; (2) elimination of quenched-in vacancies [173, 174]; (3) non-conservative relaxation of elastic stresses [175]; (4) transformation-induced generation of dislocations [175, 176]; and (5) decomposition of the β-phase and/or precipitation of second phases [44, 74, 171, 177]. These were discussed in some detail in Chapter 2.

It has been reported in the literature that $Au_7Cu_5Al_4$ is largely resistant to aging, however it has been noted that thermal history and aging can still have some effect on the transformations of $Au_7Cu_5Al_4$. In particular, the A_S and M_S temperatures can vary by

up to several degrees Celsius, depending on heat treatment [36, 66, 68]. Aging in the martensite was ascribed by Urbano *et al*. [6] to the SC-SRO phenomenon and could raise the austenite transformation temperature by up to 4°C . This aging process was also found to have an activation energy of 1.1 eV. They also found that, while an initial heat treatment of the parent phase between 150 and 550°C had a negligible effect on the next subsequent A_P (which stayed at the characteristic 80°C of this alloy), successive transformation cycles between 20 and 120°C caused the A_P of such heat-treated material to rise by between 3 and 5°C, with the largest increase associated with the highest initial heat-treatment temperature. The effect saturated at 20 cycles, after which no further increase in A_P occurred. Generally, if A_P increases, it may be deduced that the austenite phase has become less stable relative to the martensite phase. However, aging of the parent phase between 150 and 450°C can only have made it (the austenite) *more* stable, by causing it to move closer to its equilibrium degree of order and vacancy concentration. Decomposition of the β-parent phase can also be eliminated as an explanation for the increase in A_P for the following reasons: (1) there was no change in the first A_P after the high-temperature heat treatment, irrespective of whether the heat-treatment temperature was 150 or 550°C; (2) the increase in A_P with successive cycles of transformation saturated after 20 cycles; and (3) neither diffraction nor microscopy studies have shown evidence that the $Au_7Cu_5Al_4$ β-phase decomposes in this temperature range. Finally, Urbano *et al*. themselves concluded that the high-temperature annealing treatments of the *austenite* had very little effect on any subsequent SC-SRO-driven aging of the *martensite* phase. Therefore, the mechanism by which aging in the high-temperature parent phase affected the A_P remained unknown in $Au_7Cu_5Al_4$.

5.2 Experimental

Two different types of aging were performed on sample FL (5 Al wt.%) as this alloy was used in previous papers on $Au_7Cu_5Al_4$. The first aging heat treatment involved holding the sample at a range of temperatures from 85 – 450°C (i.e. while it was in its austenite form) within the DSC. The sample was then cooled past the M_p and heated again to measure the new A_p temperature of the aged material (Figure 5.1). While the

M_s, M_f, A_s and A_f are also important, the M_p and A_p were used to show the relative shift in the transformation temperatures. The second type of aging treatment was performed by cooling sections of sample FL to -4°C and then cycling them through their transformation temperatures, holding them at 90°C for different lengths of time. The cycle was then repeated to observe changes in the transformation temperatures (Figure 5.2).

Sample R6 (5.26 Al wt.%) was aged on the heated stage of an optical microscope to see if the aging results obtained from the second heat treatment related to a change in size of the austenite domains. Samples were first transformed while being imaged under Nomarski interference, and then held at 90°C. Images were taken every 30 seconds for the first 3 hours after transformation, and a subsequent series of images was taken 14 hours later for 6 hours. Images were processed using ImageJ [178] and the subtraction tool used to observe if there were any significant changes in domain size or height.

In-situ XRD was performed on the powdered FL sample while it was undergoing the second type of aging (i.e. aging at 90°C).

5.3 Results

Data shown in Figure 5.1 were extracted from aging scans performed on sample FL using the TA Universal Analysis software. It shows changes in the martensite and austenite transformation temperatures after samples had been heat treated at different temperatures. Using the 'peak maximum' tool, the transformation points were recorded, however this produced an uncertainty of approximately ±2°C due to the width of the peaks. Figure 5.2 shows aging data tabulated from samples aged for different lengths of time at 90°C and recorded using the same technique. These data are in close agreement with observations previously noted in the literature for heat treatments of 150°C and above [6, 36].

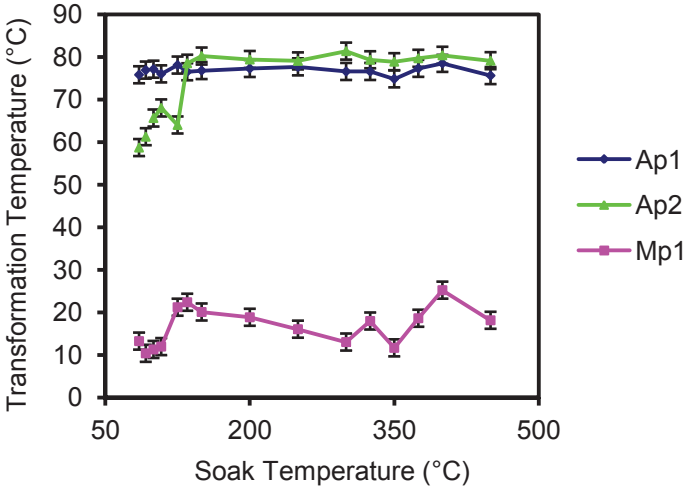

Figure 5.1Transformation temperatures of SMAs aged at given soak temperatures.

The FL series of samples used in these experiments was produced from a cast ingot produced several years earlier by Dr F Levey, and produced an initial austenite transformation temperature very similar to that of her earlier experiments [36]. This demonstrates that long-term aging of this alloy at room temperature causes no significant stabilisation of its martensite (see Chapter 2.1.4 for a description of the 'martensite stabilization' problem). This is an important property with desirable implications for future practical applications.

The data collected in Figure 5.1 can be broken down into two distinct areas - high temperature aging (between 150°C and 450°C) and low temperature aging (below 140°C). Aging in the high temperature regime resulted in a small increase in the A_p, from 76.9°C to 79.7°C (s = 1.0°C, n = 10). The increased A_p temperature is statistically identical to that reported by Urbano *et al*. for essentially the same alloy (A_P = 80.5°C, s = 0.8°C, n = 18, where s and n are standard deviation and sample size, respectively) [6]. The M_{P1} temperature was 18.2°C (s = 6.7°C, n = 20), which was within the same range as the 21.6°C (s = 4.5°C, n = 18) reported by Urbano [6]. The average of the ΔH_{M1} enthalpies was 2.92 $J.g^{-1}$ (s = 0.91 $J.g^{-1}$, n = 20). These data show that, unlike the case for many copper-based shape memory alloys [75, 171, 179] there is no sign of decompositional aging that would increase the transformation temperature and decrease the transformation enthalpy. This is true even at 450°C. This demonstrates that, for the time-scales and temperatures observed here, the β-phase is stable.

While the high temperature aging experiments confirm what was previously reported in the literature, it was noteworthy that aging in the *low* temperature regime created *large* changes in subsequent martensite and austenite transformations. When the sample was cycled below 140°C the A_{p2} decreased dramatically, with lower aging temperatures creating the greatest variation. A similar but smaller effect was seen in the M_{p1}. The combination of these two effects leads to a decrease in the martensite and austenite transformation hysteresis. Since the magnitude of the hysteresis is correlated with accumulated plastic strain [175], it can be deduced that the high-temperature treatments had the net effect of irreversibly "locking in" previous transformation strains. This is also reflected in the higher transformation enthalpies associated subsequently with material that had been aged at higher than 140°C.

The time dependence of these effects was also examined using a second disc of the same starting material (Figure 5.2). It can be seen that the effect of prolonged aging at 90°C further depressed the subsequent M_P and A_{P2}. It is evident that the A_{Pn} can be depressed by as much as 30°C by this process. This depressed A_{P2} was not permanent however, and aging at room temperature for 18 hours caused it to increase back towards the A_{P1} starting value. After several days of aging, the A_{P1} temperature of all specimens had reverted to 80°C. This systematic *decrease* in A_P on cycling, as well as on low-temperature heat treatment (<140°C), represents a completely opposite phenomenon to the *increase* found by Urbano *et al*. for high-temperature heat treatments (>140°C) and is evidently caused by a different mechanism [6]. Interestingly, in the case of TiNi, repeated cycling is reported to decrease M_P initially [176], but later to increase it [180], so these apparent inconsistencies appear to be relatively common in SMAs .

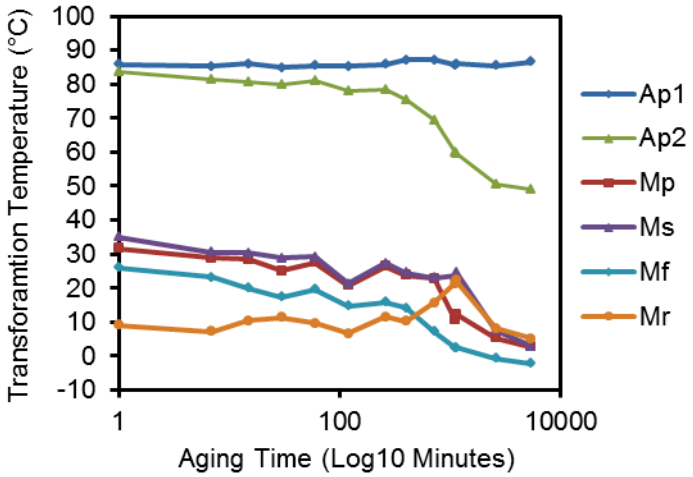

Figure 5.2 Transformation temperatures of SMAs aged at 90°C for given lengths of time.

It was initially thought that some structural change was occurring in the parent phase when aged in the low-temperature regime. The *in-situ* XRD patterns collected show the initial martensite structure at room temperature, because the sample had been cooled below the M_p transformation temperature before beginning the experiment (Figure 5.3). The initial diffraction pattern, straight after heating the sample, shows the "fresh" austenite structure, however this scan is taken over a one hour period, therefore some aging may have taken place during this period. This does not seem significant however, as there were no discernible differences between this pattern and a second one taken after a further hour of aging. Figure 5.3 shows the 90°C *in-situ* aging XRD patterns on the same 2θ scale. At longer times, changes in the diffraction pattern become noticeable. The (400) (59.7°) peak initially consisted of a doublet generated by the $K\alpha_1$ and $K\alpha_2$ radiation diffracting from the parent phase, but the heat treatment had the effect of broadening the peak width so that the two peaks were no longer resolvable. This effect is less noticeable but also present in the (420) (68°) peak. The intensity of the (220) (41.5°) peak changed throughout the heat treatment, with the intensity increasing in the first 4.3 hours, then decreasing when aged for a further 8.8 hours, and finally increasing again. Throughout this process, peak widths remained largely unchanged until about 35 hours of aging, after which an asymmetrical increase in peak width was seen, shifting towards lower 2θ angles.

After this aging treatment the sample was cooled to form the martensite phase again. Large differences in the diffraction pattern were seen between the martensite structures

before and after aging. Furthermore, the alloy did not appear to have fully transformed back to martensite even when cooled to 0°C. This was evidently due to the depression of the M_f that accompanied the protracted aging (Figure 5.2). All of these patterns were collected on a static stage, sampling the same grains and orientations, so differences between the martensite structures must be due to changes in the structure or texture of the sample.

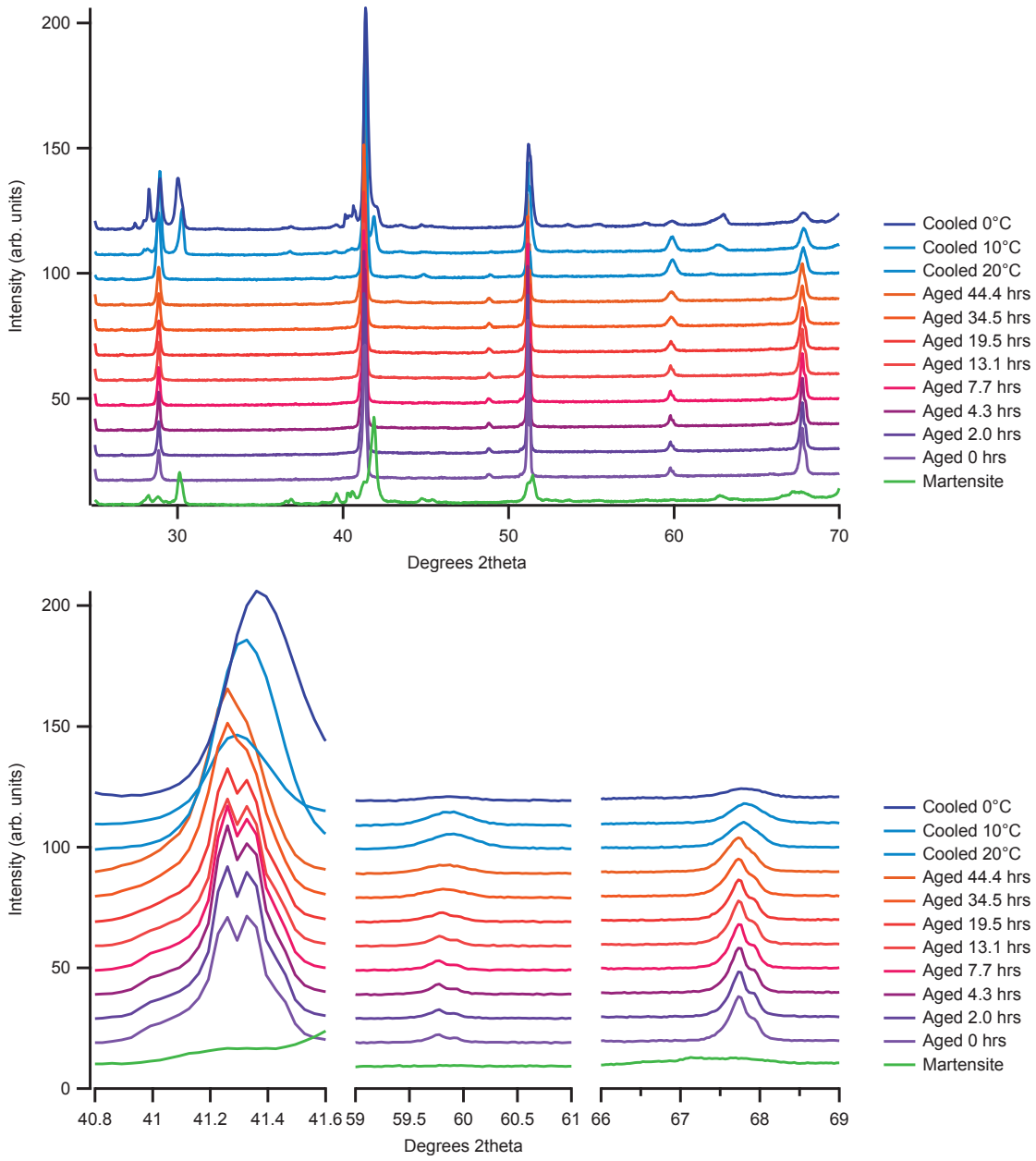

Figure 5.3 X-ray diffraction patterns of SMA during *in-situ* aging at 90°C for given lengths of time. Offset for clarity.

Optical microscopy showed that the transformation anti-laths (i.e. the surface upheavals produced by the *reverse* reaction) produced by the martensite to austenite transformation occurred within the first few seconds of transformation; there were no discernible changes in the lath size thereafter. This can be seen in the NIC (Nomarski Interference Contrast) images taken before and after the austenite transformation (Figure 5.4). Appendix A also shows a video of this transformation in real time also viewable at http://www.youtube.com/watch?v=wUvstHt3WUo. Subsequent images at both small and large time scales show no change in the Nomarski interference colour, indicating no change in the height of the laths. There was also no change in the position of the laths. Figure 5.5 shows images taken 60 seconds after the sample had reached 90°C and after 23.5 hours of aging. These images were then subtracted from each other to show no significant difference. Therefore, it can be concluded that the surface morphology (and hence the lath structure) of the samples was static while being held at 90ºC.

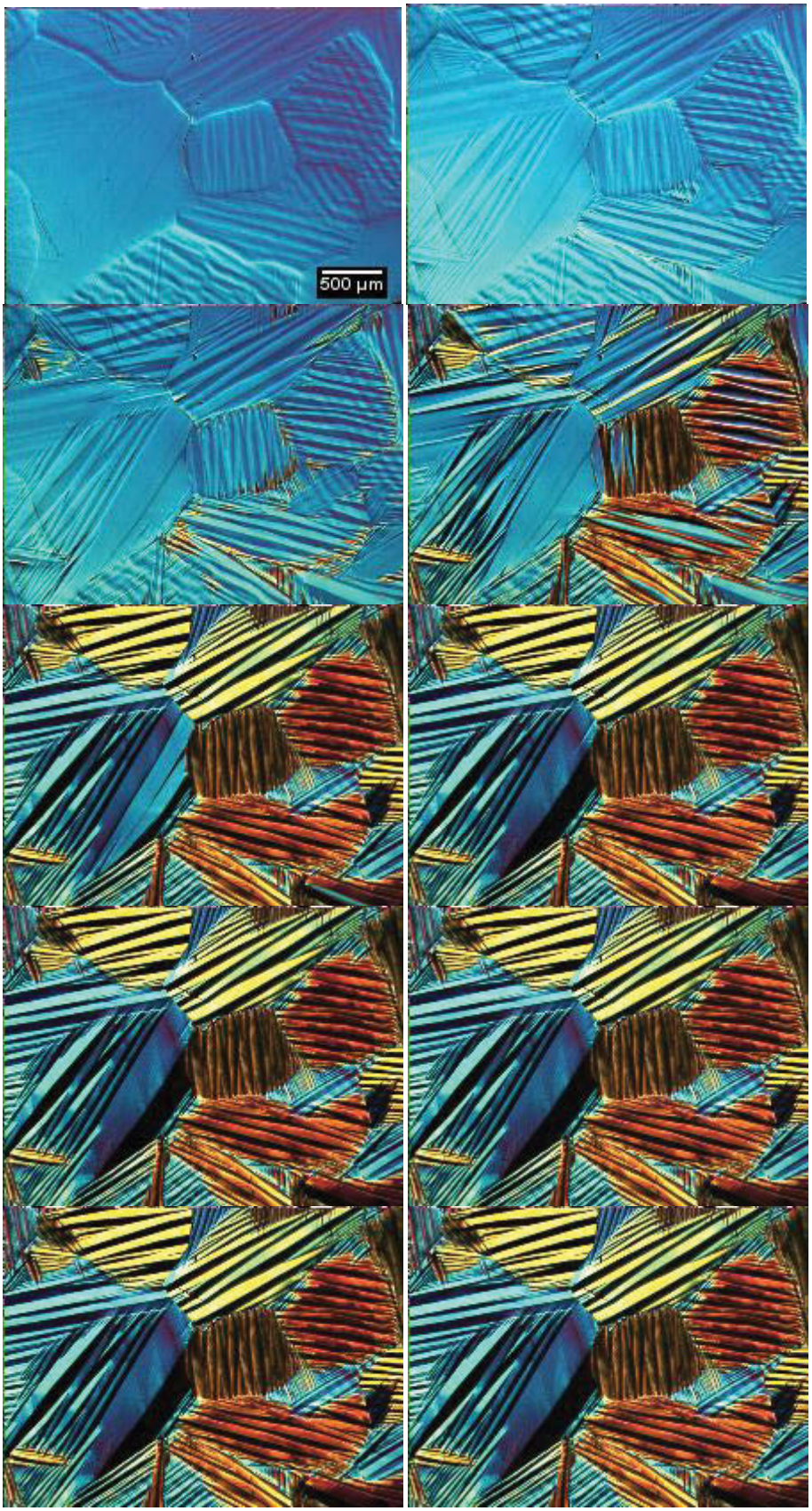

Figure 5.4 NIC images before and after martensite transformation. Extracted from video (Appendix A) from 1:00 – 4:00 minutes at 20 sec intervals.

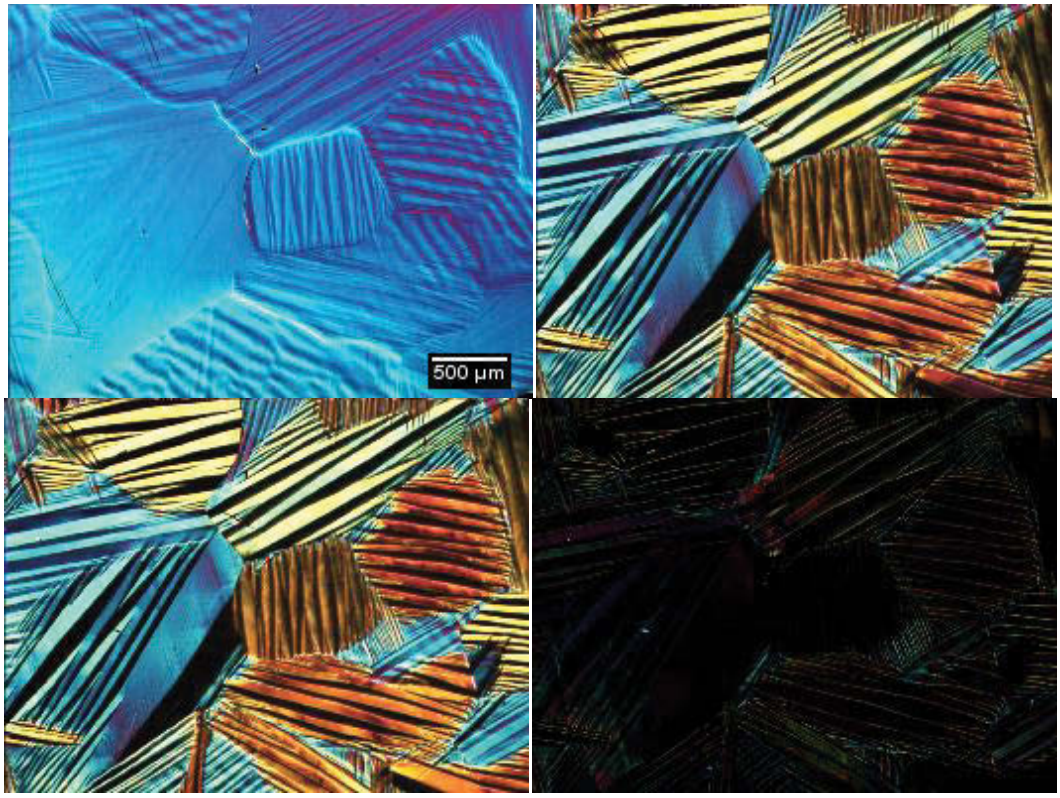

Figure 5.5 Aging of SMA under NIC imaging. Top left image before transformation, top right image 2 minutes after transformation, bottom left image 23.5hrs aging at 90°C, bottom right difference image.

5.4 Discussion

Five principal mechanisms for aging were mentioned in the introduction of this chapter. What it is necessary to determine here is which of these mechanisms can best explain the elevation of A_P after high-temperature aging of the parent phase, and its depression after low-temperature aging and low-temperature cycling. In previous work [181] it was stated that the reason for the changes seen here were due to a reduction in the elastic stress caused by a reversible, time-dependent process of lath domain migration. The work presented here disproves this as the Nomarski interference images (Figure 5.5) show no significant change in any domains after the initial transformation, even after 23.5 hours. So the possible mechanisms must be reconsidered.

The first possible explanation for this aging phenomenon is that of symmetry-conforming short range order phenomenon (SC-SRO). This mechanism of aging occurs when the SMA is transformed into the martensite structure, and is given enough energy and time to allow atoms within the same lattice structure to be re-arranged over extremely short distances. This is because the *cubic* chemical ordering that results from the austenite to martensite transformation is not the lowest energy state for the *orthorhombic* or *monoclinic* martensite crystal structure, so given some time, re-arrangements of the atoms into a conforming symmetry will occur. Once this has occurred the reverse A_p transformation temperature is increased because the martensite has become stabilized relative to the austenite. This is reversible; however, as cycling the alloy back into the austenite structure returns the chemical ordering into the preferred cubic arrangement, destabilizing the martensite structure when 'freshly' transformed [74]. This process would explain the increase in A_p transformation temperature from ~50°C (freshly cycled samples) to ~80°C (well aged samples) that occurs after leaving the alloy at room temperature for long periods. However, aging the alloy in the austenite phase at temperatures above or below 140°C would have the same effect of re-arranging chemical ordering to the preferred cubic structure. This should destabilize any subsequent martensite and should therefore have reduced the A_p to approximately 50°C regardless of austenite aging temperature, rather than the observed effect of increasing the A_p back up to 83°C when aged above 140°C. Therefore SC-SRO cannot be used to explain the aging phenomena observed here.

Removal of anti-site defects is another possible explanation for the aging process that occurred here. When martensite is aged for long periods, SC-SRO again should stabilise the martensite and by doing so raise the A_p to 80°C. When this well-aged martensite is heated through the diffusionless transformation into the austenite phase, a number of defects and dislocations would be formed in the structure due to non-conservative processes and changes in the chemical ordering. Upon reverse transformation these defects would be persist in the martensite structure, de-stabilising it and *lowering* the subsequent A_p. Aging the alloy in the martensite for several days would remove these defects, increasing the A_p back up to 80°C, which is the observed effect. Similarly, the defects would be removed in the austenite phase if the alloy was taken above 140°C. If

the alloy was cycled below the temperature required to anneal out these for a short period of time, the lowered A_p would continue to be seen and shorter time periods would increase this effect. However, prolonged annealing in the austenite phase at lower temperatures would eventually remove these defects and bring the A_p back up to 80°C. This is not the case (as seen in Figure 5.2), as the time dependent nature of this process shows that prolonged aging at 90°C decreases the A_p, which is in contradiction to the anti-site defect hypothesis.

A third possible mechanism for the change in transformation temperature is the removal of quenched-in vacancies. Quenched-in vacancies are quite common in Cu-based and other shape memory alloys [182-185] and are generated when the austenite is quenched from high temperatures to preserve the β-phase structure. In all of these examples, quenched in vacancies have a tendency to change the transformation temperature through a number of possible mechanisms. These include changes in the localised ordering and composition, changes in the fault structure or pinning of the martensite plate boundaries [182]. All of these mechanisms have the same effect of stabilising the martensite or austenite phase, decreasing the martensite transformation temperature and increasing the austenite transformation temperature in the first reverse transformation. This stabilisation effect is removed by aging the SMA above the A_p for short periods of time, allowing subsequent transformations to return to their default state. This subsequent aging mechanism is irreversible and occurs mainly in the austenite state due to the higher level of kinetic energy provided at elevated temperatures. This aging mechanism may explain the differences in transformation temperature seen when the alloy is first cycled. If we assume there are a large number of vacancies that have stabilised the austenite phase, then low temperature treatments would not remove the vacancies and the A_p temperature would be depressed, whereas high temperature treatments would result in the A_p increasing to its default value. Both of these effects were seen in these experiments. However, if vacancies were being removed after cycling the same material through the high temperature treatment, then subsequent low temperature treatments would not lower the A_p. If we consider that the martensite is being stabilised through vacancies then this would result in the stabilised transformation temperature being assigned to a M_p of 80°C and the nominal (unstabilized)

transformation to a M_p of 50°C. This would mean that after high temperature aging the M_p would decrease. This is not the case, as high temperature treatments resulted in the higher M_p temperature.

The next aging mechanism to consider is possible changes in elastic stresses in either the martensite or parent phase. In the case of shape memory alloys, the diffusionless transformation between austenite to martensite or martensite to austenite generates elastic stresses which help facilitate the reverse transformation, and therefore reduce the hysteresis between the forward and reverse transformations [186]. If these elastic stresses are removed or reduced, this would result in a change in the transformation temperatures, requiring greater degrees of over- heating or cooling in order to induce the phase transitions to austenite and martensite respectively. This mechanism can be used to explain the changes observed in these experimental data. For example, as the parent phase is formed elastic strains are generated, and if the alloy is heated in the high temperature regime above 140°C this provides enough thermal energy to remove the elastic strain, providing subsequently transformed martensite with the lowest elastic strain possible. This lowered elastic strain in the martensite has the effect of inhibiting the reverse transformation into the parent phase, increasing the A_p to approximately 80°C. Low temperature heat treatments in the parent phase however, allow for the migration of sub-laths or twins[§] to lower the elastic strain. Movement in the sub-laths can also explain the change in the austenite peak heights of Figure 5.3, with particular note to the (220) peak. The sample was not moving during the *in-situ* aging experiment and therefore the change in peak heights must be attributed to the sub-laths changing the number of reflections that satisfy the Bragg conditions for the corresponding peaks. The altered configuration of sub-laths stabilises the austenite structure and suppresses the M_p further. As the geometric sites of stabilisation are random, being based on the exact configuration of the austenite laths and sub-laths, this also has the effect of spreading out the M_s and M_f transformation temperatures, increasing the range of transformation M_r seen in Figure 5.2. Ultimately the stabilization reaches a minimum energy state,

[§] the laths of austenite and martensite in some SMAs (such as the present ones) are further sub-divided into smaller laths and/or twins, in a recursive process that ends only at the atomic scale. Here I term these secondary features ‘sub-laths’. They are at a size scale that makes them just barely discernible in optical microscopy.

converging the M_s and M_f temperatures to a smaller range. Upon transformation to the martensite, this altered structure generates additional elastic strain in the martensite as the stabilised sub-laths are optimised for the cubic structure rather than the martensite. As the sample is then heated back into the austenite structure, the A_p is lowered to approximately 50°C, due to the presence of both the normal elastic strain generated in the martensite formation as well as the additional strain produced by the transition from the stabilised austenite structure to the martensite. This aging effect will continue to be exhibited until the sample is either aged in the austenite phase above ~140°C to remove the strain, or aged at room temperature for an extended period of time to allow the SC-SRO mechanism to relieve the elastic stresses.

The final mechanism that must be considered is the formation of precipitate phases at the cost of the SMA phase. Due to the narrow v-shaped phase field of many β-phase SMAs like that seen in Figure 4.2, it is possible for the β-phase to decompose if left under equilibrium conditions below the temperature of this phase field. This process usually occurs through one of two reactions, either $\beta \rightarrow \alpha + \gamma$ or $\beta \rightarrow \alpha + \delta$. This decomposition changes the transformation temperature of the SMA by altering the chemical composition of the β-phase or by generating precipitates that pin the interfaces of the laths. Typically, it results in a lowering of the M_p and A_p temperatures [44, 187, 188]. In extreme cases, the shape memory effect can be lost entirely if the β-phase completely decomposes to form the new equilibrium phases. This aging process typically occurs in the austenite phase as high temperatures are required for the diffusive mass transfer to occur. However, this process cannot explain the aging seen in the present experimental results as it produces an irreversible change in the transformation temperatures and would lower the heat flow (W/g) output of the transformation peaks seen in the DSC.

The question of which process is responsible for the slowly increasing peak width of the austenite seen in Figure 5.3 is not settled. Although it has been proposed that aging the sample below 140°C is generating movement in the sub-laths caused by the relief of strain, it is unlikely that this mechanism is responsible for the *increase* in peak width. On the other hand, chemical re-ordering may be a suitable explanation. Jin *et al.* [67]

have suggested that the DO_3 ordered phase actually forms from the $L2_1$ below 172°C, and claimed to have found evidence for this using electrical resistance measurements. As the thermal energy at this temperature is quite low, chemical (re)ordering would need long times to occur, possibly leading to the small changes in peak widths throughout the time scale of the *in-situ* XRD experiment.

5.5 Conclusion

I have shown here that, while there are many possible mechanisms behind the rapid decrease in transformation temperature when samples are aged in the austenite form below 140°C, the most probable cause is sub-lath migration reducing the elastic stress. Overall, however, these alloys show resistance to both stabilisation aging and decomposition aging when aged at temperatures between 140 and 425°C. Aging in this temperature range produces a reversible change in transformation temperatures of only 5°C.

6 Deposition of AuCuAl Thin Films

6.1 Introduction

Thin films of gold are exploited in many different fields due to their unique optical properties (See the section in Chapter 2.3 on plasmons for a description of these optical properties.) The effect of deposition rates and conditions (such as temperature and pressure) on the crystallisation temperatures and physical characteristics of films of pure Au are well documented [189-195], but there is less information available on films of the binary and ternary alloys of Au. This information is crucial when designing systems that incorporate thin films, as properties such as roughness and density have a large impact on the final product. The variables that can affect these properties in samples produced by magnetron sputtering include substrate temperature, gas pressure, power of magnetrons and deposition rate [92, 157, 196], however none of these factors have been previously investigated for an AuCuAl thin film.

It is possible to produce different phases in thin-film alloys by varying the deposition temperature. The phases obtained, however, may not correspond exactly to those of the bulk material. One reason for this is that the deposition method itself imparts considerable kinetic energy to the material deposited so a metastable deposit may be formed. Also, impurities that might be co-deposited can alter the phase equilibria. Although the bulk AuCuAl ternary diagram has been documented [28, 30, 34], there is very little information in the literature on nanoscale AuCuAl alloys. Of particular interest here is the nature of films deposited along the 75 wt.% Au isopleth which cuts through the ternary diagram [32], as it is along this isopleth that the shape memory effect in this ternary alloy seems to be best expressed.

6.2 Experimental

An alloy sputtering target of 58 at.% Au-42 at.% Cu was produced by melting the base metals of Au (99.9999%) and Cu (99.9%), in an inert atmosphere and casting them into

a graphite mould (a description of the process is given in Chapter 3) . This composition was chosen because it provides the same ratio of Au to Cu as that in the Spangold® SMA [32, 36].

A dual-target magnetron sputterer was equipped with an Al 99.999% purity target and the Au 58 at.%-Cu target. Using these, it was possible to deposit films across the AuCuAl ternary diagram as seen in Figure 6.1. Films were deposited using three different methods. The first was used to identify an adequate deposition time and power to produce films with a thickness of the order of 100 nm within the β-phase of the AuCuAl ternary diagram. This involved sputtering of both targets, through a range of powers from 0 to 140 watts, and times ranging from 3.5 min to 40 min. The second regime involved varying the substrate temperature to increase crystallinity while still producing flat nano-thin films. In the third regime, a series of films was deposited with varying compositions in order to produce films at regular intervals across the ternary diagram. Substrates were placed on to a spinning stage using a loading chamber to help maintain the chamber pressure. Once the substrates were loaded, the chamber was left to pump down to a base pressure in the order of $1x10^{-6}$ Torr. After this, the chamber was heated, using two halogen heat lamps, while maintaining vacuum. Films were then deposited at 150°C for 5 minutes with the AuCu target power set between 30 – 70 watts and the Al target power between 22 – 70 watts. A series of films with increasing Al concentration was synthesised. Films were simultaneously deposited on both glass and Si (111) substrates, which were rotated to increase homogeneity.

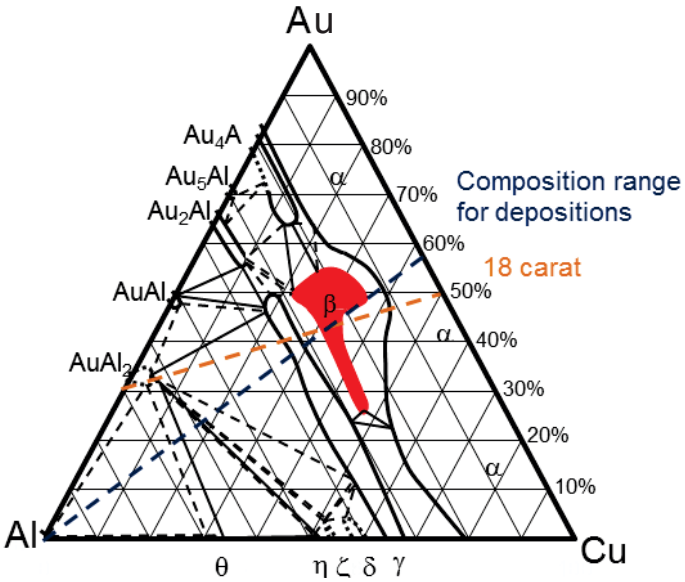

Figure 6.1 Ternary diagram showing approximate composition ranges along blue line [35].

A profilometer was used to find the thickness of the deposited films. Using a glass-tipped scribe, sections of the film were removed and the height difference between these areas was measured. These measurements were then compared to data from X-ray reflectometry (XRR) which was used to measure the thickness and quality of the deposited films, using Motofit least squares fitting software to interpret the results[159].

A Bruker D8 Advance diffractometer was set up for GIXRD and used to identify the phases in the films.

A Zeiss Supra 55 VP SEM was used to observe the topography and cross section of the films, done using the tilt stage and observing a clean fracture surface.

TEM cross sections were also prepared using a Gatan PIPS system and imaged using a JEOL FX-2010F and JEOL 2200F. EDS mapping analysis was also performed using an Oxford X-Max 80 mm^2 SD detector and measured with Oxford Instruments INCA system.

SIMS analyses were performed on films with increasing deposition temperatures to observe any diffusion and oxidation effects. More information on the SIMS measurements is available in experimental Chapter 3.14.

Digital photography images were taken of deposited films on glass to observe diffuse colour and uniformity.

6.3 Results

The thicknesses of films deposited under the first regime were measured using the profilometer and converted to a deposition rate. This was then compared to the power of both targets, Table 6.1. Deposition rates ranged from 3.3 nm/min to 49.0 nm/min. The power applied to the AuCu target was observed to have the greatest effect on the change in deposition rate. This can be seen in the deposition rate doubling when the AuCu target was set to 90 watts compared to when the Al target power was set to 90 watts (Table 6.1). This is in agreement with the literature as the sputtering efficiencies of Au and Cu are two to three times higher than that of Al with respect to Ar ion energies [92].

Table 6.1 Target power vs. deposition rate

Al Power (W)	AuCu Power (W)	Deposition Rate (nm/min)
17	20	3.3
20	30	12.3
20	30	23.7
25	30	18.9
30	30	14.2
30	30	14.4
30	30	18.1
30	30	19.1
30	30	20.6
35	30	10.9
35	30	15.1
35	30	16.2
40	30	11.1
40	30	13.3
40	30	14.1
50	30	15.5
50	30	18.7
50	30	19.2
60	30	12.8
60	30	13.5
60	30	19.5
60	30	20.8
60	30	23.3
70	30	18.0
70	30	18.9
80	30	16.3
90	30	18.1
20	35	27.8
30	40	18.1
30	50	16.5
30	60	27.2
30	70	33.0
30	90	34.5
30	100	40.1
30	120	41.9
0	140	49.0
30	140	41.9

While these measurements do provide a rough guide to the sputtering rates, the outliers (Figure 6.2) can be attributed to other factors which affect the final film thickness.

The deposition temperature influences factors such as morphology and oxide content and hence can cause the film thickness to change too, as can be seen in Figure 6.2.

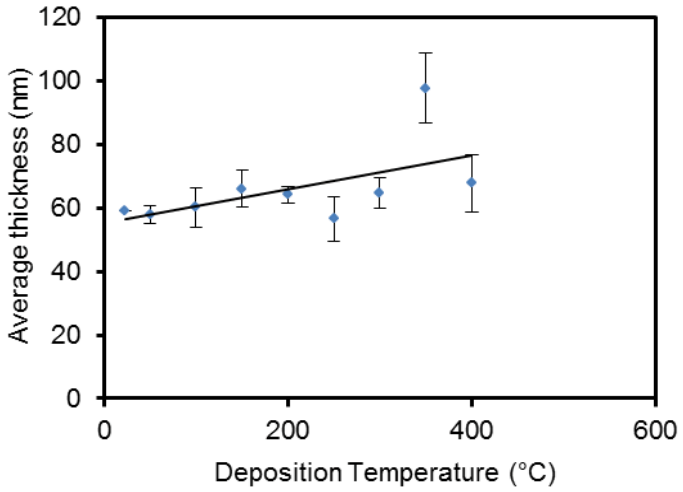

Figure 6.2 Profilometer thickness of films (nm) vs. deposition temperature (°C). Error bars given as +/-1 std deviation of 5 measurements. Line of best fit added.

GIXRD of these films revealed that they were comprised of one or (sometimes) two of the phases already known from the AuCuAl ternary diagram [28, 30, 32, 34]. These were the alpha (α), beta (β) or gamma (γ) phases, and the low temperature martensitic form of the β-phase. Higher ratios of Al to (Au+Cu) favoured formation of the γ-phase, while higher ratios of (Au+Cu) relative to Al favoured the α-phase (Table 6.2). In addition, higher base pressures favoured FCC ((Au,Cu) solid solution), but a lower base pressure favoured the presence of either austenitic or martensitic β-phase, Figure 6.3.

Table 6.2 Identified phases, and their deposition conditions

Power on AuCu target relative to total power, (%)	Set Temperature (°C)	Identified Phase	Sample Name
23.08	300	Gamma	NewTemp29
25.00	300	Gamma	NewTemp30
27.27	300	Gamma	NewTemp32
30.00	300	Beta	NewTemp35
33.33	300	Martensite	NewTemp22
33.33	300	Beta	NewTemp36
33.33	300	Beta	NewTemp39
33.33	250	Beta	NewTemp40
33.33	200	Beta	NewTemp41
37.50	300	Alpha/Martensite	NewTemp21
37.50	300	Beta	NewTemp31
37.50	300	Beta	NewTemp34
42.86	300	Alpha	NewTemp20
42.86	244	Alpha	NewTemp9
42.86	392	Martensite	NewTemp16
42.86	300	Beta	NewTemp28
46.15	340	Alpha	NewTemp14
46.15	400	Alpha	NewTemp8
50.00	244	Alpha	NewTemp10
50.00	400	Alpha	NewTemp17
50.00	340	Martensite	NewTemp13
50.00	300	Martensite	NewTemp19
50.00	300	Martensite	NewTemp38
54.05	400	Alpha	NewTemp2
54.05		Alpha	NewTemp5
54.55	400	Alpha	NewTemp15
54.55	300	Martensite	NewTemp23
57.14	300	Martensite	NewTemp24
60.00	400	Alpha	NewTemp1
60.00	360	Alpha	NewTemp12
60.00	340	Martensite	NewTemp6
62.50	300	Martensite	NewTemp25
63.64	340	Alpha	NewTemp7
66.67	300	Alpha	NewTemp26
80.00	300	Alpha	NewTemp45
82.35	300	Alpha	NewTemp46

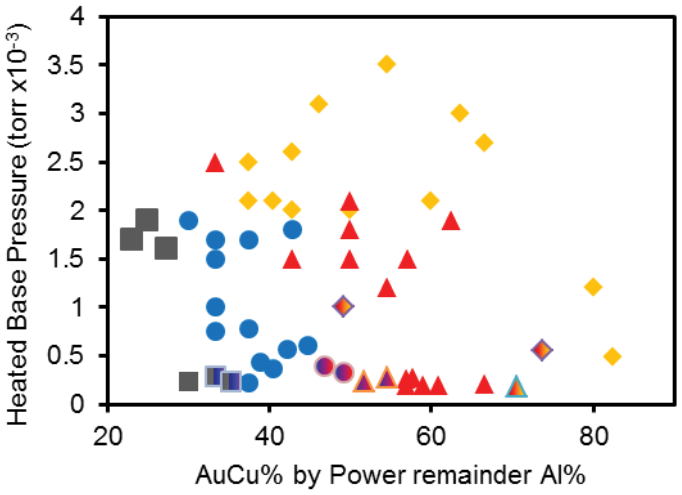

Figure 6.3 Phases produced through varying base pressure and target power. Grey - gamma phase, blue - beta phase (austenite), red - beta phase (martensite), yellow - alpha phase.

XRR scans were taken of films deposited at both room temperature and at elevated temperatures to compare the roughness and thickness of the films. Films deposited at room temperature tended to produce much better XRR data, producing fringes that went out to high ranges in Q, indicating that the films have lower surface roughness and uniform density. However, these films, while very smooth, had a very low degree of crystallinity. Initial attempts at increasing crystallinity in these films using heat treatment at 450ºC in an inert environment were unsuccessful as a reaction occurred between the deposited film and the Si substrate which formed new equilibrium phases. SEM images showed that, in extreme cases, cubic domains of pure Au segregated to the surface of the coating (Figure 6.4). Evidently this Au was deposited from a low-melting point Au-Si eutectic liquid (363ºC) that formed during the heat treatment. Care was therefore taken in subsequent experiments to not exceed a substrate temperature of ~400°C. Subsequent films deposited at elevated temperatures had a uniform structure, consisting of fine random crystallites.

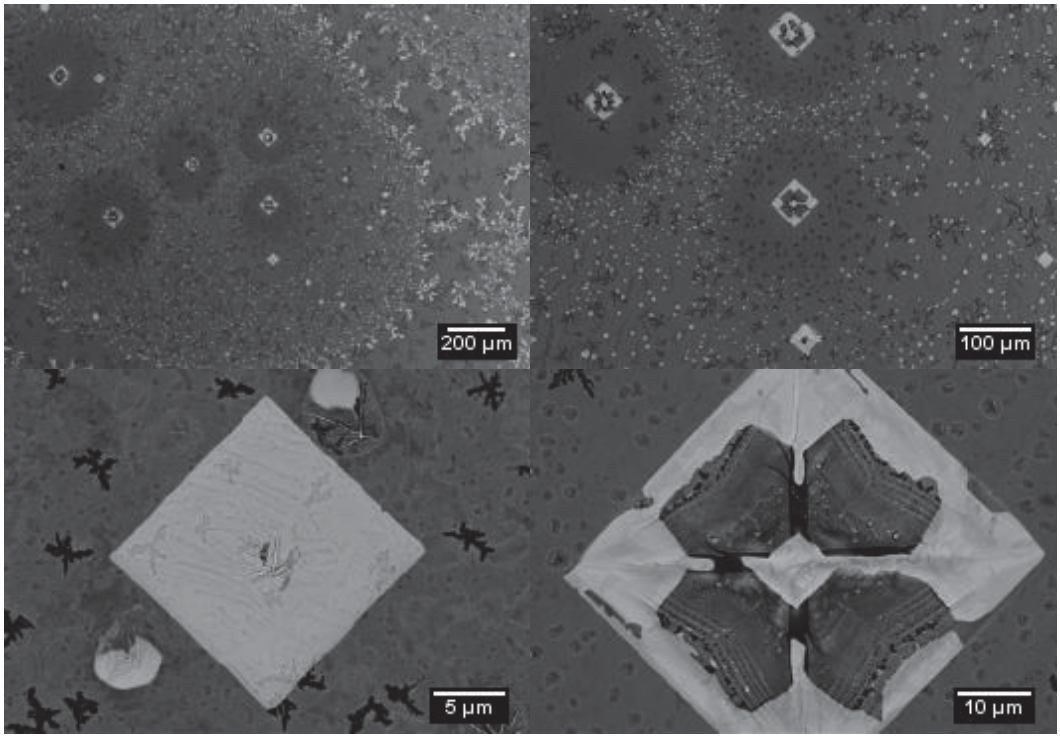

Figure 6.4 SEM images of segregated cubic domains of Au after annealing AuCuAl films at 450°C.

Films deposited at temperatures between 23°C and 400°C were also examined with XRR, and showed a steady decrease in the visibility of the fringes as the deposition temperature increased (Figure 6.5). Computer models with individual layers of varied scattering length density, thickness and roughness, were created for the 23°C, 100°C and 150°C XRR data to provide comparative values for the thickness and average roughness of these films. Figure 6.6 shows a comparison of the three reflectivity curves. From the models fitted to these curves, it was found that the thickness given by these models is consistently slightly larger than that found by the profilometer, producing values of 70, 69 and 79 nm for the 23°C, 100°C and 150°C depositions respectively (compared to 59, 60 and 66 nm as measured with the profilometer) . However both types of measurement show that the films only vary in thickness by approximately 12%. As the deposition temperature increases, the roughness also increases, changing from approximately 1.4 nm in the 23°C deposition to 2.5 nm in the 150°C deposition. It is also interesting to note that the 200°C deposition sees almost a complete removal of fringes and indicates an increased level of roughness that can also be seen in the SEM images below. No models were fitted to XRR data above this

temperature as there were very little to no fringes, implying that these films have a greater roughness.

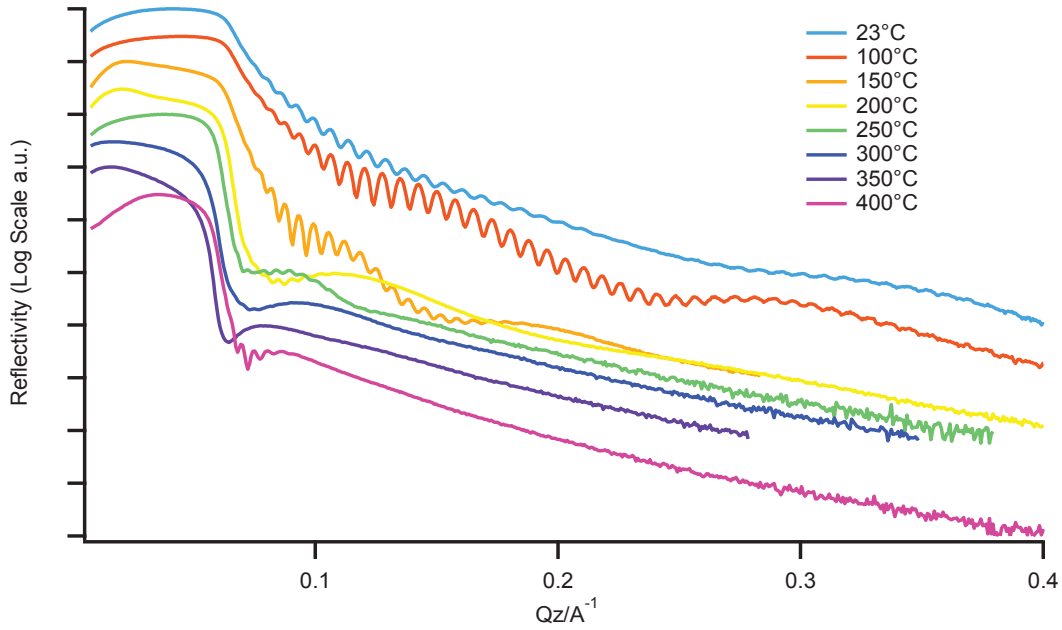

Figure 6.5 XRR curves for films deposited at given temperatures. Offset for clarity.

TEM and SEM images show that the topography and structure within the films changed dramatically with increases in substrate temperature. Films deposited at room temperature consisted of very fine crystallites evenly deposited across the surface of the substrate (seen in the 23°C image in Figure 6.7), with a dense homogenous structure throughout the thickness of the film (seen in the 23°C image in Figure 6.8). As the temperature increased, crystallites became larger in size but also contained more voids (seen in the 150°C and 200°C images in Figure 6.7 and Figure 6.8). Further increases in temperature changed the topography, generating conglomerates of particles which were clustered together rather than a solid film (seen in the 350°C and 400°C images in Figure 6.7 and Figure 6.8).

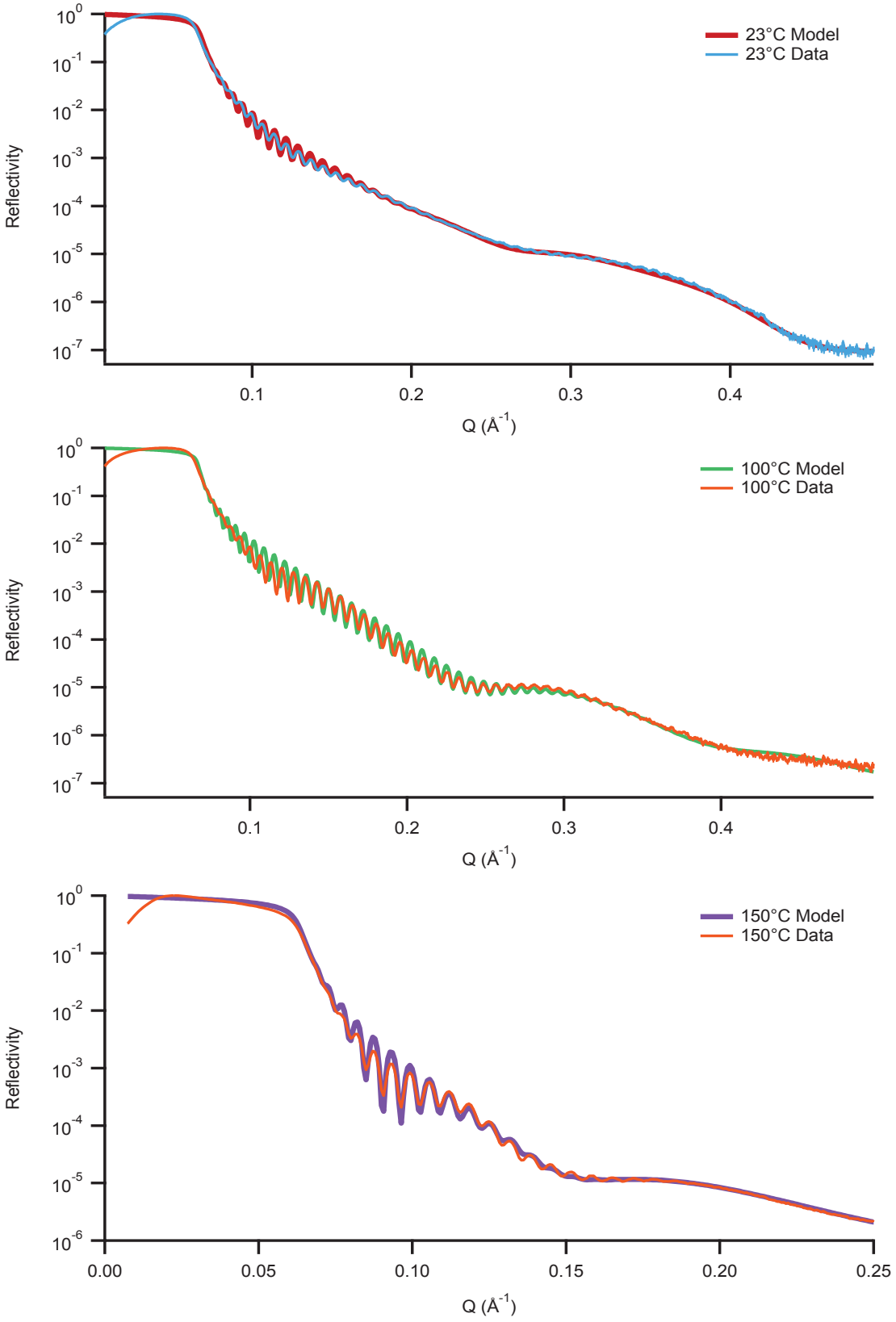

Figure 6.6 XRR data and fit models for 23, 100 and 150°C depositions.

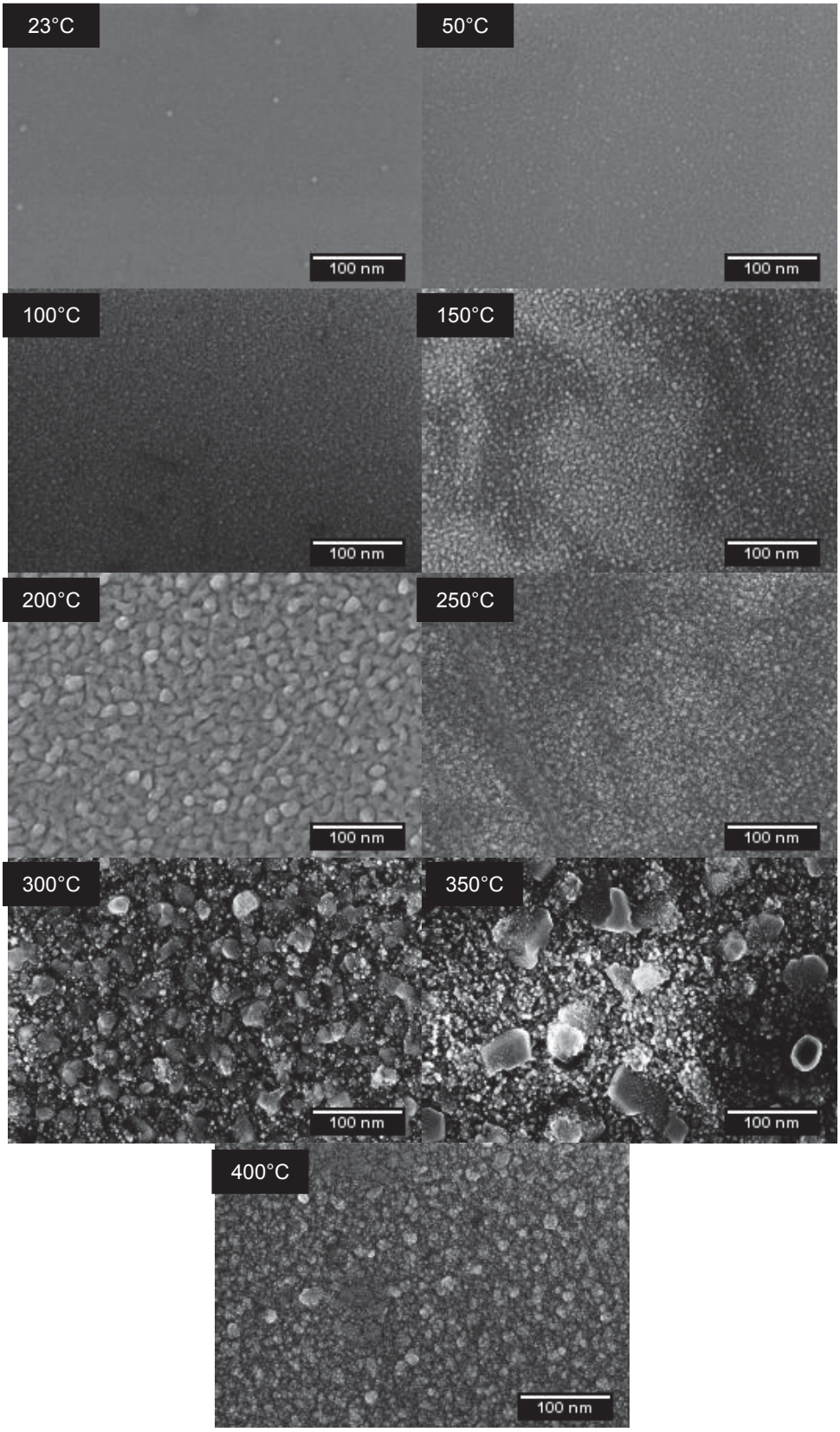

Figure 6.7 SEM images of depositions with increasing temperature.

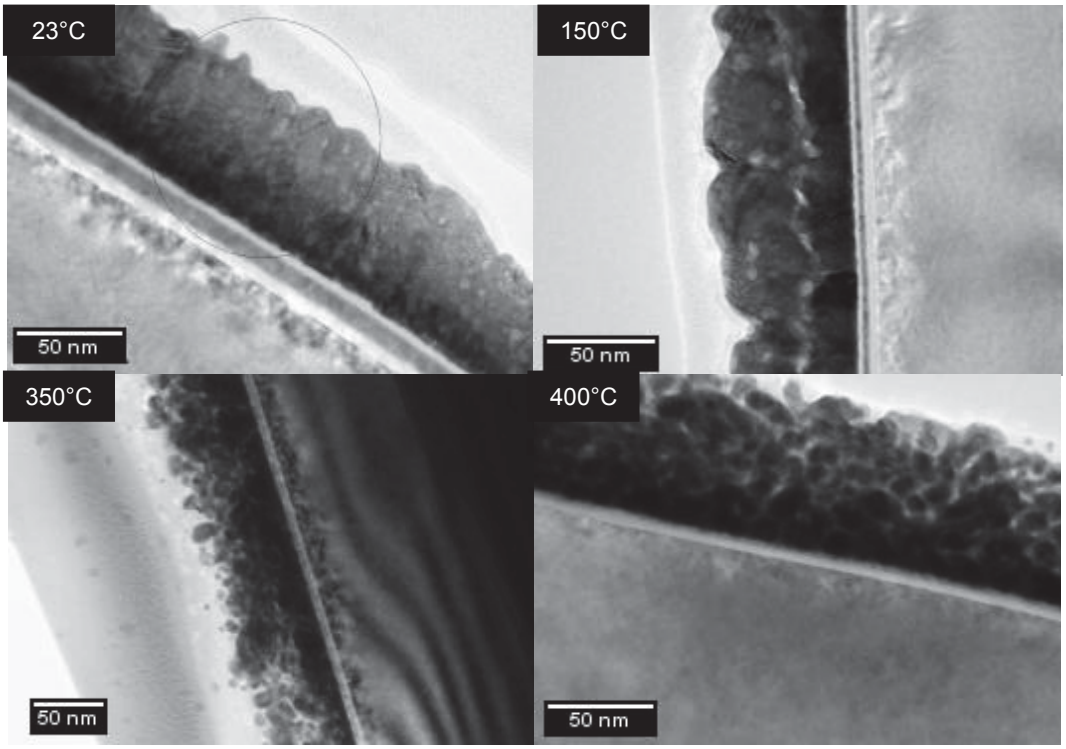

Figure 6.8 TEM images of films deposited at increasing temperature.

GIXRD of a series of deposits produced at various temperatures (Figure 6.9) showed that the films deposited at room temperature or at 50°C produced broad peaks with a simple β-phase austenite structure. As deposition temperature increased, peak intensity increased and peak width decreased in films deposited up to 200°C. At 300°C the intensity of the β-phase peaks decreased and martensite peaks became evident. These peaks became more prominent in films deposited at 350°C. As the deposition temperature increased further to 400°C, these peaks disappeared and replaced with peaks corresponding to a simple cubic structure similar to that of FCC gold. In the Discussion section to follow I will show how these changes can be attributed to decreased Al and increased O content in the coating.

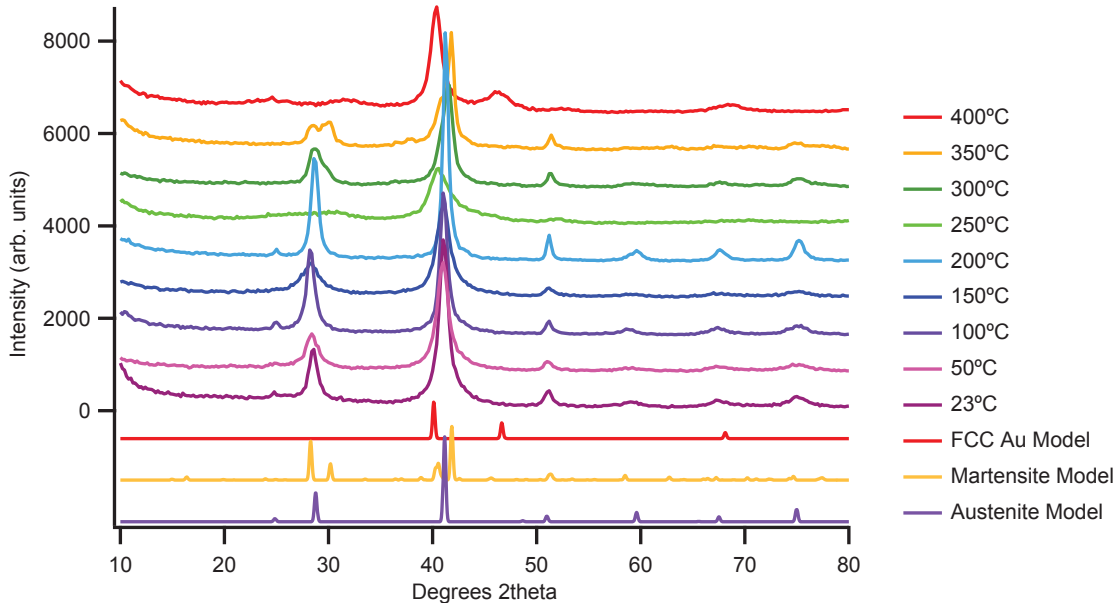

Figure 6.9 GIXRD of AuCuAl thin films deposited at temperature.

SIMS composition profiles taken from films deposited at various temperatures (Figure 6.10) show that, at low deposition temperatures, O concentration in the films was very low, while the concentration of Al, Cu and Si tended to follow similar trends, with the initial deposition being much higher in concentration and falling away throughout the thickness of the film. Films deposited at elevated temperatures were more uniform in composition on average throughout the thickness of the film, however a higher O concentration was also observed.

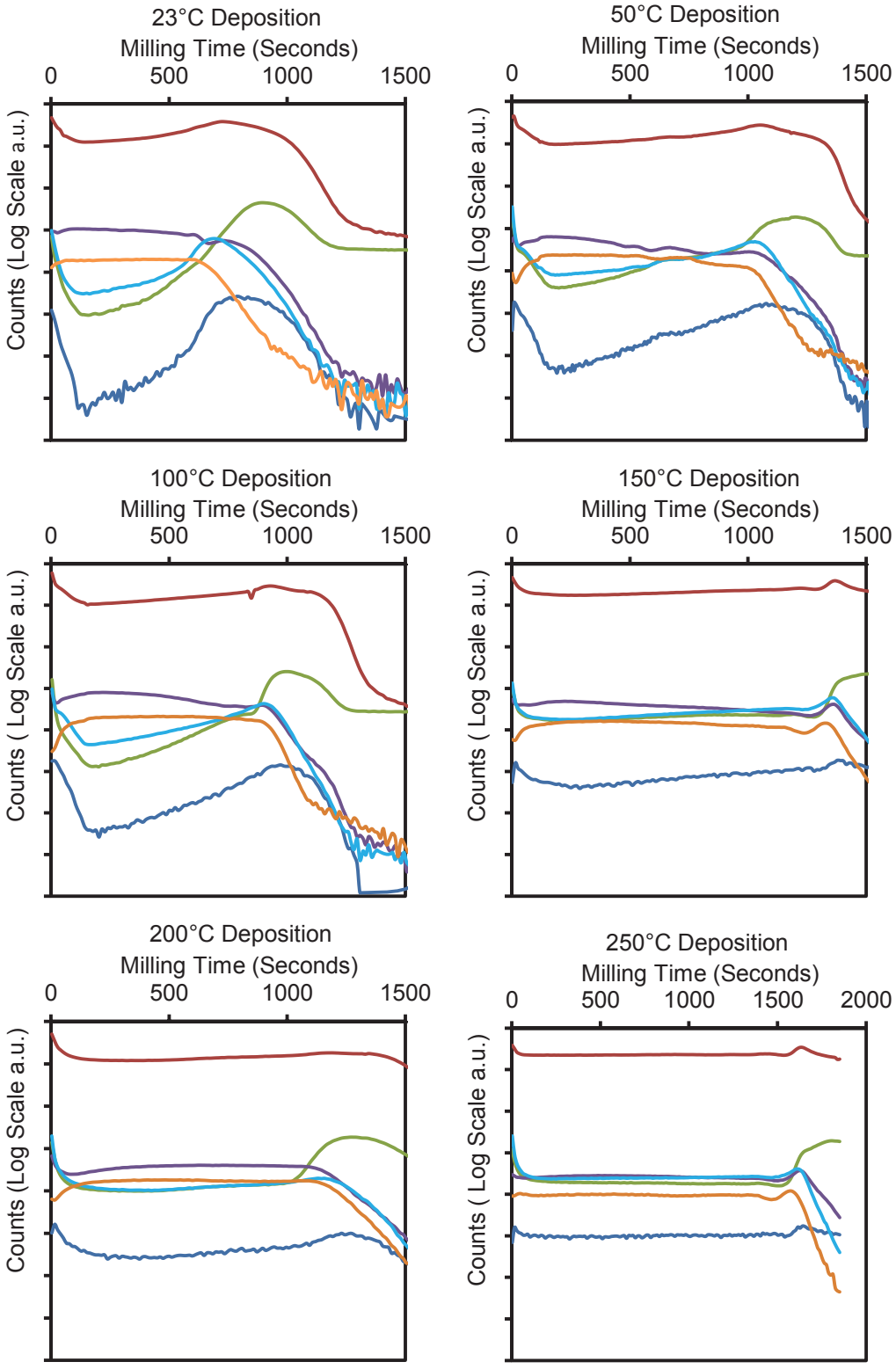
23°C Deposition
Milling Time (Seconds)
0
500
1000
1500
Counts (Log Scale a.u.)
50°C Deposition
Milling Time (Seconds)
0
500
1000
1500
Counts (Log Scale a.u.)
100°C Deposition
Milling Time (Seconds)
0
500
1000
1500
Counts (Log Scale a.u.)
150°C Deposition
Milling Time (Seconds)
0
500
1000
1500
Counts (Log Scale a.u.)
200°C Deposition
Milling Time (Seconds)
0
500
1000
1500
Counts (Log Scale a.u.)
250°C Deposition
Milling Time (Seconds)
0
500
1000
1500
2000
Counts (Log Scale a.u.)

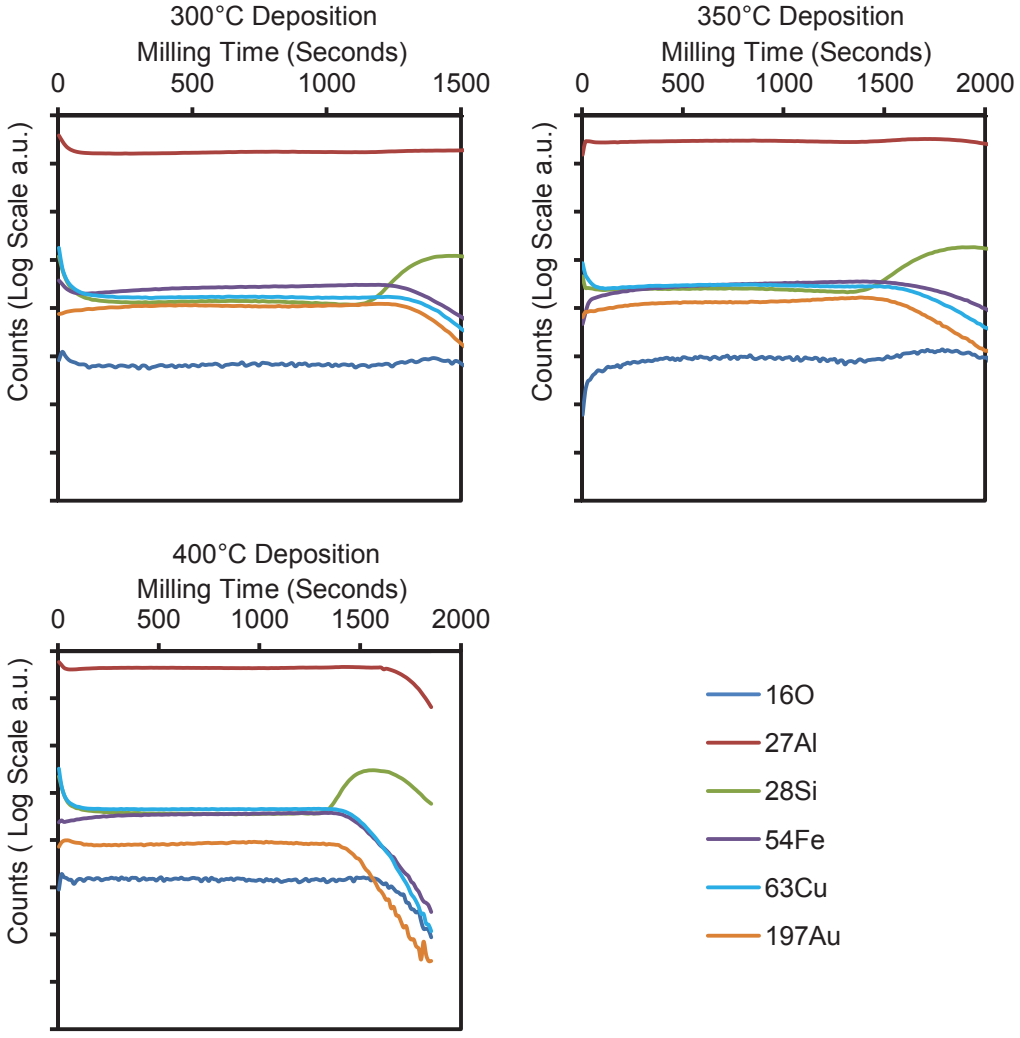

Figure 6.10 SIMS profiles of films deposited at temperature showing compositional variations throughout the thickness of the films.

TEM EDS analysis confirmed the compositional uniformity in the sample deposited at 400°C with high resolution composition map of the cross-section (Figure 6.11). Looking at the O distribution map, there was a thin 5 nm section containing higher O content at the Si interface which may be attributed to the native SiO_2 layer normally found on Si. Apart from this, there was very little contrast difference across the element maps. The small differences that did exist were quantified by grouping regions with similar compositions and averaging the EDS spectra from points within these areas. The compositions are listed in Table 6.4 and the images related to each compositional region of interest are shown in Figure 6.13. The sample deposited at 300°C (Figure 6.12) produced a similar uniformity in the composition as the 400°C sample. Compositional

EDS regions of interest from the top and bottom of the film indicate higher O concentrations that are not always visible on the actual EDS map or the SIMS results. The bottom oxide layer appears to be due to the 'native' SiO_2 layer as there was a large Si signal there as well, however the map also shows significant amounts of Al in the same region. The increase in O concentration in the top layer is typically associated with a decreased Au concentration and is therefore likely to be correspondingly higher in Al and Cu oxides. EDS of the 23°C (Figure 6.14) sample shows a large range of segregation in the elements that is not visible in the SIMS, with relatively high levels of contaminant Fe and Cr.

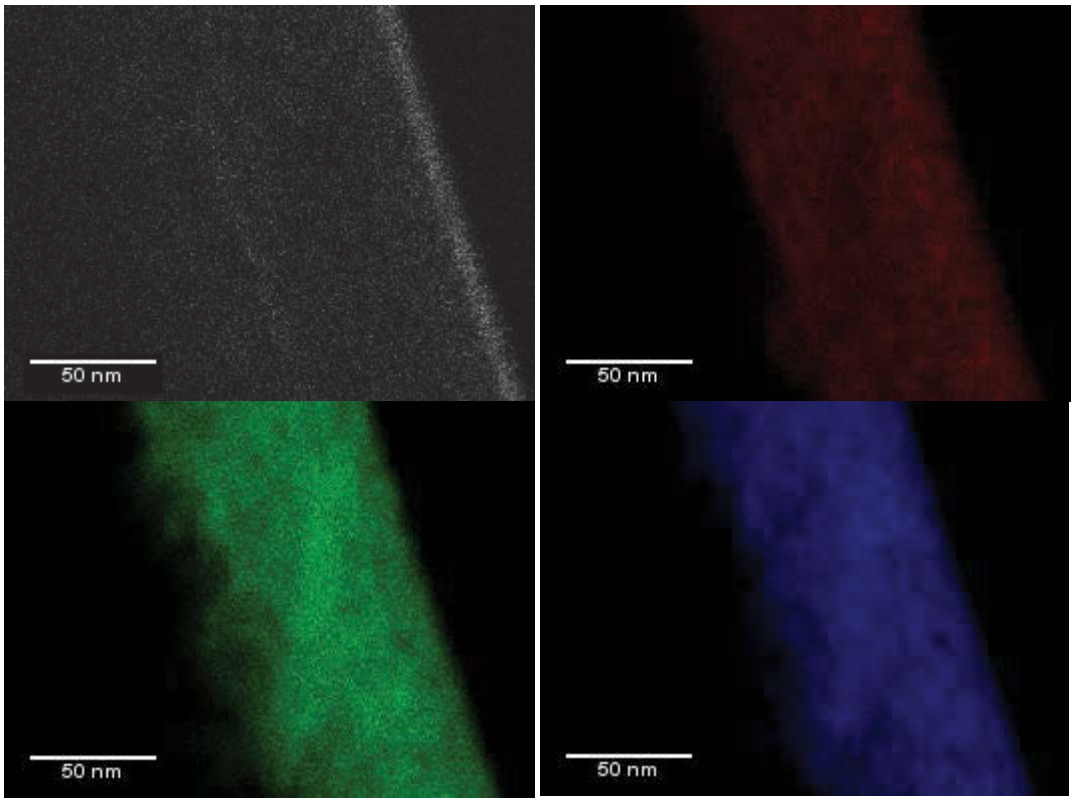

Figure 6.11 Element map of film made at 400°C. O (top left), Al (top right), Cu (bottom left) and Au (bottom right). The Si substrate is on the right hand side of these images and the top surface of the film on the left hand side.

Table 6.3 EDS composition analysis of select regions in film deposited at 300°C

Spectrum	O at.%	Al at.%	Cr at.%	Fe at.%	Cu at.%	Au at.%
Phase1	3.43	6.86	0.06	2.16	16.95	70.53
Phase2	3.71	7.10	0.07	2.29	16.52	70.32
Spectrum 3	3.58	7.36	0.04	1.55	18.18	69.3
Spectrum 4	3.28	7.20	0.07	2.33	16.17	70.96
Spectrum 5	3.73	7.18	0.05	2.01	17.24	69.79
Spectrum 6	3.10	7.10	0.08	2.92	14.6	72.19
Spectrum 7	3.52	7.31	0.07	2.13	16.73	70.24
Spectrum 9	6.52	7.63	0.02	1.36	19.81	64.66
Spectrum 10	3.08	7.04	0.08	2.75	15.16	71.88
Spectrum 11	3.83	7.82	0.03	1.53	17.75	69.04
Spectrum 12	3.17	7.13	0.07	2.46	15.83	71.34
Spectrum 13	9.48	9.33	0.33	4.89	9.77	66.19
Spectrum 14	8.98	7.81	0.04	1.41	21.05	60.71

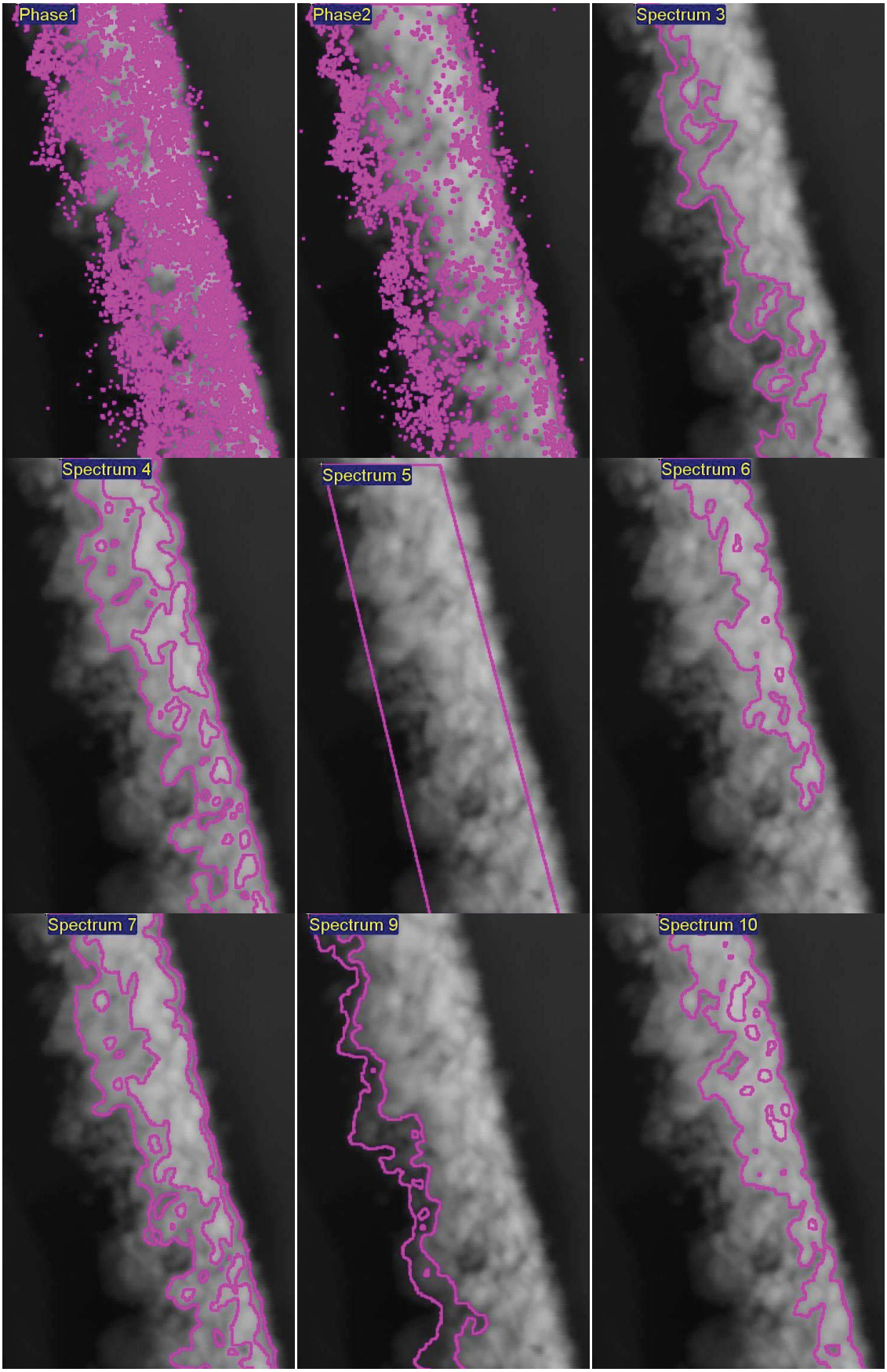
Phase1
Phase2
Spectrum 3
Spectrum 4
Spectrum 5
Spectrum 6
Spectrum 7
Spectrum 9
Spectrum 10

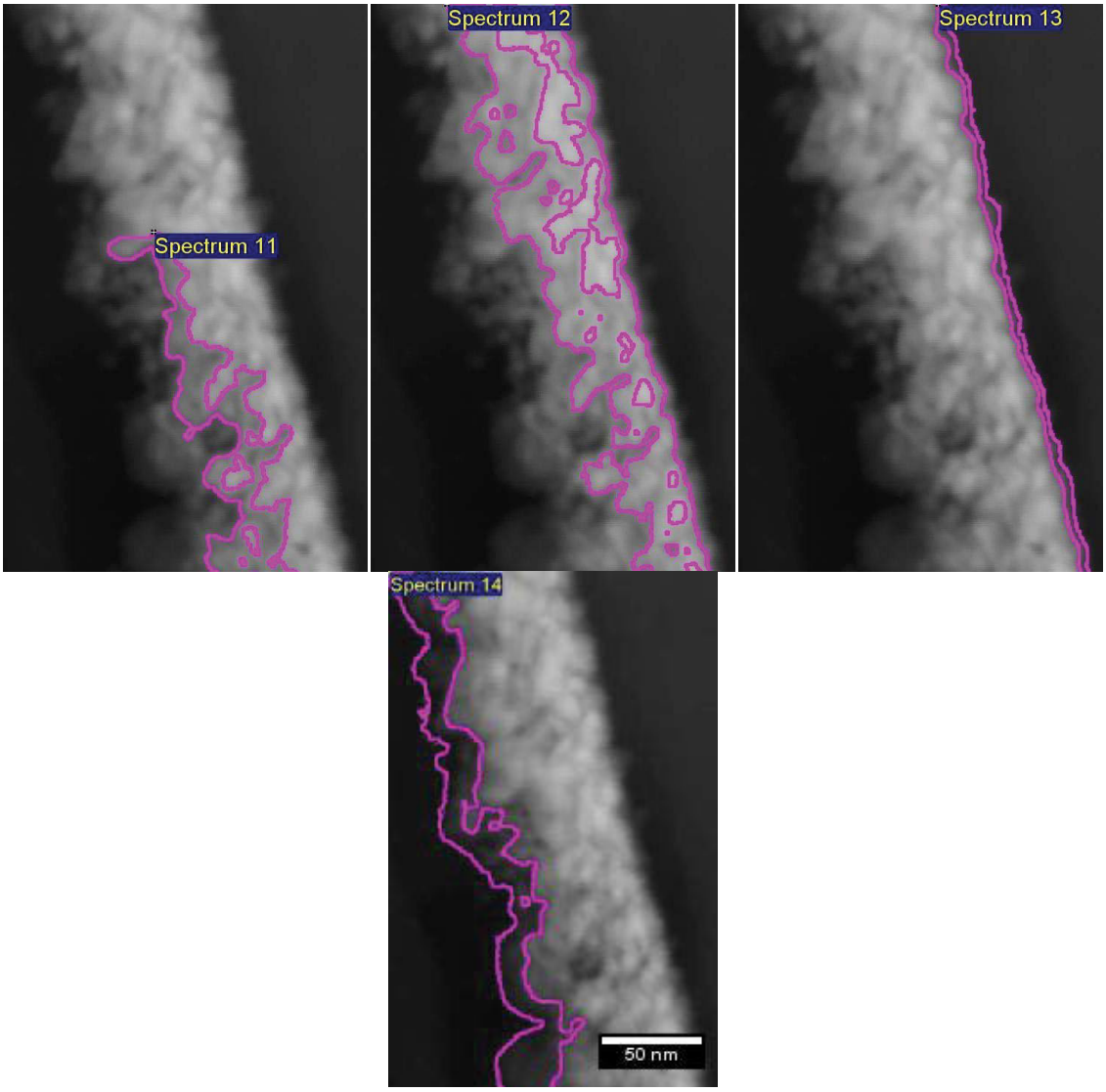

Figure 6.12 Images of regions for EDS analyses (film deposited at 300°C).

Table 6.4 EDS composition of select regions in film deposited at 400°C

Spectrum	O at.%	Al at.%	Cr at.%	Fe at.%	Cu at.%	Au at.%
Phase1	2.88	5.00	0.62	0.91	26.34	64.26
Phase2	2.94	5.07	0.61	0.94	26.23	64.2
Phase3	2.83	4.91	0.61	0.87	26.41	64.38
Spectrum 5	2.88	5.22	0.6	0.81	26.33	64.17
Spectrum 6	2.64	5.12	0.64	1.24	26.13	64.24
Spectrum 7	3.85	5.87	0.59	0.26	25.17	64.27
Spectrum 9	2.77	5.10	0.58	0.4	26.8	64.36
Spectrum 10	2.59	5.14	0.64	1.38	25.99	64.25
Spectrum 11	6.78	7.42	0.76	4.03	19.78	61.23
Spectrum 12	6.27	4.88	0.46	0.34	30.12	57.92
Spectrum 13	2.64	5.11	0.63	1.21	26.14	64.26
Spectrum 14	3.31	5.57	0.54	0.28	26	64.3

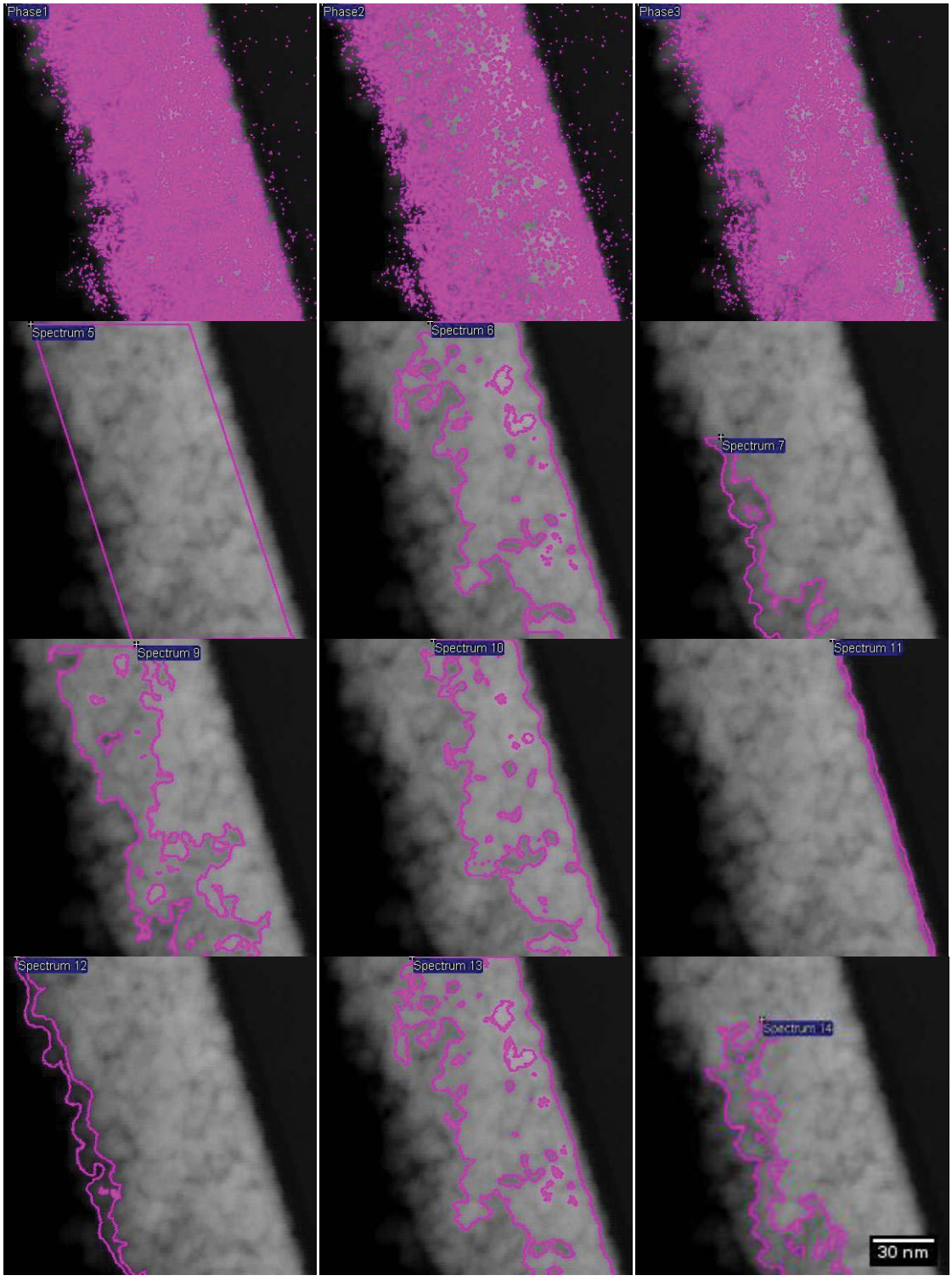

Figure 6.13 Images of regions for EDS analyses (film deposited at 400°C).

Table 6.5 EDS composition of select regions in film deposited at 23°C

Spectrum	O at.%	Al at.%	Cr at.%	Fe at.%	Cu at.%	Au at.%
Spectrum 7	3.85	5.87	0.59	0.26	25.17	64.27
Spectrum 8	2.81	5.39	0.62	1.5	24.69	64.98
Spectrum 9	2.77	5.1	0.58	0.4	26.8	64.36
Spectrum 10	2.59	5.14	0.64	1.38	25.99	64.25
Spectrum 11	6.78	7.42	0.76	4.03	19.78	61.23
Spectrum 12	6.27	4.88	0.46	0.34	30.12	57.92
Spectrum 13	2.64	5.11	0.63	1.21	26.14	64.26
Spectrum 14	3.31	5.57	0.54	0.28	26	64.3

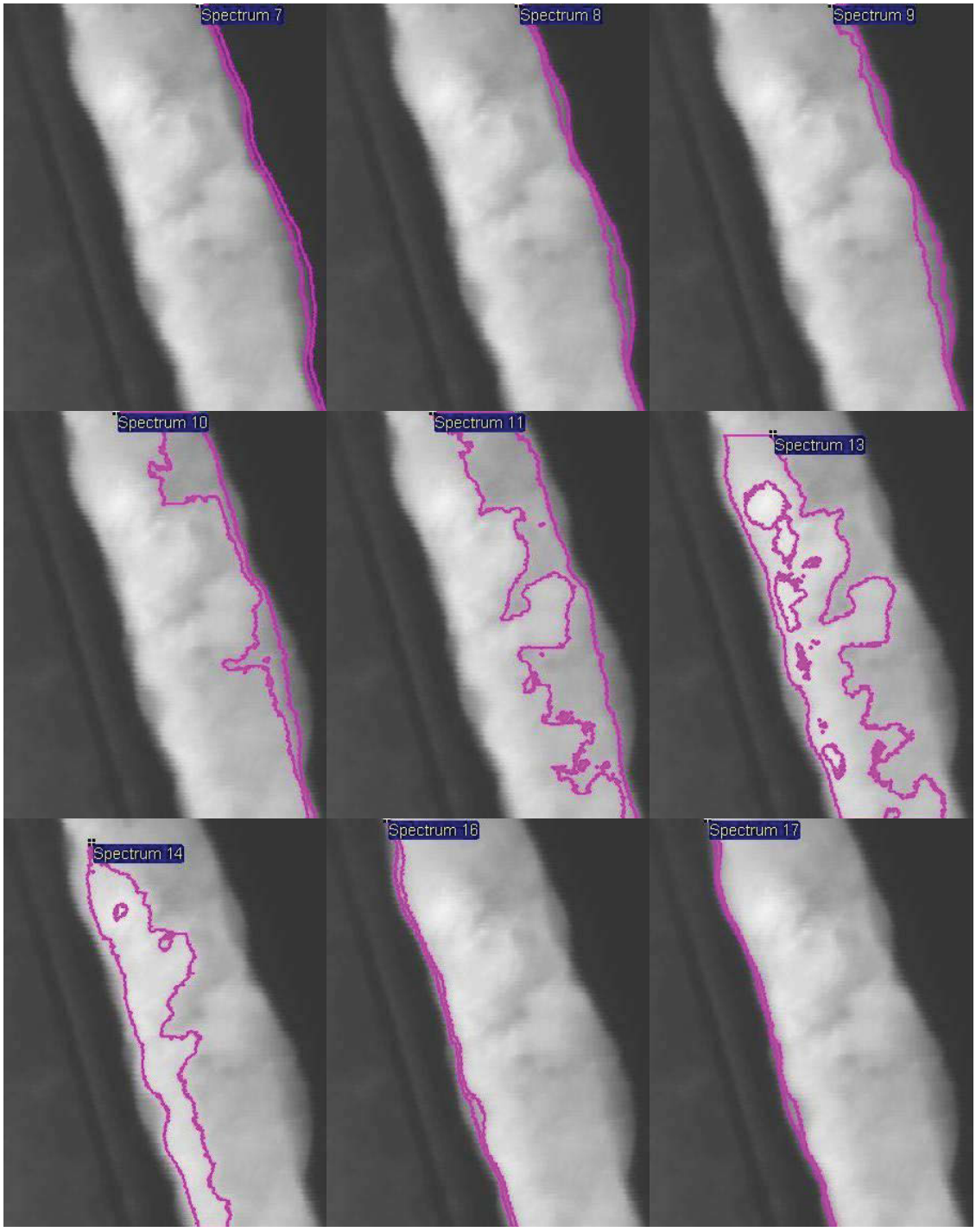
Spectrum 7
Spectrum 8
Spectrum 9
Spectrum 10
Spectrum 11
Spectrum 13
Spectrum 14
Spectrum 16
Spectrum 17

Figure 6.14 Images of regions for EDS analyses (film deposited at 23°C).

Digital photographs of the films show distinct differences in colour (Figure 6.15). Films that were deposited at high temperatures or higher pressures show a dull dark colour, while films deposited at lower temperatures are a bright yellow/orange gold colour (Figure 6.15).

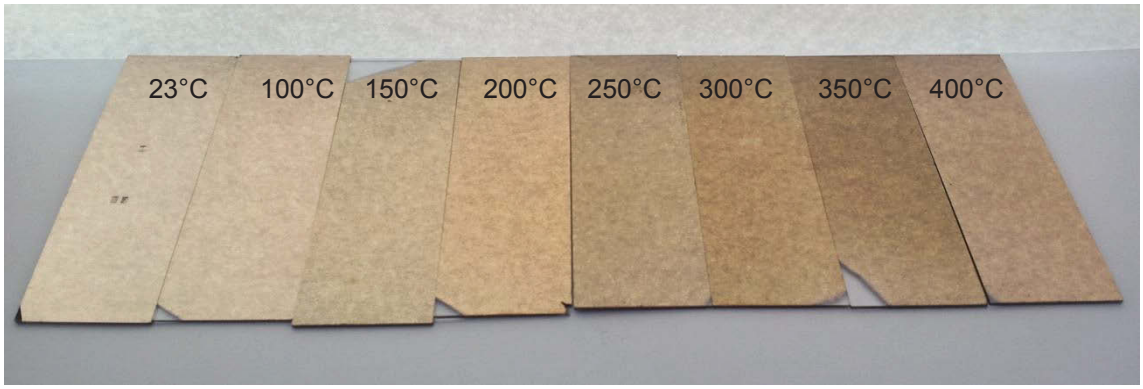

Figure 6.15 Digital photograph of films deposited at temperature as indicated show colour differences amongst films deposited at different temperatures indicating oxidation.

The twenty three films deposited with various Al concentrations were labelled Beta 1 to Beta 23 with the number indicating the order in which they were deposited. The deposition conditions of these films are listed in Table 6.6.

Table 6.6 Deposition conditions for films deposited with various Al concentrations

Sample Name	Target Power (W)		
	AuCu	Al	
Beta19	70	25	
Beta18	60	25	
Beta17	50	25	
Beta16	39	25	
Beta15	36	25	
Beta13	30	22	
Beta14	33	25	
Beta12	30	23	
Beta11	30	25	
Beta9	30	28	
Beta8	30	31	
Beta10	30	31	
Beta7	30	34	
Beta6	30	37	
Beta5	30	41	
Beta3	30	44	
Beta4	30	44	
Beta2	30	47	
Beta1	30	50	
Beta22	30	50	
Beta21	30	55	
Beta20	30	60	
Beta23	30	70	

Increasing Al Content →

These films were subjected to GIXRD to identify which phases were present in the deposited films. As films were deposited across the ternary diagram, it was expected that α, β and γ phases of Au-Cu-Al would be present. The GIXRD patterns are plotted

on a single graph (Figure 6.16). This graph shows the transition of film crystal structure from α-phase through β to γ-phase as the Al content was increased. The β-alloys displayed two characteristic phases: austenite phase in films of low Al contents, and martensite phase or phases at high Al contents. While many of the peaks present in these patterns line up with, or are very similar to, the bulk patterns, there are small differences which can possibly be attributed to strain and differences in composition. Only the strongest peaks from the $L2_1$ parent phase known from the bulk material were identified in the GIXRD pattern. The smaller peaks were not visible as the intensity is too low in GIXRD for them to be observed above the background. As the Al content decreases, peaks from bordering phases in the ternary diagram increase in intensity. This was true for most films except for some outliers such as Beta 1, Beta 3 and Beta 8, which all showed a characteristic α-phase structure.

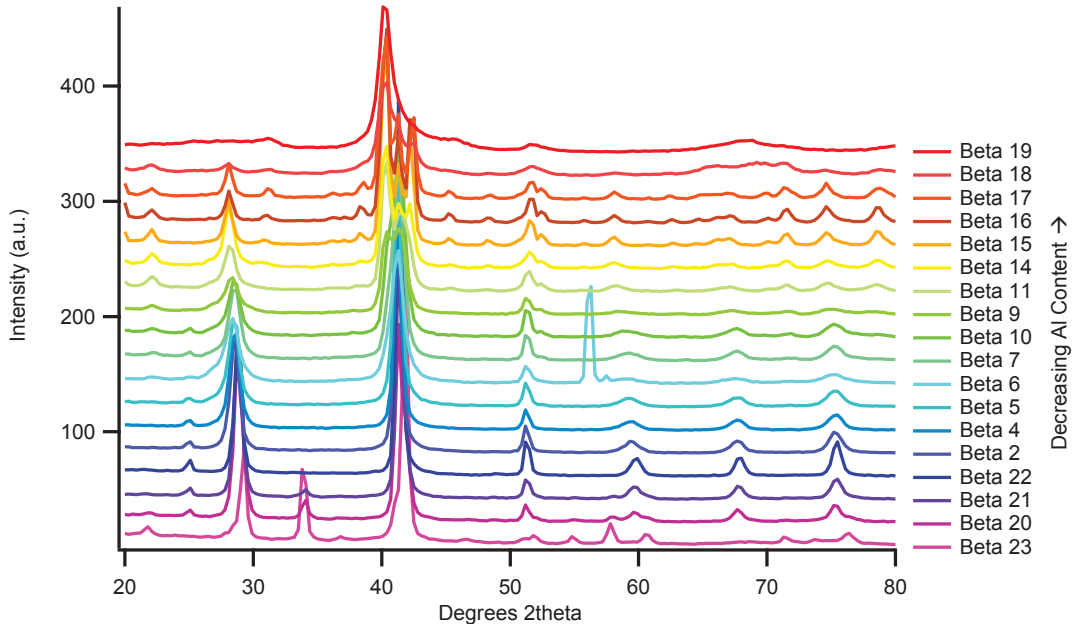

Figure 6.16 GIXRD of films deposited with various Al contents showing the gradual change in crystal structure

From the profilometer step-height measurements it was observed that, with the exception of samples Beta1, 17, 18 and 19, all of the films synthesised in this series had thicknesses well below 100 nm, with the thinnest film measuring 55 nm. These data have been summarised in Table 6.7 on page 148. TEM images for Beta 4, 11 and 17

were selected as they are representative of the films deposited across the compositional ranges. All three of these films show well crystalline, continuous films (Figure 6.17). Beta 4 and 11 have a small amount of porosity within the films and larger surface features than Beta 17. This may be attributed to the rate of deposition as Beta 17 was deposited at a rate approximately 1.5 times that of the other two sample. The crystallite sizes of these films were measured in the TEM images to be between 30 – 80 nm in most films, with some smaller particles also surrounding the larger crystallites.

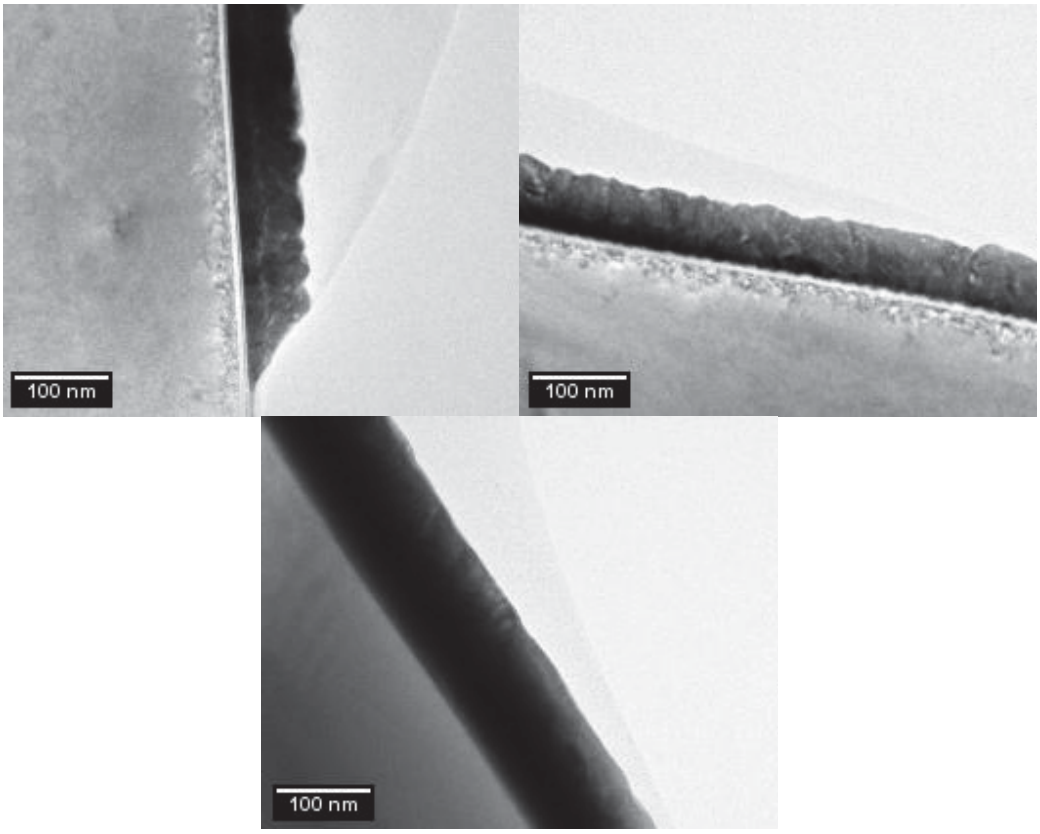

Figure 6.17 TEM images of samples deposited with various Al contents. Top left Beta 4, top right Beta 11, bottom Beta 17.

6.4 Discussion

6.4.1 Setting up deposition conditions

Producing flat, thin films of alloys has revealed some inherent problems that are difficult to overcome. When trying to produce an intermetallic compound or alloy, a

minimum temperature (or deposition energy) and composition is required for the desired phase to form [197]. Unfortunately, raising the temperature of the substrate during the deposition process affects a number of properties, as the temperature affects the atomic crystal structure, chemical composition and film quality. This often necessitates a trade-off between the crystallinity of the deposited material and surface roughness, both of which increase as the temperature is raised, as discussed in detail below.

Another issue was that of obtaining reproducible and uniform substrate temperatures. As the samples were in a vacuum and spinning, an accurate measure of substrate temperature was hard to obtain. Several methods were implemented; a thermocouple in between the heat lamps and the substrate, a thermocouple in contact with a copper ring on the edge of the sample holder, and a thermocouple in the centre of the sample stage. The thermocouple in the vacuum produced an accurate measurement of the heat emanating from the halogen heat lamps. However even though this temperature remained constant, the substrate temperature would continue to increase throughout the deposition, producing over-heated films at longer deposition times. This was most likely due to the metallic thermocouple having a higher thermal conductivity than the substrates. It was found that regulation of substrate temperature was best achieved by (1) having an additional sensor attached to the centre of the sample stage and (2) starting the deposition only after both temperatures had stabilised.

Another problem that was encountered was ensuring an adequate vacuum. For these depositions a vacuum chamber was incorporated with a rotary pump for roughing and a diffusion pump for high vacuum. While these pumps provided sufficient vacuum for physical vapour deposition, differences in operating times or temperatures produced unpredictable base pressures. This resulted in films produced under similar applied power levels and temperatures having different properties and crystal structures. Films produced in the first regime (labelled *newtemp*) were significantly affected by this and inconsistencies in the identified phase, for example, can be seen in Table 6.2. Figure 6.18 shows the GIXRD pattern for three films produced with the same target power, deposition pressure and similar temperatures, but for which the chamber was evacuated

for different lengths of time. Small differences in the base pressure of the chamber had a significant effect not only on the quality of the film, but also on the crystal structure, even though they were all below the recommended base pressure of 2.1×10^{-5} Torr [196]. In the present work it is clear that a base pressure in the order of 1×10^{-6} Torr must be achieved in order to produce a well-crystallised coating, and minimise the possibility of oxidizing the sample. An even better vacuum seems needed for higher temperature depositions. This is probably due to the higher rate of oxidation at the higher temperatures.

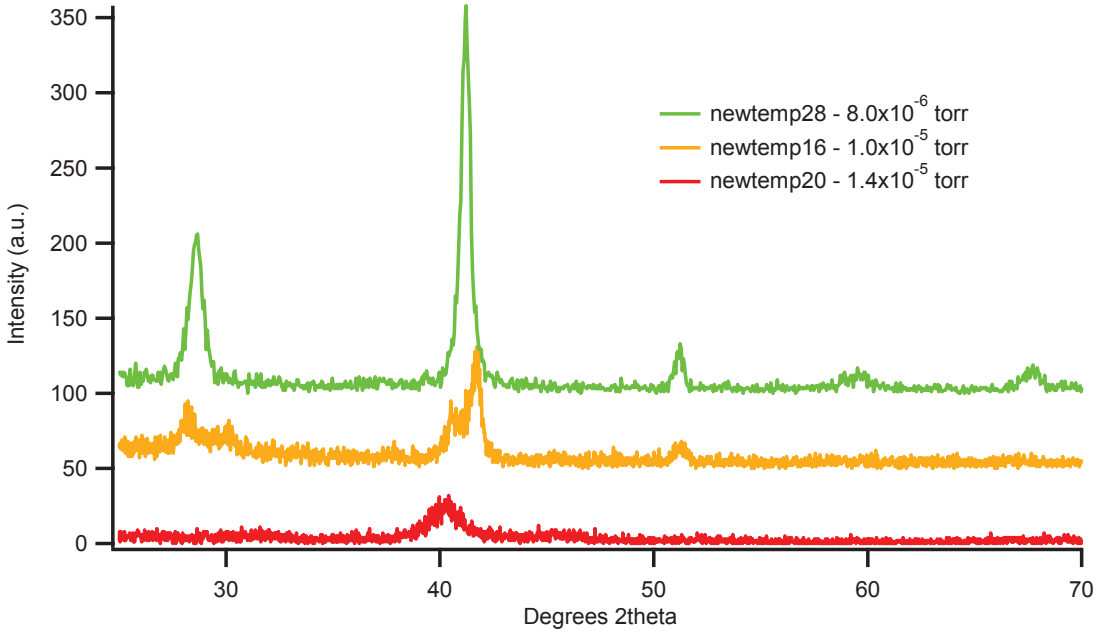

Figure 6.18 GIXRD patterns of films deposited at different base pressures. Offset for clarity.

It was also found that longer evacuation times did not always produce a lower base pressure, and that the previous operating conditions or time left at atmospheric pressure between coatings had an effect on the quality of the films. Systems using this configuration have largely been replaced with loading chambers which allow for a much smaller volume chamber to be vented to atmosphere in order to load and unload the substrate [196]. This is then evacuated and a second valve opens the loading chamber to the deposition chamber vacuum, allowing it to be placed in position for sputter coating. This change in design allows for a higher vacuum to be maintained and less contaminants to enter the chamber. Plasma cleaners are also widely used to remove

organic and water vapour contaminants from inside the deposition chamber and could be incorporated into future experimental designs [157].

Fe contamination is observed in many of these films, and is particularly evident in the sample deposited at 23°C, which was the first deposition for this series. TEM EDS maps show a high concentration of Fe at the base of the deposition layer on top of the Si (Table 6.5). From EDS analysis, this first layer consists primarily of O and Al, with a 17 at.% contamination of Fe. This higher Fe concentration has been attributed to contamination from previous users of the equipment, in particular in this case due to its previous use to produce Fe-Cr films, or due to erosion of the chamber structure itself which is made of stainless steel (containing Fe and Cr). Some Fe and Cr may have re-sputtered off the surfaces of the chamber.

Even with the greatest care taken, some oxidized films were still produced. Figure 6.9 shows the GIXRD patterns of a range of films deposited at different temperatures. These patterns show a gradual change from β-phase to a martensite structure, except for the depositions at 150°C and 250°C. When looking at the deposition conditions for these two particular films the chamber was evacuated according to the same regime but only achieved a vacuum of 5.1×10^{-6} and 3.7×10^{-6} Torr respectively before the chamber was heated. Once heated, this resulted in a base pressure of 1.6×10^{-5} and 2.1×10^{-5} which, from an Ellingham diagram, can be seen to be quite inadequate for making oxide-free samples. SIMS analysis (Figure 6.10) confirms this, showing a marked increase in the O content of these films, a result of the higher residual O partial pressure or residual water trapped on the surface of the chamber.

6.4.2 Films deposited at less than 300ºC

Observing the trends throughout the other films shows that even at low temperatures of 23°C and 50°C there is still a degree of ordering and crystallinity seen in the GIXRD (Figure 6.9), due to the energy provided by the sputtering process. However, the relatively low intensity and broad peaks mean that this crystal structure is limited to a smaller volume fraction and is less crystalline. SEM (Figure 6.7) and TEM (Figure 6.8)

images of these films show they are relatively smooth, composed of a uniform solid film of 50 nm with surface features of approximately 5 nm to 20 nm wide.

Increasing the deposition temperature causes peak intensity (as measured by diffraction) to increase and peak width to decrease, however peak width still remains relatively broad compared to that of the bulk samples measured with conventional XRD (Figure 6.9). Part of this broadening is due to the GIXRD geometry [158]. The increasing peak intensity can be seen when comparing the 50°C, 100°C and 200°C depositions, with the (220) (2θ = 41°) peak intensity increasing by 29% and 60% respectively, and the (200) (29°) peak increasing by 117% and 20%. This change shows an increased crystallinity of the film and/or an increase in the volume fraction of crystallised material. Increased deposition temperatures also create an increase in not only the surface roughness seen in the XRR data (Figure 6.6) and SEM images (Figure 6.7), but also a decrease in the internal homogeneity of the film due to voids and larger crystallites (Figure 6.8). This trade-off is important when trying to create films for practical applications as the quality of the film may limit the design of the device, especially when trying to create actuators or functional films [14, 90]. While the surface features of this film are between 50 nm to 100 nm wide, there is still a continuous layer of at least 55 nm in thickness. It is this continuous layer which is the essential factor for developing a mechanical or active device.

Another change that is seen with an increased deposition temperature is a homogenisation of the composition throughout the film (Figure 6.10). Films deposited at lower temperatures show a gradient of composition from top to bottom. The O content is high in the top layer of the film, decreases within the bulk of the film, and increases again at the base layer. The increased O level on the surface of the film is due to the formation of Cu and Al oxides, as even alloys with high gold percentages will still generate these oxides in thin films [198]. The increased O at the base of the film is due to both the native SiO_2 and the residual O present in the chamber at deposition. While the majority of the plasma is formed by the Ar gas back-pressure, there is still some O present which reacts with the initial deposition. This is then bound in the film and the O contamination decreases over the length of the deposition time. Films

deposited at higher temperatures do not exhibit this gradient as a higher O content is maintained throughout the film. This also has the effect of removing changes in the concentration of other elements as the trend of the O concentration is also seen in the Al and Cu concentrations (Figure 6.10). Au remains largely unaffected by this as it remains uniform throughout the film regardless of deposition temperature or O concentration. This change in homogeneity can be attributed to the diffusion of Al and Cu from within the bulk of the alloy towards the outer surface. This effect is also seen in Au_2Al and Al_2Au thin films [199]. In the higher temperature deposits the surface oxide layer is not present or is reduced due to the oxidised material being spread throughout the bulk, limiting the diffusion of Al or Cu towards the surface. While the majority of the Au is homogeneous throughout the film regardless of deposition temperature, a small change is observed in the Au signal of the low temperature deposits. This is due to the absence of Au from the top oxide layer which therefore produces a lower Au concentration signal in the SIMS. The lack of an oxide layer in the higher temperature deposits means this phenomenon does not occur in those samples. The compositional gradient and oxide gradient of thin films deposited at low temperatures would also result in nano-actuators moving over a range of temperatures due to the effects of composition on transformation temperature discussed earlier.

6.4.3 Films deposited at greater than 300ºC

When films are deposited at 300°C and above their properties change dramatically. The morphology of the initially deposited films takes the form of small spherical conglomerates surrounding the larger crystalline particles and, as the temperature continues to increase, the number of larger particles is reduced. This trend continues until the film consists almost entirely of spherical particles resulting in an increased porosity as the conglomerates pack together in a random arrangement creating voids. While the XRR data collected for these films does not show many fringes, it is interesting to note that the roughness sampled by the X-ray beam seems to decrease in the 400°C deposition (Figure 6.19). This is due to the removal of the larger grains seen in the 300°C and 350°C depositions, replaced by the smaller spherical particles, resulting in smaller deviations in height across the film.

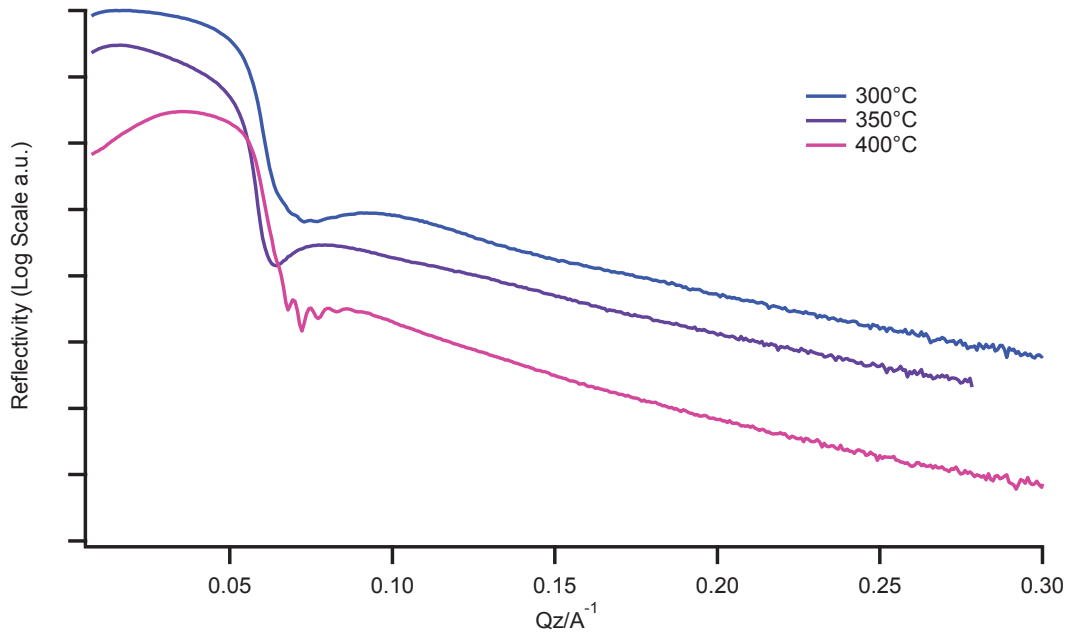

Figure 6.19 XRR of AuCuAl films deposited at 300, 350 and 400°C. Offset on vertical scale for clarity.

These higher deposition temperatures also produce a change in the crystal structure, with the samples made at 300°C and 350°C showing distinct splitting of the (220) peak of the parent phase, to form martensite peaks (Figure 6.9). These increase in intensity at high temperature depositions thereby reducing the intensity of the peaks of the parent phase. Finally, the diffraction pattern of these films transitions to a dominant FCC simple cubic pattern at films deposited at 400°C. The change in morphology coincides with the change in crystal structure and is due to the presence of these high temperature martensite and FCC phases forming as the film is deposited. From TEM EDS analysis it can be seen that there is an increase in the O content within these films up to approximately 7 - 10 at.% in some regions of the films (Table 6.3 and Table 6.4). SIMS analyses of these films show that similar levels of O concentration were obtained in the 150°C and 250°C depositions (Figure 6.10). The morphology of the 250°C depositions shared similarities with these high temperature films, containing small spherical particles (~10 nm) evenly distributed throughout the film (Figure 6.20). However, they were two to three times smaller than the particles produced at higher temperatures. These changes coincide with a change in colour with all of these films exhibiting a

darker brown colour rather than the bright yellow films seen in the lower temperature, lower pressure depositions.

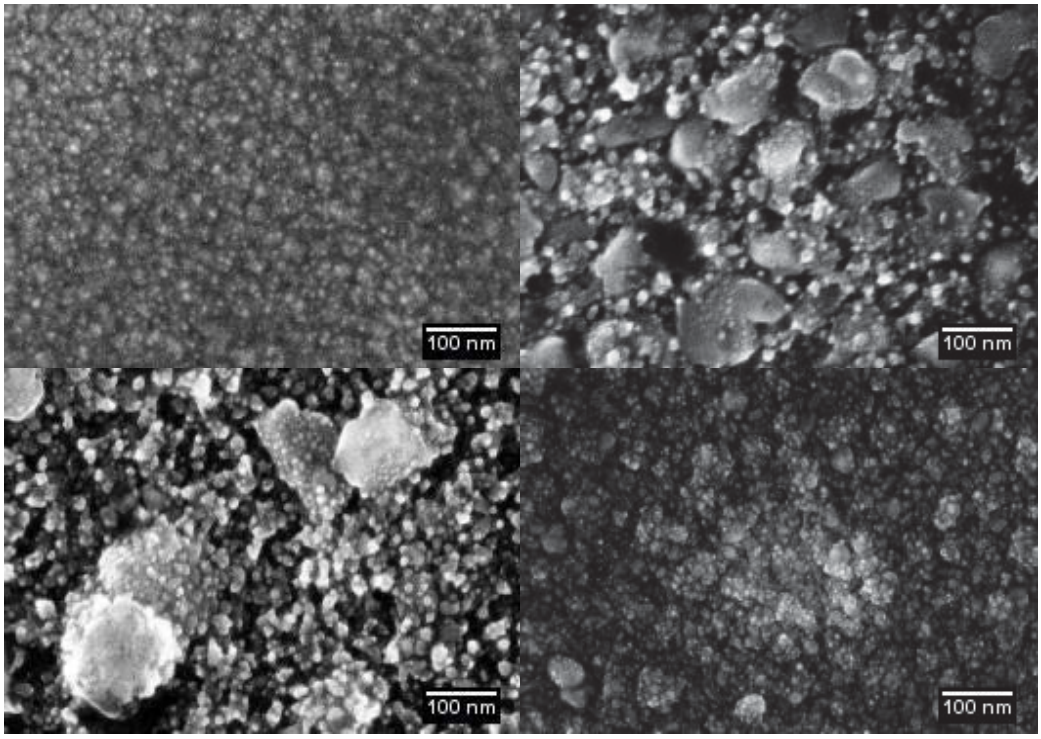

Figure 6.20 SEM images of 250, 300, 350 and 400°C depositions showing spherical particles in films.

These changes in crystal structure, morphology and colour can all be related back to the higher O content within the films. While the initial base pressures of all the films deposited were in the order of 10^{-6} Torr, when the substrate was heated this caused an increase in the base pressure. When this additional O content contaminates the film it results in a reduction of Al content of the metallic phases. In small additions of O, this has the effect of increasing the transformation temperature in the shape memory alloy, producing crystallites with transformation temperatures above room temperature. As this process continues, removing more and more Al and, to a lesser extent, Cu, from the alloy, it pushes the alloy further towards the AuCu edge of the ternary phase diagram and eventually produces an α-phase cubic structured material. The diffraction pattern of the sample produced at 400°C is similar to that of the sample produced at 250°C which presents a similar morphology, high O content and similar heated base pressure. This would suggest again that it is the O content and change in composition which is the

dominant cause for the change in crystal structure rather than just the temperature. The increased deposition temperature is merely a means by which the O concentration may be increased within the film, and increases the rate in which the O reacts with the Cu and Al. It has been shown in other materials that the substrate temperature has an effect on the extent of oxide formation given the same O partial pressure [200].

Ni–Mn–Sn shape memory alloy thin films are also subject to changes in morphology and crystal structure as a function of deposition temperature. For example, Vishnoi and Kaur [201] showed that deposition temperatures of 650°C produced thin films of Ni–Mn–Sn with a martensite structure at room temperature, but as deposition temperatures decreased to between 600°C and 450°C an austenite crystal structure was formed at room temperature. Similarly, deposition at 450°C produced smaller grains than deposition at higher temperatures, Figure 6.21. As the temperature continued to increase, small spherical particles were observed on the crystallites, until at 650°C the film was composed entirely of these small particles. This change in morphology was also accompanied by a change in the room temperature crystal structure from the β-phase to a martensite phase. While the heated base pressure is not discussed, the base pressure before heating for these samples was in the order of 10^{-7} Torr which would explain why the change in morphology and phase is only observed at higher temperatures.

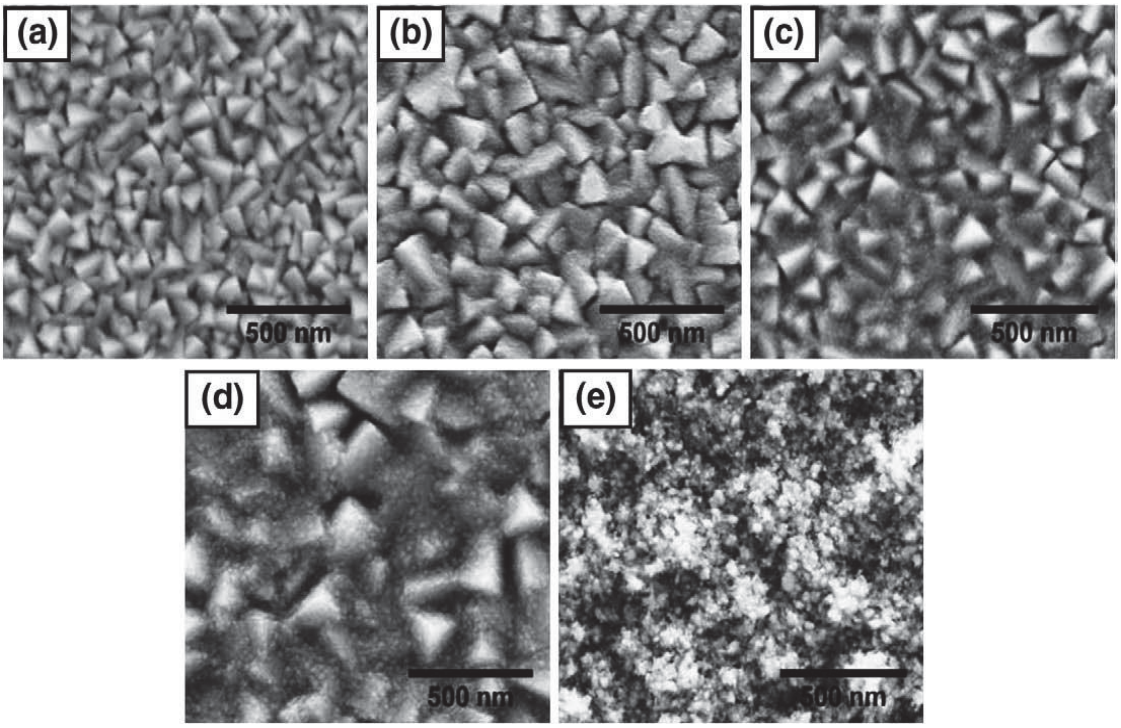

Figure 6.21 Vishnoi *et al*'s FESEM images of Ni–Mn–Sn films deposited at (a) 450, (b) 500, (c) 550, (d) 600 and (e) 650 °C, showing the effect of substrate temperature on the morphology of the films [201].

6.4.4 Films deposited with varying Al content

In the previous section, the effects of deposition temperature and oxygen content on the quality and crystal structure of the film were investigated. The films discussed in the present section were deposited after taking these effects into consideration. In particular, they were deposited at the lowest base pressure reasonably achievable through the use of a load locking chamber. This helped maintain a low pressure and prevented contaminants from entering the chamber. Pre-heating the chamber while evacuating also helped in removing water vapour attached to the walls of the chamber. This set-up showed that prolonged use without venting the entire chamber removed more contaminants over subsequent depositions, producing films with lower oxygen levels. SIMS and GIXRD analysis shows that the first deposition was very similar to the heated films described in the previous section, with an α-phase GIXRD pattern with an homogeneous composition throughout the film and oxygen content similar to that of the 250°C deposition. However, over subsequent depositions where the chamber was not vented, the oxygen concentration within the film decreased dramatically and in some films was reduced to just a few counts throughout the bulk of the film (Figure 6.23).

However, in all of these films, an oxide diffusion layer was still produced on the surface. A large number of deposited films were synthesised until high quality films were reproducibly achieved. This also emphasised the results seen in the previous section when films did not produce the desired quality.

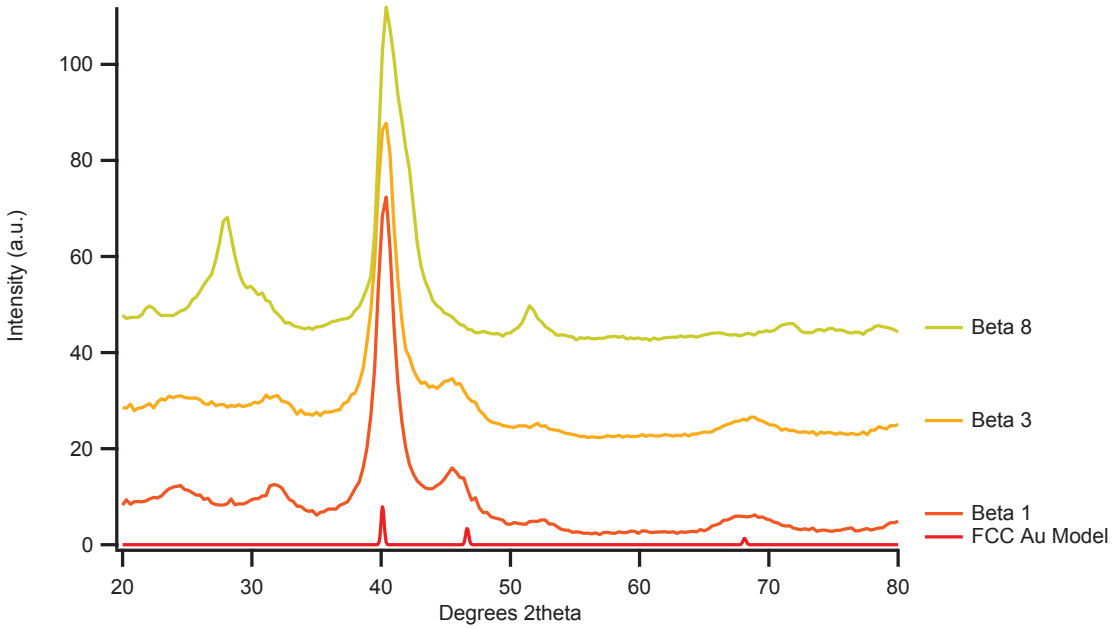

Figure 6.22 GIXRD of first depositions after venting. Nominal compositions, Beta 1 – 5.7 Al wt.%, Beta 3 – 5.4 Al wt.%, Beta 8 – 4.8 Al wt.%. Offset for clarity.

The compositions of these films were varied and, due to the relatively small amount of oxidized material, the actual compositions of the metallic portions of the films have likely remained the same as the nominal deposited compositions throughout the bulk of the film (with the exception of Beta 1, 3 and 8, where O concentrations observed in the SIMS are higher). In the methodology chapter, the AuCu target was shown to have a composition lying at the 58 at.%-Au Cu edge of the ternary diagram. However, differences in the sputtering efficiencies of these elements may lead to a small difference in the ratio of Au to Cu atoms within the film. Seshan et al. [92] states that, while the sputter *yield* of Cu is between 27 to 14% higher than that of Au for Ar ion energies of between 300 – 1000 eV, the sputtering *efficiency* of Au is 5% higher for the given set-up. Taking these two effects into account, it is expected that the sputtered films would have very similar Au:Cu ratios to those of the target. By using this as a reference, the composition of films possible would pass from this point across the ternary diagram to the 100% Al corner as seen in Figure 6.1.

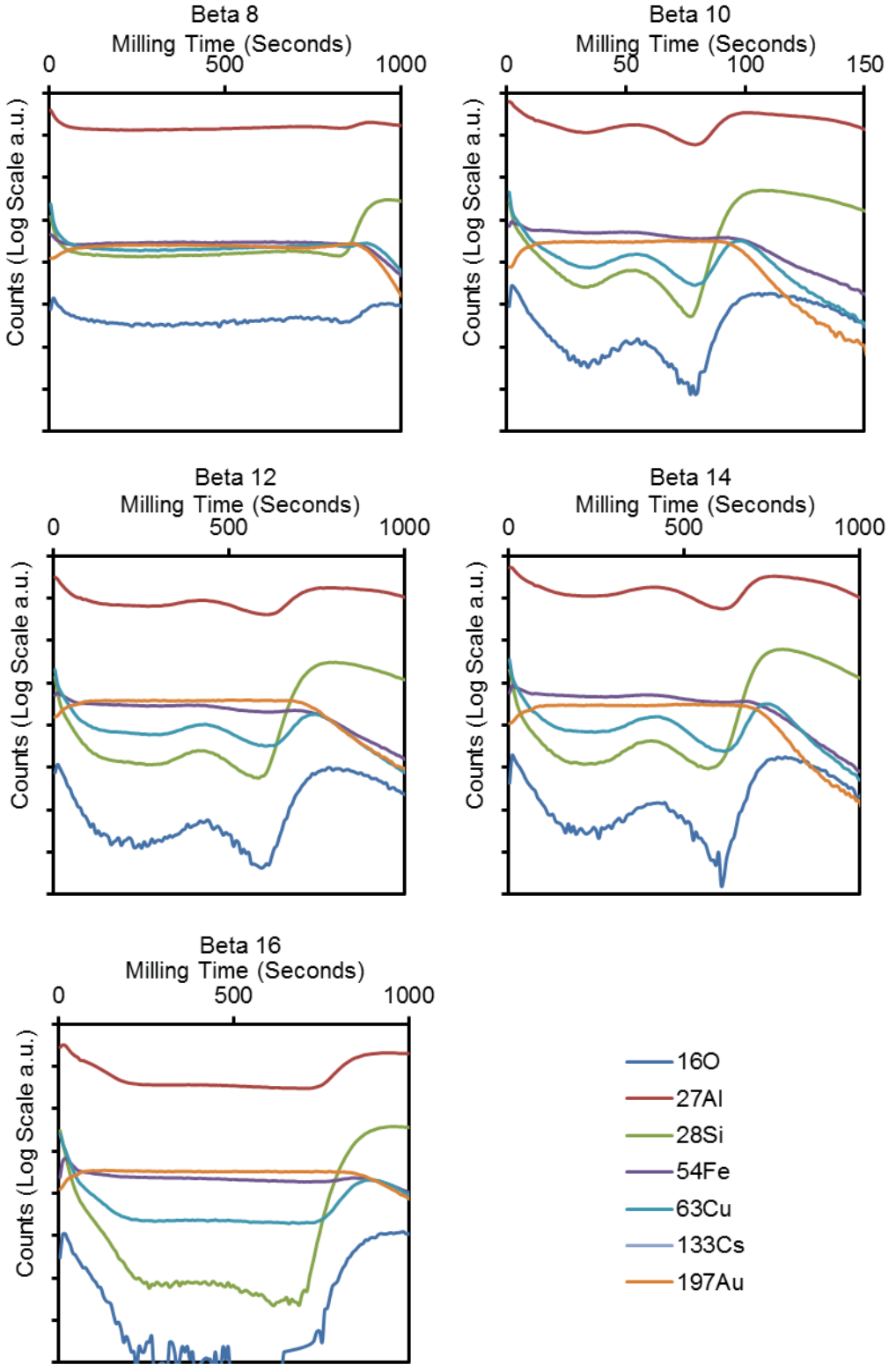

Figure 6.23 SIMS profiles of Al series films showing compositional variation. Ordered from highest to lowest Al content.

While SIMS measurements may not be able to give absolute values for the increase in the Al content across the series (Figure 6.23) they do show a distinct increase. GIXRD shows a gradual change in the ternary phases synthesised, as the ratio of the Al:AuCu target power is varied. From previous work [28, 30, 32, 34] the compositional boundaries and crystal structure of AuCuAl ternary alloys are reasonably well known and provide an estimate of the composition for the films produced here. However, the phase boundaries are subject to small differences due to factors such as differences in equilibrium temperature due to the energy provided by the sputtering process or deviation from the expected Au:Cu ratio. The data set produced here shows that these films display reproducible results, with the expected changes occurring with increasing Al.

Table 6.7 Deposited film properties and nominal Al content

Sample Name	Target Power (W)		Thickness Average (nm)	Phase	Nominal Al wt.%
	AuCu	Al			
Beta19	70	25	129	Alpha + Beta	1.5
Beta18	60	25	111	Alpha + Beta	2
Beta17	50	25	99	Beta (martensite)	3
Beta16	39	25	81	Beta (martensite)	3.5
Beta15	36	25	77	Beta (martensite)	3.7
Beta13	30	22	55	Beta (martensite)	4
Beta14	33	25	62	Beta (martensite)	4.2
Beta12	30	23	69	Beta (martensite)	4.3
Beta11	30	25	60	Beta (martensite)	4.5
Beta9	30	28	59	Beta (martensite)	4.65
Beta8	30	31	69	Beta (martensite)	4.8
Beta10	30	31	57	Beta (martensite)	4.8
Beta7	30	34	55	Beta (austenite)	4.95
Beta6	30	37	66	Beta (austenite)	5.1
Beta5	30	41	74	Beta (austenite)	5.25
Beta3	30	44	76	Beta (austenite)	5.4
Beta4	30	44	63	Beta (austenite)	5.4
Beta2	30	47	61	Beta (austenite)	5.55
Beta1	30	50	107	Beta (austenite)	5.7
Beta22	30	50	66	Beta (austenite)	5.8
Beta21	30	55	74	Beta + Gamma	6.2
Beta20	30	60	72	Beta + Gamma	6.6
Beta23	30	70	76	Beta + Gamma	7

These results have been summarised in Table 6.7 to provide a guideline for producing the desired ternary AuCuAl phase in future work.

Table 6.8 Summarised film phases relative to the power of each target

Ternary AuCuAl Phase	AuCu Target Power (W)	Al Target Power (W)	Thickness range (nm)
Alpha	>70	25	>129
Alpha + Beta	70 - 50	25	129 - 99
Beta (martensite)	50 - 30	25 - 31	99 - 57
Beta (austenite)	30	34 - 50	74 - 55
Beta + Gamma	30	50 - 70	66 - 76
Gamma	30	>70	>76

6.5 Conclusion

Here it has been shown that, in order to produce high quality films, a base pressure that is even two orders of magnitude below the deposition pressure is not adequate and, at elevated temperatures, results in highly oxidised films deposited. A base pressure of at least three orders of magnitude below the deposition pressure is required when depositing at room temperature, if depositing at high temperatures this still produces oxide levels that are likely to change the composition of the deposited film. Pre-heating the deposition chamber before sputtering reduces this effect but further precautions need to be implemented in order to produce high quality films with less oxidized material. For the deposition conditions described here, a substrate temperature of approximately 150°C is required in order to produce crystalline, nanoscale thin films of AuCuAl. Below this temperature crystallite size is very small but the films are very flat. Above this temperature oxidation of the Al constituent changes the stoichiometry of the crystallised material. Nevertheless, after taking these factors into account, it has been shown that it is possible to produce AuCuAl films under 100 nm in thickness with crystal structures that relate directly to the three main phases of the AuCuAl ternary diagram.

7 Properties of AuCuAl SMA Thin Films

7.1 Introduction

The TiNi shape memory alloy has been used extensively for practical applications in its bulk form as it exhibits a large recoverable strain and excellent super-elastic properties. This has led to the development of a wide range of TiNi thin films across size scales down to a few microns in film thickness. However, as mentioned earlier, the use of TiNi in *nano*-actuators has been limited to date, due to problems experienced when producing films of less than 100 nm thickness [13, 14]. These difficulties are due to Ti oxidation which changes the composition of the alloy to the point where it is no longer capable of exerting a shape memory effect SME. A nanoscale grain size in itself apparently does not affect the SME because it has been shown that nano-sized crystals of TiNi and TiNiCu still exhibit an austenite to martensite transformation and retain their SME. For example, recent work has shown that TiNiCu thin films can exhibit a SME down to 50 nm [202], *provided oxidation is avoided*. In contrast to TiNi, $Au_7Cu_5Al_4$ is relatively resistant to oxidation due to its high gold content. It is therefore a good candidate for the fabrication of nanoscale thin films that will still exhibit a SME. In previous chapters the fabrication and physical properties of these films has been discussed; here I discuss techniques used for identifying those of the films that exhibited a reversible austenite to martensite phase transformation.

7.2 Experimental

GIXRD was performed on a series of AuCuAl thin films to identify those that exhibited a martensite or austenite crystal structure, which respectively represent the low temperature and high temperature states of a SMA. These scans were shown in Chapter 6.

A two-point probe was used to measure the electrical resistance of the films as they were heated and cooled to precisely record both forward and reverse transformations.

In order to confirm that the changes in resistance were due to a reversible phase change, *in-situ* GIXRD was performed on the samples above and below the recorded transformation temperature in order to observe any associated reversible change in the crystal structure. See Chapter 3.10 for more details.

In-situ XRD was also performed on selected samples to show in detail the phase change over a 2θ range of 25 – 80° (Cu Kα radiation). This was performed on a PANalytical Xpert Pro with an Anton PAAR HTK450 heating stage to provide accurately controlled temperature steps.

Profilometer and X-ray reflectometry data were used to confirm film thicknesses, and is described in previous chapters.

7.3 Results

All of the films produced for these experiments were measured to be less than 100 nm thick with the exception of Beta 1, 17, 18 and 19. These results were taken from the average of six profilometer measurements. (The table of results is given in Chapter 6.4.4.)

Electrical resistance plots show a linear change with temperature in materials where no phase changes occur. Electrical resistance plots of films that began with an austenite structure showed a distinct change in the slope of the cooling and heating curves. The change in slope correlates with a resistance change typically associated with a phase transformation as documented by Piao and Meng [203, 204]. Figure 7.1 shows the change in resistance for samples Beta 22, 2, 4, 5 and 7, with nominal Al wt.% of 5.8, 5.55, 5.4, 5.25 and 4.95, respectively. A first derivative plot was overlayed on each of these graphs to emphasise the change in gradient and highlight the onset of transformation (Figure 7.2). In order to show that this is not an artefact of the experimental set-up, films that exhibited a martensite structure were also measured while cooling below room temperature. In these cases no change in the slope of electrical resistance was observed, as expected.

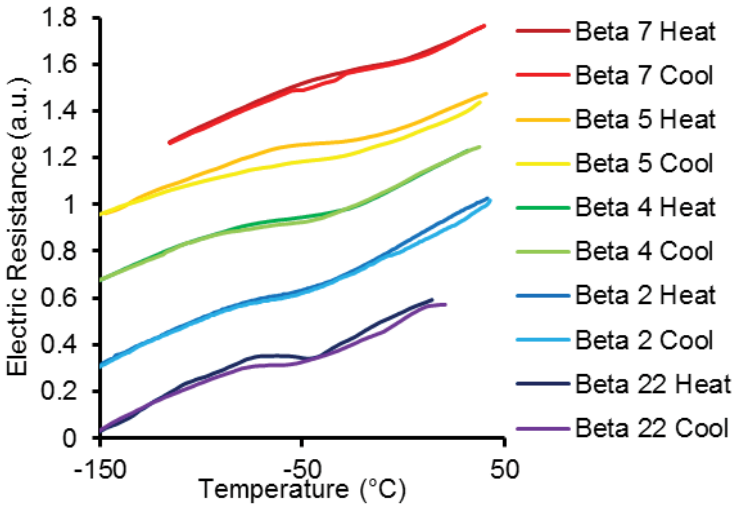

Figure 7.1 Electrical resistance measurements of select films showing phase change. Offset for clarity.

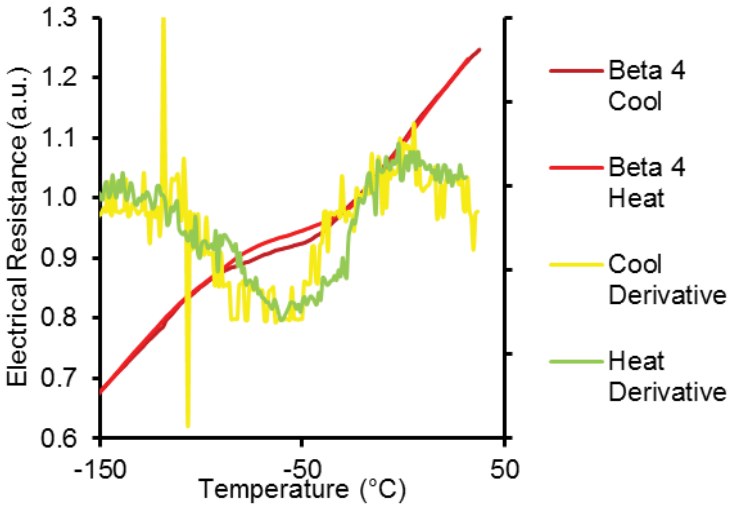

Figure 7.2 Electrical resistance measurement with first derivative.

Table 7.1 Summary of transformation values. All values in °C

Sample Name	Beta 22	Beta 2	Beta 4	Beta 5	Beta 7
Nominal Al wt.%	5.8	5.55	5.4	5.25	4.95
A_s	-80	-97	-89	-70	-60
A_f	-41	-31	-22	-12	4
M_s	-50	-38	-37	-20	17
M_f	-82	-97	-95	-78	-60
A_p	-60.5	-60	-55.5	-41	-28
M_p	-66	-66	-66	-49	-21.5
ΔA	39	66	67	58	64
ΔM	32	59	58	58	77
Peak Hysteresis	5.5	6	10.5	8	-6.5
Heating Hysteresis	9	7	15	8	-13
Cooling Hysteresis	2	0	6	8	0

Films that had a martensite phase at room temperature were heated to induce a martensite to austenite transformation but did not produce a signal that would be indicative of a transformation, and instead produced a rapidly decreasing electrical resistance when heated above 150°C (Figure 7.3). This is an indication that lattice defects are likely being removed through annealing, and upon cooling this lowered resistance is maintained which is consistent with this explanation. Subsequent heat cycles show resistance changing linearly with temperature indicating that there is still no detectible martensite to austenite phase change.

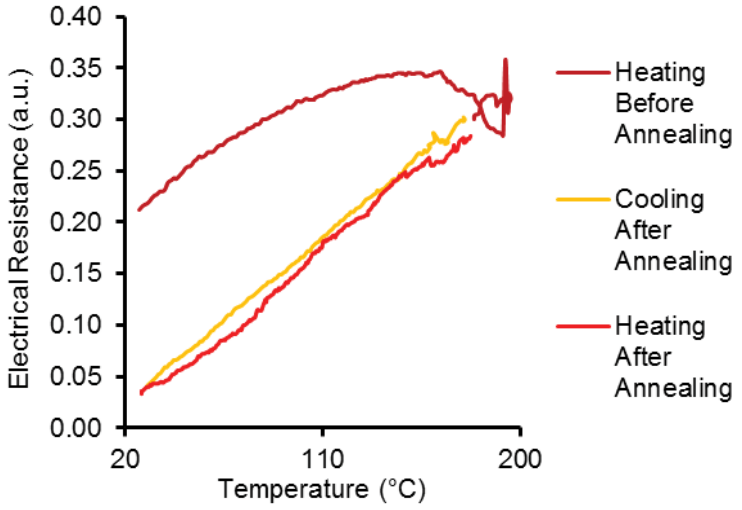

Figure 7.3 Electrical resistance measurement of martensite structured film.

Grazing incidence and Bragg-Brentano X-ray diffraction data were collected for samples identified as having a β-phase crystal structure in Chapter 6.4.4. The data were acquired during sample heating or cooling in order to observe any change in crystal structure. The intensity is quite low from the diffraction peaks due to the small total scattering volume from these thin films, however the austenite and martensite peaks can still clearly be identified. Films that exhibited the martensite structure at room temperature were heated with a hot air blower to approximately 150°C and GIXRD patterns were collected focusing on the 38 - 44° 2θ range as previously explained. *In-situ* GIXRD patterns were also collected over the same 2θ range for films that presented the austenite structure at room temperature. These films were cooled using a cold nitrogen gas blower to approximately -75°C. The formation of martensite is obvious in the austenite films that were cooled. The peak intensity of the (220) peak at 41° is reduced and the martensite peaks form either side of this at 39.8° and 43.4° 2θ (Figure 7.4). The diffraction pattern of beta 9 (nominal Al wt.% 4.65) indicates a martensite structure at room temperature and when heated, very little change is observed in its GIXRD pattern Figure 7.5. This absence of a clear phase change was also characteristic of the other martensite films that were heated.

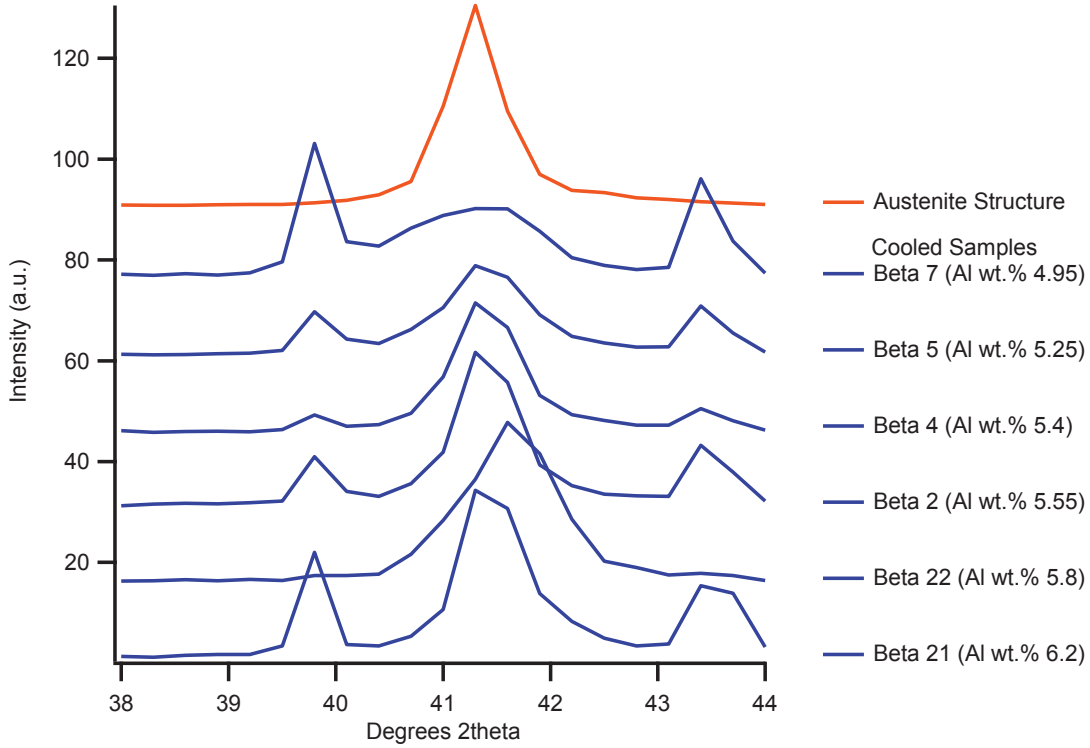

Figure 7.4 In-situ GIXRD of cooled austenite structured films at approximately -75°C.

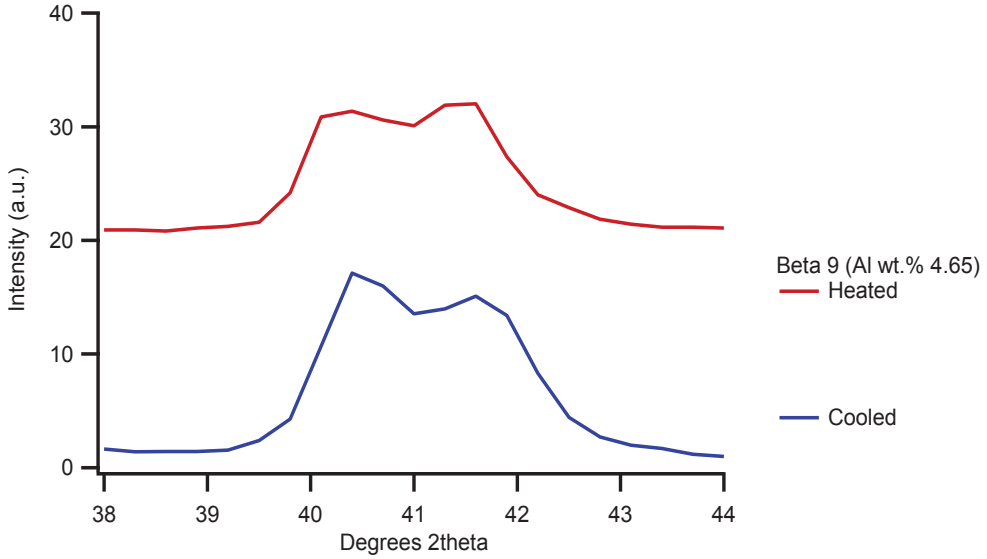

Figure 7.5 In-situ GIXRD of heated (~ 150°C) and cooled (~ -75°C) martensite structured film

As can been seen in Figure 7.6, as the austenite structured films are cooled, both the (220) and (200) austenite peaks are reduced and the martensite peaks at 29.3°, 33.5°, 40.1° and 43.7° appear. However these changes are not as prominent as those in the in-

situ GIXRD patterns, as the data were acquired in Bragg-Brentano geometry and therefore the signal intensity is poor. In addition, there are also peaks from the Si substrate at 47.39°. While these films do undergo a transformation below approximately -50°C, it is also well outside the range of the transformation temperatures of the corresponding bulk alloys of approximately 20°C. In addition, a large amount of the crystal structure undergoes no change, seen in the remaining austenite peaks, indicating the majority of the structure is "pinned" in this phase and that only a small sample volume undergoes the transformation. These results are similar to those collected by König *et al.* [202] where the TiNiCu thin films showed very little to no change in the peak position of the $(1\ 1\ 0)_{B2}/(0\ 2\ 0/1\ 1\ 1)_{B19}$, however a change in the peak intensities was noted in their 100 nm film. The existence of B19 peaks in the high temperature patterns of the TiNiCu films are attributed to a stabilised martensite layer on the SiO_2 interface, produced by the high levels of stress. The appearance of martensite structure peaks is also seen in some of the Bragg-Brentano powder diffraction of the AuCuAl films produced here as the X-rays are sampling the full depth of the film rather than just the surface layer seen in GIXRD. It is noted by König *et al.* [202] that the lack of any significant change in the powder diffraction pattern would signify that no transformation occurred in their 100 and 50 nm films, however they state that it was evident in their electrical resistance measurements that a transformation had indeed taken place. The lack of change in the diffraction patterns can be attributed to the combination of a small sample volume and presence of pinned martensite structures. These factors are also true for the AuCuAl thin films, however some changes are still observed in the powder diffraction patterns collected here.

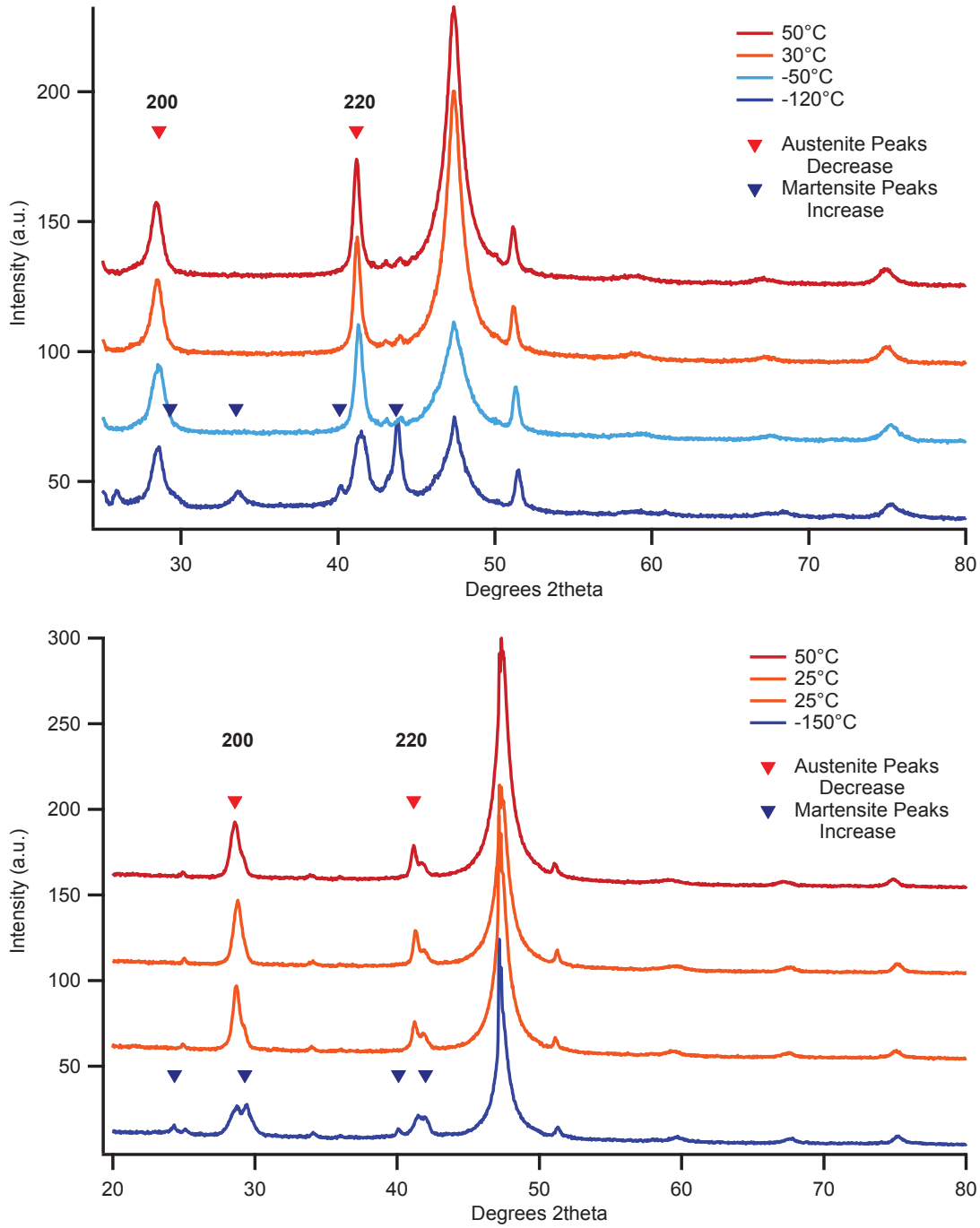

Figure 7.6 In-situ XRD of Beta 4 (top) and Beta 22 (bottom) showing change in diffraction pattern with temperature. Offset for clarity.

7.4 Discussion

7.4.1 Size limitation of SMAs

The effect of size on the properties of Cu- and Ti-based shape memory alloys has been well documented, with respect to both the grain size [99-102, 205-207] and thickness of thin films [5, 104, 201, 202, 208]. Many of the principal conclusions should also apply to the present Au-based shape memory alloys.

The dominant factor is the formation of an oxide layer on the surface of a film. This will change the average composition of the alloy due to depletion of the more easily oxidised elements, and places a lower limit on the thickness of functional SMA films. König *et al*. [202] were able to largely negate this effect in the NiTi system through the addition of Cu which decreases the sensitivity of the transformation temperatures to alloy stoichiometry. Therefore, the SME of their films was still retained even when the composition changed due to depletion of the oxidisable elements. However, this approach does not work in my alloys as the ratio of all three elements affects the transformation temperature as noted in Chapter 4.

It has also been shown that nanocrystals of TiNi can be synthesized in bulk alloys with either a nanocrystalline structure or as nanocrystals within an amorphous matrix [99-102]. In these cases an oxide layer does not make an appreciable difference to the sample composition and therefore the SME is a function of the alloy itself. Such work has shown that structures as small as 15 nm can exhibit a reversible martensite phase transformation. At least in NiTi alloys, this is the lower limit because transforming an even smaller crystallite seems to be prevented by the presence of an increased energy barrier [99-102].

It was shown in the previous chapter that, in films produced in a clean, oxygen-free deposition chamber, only a very thin oxide layer is present and that oxygen contamination within the bulk of the film is limited. Due to this, the chemical composition of the thin films remains largely unchanged. Also from the previous chapter it was shown that the crystallites in these films are of the order of 30 to 50 nm in

size (Figure 6.17), which is above the lower limit proposed for NiTi SMAs. Due to these films being free of the limiting factors listed above, they have still been able to produce a reversible phase change in films as thin as 55 nm. However they have exhibited several differences from the bulk SMAs. These will be discussed below.

7.4.2 Cause of low transformation temperature

Grain size

The SMA films synthesised here are comprised of nanoscale grains of approximately 30 to 80 nm, similar to that observed in TiNi particles [205]. However, in the latter instance the transformation temperature found by Barcikowski *et al*. was only about 7°C lower than that of bulk TiNi of a similar composition. A series of TiNiCu films from 750 nm to 50 nm thickness was documented in [202] and showed a much larger decrease in the transformation temperature as the films decreased in thickness, changing by as much as 23°C. Similarly Sawaguchi, Vishnoi and Kumar [104, 201, 208] have shown that in nano-structured thin films an increased energy barrier is formed as the grain size is reduced. This is attributed to the increased number of grain boundaries inhibiting the growth of the martensite phase, and preventing spontaneous transformation passing from one grain to the next. While grain boundaries act as nucleation sites for martensite formation, this is seen as a competitive process that is not as significant as the energy barrier created by increased grain boundary to grain volume ratios. In very small grains this results in a suppression of the transformation temperatures of up to 200°C [104, 201, 208]. Decreases in the transformation temperature due to grain refinement have also been documented in bulk alloys and are even measured with refinement on the micron scale, however this effect is less significant [206, 207]. This shows that while in some other SMAs there is a significant decrease in the transformation temperature with a reduced domain size, this is not the only possible explanation for the severely depressed transformation temperature of these AuCuAl thin films. Therefore, other factors must be considered.

Composition

There are two main factors that contribute to the transformation temperature of SMAs. The first is the chemical composition, where the ratio of elements or doping of alternate elements results in variations of the transformation temperature. This has been shown to vary the transformation temperature by up to 150°C [47]. It was shown in chapter 4 that the transformation temperature of bulk AuCuAl SMAs is dependent on the Al content within the alloy, with alloys near the high Al wt.% edge possessing much lower transformation temperatures. It is also known from Fumagalli *et al*. [31] that higher Au content also has the effect of suppressing the A_s and M_s temperatures. Fumagalli showed that even at a relatively low Al content of 3.9 wt.% but high Au content of 85.1 wt.% a martensite transformation temperature of -3°C was obtained. One might expect that the effect of a raised Au content could be combined with that of a higher Al content to produce an even lower transformation temperature. However this is unlikely to be the explanation for the sub -50°C transformation temperatures in the present samples for the following reasons: Firstly, the highest concentration of Al achievable in the β-phase is on the boundary between the β and β + γ dual phase region, which was found to have bulk transformation temperatures in the order of 20°C at an Au content of 76 wt.% [36]. Secondly, the SMA films in this research also have a composition near the β and β + γ dual phase boundary of the phase diagram (as the diffraction patterns show clear peaks from the γ-phase structure) and therefore should have a similar Al content to the bulk alloys documented by Levey *et al*. Thirdly, these films were synthesised with a AuCu target with an Au content of 81 wt.%, resulting in SMA films with a Au content much lower than that of Fumagalli *et al's* bulk alloys [31]. This indicates that while the Au contents in the films may be slightly higher than those of the bulk alloys documented by Levey *et al*., they would not be high enough to result in a decrease in the transformation temperature of greater than 70°C.

Aging

The second possibility which must be considered is that of aging. This was discussed in detail in Chapter 5 as a method by which the transformation temperature can vary. It has been shown extensively that, under normal cycling conditions, the transformation

temperature of AuCuAl shape memory alloys does not succumb to aging by way of a change in the transformation temperature, and that large variations are only caused when the alloy is cycled repeatedly *just above* the A_f. However, thermal cycling was not applied to the present thin films and is therefore unlikely to be a cause of the reduced transformation temperature. It is also impossible that decomposition aging is a possible mechanism as this would reduce the concentration of Al in the β-phase material and therefore actually *increase* the transformation temperature.

While changes in composition and aging in bulk SMAs are typically seen as the two main causes for changes in the transformation temperature, it has been shown above that these factors cannot account for the magnitude of the reduction in transformation temperature. It has also been shown that in bulk and nano-structured SMAs, a reduced grain size has the effect of lowering the transformation temperature by the increased number of grain boundaries, inhibiting martensite phase growth [104, 201, 208]. This must therefore be the mechanism behind the reduced transformation temperatures in the present films.

7.4.3 Lack of high temperature transformations

Induced strain

Both in-situ XRD and resistance measurements show it was not possible to produce a reversible transformation in films that *started* with a martensite structure at room temperature. It is unlikely that this is due to the nano-sized grains, as this typically has the effect of lowering the transformation temperature or stabilising the parent phase, which is not the case for these films. The lack of transformation must therefore be attributed to other factors, the first of which is the possibility that the martensite structure was stabilised by strain. Apart from the inherent strain produced within the deposited films, additional stresses form within the film after cooling from the deposition temperature. This is due to a mismatch of thermal expansion co-efficient between the film (approximately 1.4×10^{-5} °C^{-1} [209]) and substrate (approximately 0.3×10^{-5} °C^{-1} [209]). Strain has been shown in [202] to be able to stabilise the film into a

martensite structure, albeit for a small volume, however as the films are already in a martensite structure this may work to increase the reverse transformation temperature. The degree of stabilisation may vary throughout the film, and overheating would probably be required to overcome the induced strain from the deposition.

Martensite stabilisation

Martensite stabilisation also does not explain why those films which exhibit both austenite and martensite peaks (such as Beta 9) do not exhibit a transformation when cooled or heated. A possible explanation for this is that the intermediate phase was produced when the films were deposited. This may have occurred if the martensite transformation temperature was close to the substrate temperature at deposition, and is possible as the martensite transformation temperature in low Al wt.% samples has been shown to be as high as 169°C. This would have the same effect as quenching a bulk sample close to its martensite transformation temperature, which has been shown to result in a combination of martensite and untransformed austenite [185, 210]. This structure does not have enough chemical free energy to undergo a reverse transformation and is therefore stabilised in this state, at least until it is heat treated to order the lattice further. This would explain why these films would not exhibit a martensite or austenite transformation.

Low Al content

Another possible explanation for the lack of transformation in low Al content films is the reduced SME/energy of transformation. In bulk AuCuAl SMAs, it has been shown that the most prominent laths are observed in high Al wt.% samples. This can be seen in Chapter 4 where it was noted that the Nomarski interference images showed longer, more prominent laths (represented by the obvious change in colour in Figure 4.5) in the higher Al wt.% sample R6, whereas sample R3 (with a low Al wt.%) produced laths with very little deformation in the surface (possibly due to the formation of a different martensite structure). Fumagalli *et al*. observed a similar response to decreases in the Al content of AuCuAl SMA's. In their bulk samples there is a reduction in the enthalpy of

transformation from approximately 4 J/g down to 1.5 J/g as the Al content is changed from 5.2 wt.% to 3.9 wt.% [31]. If this is also the case for thin films, it is possible that the low Al wt.% SMA thin films do not possess a large enough transformation energy to overcome the energy barriers in the thin-film regime. This explains the gradual reduction in the extent to which a transformation is observed in the electrical resistance measurements with decreasing Al content Figure 7.1, followed by Beta 9 (4.65 Al wt.%) which did not show any change. This would also explain why martensite transformations are not observed in low Al wt.% thin films, which present both the austenite and martensite structure.

7.4.4 Increased transformation range

One other notable difference between these thin films and bulk samples is the increased differences between M_s and M_f (ΔM) and A_s and A_f (ΔA). The temperature range (ΔA and ΔM) in which these transformations take place is much larger than that in bulk alloys, spanning up to ~80 C°. This is attributed to a combination of two mechanisms. The first is a decrease in grain size (see Chapter 6) and an associated increase in grain boundary area. As stated earlier, this acts to prevent the forward and reverse transformations from occurring, by preventing the transformation propagating from one grain to adjacent grains [104, 201, 208]. Typically in a bulk alloy, as one grain undergoes a phase change, it exerts a force on adjacent grains due to its change in volume, which in turn helps to trigger the phase change in those grains, through a stress-induced transformation. The disordered lattice of the grain boundaries represents an obstacle, so with an increased volume fraction of grain boundary material, the transformation is hindered. The second mechanism is the nucleation and growth of the new phase within each grain. Variations within these grains (such as the size of the grains, number of defects or nucleation sites and slight variations in composition) can result in vast differences in the onset temperature. As the resistance technique samples a large number of grains, the combination of these two properties would act together to create a large ΔM and ΔA for each film.

Decreased hysteresis

While the transformations span a large range of temperatures, it is of particular interest that the forward and reverse transformations exhibit minimal hysteresis (Figure 7.1 and Table 7.1). When comparing the onset, peak and finish of the transformations, the difference between the martensite and austenite transformation temperatures is a maximum of 15 C°. This is much lower than that in the bulk alloys, where the hysteresis width is typically 30 to 70 C°. Similar results were found in the 75 and 50 nm SMA thin films reported in [202], where the hysteresis is completely removed. The hysteresis in bulk SMAs is typically associated with two irreversible forms of energy dissipation. The first is the internal friction generated by the movement of the austenite-martensite interface [211], and the other is the dissipation of stored elastic strain [212]. This friction is caused by the lattice mismatch between the two phases, and results in energy dissipation which is not recovered during the reverse transformation [212]. The frictional force increases with a greater concentration of lattice defects and a greater mismatch between the two phases [211, 213]. The dissipation of the stored elastic strain energy also occurs at the interface of the phases, when the strain associated with the interface is reduced through plastic deformation [212].

The narrow hysteresis in the present films can therefore be attributed to several factors. The first of these is the reduction in friction caused by the movement of the interfacial region between the two phases. The reduction of the grain size has been shown to change the compatibility between the martensite and austenite structure, reducing the mismatch in the lattice [202]. This is achieved through a change in spacing of specific crystal planes within the unit cell that are common to the structures of both phases and results in an increased compatibility between both structures, reducing the energy dissipation due to the friction of the moving interface of transformation. This theory is in line with the generalized non-linear theory of martensitic transformation (GNLTM) [214], where the hysteresis width is dependent on the compatibility (λ_2) between the high and low temperature phases calculated by the formula $\lambda_2 = \frac{b}{\sqrt{(2.a_0)}}$, where b is the lattice parameter of the martensite unit cell, a_0 is the lattice parameter for the austenite unit cell and a zero hysteresis occurs when λ_2 is equal to 1. The narrow hysteresis is also

an indication that there is very little strain in the material that is transforming, as strain would generate more plastic relaxation, resulting in greater energy dissipation and a large thermal hysteresis [212]. As the electrical resistance measurement technique is very sensitive, even small volume fractions of the thin-film undergoing a transformation would produce a signal. It is therefore possible that the signal being produced is only from non-strained crystals. These have a much smaller energy barrier to overcome in order to change from one phase to another, not being subject to the factors governing hysteresis mentioned above. This would leave a section of the film that does not transform as it is constrained by energy barriers such as the strain seen in [202] of the SiO_2 interfacial region. This explains the reduced change in peak positions and intensities of thin films that were scanned in Bragg Brentano XRD at a range of temperatures, as a proportion of the film does not undergo any phase changes.

7.4.5 Effect of Al content on transformation temperature

The relationship between Al concentration and transformation temperature is one aspect of the AuCuAl SMA thin films that is similar to the bulk SMAs. In films which exhibited a clear forward and reverse transformation, it was possible to identify the M_p and A_p as the midpoint between the start and finish of the respective transformations (Figure 7.1). These points are noted in Table 7.1, along with the nominal Al wt.% of each film, and show a clear trend of increasing transformation temperature with decreasing Al content. While these transformations occur at lower temperatures than the bulk, the relationship established in the bulk alloys between increased electron to atom ratio and its effect to decrease the transformation temperature still applies to these thin films. This an important factor when trying to develop these films for future applications.

7.5 Conclusion

Here it has been shown that it is possible to produce thin films of the AuCuAl β-phase with thicknesses as small as 55 nm. Using XRD and electrical resistance measurements, it was possible to identify that a reversible martensite to austenite phase change occurs in some films. This transformation occurs at a much lower temperature than in the bulk due to a reduction in grain size, which also causes the transformation range to increase (as one grain is hindered from interacting with the next). One important property to note in these films is the reduction in hysteresis, which becomes a maximum of ~15°C. Only those films which were austenitic at room temperature (i.e. the films with the higher Al contents) transformed. Transformations were not observable in films that presented a martensite structure at room temperature, which is attributable to a number of possible reasons including induced strain and martensite stabilisation.

Future work should include releasing the films from the substrate and observing any changes in the transformation temperature or response. This would eliminate the constraint of the silicon substrate as a possible cause of the low transformation temperature and small hysteresis. It would also allow the examination of the SME by following changes in curvature of the film when it was heated and cooled. This may also be achieved by depositing onto a dissolvable substrate.

8 Optical Properties of AuCuAl SMA Thin Films and Nanoactuators

8.1 Introduction

There has recently been much interest in plasmonic devices due to their unique optical properties and application in a wide range of areas, such as sensors[115, 215, 216], optical filters [217-219], biomedical and treatment [220-223] and imaging [224]. Most of these applications revolve around tuning the optical properties of the device to respond to specific wavelengths of light and, in the case of sensors or active materials, actively changing the response at these wavelengths when triggered by a stimulus. The resonant frequencies of these plasmonic devices are dependent on four main factors: the dielectric properties of the nanostructure, the dielectric properties of the surrounding medium, and the physical shape and orientation of the nanostructure. For most of the reported active plasmonic devices, a change in the LSPR frequency is achieved by functionalising the nanostructure so that the effective dielectric properties of the medium surrounding the nanostructure are changed when an analyte is bound in close proximity to the nanostructure. A less commonly reported method for producing active plasmonic structures is to base the structure on a material that undergoes a thermally-induced phase change with different refractive indices for the different phases, such as those based on VO_2 [128-131] or Ga [134, 135]. While these methods for achieving active plasmonic materials have been studied (although not extensively), the concept of actively changing a nanostructure's shape to induce a change in the LSPR has received minimal attention. There is however extensive literature on the LSPRs produced in different shapes of static structures, and the effect of orientation of the structure relative to the incoming electromagnetic wave.

In the previous chapters it was shown that it is possible to produce SMA thin films with a thickness of approximately 60 nm with a minimal oxidation layer. In this chapter, the optical properties of these thin films are explored. The optical properties are determined

and used to compute the dielectric function of the material, which is then in turn used as an input into theoretical calculations in order to determine whether the idea of a plasmonic nanoactuator has merit. The properties of a shape-changing plasmonic actuator are then considered in terms of its ability to support a LSPR and to modulate light at sub-wavelength dimensions.

8.2 Experimental

A range of films were deposited with various Al contents across the AuCuAl ternary diagram, as described in Chapters 6, with nominal compositions of Al ranging from 1.5 to 7 wt.%, Au fixed at Au 76 wt.% and the balance being Cu. The films produced exhibited a range of colours depending on the Al content.

Reflection spectra were collected for films of varying Al content using a Varian Cary 50 spectrometer with a Labsphere attachment over a wavelength range of 300 nm to 1100 nm with a slit width of 1 nm. This was used in conjunction with a custom piece of software, written by Prof M.B. Cortie based on the ASTM standard G173 to extract the CIE LAB colour coordinates of these films. Transmission and reflection spectra were also collected using a Perkin Elmer Lambda 950 spectrometer with a universal reflectance attachment over a wider wavelength range of 300 to 2500 nm. These data were then modelled using WVASE32 v 3.486 by Woollam to produce *n* and *k* values for the given wavelengths with the assistance of Dr Angus Gentle.

3D models of simple nano-actuators were generated which simulate different stages of a curled up rod. This was initially proposed as it would be relatively easy to produce a straight-cut rod by using any of several different lithographic techniques. It was proposed that the force of the shape memory effect (SME) would move the actuator through the different stages of conformation (Figure 8.1). The model generated was for a spiral that, when actuated, would unravel into a straight rod, analogous to the 'party blower' or 'paper tongue' sometimes used at celebratory meals. The length of this model was created using the formula $r = a + b\theta$ (polar coordinates) where a = 1 and b is varied between 1000 and 10 to provide different curvature values for the actuator.

Two different sizes of actuator were considered- a small actuator with a thickness and width of 25 nm and length of 150 nm, and a large actuator with a thickness and width of 40 nm and length of 160 nm. These two models were chosen as the calculations for smaller dimensions are faster to run in the computer simulation, whereas larger dimensions would be more easily attainable when actually fabricating a real device. No mechanical modelling (e.g. finite element modelling) was performed. This should probably be carried out in a future phase of the project. As such, the deformations shown below are illustrative only, and may not be fully attainable in real devices.

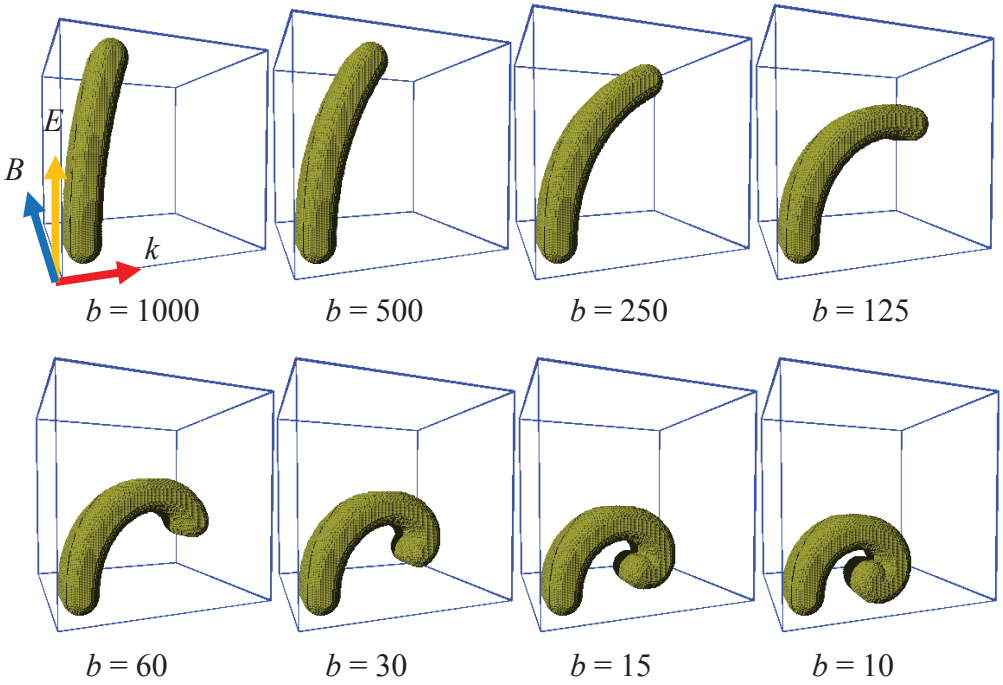

Figure 8.1 Proposed actuator movement positions. Curvature value given below each model. Orientation of incident electromagnetic wave for all simulations shown in $b = 1000$.

Numerical simulations of the optical properties of these actuators were performed using the n and k values from the thin films as well as values obtained from bulk $Au_7Cu_5Al_4$ and Au. The Discrete Dipole Approximation for Scattering and Absorption of Light by Irregular Particles (DDSCAT) software of Draine and Flatau [164] was used to calculate the optical absorption, scattering and extinction coefficient for these nanoscale actuators in the presence of electromagnetic fields in the visible spectrum of light. Simulations

were carried out for different stages of the hypothesised actuation process to observe how the extinction, transmission and absorption coefficients change through the range of motion. The vectors for the incident fields are shown in Figure 8.1. The simulations were run with the target (actuator) having an effective radius of between 35 and 50 nm and a dipole spacing of between 0.92 and 1 nm^3, suspended in vacuum. For the exact values of each model see Appendix B. For more information on the detail of the DDSCAT software see Chapter 3.17.

A custom-written program ('E and B Processor', M. Cortie) was used to visualise the electric fields and hence plasmon modes around the actuator at given frequencies. The resulting data have been visualized as a colour-coded map.

8.3 Results

Figure 8.2 shows the different colours of the deposited films. These differences are created primarily by the varying Al content, and are intrinsic to the alloy being studied. However, thickness of the coating and presence or absence of oxidation has some effect on the colour too. These differences in colour can be quantified by measuring changes of the reflection spectra (Figure 8.3) for the related films and changes in the CIE LAB colour coordinates (Figure 8.4).

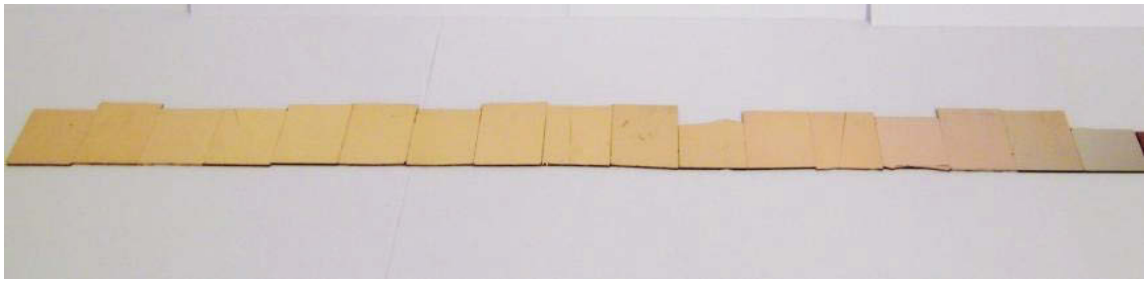

Figure 8.2 Films arranged with increasing Al concentration from a nominal 1.5 wt.% (left) to 7 wt.% (right) and show the change of colour associated with the compositional variation.

The ~100 nm thick films deposited here follow a very similar trend in colour as that observed by Levey *et al*. [33] where bulk AuCuAl alloys were cast with varying compositions. The highest Al content films (γ-phase crystal structure) have a silvery-

white appearance, but as the Al concentration is decreased, the films take on a pinkish hue, with the strongest colour seen in sample Beta 22 (nominal 5.8 Al wt.%). Further decrease in the Al content causes the reddish colour to be bleached, leaving a bright yellow colour. This colour then seems to remain constant, with very little variation seen by eye, through to the lowest Al concentrations. The reflection spectra (Figure 8.3) show this change more accurately, with the highest Al content film (nominally 7 Al wt.%) producing a relatively flat spectrum, reflecting all the wavelengths within the visible spectrum by a similar amount resulting in the silvery-white appearance. As the Al decreases, the samples show a decrease in reflection intensity over the 500 to 600 nm wavelengths, levelling out at smaller wavelengths.

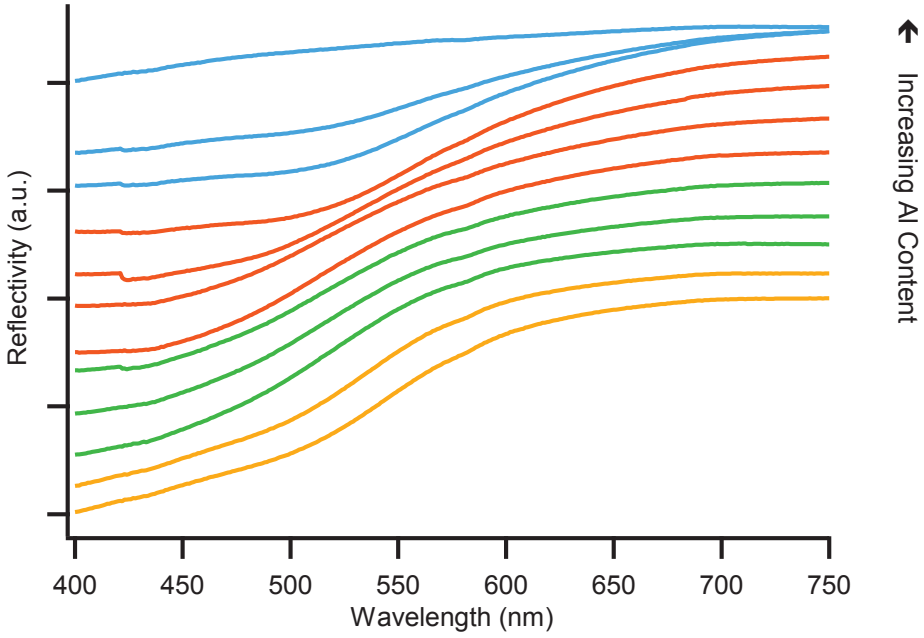

Figure 8.3 Change in reflection spectra with varying Al content films. Reflection spectra offset for clarity, varying from nominal Al concentration of 7 wt.% (top) to 1.5 wt.% (bottom).

Some of these differences are not easily seen by eye, but are much more obvious when the data are converted to colour coordinates and plotted on a CIE LAB colour chart. We can see this change in the (a*,b*) coordinates, Figure 8.4, with the white film (highest content of Al) having small values for both a* and b*[§]. As the Al concentration is *decreased*, these increase until a maximum is reached in the a* coordinate. This

[§] a* indicates the green (negative) to red (positive) colour component, and b* indicates the blue (negative) to yellow (positive) component. A neutral colour has a*=b*=0.

corresponds to the pinkish hue seen in Beta 22 (5.8 Al wt.%). As the Al content is decreased further, the films become more yellow, and the a* values decrease while b* continues to increase. The a* reaches a minimum around the composition-induced transition between the martensite- and austenite-structured films. The LAB co-ordinates of the martensite-structured films are quite tightly grouped and, as the α-phase structure appears in the films, this starts to increase the a* values again as the alloy takes on the classic "red gold" colour of (Au,Cu). These results are very similar to those shown for AuCuAl bulk alloys by Levey et al. [33], Figure 8.5. Their data follow a similar trend, changing directions in the colour space at the same phase boundaries as for the thin-film samples, however their a* and b* values are somewhat greater in magnitude, implying more intense colours. This is most likely due to the fact that the present thin films are partially transparent and therefore do not have as high a reflectance as that for the bulk alloys.

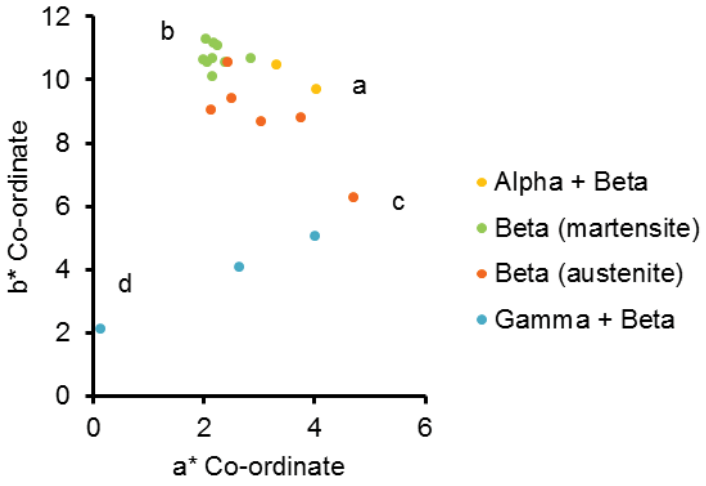

Figure 8.4 a*b* Colour chart of deposited films. Colour variation across depositions with varying nominal Al composition. a—1.5 wt.% Al, b—3 wt.% Al, c—5.8 wt.% Al, d—7 wt.% Al.

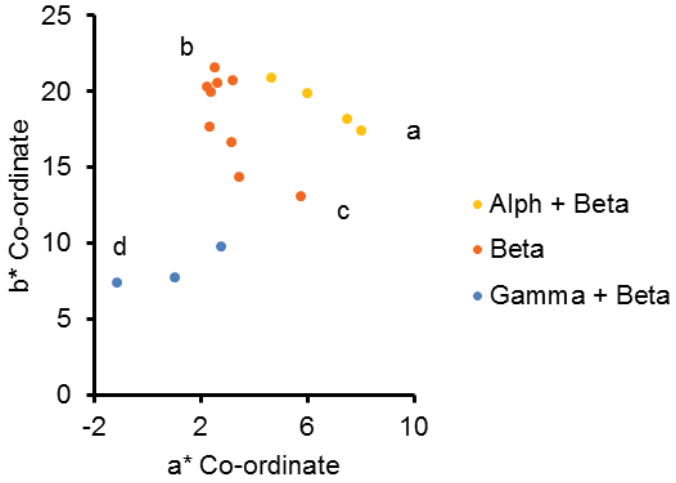

Figure 8.5 a*b* Colour chart from bulk alloys [33]. Colour variation across the76 wt.% Au vertical section; a— 0 wt.% Al, b—3 wt.% Al, c—5.8 wt.% Al, d—7.2 wt.% Al.

Modelling with WVASE 32 was performed on the transmission and reflection spectra of three films, to obtain the respective *n* and *k* values (See Chapter 3 for more details). These specific films (Beta 23 (7 Al wt.%), Beta 22 (5.8 Al wt.%) and Beta 16 (3.5 Al wt.%)) were chosen as they represented the three different colours presented from the deposition series. For the purposes of modelling the SMA actuator, the *n* and *k* values of sample Beta 22 were chosen as this film had a strong β-phase diffraction pattern, and also showed a reversible martensite phase transformation. This was important as the optical properties needed to be collected from a film that would exhibit a shape memory response. It is also worth noting that while a phase transformation would results in a change to the dielectric function, this would most likely create a larger difference in the plasmon resonance between the two states of the shape memory nano-actuator. The other two films were used to identify differences that occur in the *n* and *k* values between different coloured films.

The *n* and *k* data were converted to ε_1 and ε_2 and plotted with values for bulk $Au_7Cu_5Al_4$ [166] and Au [225] for the purpose of comparison (Figure 8.6). It can be seen that ε_2 for the bulk and thin-film SMA has a relatively high value in the visible spectrum compared to that of Au. The value of ε_2 indicates the electrical resistance or "loss" in a material at optical frequencies. The higher ε_2 values would certainly result in the damping of the

LSPR due to higher absorption. The bulk SMA appears to have a smaller ε_2 value than the SMA thin-film (Beta 22) at wavelengths shorter than about 700 nm. Therefore, the thin-film materials are 'lossier' than bulk samples, and both are lossier than pure Au. Nevertheless, as will be shown, they should still be able to support a LSPR in the visible spectrum. The differences between pure Au and alloys are explored further through the means of the extinction coefficients calculated in DDSCAT.

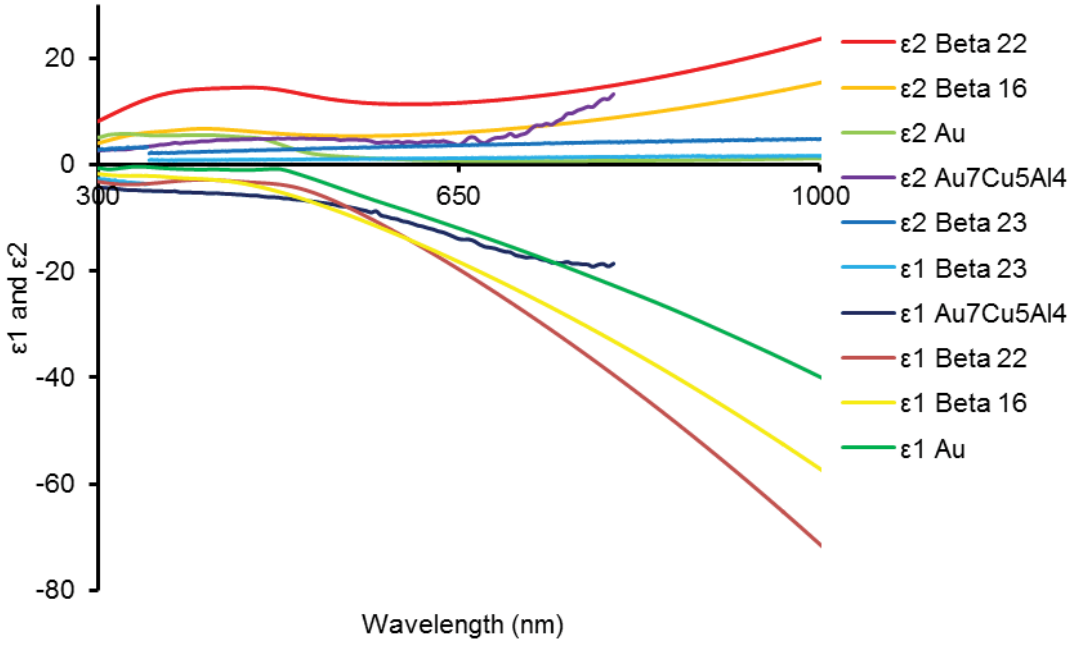

Figure 8.6 Optical ε_1 and ε_2 values for bulk materials and films.

Absorption, scattering and extinction coefficients calculated in DDSCAT for the different actuator models were plotted to show the changes in absorption as the hypothetical actuators change shape. A comparison was made between models which incorporated ε_1 and ε_2 values for pure Au and those that used values for bulk $Au_7Cu_5Al_4$. Of course a pure Au device could not be temperature actuated, and would have to be deformed by an externally-sourced force (such as a bimetallic contact for example). However, it was considered useful to benchmark the calculated optical performance of SMA actuators against that of a pure Au device.

The results of simulations on pure Au actuators are shown in Figure 8.7 and those for bulk $Au_7Al_5Cu_4$ in Figure 8.8. A general trend for all shapes of these actuators is that the Au simulations produced sharp, and well defined resonance peaks. In comparison, the models based on the optical properties of the Beta 22 (5.8 Al wt.%) film show a single, relatively broad extinction peak, Figure 8.9. The 'modulation factors' for each material were calculated by dividing the extinction co-efficient of an actuator in the *b*=1000 position by the extinction coefficients of the other actuator positions.

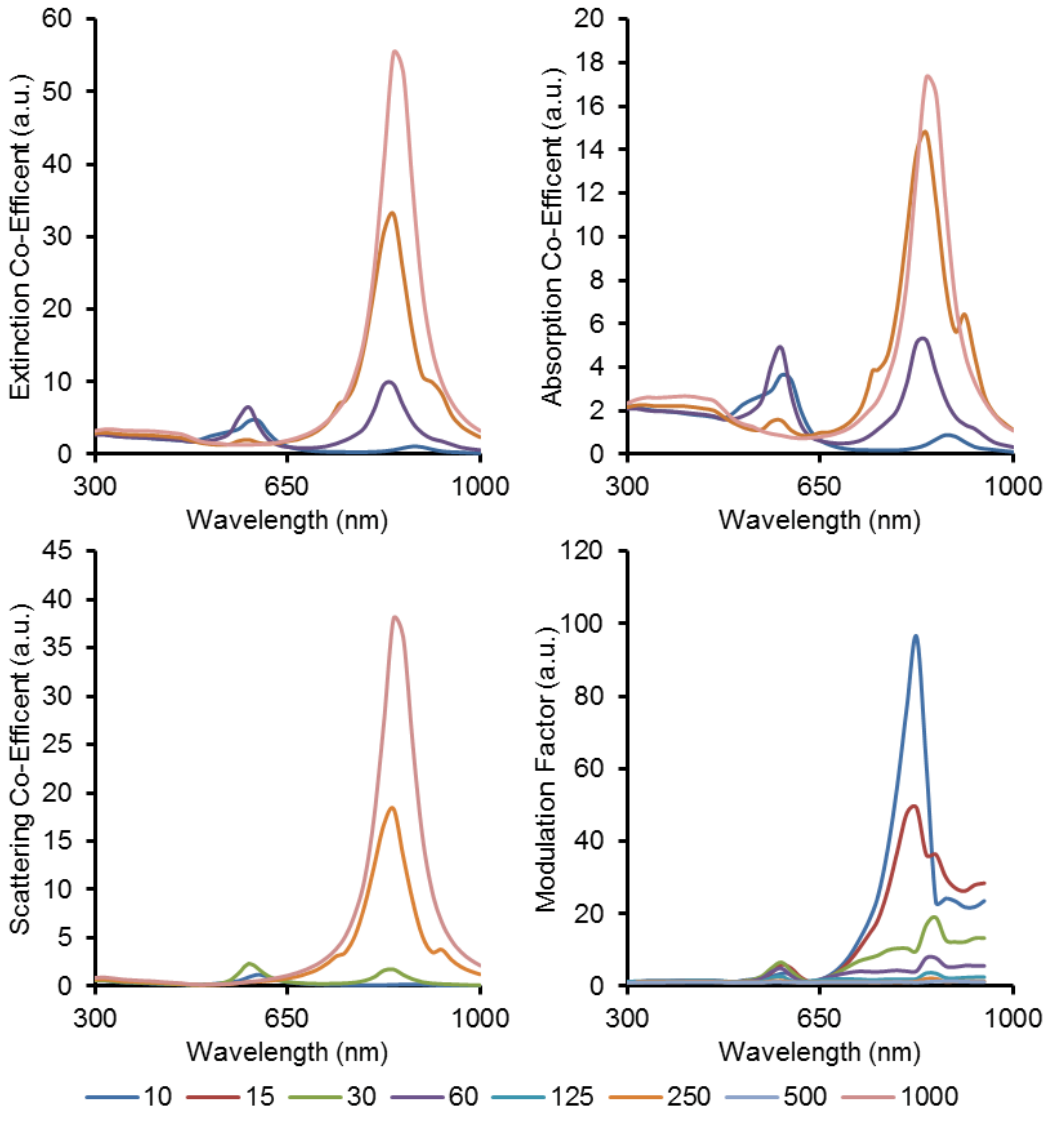

Figure 8.7 Simulated Au extinction (top left), absorption (top right), scattering (bottom left) and modulation factor (bottom right) for different states of proposed actuator conformation. The values of actuator state shown correspond to their respective values of parameter *b*.

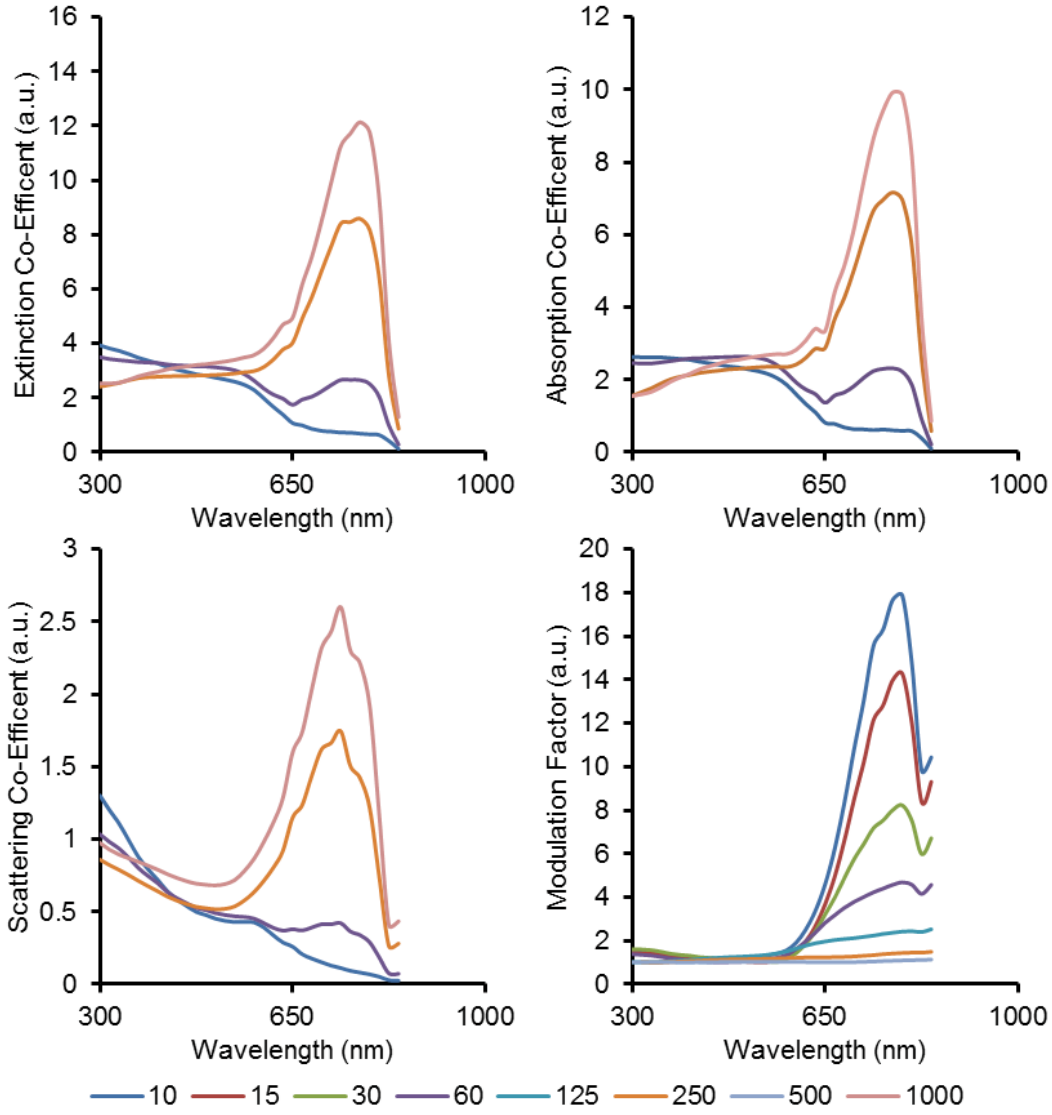

Figure 8.8 Simulated $Au_7Cu_5Al_4$ extinction (top left), absorption (top right), scattering (bottom left) and modulation factor (bottom right) for different states of proposed actuator conformation. The values of actuator state shown correspond to their respective values of parameter *b*.

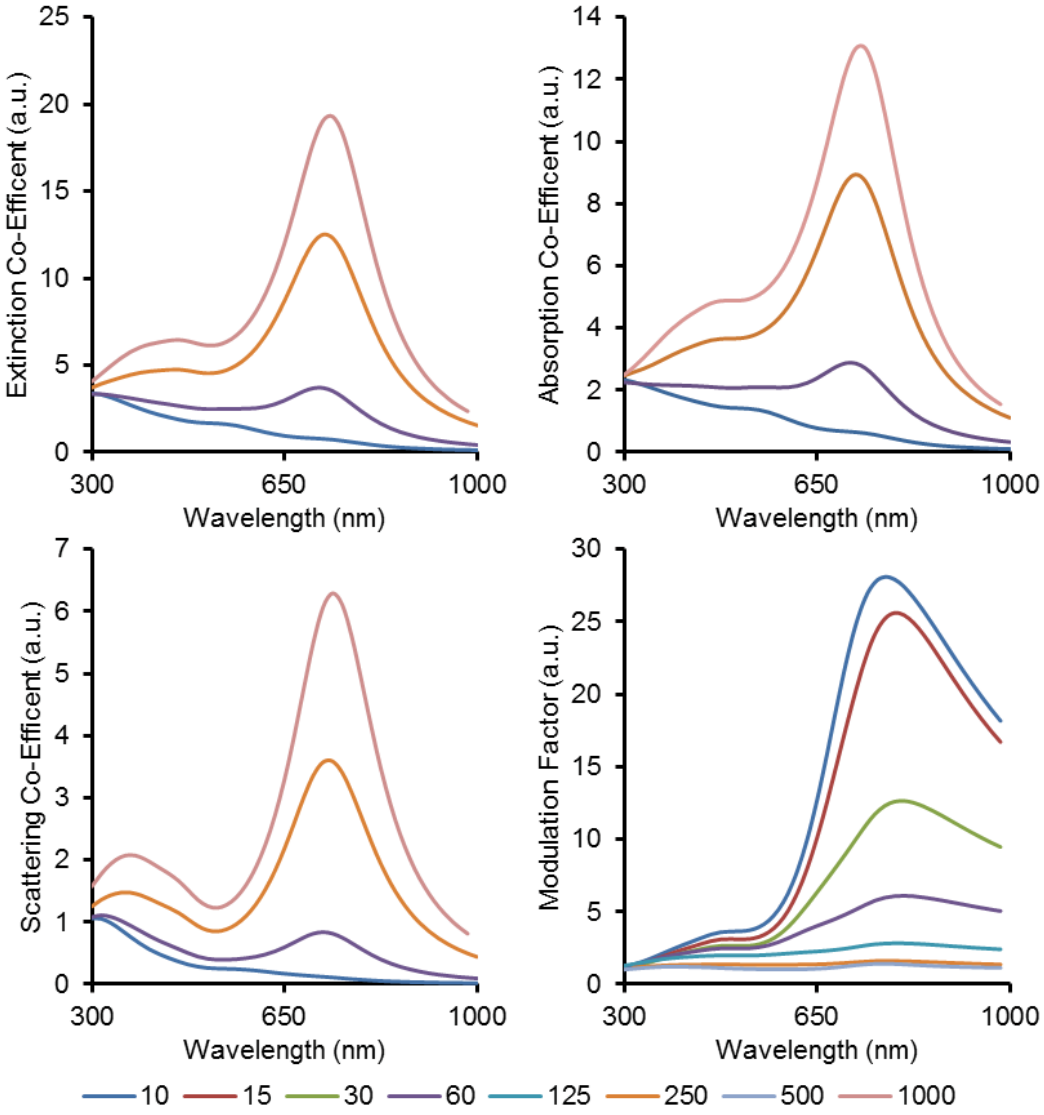

Figure 8.9 Simulated Beta 22 extinction (top left), absorption (top right), scattering (bottom left) and modulation factor (bottom right) for different states of proposed actuator conformation. The values of actuator state shown correspond to their respective values of parameter *b*.

A comparison of the peak extinction, absorption and scattering is also plotted to show more accurately the change that occurs as the actuator passes through different shapes, Figure 8.10.

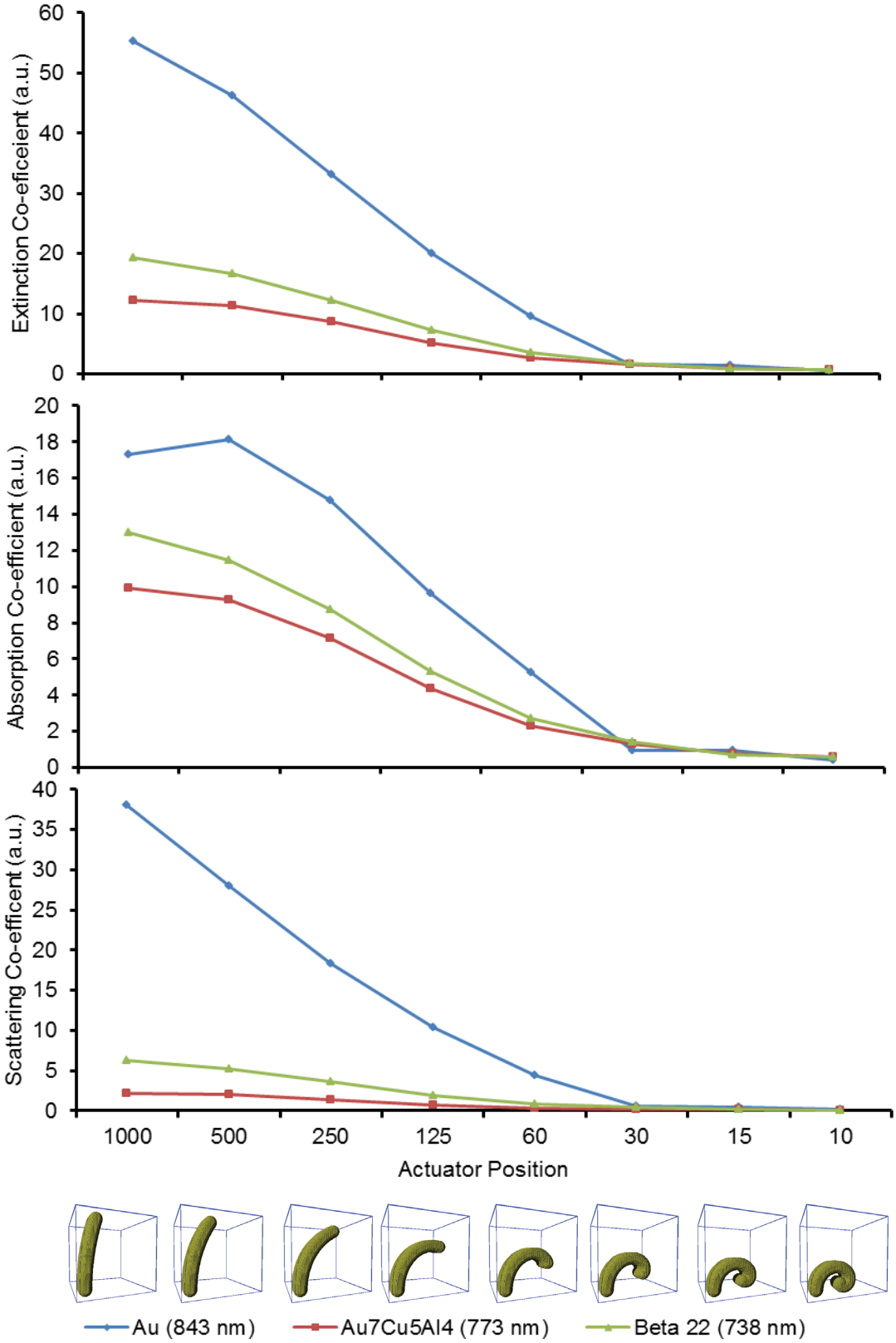

Figure 8.10 Simulated change in peak extinction (top), absorption (middle) and scattering (bottom) through a range of proposed actuations for Au, $Au_7Cu_5Al_4$ and Beta 22 actuators. The values of actuator state shown correspond to their respective values of parameter *b*.

Figure 8.11 shows graphically where in the Au actuator the electric fields due to the plasmonic resonances are being generated, and how these electric fields change as the actuators bend. The colour plot shows the strength and direction (left to right) of the electric field at a certain instant in time, with blue being negative and red being positive values. Two positions within the actuator's movement were chosen - those corresponding to values of the curvature parameter *b* of 1000 and 30, as these show the greatest change in the intensity of the extinction peaks and also have both main plasmon resonance modes found at approximately 850 nm and 580 nm. From the images it is possible to see how the same LSPR is generated in the two different conformations. These data for the electric field were used to produce videos to better visualise the movement (see Appendix C for these videos or at http://www.youtube.com/watch?v=kWJ9270l0wo, http://www.youtube.com/watch?v=RUmcor7UIZo and http://www.youtube.com/watch?v=YncbVE0bIT8).

The b=1000 actuator position behaves likes a straight rod, possessing a single longitudinal LSPR which is localized on the ends of the shape. As the actuator bends, a second resonance peak appears. The electric field maximum/antinode associated with this moves towards the centre of the actuator.

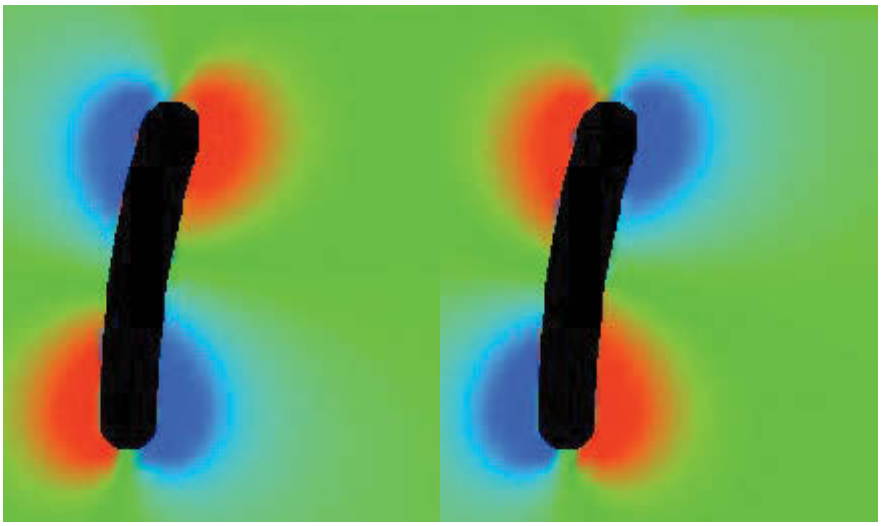

b=1000 actuator illuminated with 851 nm wavelength light

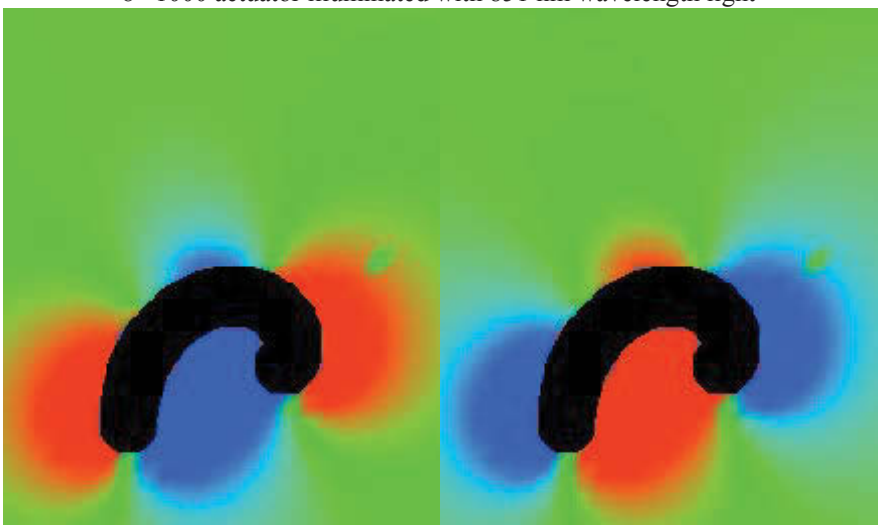

b=30 actuator illuminated with 834 nm wavelength light

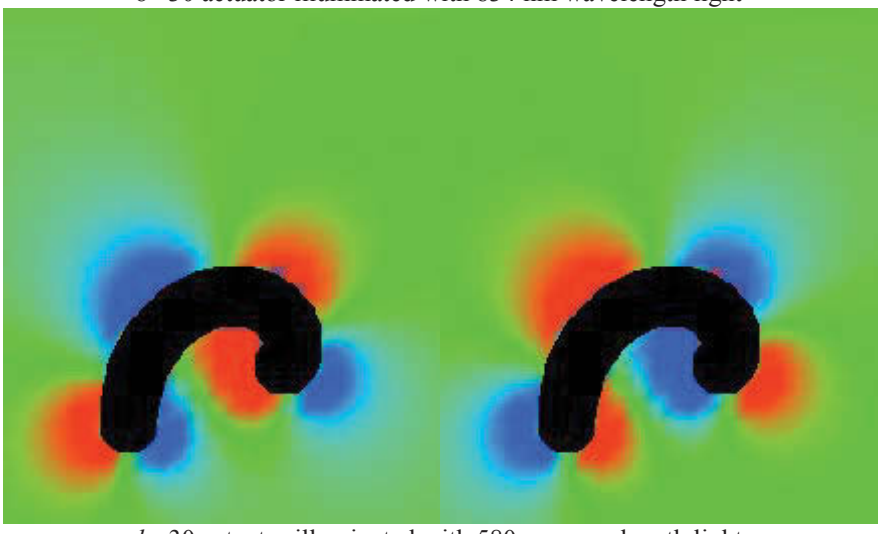

b=30 actuator illuminated with 580 nm wavelength light

Figure 8.11 Imaging of electric field as electromagnetic wave passes through Au actuator from left to right and imaged with wave at angle of 100° (left) and 280° (right). Blue indicates magnitude of field from left to right and red indicates magnitude of field from right to left.

8.4 Discussion

8.4.1 Au actuators

Due to the intrinsic low-loss characteristic of Au, it produces relatively sharp and intense resonance peaks. As the actuator's shape changes, the longitudinal resonance is replaced by new resonance peaks. In the Au model the main (longitudinal) resonance peak for the extended actuator is observed at approximately 840 nm, but as the actuator bends past b=250 (approximately 90°), a resonance peak at 580 nm starts to appear, increasing in extinction up until b=15. One point to note is that the main resonance at 840 nm shifts by approximately 10 nm as it curls, but it was initially expected (compare to Stokes *et al*. [226]), that the resonance would generate a greater shift to smaller wavelengths as the actuator became smaller. This discrepancy is explained by the fact that the aspect ratio of the rod is still maintained; the rod is merely curved and still allows the LSPR to travel the length of the rod as there is no sharp change in angle. Figure 8.11 shows this effect, where the 834 nm electromagnetic waves generate an LSPR along the full length of the curved b=30 rod. This is not seen in rods that are bent at very sharp angles (as studied by Stokes *et al*. [226]), where a sharp change in the LSPR frequency is observed as kinked rods are bent past a certain angular deflection. While the LSPR in the present geometries is able to travel the length of the curved rod, the decrease in intensity of the extinction co-efficient is due to the changed orientation of the electric field through different sections of the rod. As the rod curves, a smaller percentage of the length of the rod is aligned with the electric field which results in the decreased extinction at 840 nm. Similarly the increase in extinction at 580 nm is due to the curved rods possessing a multimode LSPR (with excitation between both ends of the actuator towards the centre). The appearance of a multimode resonance was also observed in the angular, V-shaped rods studied by Stokes et.al [226]. The b=30 and b=250 actuator positions seen in Figure 8.1 show that, as the rod curls up, the top half of the actuator aligns with the electric field which enhances the second half of the resonance generated in this section of the actuator.

The calculated values for extinction show that, when alternating between the full ranges of movement for these actuators, it should be possible for a pure Au actuator of the

design shown to generate a modulation factor of about 95 for light at a wavelength of 842.5 nm. This modulation factor can be used as a benchmark for the actuators made of SMA.

8.4.2 SMA actuators

While the Au-based simulations discussed above do show where the resonances would occur and how they would change, the actual movement required would need to be provided by some form of external force as Au is not a shape memory material. Beta 22 and $Au_7Cu_5Al_4$-based actuators would not require this external force, but would instead rely on their intrinsic SME. However, the calculations show that the individual resonances are harder to resolve in this case. In the rod-like Beta 22 actuator, the longitudinal peak is observed at 730 nm (Figure 8.9). As the actuator curves around, this main extinction peak is reduced in intensity until it is no longer visible above the background. While the disappearance of the longitudinal resonance is similar to the case of an Au actuator, there is no corresponding appearance of the peak due to a multimode resonance at smaller wavelengths. There is a small change in the extinction at 550 nm which might correlate with the 580 nm peak in the Au actuator, but it does not generate as significant a difference above the background. The maximum extinction co-efficient value of the main resonance is not as strong, with a maximum extinction co-efficient of 19 compared to that of the Au actuator of 55. This is due to Beta 22 being a higher loss material, with larger ε_2 values in the visible spectrum. This results in a damping of the main longitudinal extinction peak and an associated reduction in absorption coefficients. As the multi-mode excitation is largely produced by absorption rather than scattering (scattering is the largest contributor in these models for the main longitudinal resonance due to the high ε_2) this eliminates most of the effect of the multimode excitation in these materials.

Similar results are seen in the calculations performed using the dielectric function of bulk $Au_7Cu_5Al_4$ (Figure 8.8), however in that case the main extinction peak is at 770 nm and has a value of 12.1. In these materials the *maximum* modulation factor between the b=1000 and b=10 extinction coefficients is greater than 26 at a wavelength of 738 nm in

the Beta 22 actuator and 17 at 773 nm in the $Au_7Cu_5Al_4$ actuator. (This wavelength was chosen because it was associated with the biggest modulation factor.) While these theoretical values are significantly smaller than the values theoretically obtainable from Au-based actuators, they still show a practical potential to modulate light actively.

8.4.3 Limitations

The graphs in Figure 8.7, Figure 8.8 and Figure 8.9 show large changes in the optical extinctions as the actuator geometry is varied. While these theoretical models have been chosen to move through a large range of motion, as mentioned earlier it is unlikely that these actuators would move to this extent in practice. It is more likely that they would perform over some intermediate range of movement, located well within the two extremes shown in the simulation. Nevertheless, this could still correlate to a significant change in the optical extinction. For example, at a wavelength of 720 nm, a modulation factor of 8.8 is achieved between b=500 and b=30 or at 738 nm a 10.9 times modulation of light is achieved when going between b=1000 and b=30, in the Beta 22 actuators. This is one of the most likely situations as the actuator would be synthesised from a thin-film that is templated or milled with the actuator shape. The initial strain relief would likely cause this material to curl up to a certain extent. When cooled past the martensite transformation the actuator would then straighten out as the strain was accommodated by the martensite structure.

When looking at the practical application of any of the actuators it is important to take into consideration not only the factor of change in the extinction co-efficient (modulation factor) of an individual device but also the aggregated value of an array of devices. In the case of a sparse array, for example, even a large modulation factor may not attenuate the light significantly. In addition, the concept of a modulation factor does not capture all aspects of the problem. When the extinction coefficient drops below 1, there is an increased modulation factor without a significant increase in the absolute difference in the amount of light attenuated. For example in the Beta 22 actuators at 980 nm, the modulation factor is relatively high at 18 times when alternating between b=1000 and b=10, however the absolute difference between extinction coefficients is

only 2.2 (Figure 8.9). A similar modulation factor is also seen at approximately 680 nm however the absolute difference in extinction coefficients is 15. This would result in a much greater difference in the attenuation of an *amount* of light at 680 nm (although the difference as perceived by the human eye would be small).

One other aspect that has not been discussed is the practical issue of developing nano-actuators at this size scale. While these ratios have provided strong resonances in the visible spectrum, producing actuators with dimensions of 150 nm by 25 nm by 25 nm through magnetron sputtering is difficult as many of the defects in the thin films discussed in Chapter 6 are larger than these dimensions. One solution could be to use larger devices. This was investigated here by generating thicker models to see what effect this would have on the extinction co-efficient, and to generate a design of device that would be more feasible to synthesize. These larger actuators were 160 nm by 40 nm by 40 nm. They performed similarly to the smaller ones (Figure 8.12, Figure 8.13, Figure 8.14), however an actuator with a curvature factor of b=10 could not be generated at this thickness, as this would lead to a large proportion of the material curving into itself and hence would be physically unrealistic. While these simulations show the theoretical properties of nano-actuators, no physical actuators were produced to compare the results. Similar studies with other nano particle shapes however have shown good agreement between DDA modelling techniques and physical measurements provided that a sufficiently fine mesh is used and appropriate dielectric data are input [25, 141, 227-229].

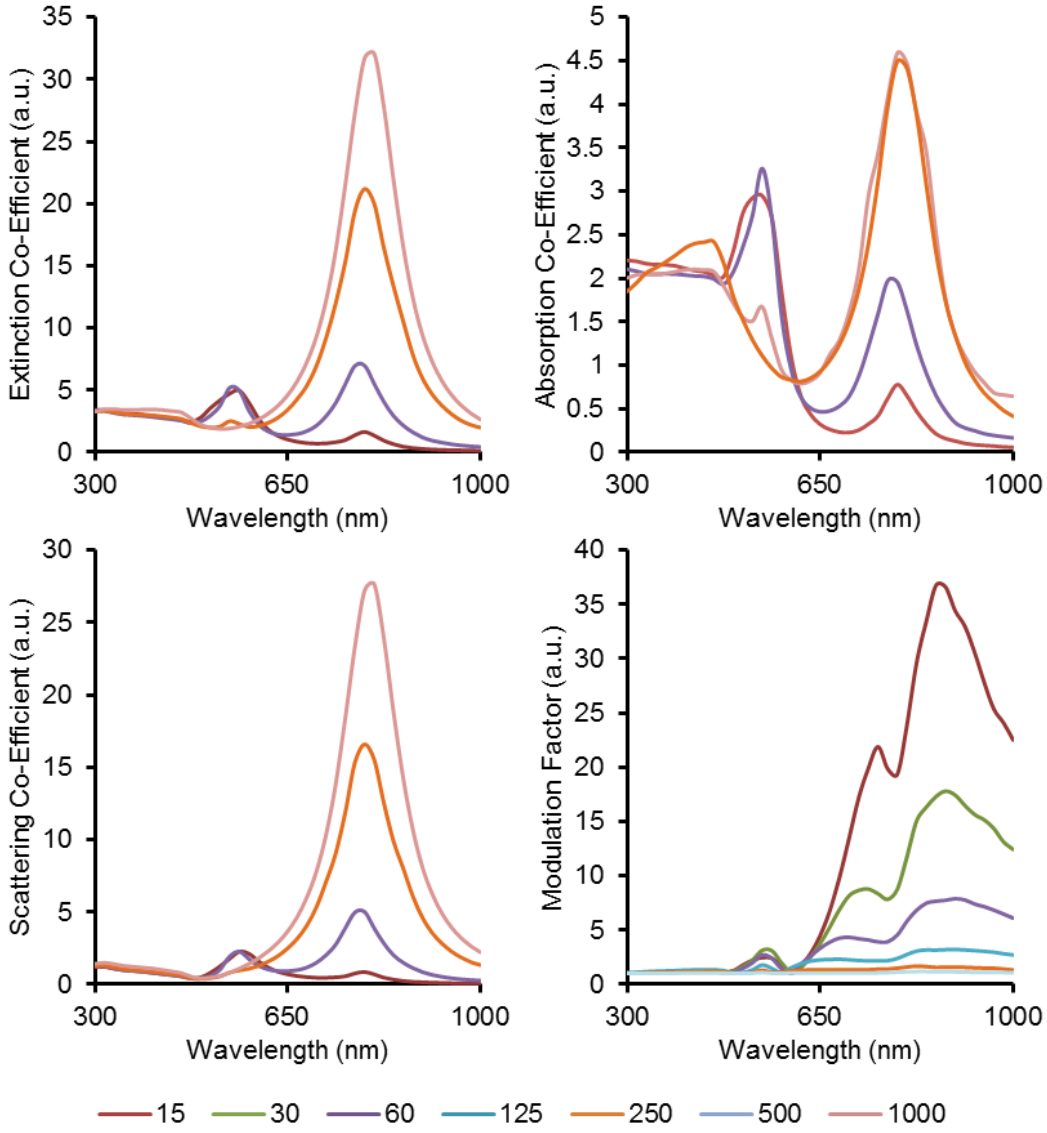

Figure 8.12 Simulated thick Au actuator extinction (top left), absorption (top right), scattering (bottom left) and modulation factor (bottom right) for different states of proposed actuator conformation. The values of actuator state shown correspond to their respective values of parameter *b*.

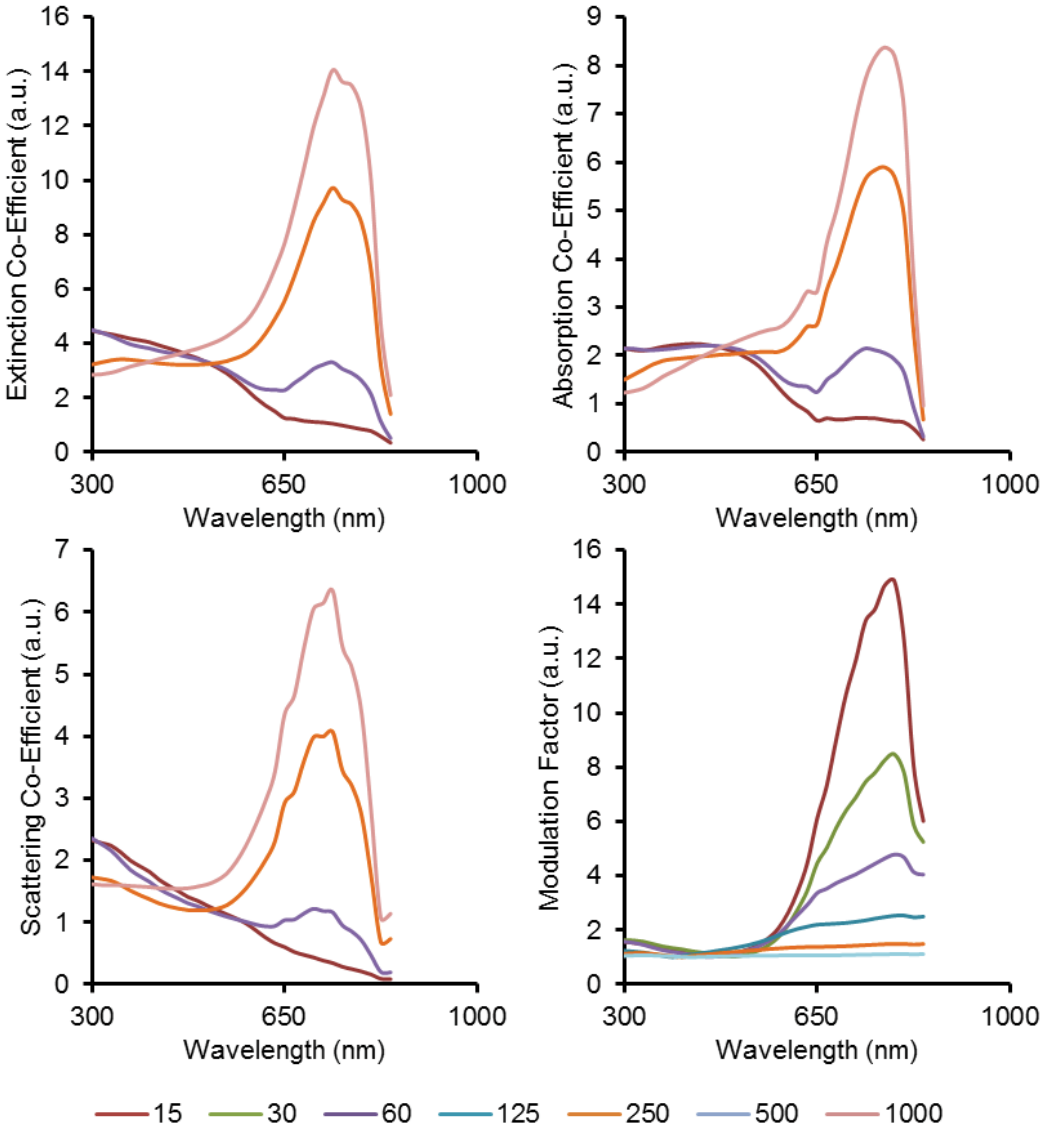

Figure 8.13 Simulated thick $Au_7Cu_5Al_4$ actuator extinction (top left), absorption (top right), scattering (bottom left) and modulation factor (bottom right) for different states of proposed actuator conformation. The values of actuator state shown correspond to their respective values of parameter *b*.

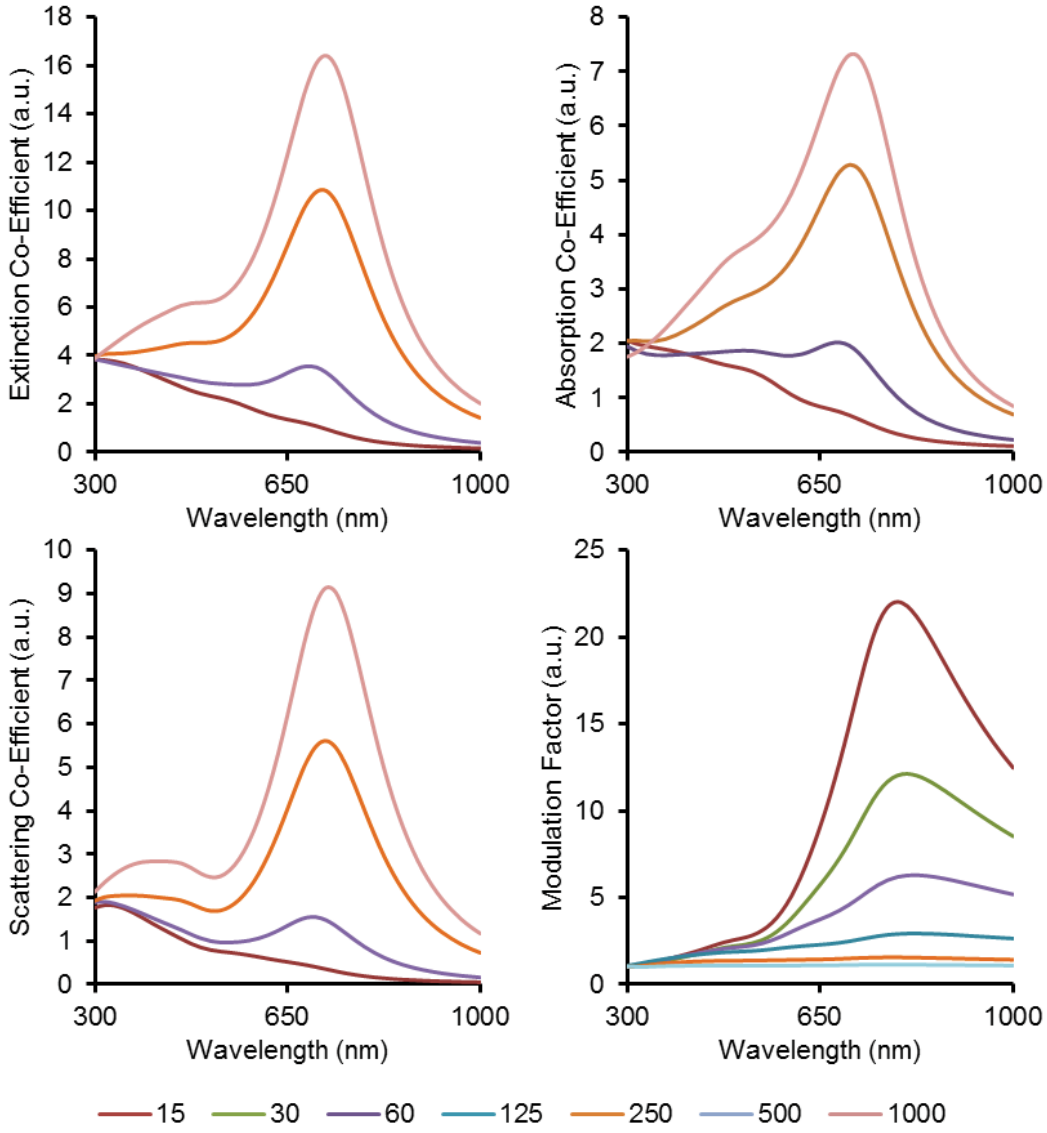

Figure 8.14 Simulated thick Beta 22 actuator extinction (top left), absorption (top right), scattering (bottom left) and modulation factor (bottom right) for different states of proposed actuator conformation. The values of actuator state shown correspond to their respective values of parameter *b*.

One change that was noted in the thicker models was a blue shift of the extinction peaks, due to the decrease in the length to width ratio (i.e. aspect ratio) of the actuator from 6 to 4. This change is more obvious in the Au actuators due to their sharper resonances. One of the most notable differences, however, is the reduced coefficient of extinction seen in the thick Au actuator. At the main peak the extended actuators extinction coefficient is reduced by 44%. This decreased peak intensity also related to a

decrease in the modulation effect with a maximum modulation of 36 times between b= 1000 and b=15.

However, in the case of the Beta 22 actuator, the extinction decreases by only 14%, changing the modulation factor of the b=1000 to b=15 transition from 25 to 22 times. The larger sized $Au_7Cu_5Al_4$ actuator, however, does not follow this same trend, as the maximum extinction co-efficient is increased rather than decreased. This changing trend can be attributed to an increase in the scattering co-efficient of the larger Beta 22 and $Au_7Cu_5Al_4$ actuators. In the Au actuator the increased size results in a 74% decrease in the absorption co-efficient and a 27% decrease in the scattering co-efficient, however this is not the case for the SMA actuators. In the Beta 22 and $Au_7Cu_5Al_4$ actuators there is a decrease in the absorption of 44% and 15.5% from the peak absorption respectively but the scattering actually shows an increase of 45% and 44% from the peak scattering respectively. This increased scattering accounts for the reduced change in extinction coefficient of the large actuators and is attributed to the extinction coefficient of the more lossy material being largely contributed to by scattering, rather than the dominant absorption contribution that is predicted to occur in the thinner actuator design. As the extinction coefficient in larger particles is mainly contributed by scattering [230], materials with a low loss will produce a smaller extinction in larger particles.

8.4.4 Alternate designs and practical applications

The actuator described here would be one of the simplest moving devices to be synthesized from a thin film; however the principles could be applied to other actuator designs. One potential design would be a spring-shaped actuator that would extend or contract out of the plane of the thin film. While there is an endless number of possible designs for opto-mechanical actuators, the greatest change in the extinction occurs when the longest axis of the actuator is parallel and perpendicular to the electric field. This is an important aspect which should be considered in order to maximise the efficiency of the design.

One practical application for these types of actuators would be to modulate transmitted light based on a temperature change. As shown above, the change in extinction coefficients can be quite large, and this also relates to a significant difference in the amount of light expected to be transmitted by an array of such devices. The extinction values from the large size actuators were used to simulate the effect of an array of these actuators in two orthogonal orientations relative to the polarization of incoming light and with a void space of five times the actuator size, with approximately a 90 nm space (visualised in Figure 8.15). For the Au actuator, two values were used for the concentration of actuators covering the film, as the layout given in Figure 8.15 provided values with no transmission for wavelengths between 800 and 930 nm. A lower concentration was also simulated.

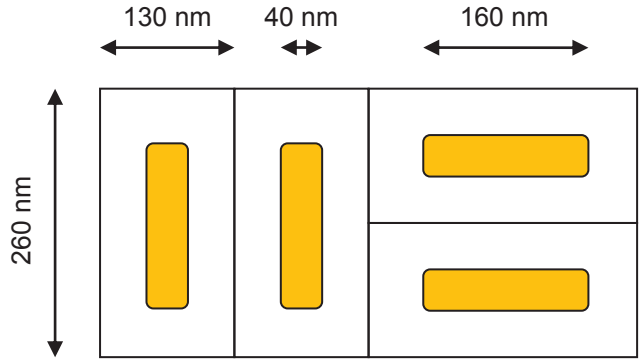

Figure 8.15 Proposed actuator orientations in a hypothetical array.

The simulated transmission spectra for b=30 and b=1000 actuator geometries are given below (Figure 8.16) and show a peak change at 720 nm, varying from approximately 90% transmitted light to less than 5% when alternating between the two shapes. This is an optimal result and shows that in the tightly curled position the average transmission of visible light is approximately 80%.

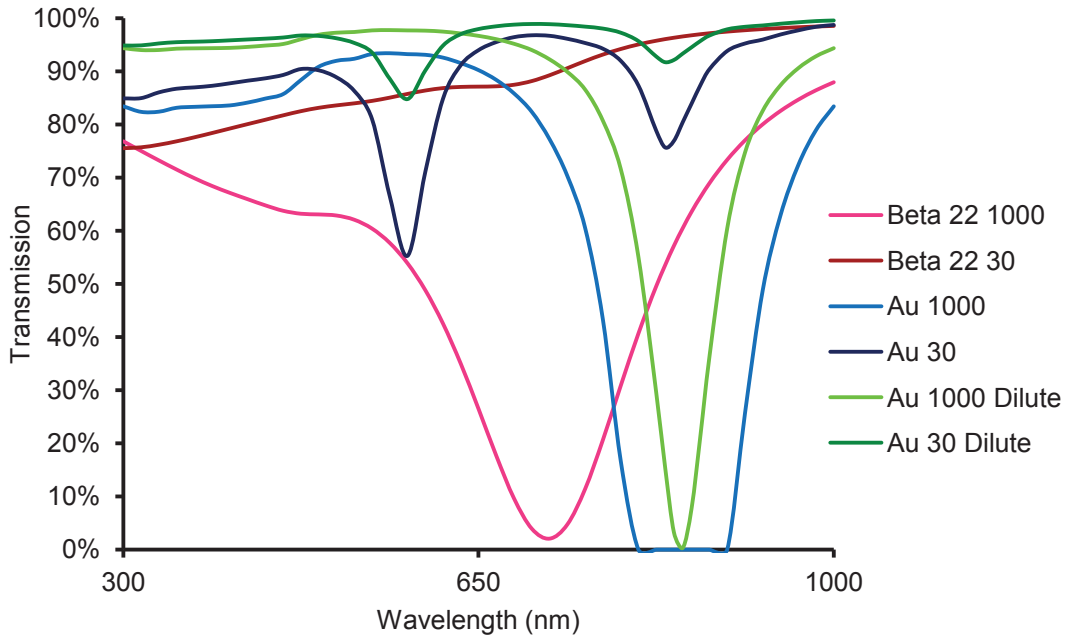

Figure 8.16 Simulated transmission spectra for array of nano-actuators.

The effect of this on a window coating would be quite evident to the human eye, with a colour change as represented in Figure 8.17. The value for the percentage of transmitted solar light (Sol value) is written next to the perceived colour. This does show some variations, where the perceived colour or transmitted light seems to fade or decrease but the 'Sol value' increases, for example in the Au actuators. This is due to the fact that the amount of visible light being transmitted is increasing when going from the tight curled actuator to the straight actuator, however light being transmitted in the near infrared region decreases significantly. The overall effect is to decrease the total transmitted solar radiation.

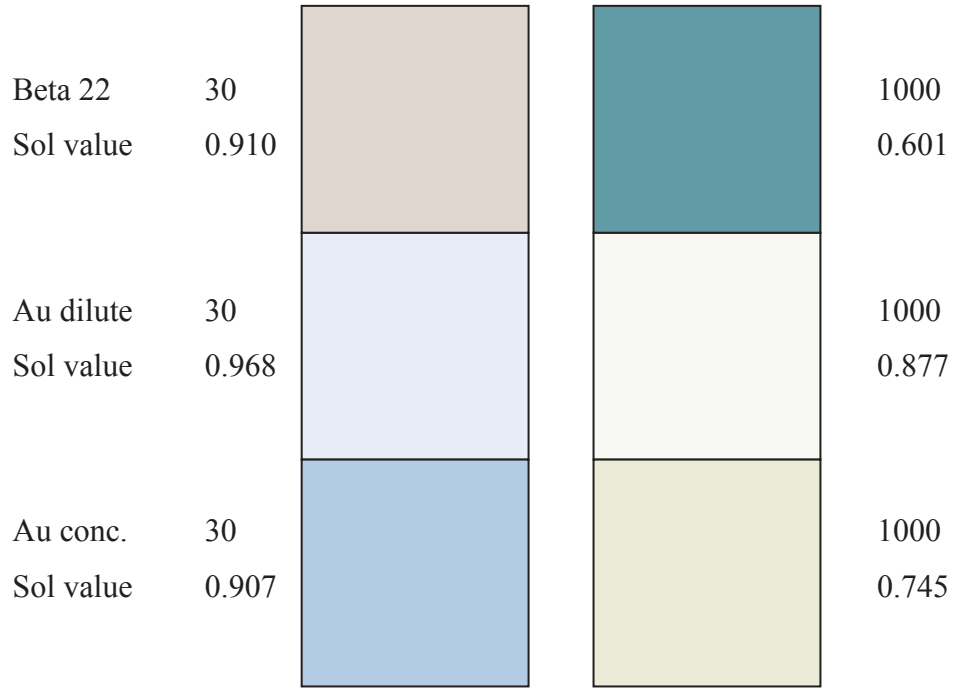

Figure 8.17 Simulated colour change for an array of nano-actuators. Left column shows simulated colour for actuators with *b*=30, right column shows simulated colour for actuators with *b*=1000.

The initial extinction values for these actuators were simulated in a vacuum for the sake of computational simplicity. A glass substrate was NOT used in the calculations due to the very large number of dipoles that would be required - more than a typical PC could handle. However, the main consequence of locating these hypothetical devices on the surface of a higher refractive index medium such as glass would be to red-shift the resonance. In the case of an active window coating, this red shifting of the resonances would actually be beneficial as it would attenuate more of the heat transferred at the wavelengths of the near-infrared. It is also possible to tune the actuator geometry so that it modulates more of the infra-red spectrum by changing the aspect ratio of the actuator. This would also change the response of the extinction co-efficient and is an area for future research.

With such a significant attenuation of specific wavelengths of light, the possible applications of these actuators could be increased through the use of electrical resistance heating. This would allow more precise control over the modulation, as opposed to merely through changes in the ambient temperature. However, at present the major

limitation for practical applications lies in the problem of finding a means of mass production of these actuators. Currently the actuators could be produced through lithography, electron beam chemistry or FIB milling. Unfortunately, the size scale on which these can be produced is relatively small, and the cost of production is exceedingly high. Nevertheless, small-scale arrays of these actuators might have possible applications in the attenuation of spot sources of light such as lasers or as a feedback system for small sensors.

As stated previously, this effect is very sensitive to the alignment of the actuators with respect to the electric field of the incident photons. Due to this, if the actuators were aligned in only one orientation the effect would be to modulate only one plane of polarisation of the incoming light. This would result in a higher modulation factor for that specific polarization compared to an array of random or mixed orientation due to the increased packing density that is possible.

One small-scale practical application of these actuators is in NEMS, where nano-manipulators may require individual or small groups of the actuators to manipulate other nanoscale objects. This would require further investigation into the work and force output of these devices and does not necessarily involve their optical properties. Similarly, micron-sized actuators would also be possible. By scaling up the thickness and dimensions, a range of MEMS actuators could be developed. The use of NiTi SMA thin films in MEMS has already been widely explored [11, 14, 90, 105, 112, 170, 231-234] (see Chapter 2.2.6) however this material still has oxidation and temperature limitations that are not present in AuCuAl SMA actuators. Most of the existing actuator designs based on TiNi (such as micro valves and pump, micro grippers, and micro switches) may therefore be transferable to the AuCuAl SMA. Fabrication cost should dwarf the value of the raw materials used so it could be viable to use the precious metal-based alloy.

8.5 Conclusion

The simulations performed here show that, while an actuator of these dimensions may be on the limit of current fabrication techniques, it would certainly produce a significant change in the extinction coefficient of light. This area of research has not been pursued to the knowledge of the writer, with most of the focus in the prior literature on materials which change the dielectric properties of either the surrounding medium or the particle itself. Alternating between two different conformations would cause a significant effect on the transmission of light within the visible spectrum, and shows promise for use in modulation in the near infra-red region as well. Further research should be considered on the fabrication and real-world optical response of AuCuAl nano-actuators.

9 Overall Conclusion

The work presented here has focused on the AuCuAl shape memory alloy (SMA). The properties of the bulk material have been studied extensively, focusing on the effect of composition on structure and phase relationships, and the alloy's unique resistance to the phenomena of 'martensite stabilization' and aging. After these properties had been well established, an effort was made to produce thin films across the AuCuAl ternary diagram in an attempt to produce films that exhibited the characteristic properties of the SMA. The optical properties of these films were then measured and used to simulate the change in the localised surface plasmon resonance (LSPR) of nano-actuators as they changed shape.

9.1 Bulk AuCuAl SMAs

A series of AuCuAl alloys were cast along the ~80 wt.% Au line on the ternary diagram with various Al concentrations. These samples all comprised at least 80 vol.% β-phase. This was important as it is the β-phase that has the desired SMA properties. The shape memory properties of the alloys were tested using DSC and the effect of composition and electron-to-atom (*e*/*a*) ratio established. Increasing Al content (equivalent to an increasing *e*/*a* ratio) decreased the transformation temperature. The minimum austenite transformation temperature was about 80°C, with the martensite transformation temperature being about 50 to 70ºC lower. High Al content also resulted in a smaller difference between the first and second austenite transformations, a factor which indicates a suppression of aging in the alloy.

The changes in site occupancy for these alloys were also investigated. This showed that in the austenite $L2_1$ structure the A, B and C sites of the A_2BC stoichiometry are mainly occupied by Au, Al and Cu respectively. In lower Au and Al content alloys there is an increased occupancy of Cu on the A and B sites respectively.

The martensite structures of these alloys presented a range of different diffraction patterns, depending on the composition of the alloys and the temperature to which they had been cooled. By looking at the β-phases of the four alloys synthesised here, as well as two other alloys with similar composition, it was possible to group the diffraction patterns into three possible crystal structures. Samples at the low Al wt.% (2.64 to 3.58 Al wt.%) end of the β-phase formed an orthorhombic structured martensite. Increasing the Al content to between 4.36 and 4.96 Al wt.% produced a lower symmetry monoclinic martensite. In the highest Al wt.% samples (5.26 to 5.79 Al wt.%) both a monoclinic and orthorhombic martensite were present, however cooling in liquid N_2 resulted in conversion of the monoclinic martensite present to the orthorhombic structured martensite. This shows that, depending on the composition, temperature and thermal history, different martensite structures may form. This is a analogous to the Ti- and Cu- based SMAs.

Samples of the $Au_7Cu_5Al_4$ alloy were used to test the extent to which these materials can resist aging. The alloy retained shape memory properties after high temperature cycling up to 450°C, while showing neither decomposition nor significant changes in the transformation temperature. Cycling the alloy at any temperature between 140 and 450ºC produced similar results with no permanent change in the transformation temperature and only a small variation in the second austenite transformation temperature. Surprisingly however, aging below 140°C resulted in a significant decrease of both the martensite transformation temperature and the second austenite transformation temperature. There was an isothermal aspect to this effect: aging the alloy for prolonged periods of time at 90°C resulted in an increasing depression of the subsequent transformation temperatures. This aging was not permanent however and aging at room temperature for 18 hours reset the austenite transformation temperature to 80°C. The mechanism of this peculiar low temperature aging was investigated. The common aging mechanisms such as SC-SRO, removal of anti-site defects and quenched in vacancies, and the formation of precipitate phases were eliminated as explanations as they seemed unable to account for the observed facts. This left changes in elastic stress to be the most probable mechanism, driven by movements (relaxation) below the scale of individual laths. This was validated with changes in XRD peak intensity of a static

sample aged *in-situ*. No observable movement in laths aged under Nomarski interference was seen indicating that the mechanism was sub-microscopic.

9.2 AuCuAl Thin-film SMAs

Using DC magnetron sputtering with an alloyed AuCu (58 at.% Au) target and an Al target it was possible to produce a range of AuCuAl thin films under 100 nm with well defined crystal structures. It was shown that the AuCuAl ternary phases α, β and γ were produced. These films exhibited sensitivity to oxygen contamination during deposition. The oxygen removed Al from the composition of the metallic phase, both shifting the crystal structure to that of a phase of lower Al content and broadening the powder diffraction patterns. Ideal deposition conditions were noted and a calibration table was made so as to allow for future synthesis of the desired phase (Table 6.7).

Thin films that exhibited β-phase (austenite) powder diffraction patterns were tested for the reversible austenite to martensite phase transformation, which is indicative of shape memory alloys. Using *in-situ* XRD and electrical resistance measurements, this diffusionless phase transformation was observed at cryogenic temperatures in films which had an austenite structure at room temperature. This is a much lower transformation temperature than that of the bulk alloys. Other differences between the thin-film and bulk alloys include a reduced hysteresis and an increased range in temperature between the initial and final transformation temperature. Films that had a martensite structure at room temperature did not transform when heated. This was attributed to a number of possible factors including a reduced shape memory effect in alloys with lower Al content, post-deposition oxidation, martensite stabilisation or induced strain.

The optical properties of these films were measured from their transmission and reflection spectra, so as to show quantitatively the changes in colour that occur as the Al content varies across the 86 wt.% Au line of the AuCuAl ternary diagram. This colour change follows a similar trend to that of the bulk alloys found by F. Levey *et al*. [33]. Of particular interest were the n and k (or, equivalently, the ε_1 and ε_2) values for the

films which exhibited a shape memory transformation. Reflection and transmission data were used to model the dielectric function which could be used to simulate the optical properties of nanostructures made from this film. A theoretical actuator was proposed that would curl up/stretch out under the force of the shape memory effect. The plasmonic response of these actuators was then modelled for different positions using the optical constants of Au, a bulk $Au_7Cu_5Al_5$ shape memory alloy and an AuCuAl shape memory alloy thin film. The simulations showed that a significant change in the extinction coefficient should occur in all three materials, as the hypothetical actuator passed through its range of motion. While the Au actuator presented the largest extinction co-efficient due to it being less lossy than the other materials, this would require an external force to provide the movement within the actuator, as Au does not possess shape memory properties. However, the sharp extinction peaks in the Au actuator were helpful when identifying the modes of the plasmonic resonances. The straight actuator had a single extinction peak due to a resonance that oscillates the whole length of the actuator (i.e. a 'longitudinal resonance'). As the actuator begins to bend, this resonant intensity decreases due to the misalignment with the electric field. A small resonance peak also begins to appear at a smaller wavelength which is generated by a multipole resonance between the two ends of the actuator, towards the centre. This extinction peak increases in intensity as the top half of the actuator aligns with the electric field. One important property of these actuators is that, as the actuators bend, the main longitudinal resonance peak does not undergo a significant shift in wavelength. The is probably due to the fact that electromagnetic oscillation that causes the resonances can travel the entire length of the actuator even as it changes shape due to the gentle curve in the actuator.

Compared to pure gold, the shape memory alloy actuators have a more muted response. This is due to the higher ε_2 value of these materials, causing the extinction peaks to be much broader and suppressing the multimode resonances. However, a significant modulation of light is still observed in longitudinal excitation. In addition, this broad extinction peak is actually more favourable for modulation of light over a range of wavelengths and could therefore be more suitable for use in a device that modulates white light.

After understanding the properties of the bulk AuCuAl SMAs it was shown that it is possible to produce this material in thin films of approximately 55 nm while still retaining the austenite to martensite transformation. This material is a good candidate for an opto-mechanical nanoactuator as simulations show that it can support a surface plasmon in the visible and near infrared region, and that it is able to significantly modulate light at these wavelengths as it changes shape.

9.3 Future Work

The work presented here lays the foundation for the next stage of our research group's quest to design and build devices based on AuCuAl shape memory alloy nanoactuators. The next step would be to use e-beam chemistry, ion beam milling or a lithographic technique to "cut" these simple actuators out of a deposited film. Once detached from the films, cooling and heating these actuators in an electron microscope would show their physical response and the extent to which they demonstrate a reversible shape memory effect. This could be followed with dark field optical microscopy to obtain scattering spectra from single devices. Further work could look at improving these properties and possible variations in Au content to change the transformation temperature while retaining the shape memory properties.

10 References

1. Cai, W., X.L. Meng, and L.C. Zhao, *Recent development of TiNi-based shape memory alloys.* Current Opinion in Solid State & Materials Science, 2005. **9**(6): p. 296-302.
2. Chopra, I., *Review of state of art of smart structures and integrated systems.* Aiaa Journal, 2002. **40**(11): p. 2145-2187.
3. Es-Souni, M. and H. Fischer-Brandies, *Assessing the biocompatibility of NiTi shape memory alloys used for medical applications.* Analytical and Bioanalytical Chemistry, 2005. **381**(3): p. 557-567.
4. Otsuka, K. and X. Ren, *Physical metallurgy of Ti-Ni-based shape memory alloys.* Progress in Materials Science, 2005. **50**(5): p. 511-678.
5. Fu, Y.Q., et al., *On the lower thickness boundary of sputtered TiNi films for shape memory application.* Thin Solid Films, 2006. **515**(1): p. 80-86.
6. Urbano, S., et al., *Martensite ageing effects in Au7Cu5Al4.* Scripta Materialia, 2005. **52**(4): p. 317-321.
7. Wolff, I.M., *Spangold: a new aura for intermetallics.* Endeavour, 1995. **19**(1): p. 16-19.
8. Kasper, E.P., *Shape Memory Materials: Constitutive Modeling and Finite Element Analysis*. 1997, University of California, Berkeley: Berkeley. p. 191.
9. Wei, Z.G., R. Sandstrom, and S. Miyazaki, *Shape-memory materials and hybrid composites for smart systems - Part I Shape-memory materials.* Journal of Materials Science, 1998. **33**(15): p. 3743-3762.
10. Corti, C.W., *Technology is irrelevant to Jewellery Design—or is it?* The Santa Fe Symposium on Jewelry Manufacturing Technology, 2003: p. 455-467.
11. Sreekumar, M., et al., *Critical review of current trends in shape memory alloy actuators for intelligent robots.* Industrial Robot-an International Journal, 2007. **34**(4): p. 285-294.
12. El Feninat, F., et al., *Shape memory materials for biomedical applications.* Advanced Engineering Materials, 2002. **4**(3): p. 91-104.
13. Barras, C.D.J. and K.A. Myers, *Nitinol - Its use in vascular surgery and other applications.* European Journal of Vascular and Endovascular Surgery, 2000. **19**(6): p. 564-569.
14. Fu, Y., et al., *TiNi-based thin films in MEMS applications: a review.* Sensors and Actuators A: Physical, 2004. **112**(2-3): p. 395-408.
15. Bellouard, Y., *Shape memory alloys for microsystems: A review from a material research perspective.* Materials Science and Engineering: A, 2008. **481-482**: p. 582-589.
16. Adams, T.M., et al., *NiTi shape memory alloy thin films deposited by co-evaporation.* Materials Letters, 2005. **59**(10): p. 1161-1164.
17. Huang, W.M., et al., *Micro NiTi-Si cantilever with three stable positions.* Sensors and Actuators A: Physical, 2004. **114**(1): p. 118-122.
18. Muralt, P., et al., *Piezoelectric Thin Films for MEMS*, in *Encyclopedia of Materials: Science and Technology*. 2001, Elsevier: Oxford. p. 6999-7008.

19. Fu, Y., et al., *Characterization of TiNi shape-memory alloy thin films for MEMS applications.* Surface and Coatings Technology, 2001. **145**(1-3): p. 107-112.
20. Ohta, A., et al., *Novel fabrication technique of TiNi shape memory alloy film using separate Ti and Ni targets.* Sensors and Actuators A: Physical, 2000. **86**(3): p. 165-170.
21. Zorman, C.A., et al., *New developments in MEMS using SiC and TiNi shape memory alloy materials.* Current Opinion in Solid State & Materials Science, 1997. **2**(5): p. 566-570.
22. Miyazaki, S. and K. Nomura. *Development of perfect shape memory effect in sputter-deposited Ti-Ni thin films*. in *Micro Electro Mechanical Systems, 1994, MEMS '94, Proceedings, IEEE Workshop on*. 1994.
23. The-British-Museum. *The Lycurgus Cup*. Highlights 25/08/2011].
24. Newhouse, R.J. and J.Z. Zhang, *Optical Properties and Applications of Shape-Controlled Metal Nanostructures Reviews in Plasmonics 2010*, C.D.D. Geddes, Editor. 2012, Springer New York. p. 205-238.
25. Kelly, K.L., et al., *The optical properties of metal nanoparticles: the influence of size, shape, and dielectric environment.* The Journal of Physical Chemistry B, 2003. **107**(3): p. 668-677.
26. Sosa, I.O., C. Noguez, and R.G. Barrera, *Optical properties of metal nanoparticles with arbitrary shapes.* The Journal of Physical Chemistry B, 2003. **107**(26): p. 6269-6275.
27. Raghavan, V., *Al-Au-Cu (Aluminum-Gold-Copper).* Journal of Phase Equilibria and Diffusion, 2008. **29**(3): p. 260-261.
28. Bhatia, V.K., et al., *The aluminium copper gold ternary system.* Gold Bull., 2009. **42**(3): p. 201-208.
29. Bhatia, V.K., et al., *New Shape-Memory Compositions in the $Au_{2-x}Cu_{1+x}Al$ ($0<x<2$) β-Phase*, in *33rd Annual Condensed Matter and Materials Meeting*. 2009, Australian Institute of Physics: Wagga Wagga. p. F8.
30. Bhatia, V.K., et al., *Ternary [beta] and [gamma] phases in the Al-Au-Cu system at 750 °C.* Journal of Alloys and Compounds, 2009. **488**(1): p. 100-107.
31. Fumagalli, L., et al., *Thermoelastic martensitic transformation in Au–Cu–Al alloys doped with Co or Ir.* Journal of Alloys and Compounds, 2007. **433**(1-2): p. 332-337.
32. Levey, F.C., M.B. Cortie, and L.A. Cornish, *Determination of the 76 wt.% Au section of the Al-Au-Cu system.* Journal of Alloys and Compounds, 2003. **354**(1-2): p. 171-180.
33. Levey, F.C., M.B. Cortie, and L.A. Cornish, *Hardness and colour trends across the 76 weight % Au section of the Au-Cu-Al system.* Scripta Materialia, 2002. **47**: p. 95-100.
34. Levey, F.C., M.B. Cortie, and L.A. Cornish, *A 500°C isothermal section for the Al-Au-Cu system.* Metall. Mater. Trans. A., 2002. **33A**: p. 987-994.
35. Cortie, M.B. and F.C. Levey, *Formation, modulation and adaptive twinning of martensite in the $Au_7Cu_5Al_4$ shape memory system.* Intermetallics, 2002. **10**: p. 23-31.
36. Levey, F., M. Cortie, and L. Cornish, *Displacive transformations in Au-18 wt pct Cu-6 wt pct Al.* Metallurgical and Materials Transactions A, 2000. **31**(8): p. 1917-1923.

37. Cortie, M.B. and F.C. Levey, *Structure and ordering of the 18-carat Al–Au–Cu ß-phase.* Intermetallics, 2000. **8**(7): p. 793-804.
38. Wan, D., *Thickness effect on thermally induced phase transformations in sputtered titanium-nickel shape-memory films.* Journal of Materials Research, 2005. **20**(6): p. 1606.
39. Kumar, P.K. and D.C. Lagoudas, *Introduction to Shape Memory Alloys Shape Memory Alloys*. 2008, Springer US. p. 1-51.
40. Kurdjumov, G. and L. Khandros, *First reports of the thermoelastic behaviour of the martensitic phase of Au-Cd alloys.* Doklady Akademii Nauk SSSR, 1949. **66**: p. 211-213.
41. Wang, Y., X. Ren, and K. Otsuka, *Shape Memory Effect and Superelasticity in a Strain Glass Alloy.* Physical Review Letters, 2006. **97**(22): p. 225703.
42. Wayman, C.M., *Shape memory and related phenomena.* Progress in Materials Science, 1992. **36**: p. 203-224.
43. Ryhänen, J. *Biocompatibility evaluation of nickel-titanium shape memory metal alloy*. 1999 2000 [cited 2008 20/5/08]; Available from: http://herkules.oulu.fi/isbn9514252217/html/x317.html.
44. Kennon, N.F., D.P. Dunne, and L. Middleton, *Aging Effects in Copper-Based Shape Memory Alloys.* Metallurgical Transactions a-Physical Metallurgy and Materials Science, 1982. **13**(4): p. 551-555.
45. Murakami, Y., et al., *Effect of Aging Zeta'2 Marteniste on the Enthalpy of Transformation in a Au-49.5 at% Cd- Alloy.* Materials Letters, 1994. **21**(3-4): p. 275-278.
46. Hartl, D.J. and D.C. Lagoudas, *Aerospace applications of shape memory alloys.* Proceedings of the Institution of Mechanical Engineers, Part G: Journal of Aerospace Engineering, 2007. **221**(4): p. 535-552.
47. Funakubo, H., *Shape Memory Alloys.* Hiroyasu Funakubo, University of Tokyo, 1987.
48. Titov, P.V., *Effect of shape memory in alloys based on the system Cu−Al.* Metal Science and Heat Treatment, 1984. **26**(3): p. 239-243.
49. Tang, S.M., C.Y. Chung, and W.G. Liu, *Preparation of Cu-Al-Ni-based shape memory alloys by mechanical alloying and powder metallurgy method.* Journal of Materials Processing Technology, 1997. **63**(1-3): p. 307-312.
50. Recarte, V., et al., *Precipitation of the stable phases in Cu-Al-Ni shape memory alloys.* Scripta Materialia, 1996. **34**(2): p. 255-260.
51. Belkahla, S., H. Flores Zuniga, and G. Guenin, *Elaboration and characterization of new low temperature shape memory Cu-Al-Be alloys.* Materials science & engineering. A, Structural materials: properties, microstructure and processing, 1993. **169**(1-2): p. 119-124.
52. Asanovic, V., K. Delijic, and N. Jaukovic, *A study of transformations of Beta-phase in Cu-Zn-Al shape memory alloys.* Scripta Materialia, 2008. **58**(7): p. 599-601.
53. Arneodo Larochette, P., et al., *On the stability of the martensitic phases in Cu–Zn–Al, and its relationship with the equilibrium phases.* Materials Science & Engineering A, 2006. **438**: p. 747-750.
54. Xu, J.W., *Effects of Gd addition on microstructure and shape memory effect of Cu-Zn-Al alloy.* Journal of Alloys and Compounds, 2008. **448**(1-2): p. 331-335.

55. Zheng, Y., et al., *Cu–Al–Mn alloy with shape memory effect at low temperature.* Journal of Alloys and Compounds, 2007. **441**(1-2): p. 317-322.
56. Mallik, U.S. and V. Sampath, *Effect of composition and ageing on damping characteristics of Cu–Al–Mn shape memory alloys.* Materials Science & Engineering A, 2008. **478**(1-2): p. 48-55.
57. Mallik, U.S. and V. Sampath, *Effect of alloying on microstructure and shape memory characteristics of Cu–Al–Mn shape memory alloys.* Materials Science & Engineering A, 2008. **481**: p. 680-683.
58. Sutou, Y., R. Kainuma, and K. Ishida, *Effect of alloying elements on the shape memory properties of ductile Cu–Al–Mn alloys.* Materials Science and Engineering: A, 1999. **273–275**(0): p. 375-379.
59. Montecinos, S., A. Cuniberti, and A. Sepulveda, *Grain size and pseudoelastic behaviour of a Cu-Al-Be alloy.* Materials Characterization, 2008. **59**(2): p. 117-123.
60. Survey, U.S.G., *Metal Prices in the United States through 1998*. 1999.
61. Levey, F.C. and M.B. Cortie, *Body-centred tetragonal martensite formed from $Au_7Cu_5Al_4$ β phase.* Mater. Sci. Engng A, 2001. **303**: p. 1-10.
62. Besseghini, S., et al., *Gold with a Martensitic Transformation: Which Opportunities?* Gold Bulletin, 2007. **40**(4): p. 328-335.
63. Isobe, Y., *Form retaining alloy*. 1991: Japan.
64. Wolff, I.M. and M.B. Cortie, *The development of Spangold.* Gold Bull., 1994. **27**(2): p. 44-54.
65. Sato, H. and R.S. Toth, *Effect of additional elements on the period of CuAuII and the origin of the long-period superlattice.* Physical Review, 1961. **124**(6): p. 1833-1847.
66. Battezzati, L., G. Fiore, and M. Massazza, *A shape memory gold alloy processed by rapid solidification.* J. Alloys and Compounds, 2007. **434/435**: p. 264-267.
67. Jin, M., J. Liu, and X. Jin, *Ordering transitions in quenched Au7Cu5Al4 alloy and effect of order on martensitic transformation.* Intermetallics, 2010. **18**(5): p. 846-850.
68. Cortie, M.B., et al., *High temperature transformations of the Au7Cu5Al4 shape-memory alloy.* Journal of Alloys and Compounds, 2010.
69. Abu Arab, A. and M. Ahlers, *The stabilization of martensite in Cu–Zn–Al alloys.* Acta Metall, 1988. **36**: p. 2627–2638.
70. Kustov, S., et al., *Chemical and mechanical stabilization of martensite.* Acta Materialia, 2004. **52**(15): p. 4547-4559.
71. Abu-Arab, A., M. Chandrasekaran, and M. Ahlers, *Martensite ageing and its stabilisation in Cu? Zn? Al shape memory alloys.* Scripta Metallurgica, 1984. **18**(7): p. 709-714.
72. Kustov, S., et al., *Pinning-induced stabilization of martensite Part I. Stabilization due to static pinning of interfaces.* Acta Materialia, 2004. **52**(10): p. 3075-3081.
73. Adigüzel, O., *Martensite ordering and stabilization in copper based shape memory alloys.* Materials Research Bulletin, 1995. **30**(6): p. 755-760.
74. Otsuka, K. and X. Ren, *Mechanism of martensite aging effect.* Scripta Materialia, 2004. **50**(2): p. 207-212.

75. Ahlers, M. and J.L. Pelegrina, *Ageing of martensite: stabilisation and ferroelasticity in Cu-based shape memory alloys.* Materials Science & Engineering A, 2003. **356**(1-2): p. 298-315.
76. Ishida, A., A. Takei, and S. Miyazaki, *Shape memory thin film of Ti---Ni formed by sputtering.* Thin Solid Films, 1993. **228**(1-2): p. 210-214.
77. Ho, K.K. and G.P. Carman, *Sputter deposition of NiTi thin film shape memory alloy using a heated target.* Thin Solid Films, 2000. **370**(1-2): p. 18-29.
78. Quandt, E., et al., *Sputter deposition of TiNi, TiNiPd and TiPd films displaying the two-way shape-memory effect.* Sensors and Actuators A: Physical, 1996. **53**(1-3): p. 434-439.
79. Ren, M.H., et al., *Sputter-deposited Ti-Ni-Cu shaped memory alloy thin films.* Materials & Design, 2000. **21**(6): p. 583-586.
80. Fu, Y., H. Du, and S. Zhang, *Sputtering deposited TiNi films: relationship among processing, stress evolution and phase transformation behaviors.* Surface and Coatings Technology, 2003. **167**(2-3): p. 120-128.
81. Meng, X.L., M. Sato, and A. Ishida, *Structure of martensite in sputter-deposited (Ni,Cu)-rich Ti-Ni-Cu thin films containing Ti(Ni,Cu)2 precipitates.* Acta Materialia, 2009. **57**(5): p. 1525-1535.
82. Huang, X. and Y. Liu, *Substrate-induced stress and the transformation behavior of sputter-deposited NiTi thin films.* Materials Science and Engineering A, 2003. **352**(1-2): p. 314-317.
83. Nanda Kumar, A.K., et al., *TEM and nanoindentation studies on sputtered Ti40Ni60 thin films.* Materials Chemistry and Physics, 2006. **97**(2-3): p. 308-314.
84. Fu, Y., et al., *XPS characterization of surface and interfacial structure of sputtered TiNi films on Si substrate.* Materials Science and Engineering: A, 2005. **403**(1-2): p. 25-31.
85. Baldwin, E., et al., *Processing TiPdNi base thin-film shape memory alloys using ion beam assisted deposition.* Surface and Coatings Technology, 2005. **200**(7): p. 2571-2579.
86. Otsuka, K. and X. Ren, *Recent developments in the research of shape memory alloys.* Intermetallics, 1999. **7**(5): p. 511-528.
87. Surbled, P., et al., *Effect of the composition and thermal annealing on the transformation temperatures of sputtered TiNi shape memory alloy thin films.* Thin Solid Films, 2001. **401**(1-2): p. 52-59.
88. Fu, Y., H. Du, and S. Zhang, *Adhesion and interfacial structure of magnetron sputtered TiNi films on Si/SiO2 substrate.* Thin Solid Films, 2003. **444**(1-2): p. 85-90.
89. Rumpf, H., et al., *High ultimate tensile stress in nano-grained superelastic NiTi thin films.* Materials Science and Engineering: A, 2006. **415**(1-2): p. 304-308.
90. Kohl, M., *Shape memory microactuators*. 2004: Springer Verlag.
91. Miyazaki, S., Y.Q. Fu, and W.M. Huang, *Thin film shape memory alloys: fundamentals and device applications*. 2009: Cambridge University Press.
92. Seshan, K., *Handbook of thin film deposition processes and techniques*. 2002: Noyes Publ.
93. Sree Harsha, K.S., *Structure and Properties of Films*, in *Principles of Vapor Deposition of Thin Films (First Edition)*. 2005, Elsevier: Oxford. p. 961-1072.

94. Zhang, C., et al., *Characteristics of Ti-Ni-Pd shape memory alloy thin films.* Materials Characterization, 2005. **55**(4-5): p. 340-344.
95. Kim, H.Y., M. Mizutani, and S. Miyazaki, *Crystallization process and shape memory properties of Ti-Ni-Zr thin films.* Acta Materialia, 2009. **57**(6): p. 1920-1930.
96. Inoue, S., N. Sawada, and T. Namazu, *Effect of Zr content on mechanical properties of Ti-Ni-Zr shape memory alloy films prepared by dc magnetron sputtering.* Vacuum, 2008. **83**(3): p. 664-667.
97. Wang, X., Y. Bellouard, and J.J. Vlassak, *Laser annealing of amorphous NiTi shape memory alloy thin films to locally induce shape memory properties.* Acta Materialia, 2005. **53**(18): p. 4955-4961.
98. Martins, R.M.S., et al., *In-situ study of Ni-Ti thin film growth on a TiN intermediate layer by X-ray diffraction.* Sensors and Actuators B: Chemical, 2007. **126**(1): p. 332-337.
99. Waitz, T., V. Kazykhanov, and H. Karnthaler, *Martensitic phase transformations in nanocrystalline NiTi studied by TEM.* Acta Materialia, 2004. **52**(1): p. 137-147.
100. Waitz, T. and H. Karnthaler, *Martensitic transformation of NiTi nanocrystals embedded in an amorphous matrix.* Acta Materialia, 2004. **52**(19): p. 5461-5469.
101. Waitz, T., et al., *Size effects on the martensitic phase transformation of NiTi nanograins.* Journal of the Mechanics and Physics of Solids, 2007. **55**(2): p. 419-444.
102. Waitz, T., et al., *Size-dependent martensitic transformation path causing atomic-scale twinning of nanocrystalline NiTi shape memory alloys.* EPL (Europhysics Letters), 2005. **71**: p. 98.
103. Ishida, A. and M. Sato, *Thickness effect on shape memory behavior of Ti-50.0at.%Ni thin film.* Acta Materialia, 2003. **51**(18): p. 5571-5578.
104. Sawaguchi, T., M. Sato, and A. Ishida, *Grain-size effect on shape-memory behavior of Ti35.0;Ni49.7;Zr15.4 thin films.* Metallurgical and Materials Transactions A, 2004. **35**(1): p. 111-119.
105. Quandt, E., et al., *Actuator Materials for Small-scale Devices*, in *Encyclopedia of Materials: Science and Technology*. 2001, Elsevier: Oxford. p. 35-38.
106. Tomozawa, M., H.Y. Kim, and S. Miyazaki, *Shape memory behavior and internal structure of Ti-Ni-Cu shape memory alloy thin films and their application for microactuators.* Acta Materialia, 2009. **57**(2): p. 441-452.
107. Mineta, T., et al., *Flash-evaporated TiNiCu thick film for shape memory alloy micro actuator.* Microelectronic Engineering, 2009. **86**(4-6): p. 1274-1277.
108. Zarnetta, R., et al., *Influence of precipitates on the thermal hysteresis of Ti-Ni-Pd shape memory thin films.* Scripta Materialia, 2009. **60**(5): p. 352-355.
109. Panduranga, M.K., D.D. Shin, and G.P. Carman, *Shape memory behavior of high temperature Ti-Ni-Pt thin films.* Thin Solid Films, 2006. **515**(4): p. 1938-1941.
110. Fu, Y. and H. Du, *Magnetron sputtered Ti50Ni40Pt10 shape memory alloy thin films.* Journal of Materials Science Letters, 2003. **22**(7): p. 531-533.

111. Sanjabi, S., Y.Z. Cao, and Z.H. Barber, *Multi-target sputter deposition of Ni50Ti50 - xHfx shape memory thin films for high temperature microactuator application.* Sensors and Actuators A: Physical, 2005. **121**(2): p. 543-548.
112. Krulevitch, P., et al., *Thin film shape memory alloy microactuators.* Microelectromechanical Systems, Journal of, 1996. **5**(4): p. 270-282.
113. Kik, P. and M. Brongersma, *Surface plasmon nanophotonics*, M. Brongersma and P. Kik, Editors. 2007, Springer Berlin / Heidelberg. p. 1-9.
114. Kim, Y.K., et al., *Focused ion beam nanopatterning for optoelectronic device fabrication.* Selected Topics in Quantum Electronics, IEEE Journal of, 2005. **11**(6): p. 1292-1298.
115. Cabrini, S., et al., *Focused ion beam lithography for two dimensional array structures for photonic applications.* Microelectronic Engineering, 2005. **78**: p. 11-15.
116. Watt, F., et al., *Ion beam lithography and nanofabrication: a review.* International Journal of Nanoscience, 2005. **4**(3): p. 269-286.
117. Randolph, S., J. Fowlkes, and P. Rack, *Focused, nanoscale electron-beam-induced deposition and etching.* Critical reviews in solid state and materials sciences, 2006. **31**(3): p. 55-89.
118. Homola, J., S.S. Yee, and G. Gauglitz, *Surface plasmon resonance sensors: review.* Sensors and Actuators B: Chemical, 1999. **54**(1-2): p. 3-15.
119. Fägerstam, L.G., et al., *Detection of antigen—antibody interactions by surface plasmon resonance. Application to Epitope Mapping.* Journal of Molecular Recognition, 1990. **3**(5-6): p. 208-214.
120. Mayo, C.S. and R.B. Hallock, *Immunoassay based on surface plasmon oscillations.* Journal of Immunological Methods, 1989. **120**(1): p. 105-114.
121. Cullen, D.C., R.G.W. Brown, and C.R. Lowe, *Detection of immuno-complex formation via surface plasmon resonance on gold-coated diffraction gratings.* Biosensors, 1987. **3**(4): p. 211-225.
122. Miwa, S. and T. Arakawa, *Selective gas detection by means of surface plasmon resonance sensors.* Thin Solid Films, 1996. **281-282**(1-2): p. 466-468.
123. Abdelghani, A., et al., *Surface plasmon resonance fibre-optic sensor for gas detection.* Sensors and Actuators, B: Chemical, 1997. **39**(1-3): p. 407-410.
124. Podgorsek, R.P., et al., *Optical gas sensing by evaluating ATR leaky mode spectra.* Sensors and Actuators, B: Chemical, 1997. **39**(1-3): p. 349-352.
125. Niggemann, M., et al., *Remote sensing of tetrachloroethene with a micro-fibre optical gas sensor based on surface plasmon resonance spectroscopy.* Sensors and Actuators, B: Chemical, 1996. **34**(1-3): p. 328-333.
126. Weiss, M., R. Srivastava, and H. Groger, *Experimental investigation of a surface plasmon-based integrated-optic humidity sensor.* Electronics Letters, 1996. **32**(9): p. 842-843.
127. Özdemir, S.K. and G. Turhan-Sayan, *Temperature effects on surface plasmon resonance: design considerations for an optical temperature sensor.* Journal of lightwave technology, 2003. **21**(3): p. 805.
128. Bai, H., et al., *The preparation of a plasmonically resonant VO2 thermochromic pigment.* Nanotechnology, 2009. **20**: p. 085607.
129. Cortie, M., et al., *Core-shell nanoparticles with self-regulating plasmonic functionality.* Physical Review B, 2007. **75**(11): p. 113405.

130. Rini, M., et al., *Giant, ultrafast optical switching based on an Insulator-to-Metal Transition in VO2 Nano-particles: Photo-activation of shape-controlled plasmons at 1.55 mu-m*. 2004.
131. Xu, G., et al., *Nano-Ag on vanadium dioxide. II. Thermal tuning of surface plasmon resonance.* Journal of Applied Physics, 2008. **104**(5): p. 053102-053102-6.
132. Mott, N.F. and G.B. Physicist, *Metal-insulator transitions*. 1990: Taylor & Francis London.
133. Morin, F.J., *Oxides Which Show a Metal-to-Insulator Transition at the Neel Temperature.* Physical Review Letters, 1959. **3**(1): p. 34-36.
134. Soares, B.F., et al., *Light-induced switching between structural forms with different optical properties in a single gallium nanoparticulate.* Nano letters, 2005. **5**(10): p. 2104-2107.
135. Soares, B.F., F. Jonsson, and N.I. Zheludev, *All-optical phase-change memory in a single gallium nanoparticle.* Physical Review Letters, 2007. **98**(15): p. 153905.
136. Lee, K.S. and M.A. El-Sayed, *Gold and silver nanoparticles in sensing and imaging: sensitivity of plasmon response to size, shape, and metal composition.* The Journal of Physical Chemistry B, 2006. **110**(39): p. 19220-19225.
137. Noguez, C., *Surface Plasmons on Metal Nanoparticles: The Influence of Shape and Physical Environment.* The Journal of Physical Chemistry C, 2007. **111**(10): p. 3806-3819.
138. Wiley, B.J., et al., *Maneuvering the Surface Plasmon Resonance of Silver Nanostructures through Shape-Controlled Synthesis.* The Journal of Physical Chemistry B, 2006. **110**(32): p. 15666-15675.
139. Hulst, H.C. and H. Van De Hulst, *Light scattering by small particles*. 1957: Dover Pubns.
140. Veronis, G. and S. Fan, *Overview of simulation techniques for plasmonic devices Surface Plasmon Nanophotonics*, M. Brongersma and P. Kik, Editors. 2007, Springer Berlin / Heidelberg. p. 169-182.
141. Yurkin, M.A. and A.G. Hoekstra, *The discrete dipole approximation: An overview and recent developments.* Journal of Quantitative Spectroscopy and Radiative Transfer, 2007. **106**(1–3): p. 558-589.
142. Otsuka, K. and C.M. Wayman, *Shape memory materials*. 1999: Cambridge University Press.
143. Aliya, D., *Metallographic Sectioning and Specimen Extraction*, in *Metallography and Microstructures*. 2004, ASM International. p. 229–241.
144. Voort, V. and F. George, *Metallography, principles and practice, ASM Int.* Mater. Park, Ohio, 1999. **487**.
145. *Mounting of Specimens*, in *Metallography and Microstructures*. 2004, ASM International. p. 242–256.
146. *Mechanical Grinding and Polishing*, in *Metallography and Microstructures*. 2004, ASM International. p. 257–280.
147. Höhne, G., W. Hemminger, and H.J. Flammersheim, *Differential Scanning Calorimetry*. 2003: Springer.

148. Recarte, V., et al., *High temperature β phase decomposition process in a Cu–Al–Ni shape memory alloy.* Materials Science and Engineering: A, 2004. **378**(1): p. 238-242.
149. Voort, G.F.V., *Light Microscopy*, in *Metallography and Microstructures*. 2004, ASM International. p. 332–354.
150. Clarke, A.R. and C.N. Eberhardt, *Microscopy Techniques for Materials Science*. 2002: CRC Press.
151. H.E. Exner, S.W., *Scanning Electron Microscopy*, in *Metallography and Microstructures*. 2004, ASM International. p. 355–367.
152. Jenkins, R. and R.L. Snyder, *Introduction to X-ray Powder Diffractometry.* Chemical Analysis, 1996. **138**: p. 64–81.
153. *How does the australian synchrotron work?* 2012 [cited 2012 12/11/2012]; Available from: http://www.synchrotron.org.au/index.php/about-us/our-facilities/accelerator-physics/how-does-the-australian-synchrotron-work.
154. *Technical information (Powder)*. 2012 12/11/2012]; Available from: http://www.synchrotron.org.au/index.php/aussyncbeamlines/powder-diffraction/technical-information.
155. Copley, J.R.D., *Methods and Applications of Neutron Spectroscopy*, in *Dynamics and Neutron Scattering*. 2007, NIST.
156. *Echidna Specifications*. 2012 [cited 2012 12/11/2012]; Available from: http://www.ansto.gov.au/research/bragg_institute/facilities/instruments/echidna/specifications.
157. Mattox, D.M., *Handbook of Physical Vapor Deposition (PVD) Processing*. 1998, William Andrew Publishing/Noyes. p. 664-743.
158. Birkholz, M., *Grazing Incidence Configurations*, in *Thin Film Analysis by X-Ray Scattering*. 2006, Wiley-VCH Verlag GmbH & Co. KGaA. p. 143-182.
159. Nelson, A., *Co-refinement of multiple-contrast neutron/X-ray reflectivity data using MOTOFIT.* Journal of Applied Crystallography, 2006. **39**(2): p. 273-276.
160. Williams, D.B. and C.B. Carter, *The Instrument Transmission Electron Microscopy*. 2009, Springer US. p. 141-171.
161. Rossiter, P.L., *The electrical resistivity of metals and alloys*. 1991: Cambridge Univ Pr.
162. Löbel, R., et al., *Combinatorial fabrication and high-throughput characterization of a Ti–Ni–Cu shape memory thin film composition spread.* Materials Science and Engineering: A, 2008. **481-482**(0): p. 151-155.
163. Benninghoven, A., F. Rudenauer, and H.W. Werner, *Secondary ion mass spectrometry: basic concepts, instrumental aspects, applications and trends.* 1987.
164. Draine, B.T. and P.J. Flatau, *User Guide for the Discrete Dipole Approximation Code DDSCAT 7.2.* Arxiv preprint arXiv:1202.3424, 2012.
165. Ira M Wolff, M.B.C., *The Development of Spangold* Gold Bulletin, 1994. **27**(2): p. 44 - 54.
166. Bhatia, V., et al., *Thin Films of AuCuAl Shape Memory Alloy for Use in Plasmonic Nano-actuators.* MRS Online Proceedings Library, 2011. **1295**.
167. Recarte, V., et al., *Influence of Al and Ni concentration on the Martensitic transformation in Cu-Al-Ni shape-memory alloys.* Metallurgical and Materials Transactions A, 2002. **33**(8): p. 2581-2591.

168. Swann, P.R. and H. Warlimont, *The electron-metallography and crystallography of copper-aluminum martensites.* Acta Metallurgica, 1963. **11**(6): p. 511-527.
169. Rodríguez-Aseguinolaza, J., et al., *Kinetic effects in the mixed β to martensitic transformation in a Cu–Al–Ni shape memory alloy.* Acta Materialia, 2010. **58**(2): p. 692-701.
170. Tabib-Azar, M., B. Sutapun, and M. Huff, *Applications of TiNi thin film shape memory alloys in micro-opto-electro-mechanical systems.* Sensors and Actuators A: Physical, 1999. **77**(1): p. 34-38.
171. Suresh, N. and U. Ramamurty, *Aging response and its effect on the functional properties of Cu–Al–Ni shape memory alloys.* Journal of Alloys and Compounds, 2008. **449**(1-2): p. 113-118.
172. Ren, X. and K. Otsuka, *Origin of rubber-like behaviour in metal alloys.* Nature, 1997. **389**(6651): p. 579-581.
173. Van Petegem, S., et al., *Characterization of defects in a martensitic CuAlNi shape-memory alloy.* Applied Physics A: Materials Science & Processing, 2005. **81**(5): p. 1039-1044.
174. Ishibashi, H., et al., *Vacancy migration and long-range ordering due to ageing in AuCd shape memory alloys.* Materials Science and Engineering: A, 2002. **329**: p. 568-572.
175. Plotnikov, V. and Y.I. Paskal, *Accommodation and relaxation in martensite transformations.* Russian Physics Journal, 1997. **40**(5): p. 448-456.
176. Simon, T., et al., *On the multiplication of dislocations during martensitic transformations in NiTi shape memory alloys.* Acta Materialia, 2010. **58**(5): p. 1850-1860.
177. Rodriguez, P. and G. Guenin, *Thermal aging behaviour and origin of a Cu---Al--Ni shape memory alloy.* Materials Science and Engineering: A, 1990. **129**(2): p. 273-277.
178. Abràmoff, M.D., P.J. Magalhães, and S.J. Ram, *Image processing with ImageJ.* Biophotonics international, 2004. **11**(7): p. 36-42.
179. Maṇosa, L.I., et al., *A comparative study of the post-quench behaviour of Cu-Al-Be and Cu-Zn-Al shape memory alloys.* Acta Materialia, 1998. **46**(3): p. 1045-1053.
180. Grossmann, C., et al., *Elementary Transformation and Deformation Processes and the Cyclic Stability of NiTi and NiTiCu Shape Memory Spring Actuators.* Metallurgical and Materials Transactions A, 2009. **40**(11): p. 2530-2544.
181. Bhatia, V., et al., *Martensite destabilization in Au7Cu5Al4 shape-memory alloy.* Acta Materialia, 2011.
182. Scarsbrook, G., J. Cook, and W. Stobbs, *The stabilization of martensite in Cu-Zn-AI shape memory alloys.* Metallurgical and Materials Transactions A, 1984. **15**(11): p. 1977-1986.
183. Romero, R., et al., *Quenched-in defects and martensitic transformation in Cu-Al-Be shape memory alloys.* Acta mater., 1997. **45**(5): p. 2101-2107.
184. Kong, Y., et al., *The Behavior of Quenched-in Vacancies and Stabilization of Martensite in Copper-Based Shape Memory Alloys.* physica status solidi (a), 1992. **133**(2): p. 269-275.

185. Lai, M.O., L. Lu, and W.H. Lee, *Influence of heat treatment on properties of copper-based shape-memory alloy.* Journal of Materials Science, 1996. **31**(6): p. 1537-1543.
186. Plotnikov, V. and Y. Paskal, *Accommodation and relaxation in martensite transformations.* Russian Physics Journal, 1997. **40**(5): p. 448-456.
187. Sutou, Y., et al., *Effects of ageing on bainitic and thermally induced martensitic transformations in ductile Cu–Al–Mn-based shape memory alloys.* Acta Materialia, 2009. **57**(19): p. 5748-5758.
188. Miura, S., S. Maeda, and N. Nakanishi, *Pseudoelastic and shape memory phenomena related to stress-induced martensite in Cu-15.0 at .% Sn alloy.* Scripta Metallurgica, 1975. **9**(6): p. 675-680.
189. Murakami, M., et al., *Ternary diffusion in multilayer Ag-Au-Cu thin films.* Thin Solid Films, 1975. **25**(2): p. 465-482.
190. Poate, J., et al., *Thin-film interdiffusion. I. Au-Pd, Pd-Au, Ti-Pd, Ti-Au, Ti-Pd-Au, and Ti-Au-Pd.* Journal of Applied Physics, 1975. **46**(10): p. 4275-4283.
191. Majni, G., et al., *Gold-aluminum thin-film interactions and compound formation.* Journal of Applied Physics, 1981. **52**(6): p. 4047-4054.
192. Maldonado, R. and A. Oliva, *Morphology and Electrical Resistivity of AuCu Nanofilm Alloys.* Surface Review and Letters, 2009. **15**(6): p. 881.
193. Golan, Y., L. Margulis, and I. Rubinstein, *Vacuum-deposited gold films: I. Factors affecting the film morphology.* Surface Science, 1992. **264**(3): p. 312-326.
194. Schug, C., et al., *Surface roughness of sputter-deposited gold films: a combined x-ray technique and AFM study.* Surface and Interface Analysis, 1999. **27**(7): p. 670-677.
195. Chiarello, R., et al., *X-ray reflectivity study on gold films during sputter deposition.* Surface Science, 1997. **380**(2): p. 245-257.
196. Seshan, K., *Handbook of Thin-Film Deposition Processes and Techniques - Principles, Methods, Equipment and Applications (2nd Edition)*. 2002, William Andrew Publishing/Noyes. p. 319-348.
197. Westbrook, J.H. and R.L. Fleischer, *Intermetallic Compounds, Volume 1 - Crystal Structures of Intermetallic Compounds*. John Wiley & Sons. p. 1-49.
198. Piao, H. and N.S. McIntyre, *Oxidation studies of Au-Al alloys using x-ray photoelectron spectroscopy (XPS) and x-ray absorption near-edge structure (XANES).* Surface and Interface Analysis, 2001. **31**(9): p. 874-880.
199. Piao, H., et al., *A study of thin film Au–Al alloy oxidation in ambient air by X-ray photoelectron spectroscopy (XPS), X-ray absorption near edge structure (XANES), and secondary ion mass spectrometry (SIMS).* Applied Surface Science, 2002. **187**(3-4): p. 266-274.
200. Uthanna, S., et al., *Process-parameter-dependent structural, electrical, and optical properties of reactive magnetron sputtered Ag-Cu-O films.* Journal of Nanotechnology, 2011.
201. Vishnoi, R. and D. Kaur, *Size dependence of martensite transformation temperature in nanostructured Ni–Mn–Sn ferromagnetic shape memory alloy thin films.* Surface and Coatings Technology, 2010. **204**(23): p. 3773-3782.

202. König, D., et al., *Thickness-dependence of the B2–B19 martensitic transformation in nanoscale shape memory alloy thin films: Zero-hysteresis in 75nm thick Ti51Ni38Cu11 thin films.* Acta Materialia, 2012. **60**(1): p. 306-313.
203. Piao, M., S. Miyazaki, and K. Otsuka, *Characteristics of deformation and transformation in Ti 44 Ni 47 Nb 9 shape memory alloy.* JIM, Materials Transactions, 1992. **33**(4): p. 346-353.
204. Meng, X., et al., *Effect of aging on the phase transformation and mechanical behavior of Ti36Ni49Hf15 high temperature shape memory alloy.* Scripta Materialia, 2000. **42**(4): p. 341-348.
205. Barcikowski, S., et al., *Biocompatibility of nanoactuators: stem cell growth on laser-generated nickel–titanium shape memory alloy nanoparticles.* Journal of Nanoparticle Research, 2010. **12**(5): p. 1733-1742.
206. Montecinos, S., A. Cuniberti, and R. Romero, *Effect of grain size on the stress–temperature relationship in a β CuAlBe shape memory alloy.* Intermetallics, 2011. **19**(1): p. 35-38.
207. Adnyana, D.N., *Effect of grain size on transformation temperatures in a grain-refined, copper-based, shape-memory alloy.* Metallography, 1986. **19**(2): p. 187-196.
208. Kumar, A., D. Singh, and D. Kaur, *Grain size effect on structural, electrical and mechanical properties of NiTi thin films deposited by magnetron co-sputtering.* Surface and Coatings Technology, 2009. **203**(12): p. 1596-1603.
209. Taylor, R.E., *Thermal expansion of solids*. Vol. 4. 1998: ASM International (OH).
210. Van Humbeeck, J., et al., *The stabilisation of step-quenched copper-zinc-aluminum martensite part I: The reverse transformation temperatures.* Scripta Metallurgica, 1984. **18**(9): p. 893-898.
211. Tong, H.C. and C.M. Wayman, *Thermodynamics of thermoelastic martensitic transformations.* Acta Metallurgica, 1975. **23**(2): p. 209-215.
212. Hamilton, R.F., et al., *Stress dependence of the hysteresis in single crystal NiTi alloys.* Acta Materialia, 2004. **52**(11): p. 3383-3402.
213. Zarinejad, M. and Y. Liu, *Dependence of Transformation Temperatures of NiTi-based Shape-Memory Alloys on the Number and Concentration of Valence Electrons.* Advanced Functional Materials, 2008. **18**(18): p. 2789-2794.
214. Delville, R., et al., *Transmission electron microscopy investigation of microstructures in low-hysteresis alloys with special lattice parameters.* Scripta Materialia, 2009. **60**(5): p. 293-296.
215. Yang, Y., et al., *Aligned silver nanorod arrays for surface-enhanced Raman scattering.* Nanotechnology, 2006. **17**: p. 2670–2674.
216. Orendorff, C.J., et al., *Aspect ratio dependence on surface enhanced Raman scattering using silver and gold nanorod substrates.* Physical Chemistry : Chemical Physics, 2006. **8**: p. 165-170.
217. Charnay, C., et al., *Reduced symmetry metallodielectric nanoparticles: chemical synthesis and plasmonic properties.* Journal of Physical Chemistry B, 2003. **107**(30): p. 7327-7333.
218. Liu, J., et al., *Anisotropic optical properties of semitransparent coatings of gold nanocaps.* Adv. Funct. Mater., 2006. **16**(11): p. 1457 - 1461.

219. Stokes, N., A. McDonagh, and M.B. Cortie, *Spectrally Selective Coatings Based on Anisotropic Gold Nanoparticles.* J. Nanopart. Res. , 2010. **12**(8): p. 2821-2830.
220. Hirsch, L.R., et al., *Nanoshell-Mediated Near-Infrared Thermal Therapy of Tumors under Magnetic Resonance Guidance.* Proc. Natl. Acad. Sci. U. S. A., 2003. **100**(23): p. 13549-13554.
221. Huang, X., et al., *Cancer cell imaging and photothermal therapy in the near-infrared region by using gold nanorods.* J. Am. Chem. Soc., 2006. **128**(6): p. 2115-2120.
222. Pissuwan, D., S. Valenzuela, and M.B. Cortie, *Therapeutic possibilities of plasmonically heated gold nanoparticles.* Trends Biotechnol., 2006. **24**(2): p. 62-67.
223. Pissuwan, D., et al., *A golden bullet? Selective targeting of Toxoplasma gondii tachyzoites using antibody-functionalised gold nanoparticles.* Nano Lett., 2007. **7**(12): p. 3808-3812.
224. Xu, C., et al., *Au-Fe3O4 dumbbell nanoparticles as dual-functional probes.* Angew. Chem., Int. Ed., 2008. **47**(1): p. 173-176.
225. Weaver, J. and H. Frederikse, *Optical properties of selected elements.* CRC Handbook of Chemistry and Physics, CRC Press, Boca Raton, 2001: p. 12-133.
226. Stokes, N., et al., *Plasmon Resonances in V-Shaped Gold Nanostructures.* Plasmonics, 2012(7): p. 235-243.
227. Brioude, A., X. Jiang, and M. Pileni, *Optical properties of gold nanorods: DDA simulations supported by experiments.* The Journal of Physical Chemistry B, 2005. **109**(27): p. 13138-13142.
228. Myroshnychenko, V., et al., *Modelling the optical response of gold nanoparticles.* Chemical Society Reviews, 2008. **37**(9): p. 1792-1805.
229. Nebeker, B.M., J.L. de la Peña, and E.D. Hirleman, *Comparisons of the discrete-dipole approximation and modified double interaction model methods to predict light scattering from small features on surfaces.* Journal of Quantitative Spectroscopy and Radiative Transfer, 2001. **70**(4): p. 749-759.
230. Jain, P.K., et al., *Calculated absorption and scattering properties of gold nanoparticles of different size, shape, and composition: applications in biological imaging and biomedicine.* The Journal of Physical Chemistry B, 2006. **110**(14): p. 7238-7248.
231. Vitushinsky, R., S. Schmitz, and A. Ludwig, *Bistable Thin-Film Shape Memory Actuators for Applications in Tactile Displays.* Microelectromechanical Systems, Journal of, 2009. **18**(1): p. 186-194.
232. Makino, E., T. Mitsuya, and T. Shibata, *Fabrication of TiNi shape memory micropump.* Sensors and Actuators A: Physical, 2001. **88**(3): p. 256-262.
233. Makino, E., M. Uenoyama, and T. Shibata, *Flash evaporation of TiNi shape memory thin film for microactuators.* Sensors and Actuators A: Physical, 1998. **71**(3): p. 187-192.
234. Sreekumar, M., et al., *Recent advances in nonlinear control technologies for shape memory alloy actuators.* Journal of Zhejiang University-Science A, 2007. **8**(5): p. 818-829.